ADVANCED STEEL CONSTRUCTION

An International Journal

Volume 19 Number 1

March 2023

CONTENTS

Technical Papers

The Hong Kong Institute of Steel Construction
Website: *http://www.hkisc.org*
ISSN 1816-112X
Science Citation Index Expanded, Materials Science Citation Index and ISI Alerting
Cover: A composite tall building in Hong Kong. Photo@ Liu Yao-Peng
e-copy of IJASC is free to download at "www.ascjournal.com" in internet and mobile apps.

ADVANCED STEEL CONSTRUCTION

VOL.19, NO.1 (2023)

ADVANCED STEEL CONSTRUCTION

an International Journal

ISSN 1816-112X

Volume 19 Number 1 *March 2023*

Advanced Steel Construction

an international journal

ISSN 1816-112X

Science Citation Index Expanded, Materials Science Citation Index and ISI Alerting

EDITORS-IN-CHIEF

Asian Pacific, African and organizing Editor
S.L. Chan
The Hong Kong Polyt. Univ., Hong Kong, China

American Editor
W.F. Chen
Univ. of Hawaii at Manoa, USA

European Editor
R. Zandonini
Trento Univ., Italy

ASSOCIATE EDITORS

Y.P. Liu
The Hong Kong Polyt. Univ., Hong Kong, China

S.W. Liu
The Hong Kong Polyt. Univ., Hong Kong, China

INTERNATIONAL EDITORIAL BOARD

F.G. Albermani
Central Queensland Univ., Australia

I. Burgess
Univ. of Sheffield, UK

F.S.K. Bijlaard
Delft Univ. of Technology, The Netherlands

R. Bjorhovde
The Bjorhovde Group, USA

M.A. Bradford
The Univ. of New South Wales, Australia

D. Camotim
Technical Univ. of Lisbon, Portugal

C.M. Chan
Hong Kong Univ. of Science & Technology, Hong Kong, China

T.H.T. Chan
Queensland Univ. of Technology, Australia

T.M. Chan
The Hong Kong Polyt. Univ., Hong Kong, China

Z.H. Chen
Tianjin Univ., China

S.P. Chiew
Nanyang Technological Univ., Singapore

W.K. Chow
The Hong Kong Polyt. Univ., Hong Kong, China

G.G. Deierlein
Stanford Univ., California, USA

L. Dezi
Univ. of Ancona, Italy

D. Dubina
The Politehnica Univ. of Timosoara, Romania

R. Greiner
Technical Univ. of Graz, Austria

L. Gardner
Imperial College of Science, Technology and Medicine, UK

Y. Goto
Nagoya Institute of Technology, Japan

L.H. Han
Tsinghua Univ. China

S. Herion
University of Karlsruhe, Germany

G.W.M. Ho
Ove Arup & Partners Hong Kong Ltd., Hong Kong, China

B.A. Izzuddin
Imperial College of Science, Technology and Medicine, UK

J.P. Jaspart
Univ. of Liege, Belgium

S. A. Jayachandran
IIT Madras, Chennai, India

S.E. Kim
Sejong Univ., South Korea

S. Kitipornchai
The Univ., of Queensland, Australia

D. Lam
Univ. of Bradford, UK

H.F. Lam
City Univ. of Hong Kong, Hong Kong, China

G.C Li
Shenyang Jianzhu Univ., China

G.Q. Li
Tongji Univ., China

J.Y.R. Liew
National Univ. of Singapore, Singapore

E.M. Lui
Syracuse Univ., USA

Y.L. Mo
Univ. of Houston, USA

J.P. Muzeau
CUST, Clermont Ferrand, France

D.A. Nethercot
Imperial College of Science, Technology and Medicine, UK

Y.Q. Ni
The Hong Kong Polyt. Univ., Hong Kong, China

D.J. Oehlers
The Univ. of Adelaide, Australia

J.L. Peng
Yunlin Uni. of Science & Technology, Taiwan, China

K. Rasmussen
The Univ. of Sydney, Australia

J.M. Rotter
The Univ. of Edinburgh, UK

C. Scawthorn
Scawthorn Porter Associates, USA

P. Schaumann
Univ. of Hannover, Germany

Y.J. Shi
Tsinghua Univ., China

G.P. Shu
Southeast Univ. China

L. Simões da Silva
Department of Civil Engineering, University of Coimbra, Portugal

J.G. Teng
The Hong Kong Polyt. Univ., Hong Kong, China

G.S. Tong
Zhejiang Univ., China

K.C. Tsai
National Taiwan Univ., Taiwan, China

C.M. Uang
Univ. of California, USA

B. Uy
University of Western Sydney, Australia

M. Veljkovic
Univ. of Lulea, Sweden

F. Wald
Czech Technical Univ. in Prague, Czech

Y.C. Wang
The Univ. of Manchester, UK

Y.L. Xu
The Hong Kong Polyt. Univ., Hong Kong, China

D. White
Georgia Institute of Technology, USA

E. Yamaguchi
Kyushu Institute of Technology, Japan

Y.B. Yang
National Taiwan Univ., Taiwan, China

Y.Y. Yang
China Academy of Building Research, Beijing, China

B. Young
The Univ. of Hong Kong, Hong Kong, China

X.L. Zhao
Monash Univ., Australia

X.H. Zhou
Chongqing University, China

Z.H. Zhou
The Hong Kong Polyt. Univ., Hong Kong, China

S.Y. Zhu
The Hong Kong Polyt. Univ., Hong Kong, China

R.D. Ziemian
Bucknell Univ., USA

Cover: A composite tall building in Hong Kong. Photo @Liu Yao-Peng

e-copy of IJASC is free to download at “www.ascjournal.com” in internet and mobile apps.

General Information
Advanced Steel Construction, an international journal

Aims and scope

The International Journal of Advanced Steel Construction provides a platform for the publication and rapid dissemination of original and up-to-date research and technological developments in steel construction, design and analysis. Scope of research papers published in this journal includes but is not limited to theoretical and experimental research on elements, assemblages, systems, material, design philosophy and codification, standards, fabrication, projects of innovative nature and computer techniques. The journal is specifically tailored to channel the exchange of technological know-how between researchers and practitioners. Contributions from all aspects related to the recent developments of advanced steel construction are welcome.

Subscription inquiries and change of address. Address all subscription inquiries and correspondence to Member Records, IJASC. Notify an address change as soon as possible. All communications should include both old and new addresses with zip codes and be accompanied by a mailing label from a recent issue. Allow six weeks for all changes to become effective.
The Hong Kong Institute of Steel Construction
HKISC
c/o Department of Civil and Environmental Engineering,
The Hong Kong Polytechnic University,
Hunghom, Kowloon, Hong Kong, China.
Tel: 852- 2766 6047 Fax: 852- 2334 6389
Email: *ceslchan@polyu.edu.hk* Website: *http://www.hkisc.org/*
ISSN 1816-112X
Science Citation Index Expanded, Materials Science Citation Index and ISI Alerting

ISSN 1816-112X

Science Citation Index Expanded, Materials Science Citation Index and ISI Alerting

Advanced Steel Construction
an international journal

VOLUME 19 NUMBER 1 **March 2023**

Technical Papers

Advanced Steel Construction – Vol. 19 No. 1 (2023) 1–8
DOI:10.18057/IJASC.2023.19.1.1
(**Special Issue:** *10th International Conference on Advances in Steel Structures, ICASS'2020, Chengdu, China*)

COLLAPSE RESISTANCE CALCULATION WITH DIFFERENT STIFFNESS CONNECTIONS BASED ON THE COMPONENT METHOD

Zheng Tan [1], Wei-Hui Zhong [1, 2, *], Shi-Chao Duan [1], Chao-Fan Li [1], Yu-Hui Zheng [1] and Bao Meng [1]

[1] School of Civil Engineering, Xi'an University of Architecture and Technology, Xi'an 710055, China
[2] Key Laboratory of Structural Engineering and Earthquake Resistance, Ministry of Education, Xi'an University of Architecture and Technology, Xi'an 710055, China
** (Corresponding author: E-mail: zhongweihui1980@163.com)*

ABSTRACT

The collapse performance of steel frames generally depends on their ability to resist local damage. However, this ability is decided by the connection behavior, which has not been determined methodically and reliably. Thus, developing a simplified connection model for predicting the structural collapse resistance is critical for preventing progressive collapse. In this study, component models were constructed with different stiffness connections, including the double web angle (DWA), top-seat with double web angle (TSDWA), and welded flange-bolted web (WUF) connections, according to the component method by simplifying its geometry and dividing it into several basic springs. The proposed component-based connection models with detailed components were implemented within the finite element program, ANSYS. The models were validated against previous experimental tests. The analysis results indicate that the component models can accurately reflect the load response and post-fracture path of the assemblies with a cost-effective solution. This indicates that the component method is significant for progressive collapse analysis, providing a simple and effective tool for designers and engineers to evaluate the load-resisting capacities of steel frame structures.

ARTICLE HISTORY

Received:	20 July 2022
Revised:	22 August 2022
Accepted:	10 January 2023

KEYWORDS

Steel frame;
Different stiffness connections;
Progressive collapse;
Component method;
Numerical simulation

1. Introduction

In recent years, structural progressive collapse has become a topic of considerable research interest in the field of the civil engineering [1–2]. Preventing progressive collapse is a necessary task in structural engineering theory and practice. Progressive collapse primarily results from a chain reaction caused by local damage spreading to other structural components owing to overloading or accidental loads.

Connection failure primarily triggers structural failure and determines whether the internal force can be transmitted effectively. Many experimental studies and numerical analyses have showed that the connection behavior determines the mechanism resistances of frame structures, including compressive arch action, flexural action, and catenary action [3-4]. Therefore, beam–to–column connections are critical components in the anti-collapse design of steel frame structures. Accordingly, it is urgent to develop a simplified connection component model for predicting the mechanical behavior of beam–to–column connections. The most used modeling methods for the numerical simulation analysis of the frame structure collapse resistance include micro (refined modeling) [5–9], macro (node models based on beam or shell elements and component methods) [10], and multiscale hybrid (mixed elements of various types) [11–12] modeling methods. The results obtained by the refined modeling method are the most accurate; however, a systematic parameter analysis using the refined modeling method typically results in high modeling costs and long calculation time, particularly for full-size multistory frame structures. A reasonable component model can significantly increase computational efficiency of the numerical model when replacing the refined model for the structure design and collapse analysis.

With respect to the simplified modeling of steel structures, to investigate the relative performance of the beam–to–column connection, Sarraj et al. [13] and Liu et al. [14] performed component modeling. Yang et al. [15] tested seven different connections under failure condition of middle column through a static loading test. They found that the axial force and rotation of beam end determine the failure mode of the connections. Tan et al. [16] studied the performance of a beam–column assembly with different stiffnesses via static loading tests and demonstrated that different types of connections significantly influence the collapse resistance. Beam–to–column connections are typically subjected to combined tension, bending, and shear forces during the progressive collapse process.

In this study, numerical models of the beam–column assemblies were constructed with different stiffness connections, including the double web angle connection (DWA), top-seat with double web angle connection (TSDWA), and welded flange-bolted web connection (WUF), according to the component method proposed by Eurocode 3 (EC3) [17] by simplifying the geometrical composition of the connections. Subsequently, the applicability and efficiency of these simplified models were validated against previous experimental results.

2. Construction of the component models with different stiffness connections

2.1. Simplified component method modeling

A connection can be simplified into a series of independent fundamental components using the component method (each fundamental component may consist of several mechanical springs). The overall mechanical properties of the connections can be analyzed by studying the nonlinear mechanical characteristics of each component of the connections. Accordingly, the overall response of the connections can be obtained through the collection of components. Applying the component method is significant for analyzing the working mechanism of each connection part. In addition, it can rapidly analyze and accurately acquire the mechanical properties of the beam–column assembly.

2.2. Mechanical behavior analysis of each spring (component)

Determining the mechanical properties of a connection by directly analyzing the deformation mechanism is challenging. The European code EC3 [17] proposes that the connections can be discretized into multiple mechanical units contributing to the force. The components (springs) were integrated to simulate the force state of the connections accurately, with appropriate assumptions. Accordingly, the DWA, TSDWA, and WUF connections comprised the following individual spring forces: connecting plate bolt hole compression (S1), bolt shear (S2), beam web bolt hole compression (S3), bolt tension (S4), angle bending (S5), and beam flange tension–compression (S6) springs. The DWA connection comprised the bolt hole compression spring at the connecting plate, compression spring at the beam web, and bolt shear spring. The TSDWA connection comprised the following individual spring forces: bolt hole compression spring at the angle, bolt shear spring, bolt hole compression spring at the beam, and bolt tension and angle bending springs. The WUF connection comprised the connecting plate compression, beam web compression, bolt shear, and beam flange tension–compression spring forces. These springs can be simplified further according to their serial and parallel relationships. Different springs were combined to form an equivalent component in series to model the different connections, as shown in Fig. 1.

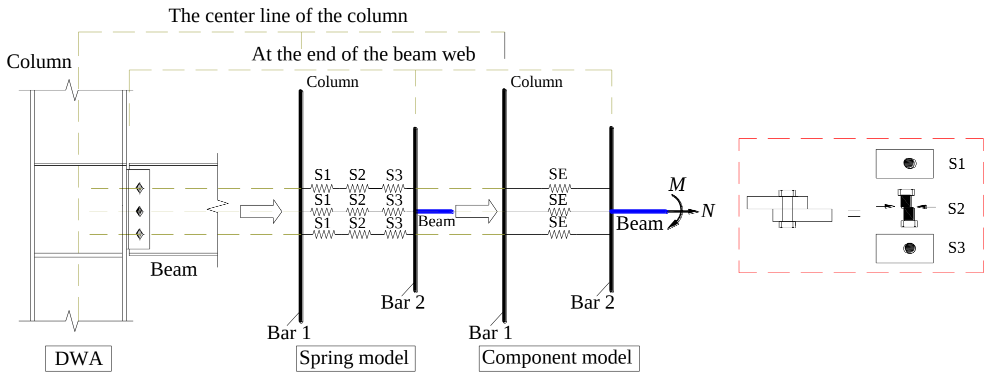

(a) DWA connection

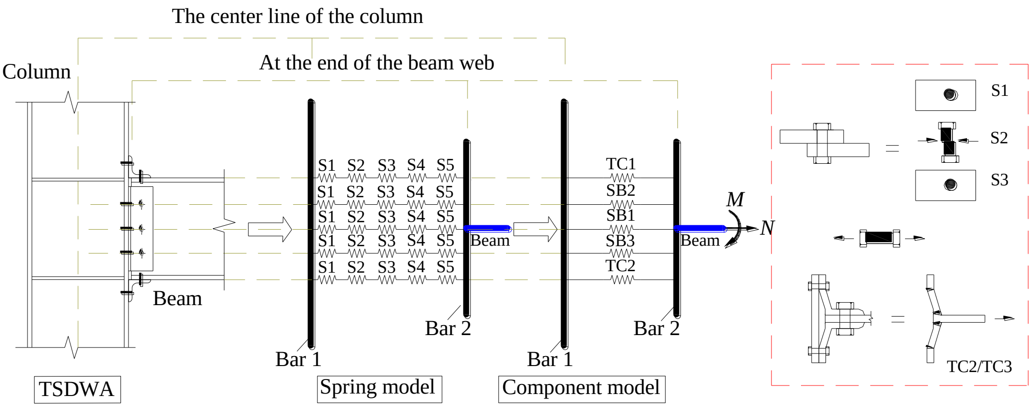

(b) TSDWA connection

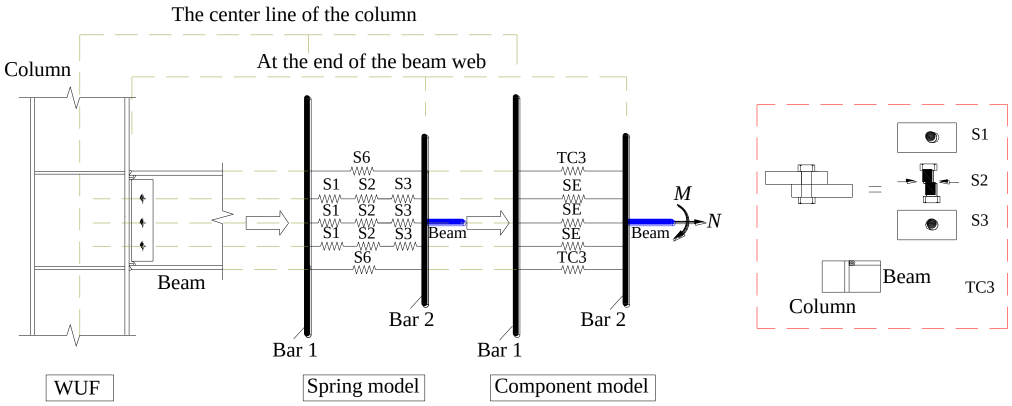

(c) WUF connection

Fig. 1 Component model of different stiffness connections

2.2.1. Bolt hole compression spring (S1/S3)

The S1 and S3 springs correspond to the deformation of the bolt holes of the connecting plate and beam web, respectively, as illustrated in Fig. 2. Deformation was significantly affected by the end and edge distances of the bolt holes.

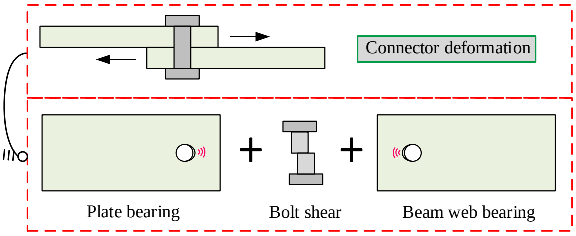

Fig. 2 Deformation decomposition of a single component

Elsalti and Richard [18] proposed the following equations to define the relationship between the load and deformation of a bolt hole compression spring:

$$\frac{F}{F_{\mathrm{b,Rd}}} = \frac{1.74\Lambda}{(1+\Lambda^{0.5})^2} - 0.009\Lambda \tag{1}$$

$$\Lambda = \Delta\beta k_{\mathrm{i}} F_{\mathrm{b,Rd}} \tag{2}$$

where F is the load applied to the bolt hole (plate), $F_{\mathrm{b,Rd}}$ is the ultimate bearing capacity of the bolt hole (plate), Λ is the nominal pressure deformation of the bolt hole, Δ is the pressure deformation of the bolt hole, and β is the material correction factor (steel is typically 1.0).

Fisher and Struik [19] derived the ultimate bearing capacity formula with considering the bolt hole shear failure mode:

$$F_{\mathrm{T,Rd}} = \frac{e_2}{d_{\mathrm{h}}} \times f_{\mathrm{u}} \times d_{\mathrm{h}} \times t \le 2.4 f_{\mathrm{u}} dt \tag{3}$$

where e_2 is the distance between the bolt holes (the distance between the center of the bolt hole and the edge of the plate along the direction of the main force), d_h is the diameter of the bolt hole, f_u is the tensile strength, and t and d are the thickness and width of the plate, respectively.

The deformation of the bolt hole consists of three parts [18]: extrusion of the bolt hole (corresponding stiffness k_{br}), bending deformation of the steel plate at the outer end of the bolt hole (corresponding stiffness k_b), and shear deformation of the steel plate at the outer end of the bolt hole (corresponding stiffness k_v), as shown in Fig. 3. Each stiffness can be calculated using the following formula [20]:

$$k_{\mathrm{br}} = 120tf_{\mathrm{y}}(d_{\mathrm{b}}/25.4)^{0.8} \tag{4}$$

$$k_{\mathrm{b}} = 32Et(e_2/d_{\mathrm{b}} - 1/2)^3 \tag{5}$$

$$k_{\mathrm{v}} = 6.67Gt(e_2/d_{\mathrm{b}} - 1/2) \tag{6}$$

where f_y, E, and G are the yield strength, modulus of elasticity, and shear modulus, respectively, and d_b is the bolt shank diameter.

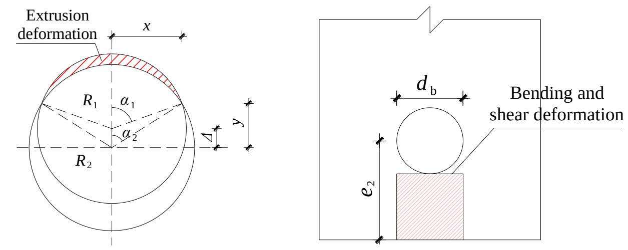

(a) Extrusion deformation of bolt hole (b) Bending and shear deformation of bolt hole

Fig. 3 Deformation of the bolt hole

Thus, the bolt hole compression stiffness k_i can be represented by the following equation:

$$k_{\mathrm{i}} = \frac{1}{\dfrac{1}{k_{\mathrm{br}}} + \dfrac{1}{k_{\mathrm{b}}} + \dfrac{1}{k_{\mathrm{v}}}} \tag{7}$$

Fig. 4 shows the load–deformation (F–Δ) curve of the bearing deformation spring of the bolt hole (only the plate thickness was different for the connecting plate, angle, beam flange, and beam web) [13].

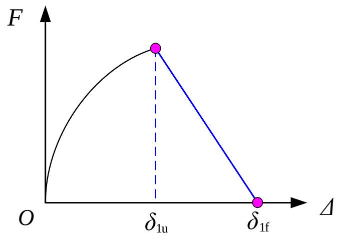

Fig. 4 Load–deformation curve of bearing deformation spring of a bolt hole

2.2.2. Bolt shear spring (S2)

The relationship between the shear force and shear deformation curve of the S2 spring can be determined using the modified Raberg–Osgood formula [21]:

$$v_{\mathrm{v,b}} = \frac{F_{\mathrm{v}}}{k_{\mathrm{v,b}}} + \Omega\left(\frac{F_{\mathrm{v}}}{F_{\mathrm{v,Rb}}}\right)^6 \tag{8}$$

where $v_{v,b}$ and F_v are the shear deformation and shear force of the bolts, respectively, $k_{v,b}$ is the shear stiffness of the bolts, Ω is a coefficient related to the temperature and remains to be 2.5 at normal temperature, and the ultimate shear strength of the bolts is

$$F_{\mathrm{v,Rb}} = 0.6 \times F_{\mathrm{u,b}} \times A_{\mathrm{b}} \tag{9}$$

where $f_{u,b}$ is the ultimate tensile strength of the bolts and, A_b is the effective area of the bolt shank.

The shear stiffness of bolts can be obtained as follows:

$$k_{\mathrm{v,b}} = \frac{kGA}{d_{\mathrm{b}}} \tag{10}$$

where k is the correction coefficient for bolt shear deformation, equal to 0.15 [22].

2.2.3. Bolt tension spring (S4)

The load–deformation curve of S4 can be determined by the simple tensile deformation method according to the effective area and material properties of the bolt and can be simplified to a bilinear strength relationship model.

2.2.4. Angle bending spring (S5)

The load–deformation curve of S5 can be simplified into three stages [23] according to EC3 [17], as shown in Fig. 5.

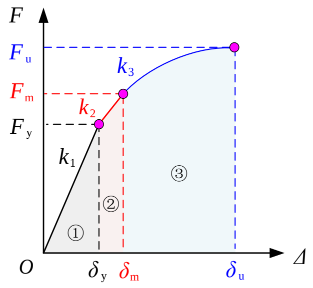

Fig. 5 Load–deformation curve of bearing deformation spring of a bolt hole

The values of F_y and F_m can be determined using the following formulas [24]:

$$F_{\mathrm{y}} = \frac{2}{3}F_{\mathrm{T,Rd}} \tag{11}$$

$$F_{\mathrm{m}} = F_{\mathrm{T,Rd}} \tag{12}$$

where $F_{T,Rd}$ is the yield-bearing capacity of angle steel connectors.

The initial stiffness k_1 [23] of angles in bending is

$$k_1 = \frac{0.5Eb_{\mathrm{eff,a}}t_{\mathrm{a}}{}^3}{(m - t_{\mathrm{a}} - 0.8r_a)3}\left(\frac{4\gamma_{\mathrm{a}}}{\gamma_{\mathrm{a}} + 3}\right) \tag{13}$$

$$\gamma_{\mathrm{a}} = \frac{I_2/L_2}{I_1/L_1} \tag{14}$$

where I_1, I_2, L_1, and L_2 are defined in Fig. 6, $b_{eff,a}$ is the effective effect width of the bolted angles, $b_{eff,a}$ can be calculated using Table 1 (Fig. 7 shows the dimension parameters of the connection), t_a is the thickness of the angles, the value of m and r_a are defined in Fig. 7.

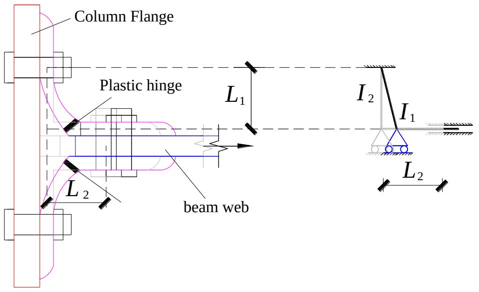

Fig. 6 Mechanical bending model of angle component

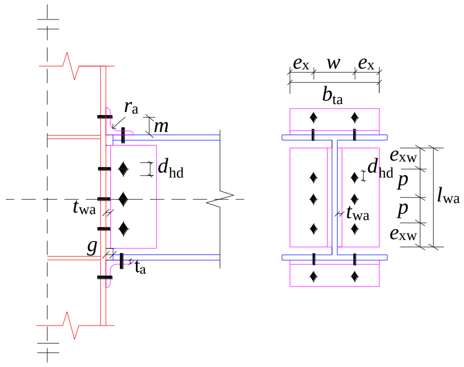

Fig. 7 Dimension parameters of the connection

Table 1
Effective width of angle components [25]

Bolt row	Effective width
Top angle, Bottom angle	$b_{\mathrm{efft,ta}} = \min(d_h+2m_a,\ d_h/2+m_a+w/2;\ b_{ta}/2;\ e_x+d_h/2+m_a)$
Inner bolt row web angle	$b_{\mathrm{efft,ta}} = \min(d_h+2m_a,\ p)$
End bolt row of web angle	$b_{\mathrm{efft,ta}} = \min(d_h+2m_a,\ d_h/2+m_a+p/2;\ e_x+p/2;\ e_{xw}+d_h/2+m_a)$

k_2 is the stiffness of the transitional period, which was set as $1/7k_1$ [22] until it reached the yield capacity of the angles. For the convenience of analysis, the component of the bending angles can be considered as an equivalent bolted T-stub, and the design resistance of the T-stub can be calculated as the smallest value among the three possible failure modes, as illustrated in Fig. 8.

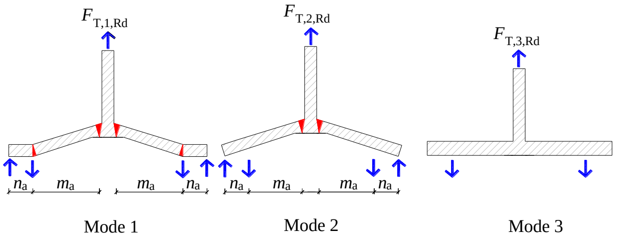

Fig. 8 Three possible failure modes of T-stub component

Mode 1: A plastic hinge appeared near the bolt of the T-stub flange (complete yielding of the T-stub flange).

$$F_{\mathrm{T,1,Rd}} = \frac{4M_{\mathrm{a}}}{m_{\mathrm{a}}} = \frac{b_{\mathrm{eff,a}} t_{\mathrm{a}}^{2} f_{\mathrm{y}}}{m_{\mathrm{a}}} \tag{15}$$

Mode 2: A plastic hinge appeared near the bottom of the T-stub flange (bolt failure with yielding of the T-stub flange).

$$F_{\mathrm{T,2,Rd}} = \frac{2M_{\mathrm{a}} + n_{\mathrm{a}} \sum B_{\mathrm{T,Rd}}}{m_{\mathrm{a}} + n_{a}} \tag{16}$$

Mode 3: The bolt rod reached its tensile design bearing capacity (bolt failure).

$$F_{\mathrm{T,3,Rd}} = \sum B_{\mathrm{T,Rd}} \tag{17}$$

where M_a is the plastic bearing capacity of the T-stub, $B_{T,Rd}$ is the bolt design resistance, and m_a and n_a are the distance between the two plastic hinges and the distance between the bolt center lines and prying force position, respectively, as shown in Fig. 8.

m_a can be calculated as follows [23]**:**

$$m_{\mathrm{a}} = m_{\mathrm{a,EC3}} - \psi_1 \left(\frac{d_{\mathrm{bd}}}{2} + \frac{t_{\mathrm{a}}}{2} + 0.2 r_{\mathrm{a}} \right) \tag{18}$$

$$\psi_1 = 1.89 - \frac{3.22 t_{\mathrm{a}}}{d_{\mathrm{b}} \sqrt{m_{\mathrm{a,EC3}} / d_{\mathrm{b}}}} \tag{19}$$

where ψ_1 is a coefficient in the range 0–1, and d_{bd} is the bolt head diameter. $m_{a,EC3}$ can be calculated as follows:

$$m_{\mathrm{a,EC3}} = \begin{cases} m - t_{\mathrm{a}} - 0.8 r_{\mathrm{a}} & g \le 0.4 t_{\mathrm{a}} \\ m - 0.5 t_{\mathrm{a}} & g > 0.4 t_{\mathrm{a}} \end{cases} \tag{20}$$

where g is the gap between the column flange and beam flange, as shown in Fig. 7.

Relevant tests show that when one of the aforementioned stress modes is formed, the angle steel connection will yield in bending, and its bearing capacity can be improved further. This indicates that the load–deformation curve will continue to rise in the later stage, causing the stiffness to decline and enter the large deformation stage. The incremental iteration method [24] can be employed to determine the bearing capacity according to the analysis model shown in Fig. 9 as follows:

$$\begin{aligned} \varDelta F &= F_2 - F_1 = N_{\mathrm{a}} (\sin \theta_2 - \sin \theta_1) \\ &= N_{\mathrm{a}} \left(\frac{\delta_1 + \varDelta}{\sqrt{m^2 + (\delta_1 + \varDelta)^2}} - \frac{\delta_1}{\sqrt{m^2 + {\delta_1}^2}} \right) \end{aligned} \tag{21}$$

$$N_{\mathrm{a}} = (b_{\mathrm{eff,a}} - n d_{\mathrm{b}}) t_{\mathrm{a}} f_{\mathrm{u}} \tag{22}$$

where n is the number of bolts.

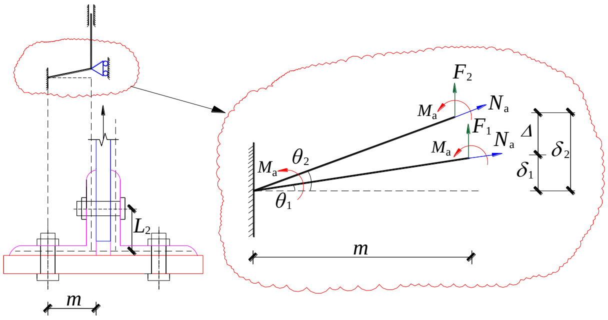

Fig. 9 Mechanical model of the angle at the large deformation stage

When mode 1 or 2 is formed, a plastic hinge appears in the component, and the ultimate displacement δ_u of spring S6 [25] can be refereed as follows:

$$\delta_{\mathrm{u}} = m^{*} (1 + \varepsilon_{\mathrm{u}}) \sin\left(\frac{\varepsilon_{\mathrm{u}} m^{*}}{2 t_{\mathrm{a}}} \right) \tag{23}$$

where ε_u is the ultimate displacement and m^* is the distance between the two plastic hinges at the horizontal legs of the angles.

$$m^{*} = m - t_{\mathrm{a}} - 0.8 r_{\mathrm{a}} + \eta d_{\mathrm{b}} \tag{24}$$

where η is a coefficient, which can be calculated as follows:

$$\eta = \begin{cases} 1.1335 - 0.00242 \dfrac{f_{\mathrm{y,b}} A_{\mathrm{b}} b_{\mathrm{eff,a}}}{F_{\mathrm{T,Rd}}} & \dfrac{f_{\mathrm{y,b}} A_{\mathrm{b}} b_{\mathrm{eff,a}}}{F_{\mathrm{T,Rd}}} \le 560 \\ -0.22 & \dfrac{f_{\mathrm{y,b}} A_{\mathrm{b}} b_{\mathrm{eff,a}}}{F_{\mathrm{T,Rd}}} > 560 \end{cases} \tag{25}$$

where $f_{y,b}$ is the yield strength of bolts.

When stress mode 3 is formed, the ultimate displacement of S6 can be calculated using Eq. (21), and the load–deformation curve of S4 can be determined.

2.2.5. Beam flange tension–compression spring (S6)

The beam flange tension–compression spring S6 (the component comprises a deformation spring) was used to simulate the tension and compression effects of the upper and lower flange ends; Fig. 10 shows its load–deformation curve [25] (a positive value represents tension, and a negative value represents compression). The stress state must be distinguished first before determining the ultimate bearing capacity of the tension and compression of spring S5. The ultimate state is the material yield under compression and fracture under tension (ignoring compression flange buckling).

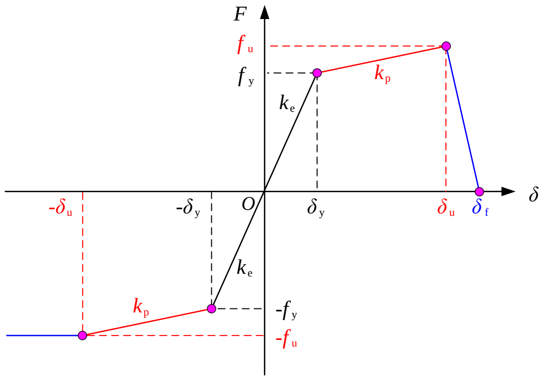

Fig. 10 Load–deformation curve of tension and compression spring at the beam flange

The relevant parameters of the TC component before yielding can be calculated as [25]

$$k_e = \frac{E b_f t_f}{\rho b_s} \tag{26}$$

$$F_y = b_f t_f f_y \tag{27}$$

where k_e is the elastic stiffness of the flange tension compression component, b_f and t_f are the width and thickness of the beam flange, respectively, b_s is the width of the shear plate, and ρ is the coefficient [25] related to the failure modes (equal to 1.0 and 1.5 when the failure mode is controlled by the beam–to–column connection and beam flange, respectively).

The elastic–plastic stiffness at the strengthening stage can be calculated as

$$k_p = \frac{E_s k_e}{E} \tag{28}$$

where E_s is the strengthening modulus of the steel.

The ultimate bearing capacity of flange components in tension can be calculated as follows:

$$F_u = b_f t_f f_u \tag{29}$$

The load–deformation curves of the first two stages of the compression flange component were the same as those of the tension flange component. When the deformation reached δ_u, the load reached its limit and no longer increased in the final stage; however, the deformation continued to increase.

3. Component method application

3.1. Model verification tests

3.1.1. Specimens with DWA and TSDWA connections

Yang et al. [15] performed collapse tests with DWA and TSDWA connections; Fig. 11 presents the test setup and details of the two types of connections. The beam and column adopted standard sections of 256 mm × 146.4 mm × 6.3 mm × 10.9 mm and 215.8 mm × 206.4 mm × 10 mm × 17.3 mm, respectively. The sections of the top/seat and web angles were both L90 mm × 8 mm. The connections between beam ends and column flanges were realized by the steel angles and M20 Grade 8.8 bolts (the bolt hole diameter was 22 mm). The related material properties can be found in [15].

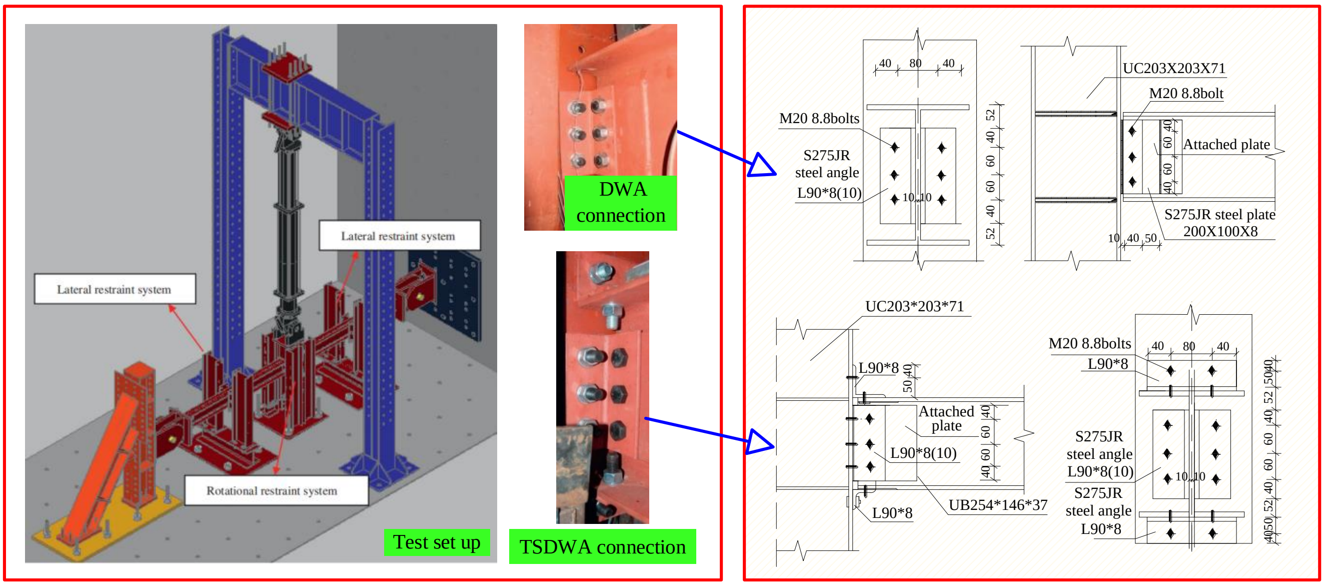

Fig. 11 Collapse tests of beam–column assemblies with DWA and TSDWA connections [15] (dimension units: mm)

Fig. 12 illustrates the final failure modes of the two specimens. During the actual test, the left and right sides of the middle column showed asymmetrical characteristics owing to the initial errors of steel and installation error of the specimens. Moreover, only three bolts on one side of the middle connection were broken in sequence during the entire loading process.

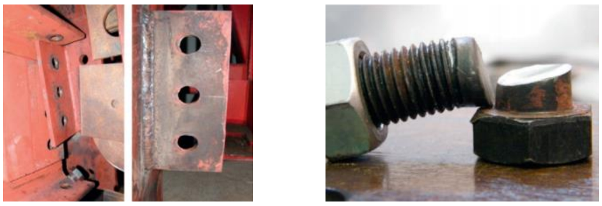

(a) DWA connection

(b) TSDWA connection

Fig. 12 Failure modes of the beam–column assemblies with DAW and TSDWA connections [15]

3.1.2. Specimen with WUF connection

A beam–column assembly with a WUF connection was tested in [26]; Fig. 13 shows the dimensions of the connections. The column and beam section dimensions were H539.5 mm × 210.69 mm × 11.56 mm × 18.8 mm and H481.84 mm × 286.13 mm × 16.64 mm × 26.92 mm, respectively. The dimensions of the connecting plate were 304.8 mm × 152.4 mm × 12.7 mm, and the diameter of the bolt was 25.4 mm (the bolt hole diameter was 27.4 mm). The material properties of all components are given in [26]. The bolt spacing was 101.6 mm, the edge distance between the bolt hole and beam web was 57.15 mm, and that between the bolt hole and connecting plate was 69.85 mm. Fig. 14 presents the final failure modes of the specimens with WUF connection.

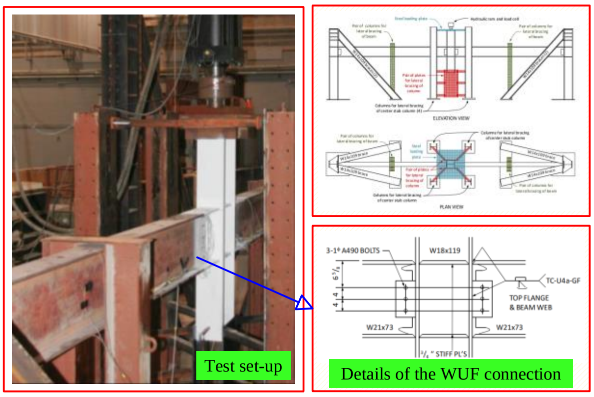

Fig. 13 Collapse tests of beam–column assemblies with WUF connection [26] (dimension units: in)

(a) Failure mode of the WUF connection

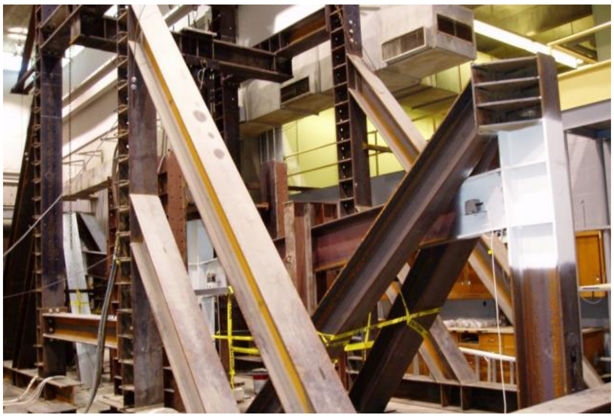

(b) Overall view of the specimen with WUF connection

Fig. 14 Final phenomenon of the specimen with WUF connection [26]

3.2. Load–deformation curves of equivalent components

Fig. 14 shows the load–deformation relationship of each component of the DWA, TSDWA, and WUF connections, calculated based on the discussion in Section 2.2.

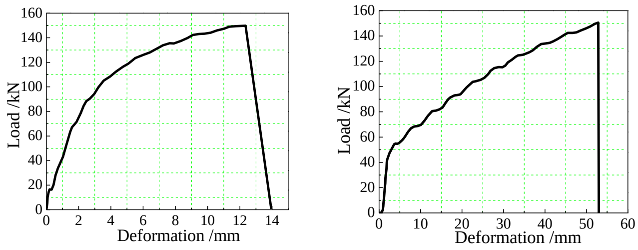

(a) SE-DWA

(b) SB1-TSDWA

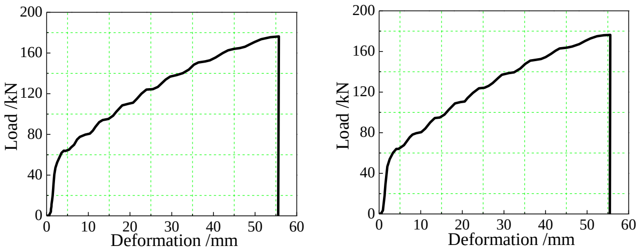

(c) SB2-TSDWA

(d) SB3-TSDWA

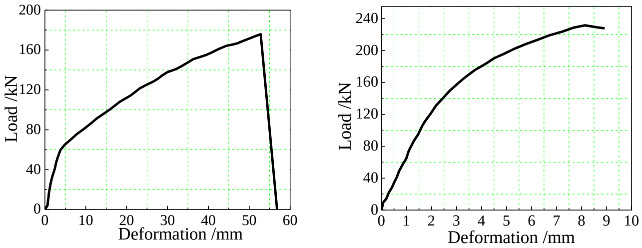

(e) TC1-TSDWA

(f) TC2-TSDWA

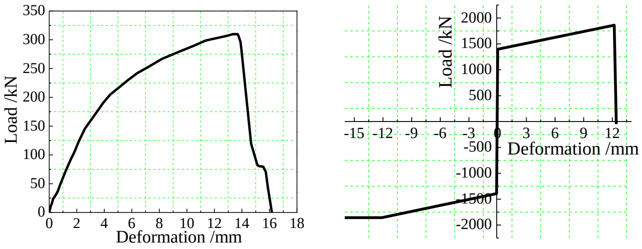

`(g) SE-WUF

(h) TC3-WUF

Fig. 14 Component properties of different connections

3.3. Comparison of finite element modeling and test results by component method

In this study, numerical analysis models were established for the collapse resistant performance of single-story steel frames with different connections using LS-DYNA based on the geometrical dimensions and material properties of the specimens. The rigid rods in the beams, columns, and connection zone used the Hughes–Liu beam elements, and the MAT119 spring elements were used in each component. The beam–to–column connection domain was assumed to be a rigid zone consisting of four rigid rods. The end of the beam was provided with a rigid rod, and the two ends of the component were connected to the rigid rod and rigid zone, respectively. The upper and lower ends of the failure columns were connected to the rigid zone. The rigid rod and zone were coupled to realize the transmission of internal force. A vertical load under displacement-controlled was selected to the top of the failed column, and only vertical movement was allowed. The boundary conditions of the DWA and TSDWA were set to hinge connections, and the bottom of the side columns of the WUF was fixed. The component models of steel frames with different connections are shown in Fig. 15. During the analysis and calculation, the constitutive relationship of each component was defined by the load–displacement curves in Fig. 14, while fracture occurs when a particular component unit fails during the loading process.

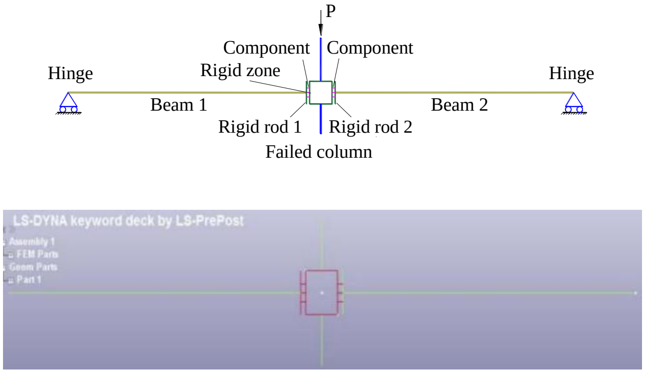

(a) DWA connection

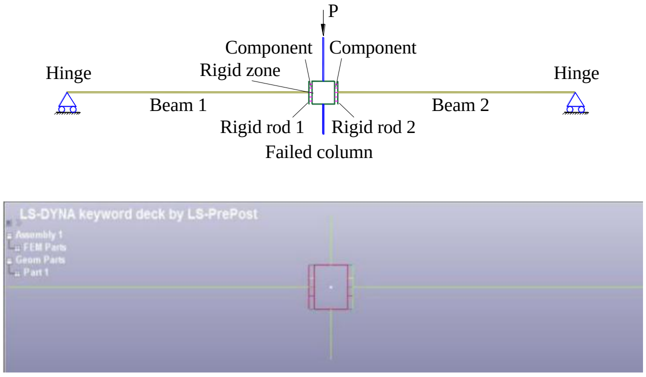

(b) TSDWA connection

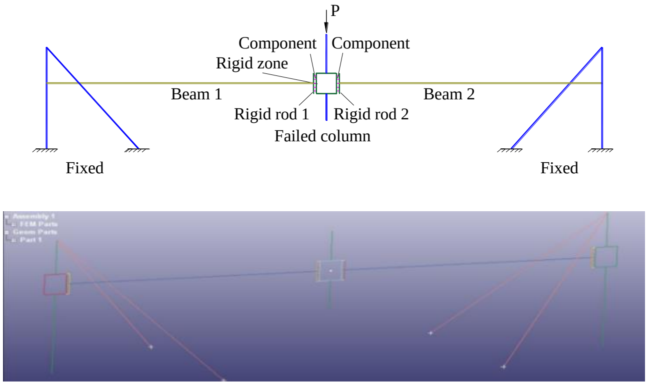

(c) WUF connection

Fig. 15 Component models of steel frames with different connections

According to the proposed component models with DWA, TSDWA, and WUF connections, the load–displacement curves and failure modes of the three specimens under an internal column removal scenario were obtained by numerical simulation are presented in Figs. 16 and 17. It can be observed that the results of the component model were consistent with the test results. Therefore, this method can reflect the primary progressive collapse responses of the beam–column assemblies with different stiffness connections. The fracture position and sequence can be simulated accurately, providing important reference for research on the resistance evaluation of steel frames with connections of different stiffnesses.

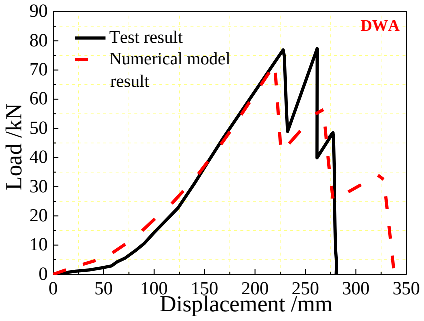

(a) DWA connection

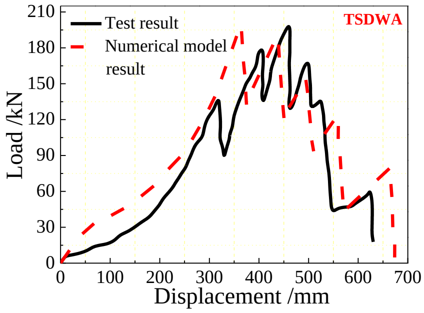

(b) TSDWA connection

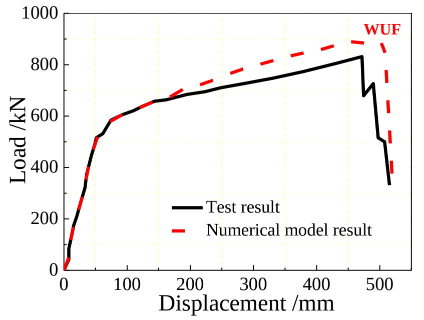

(c) WUF connection

Fig. 16 Comparison of load–displacement curves between tests and numerical models

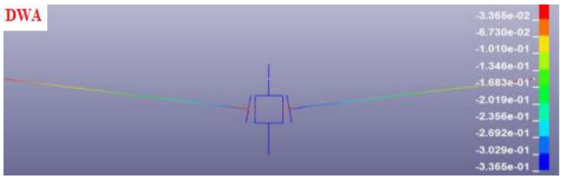

(a) DWA connection

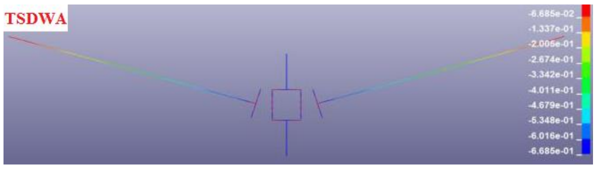

(b) TSDWA connection

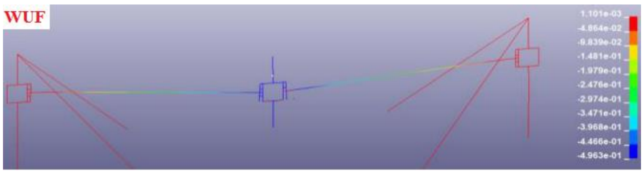

(c) WUF connection

Fig. 17 Final deformation of models with different connections predicted by the component models

4. Conclusion

(1) The connections of the steel structure with different stiffnesses can be divided into a series of independent basic mechanical springs according to their bearing mechanisms: bolt hole compression (S1/S3), bolt shear (S2), bolt tension (S4), angle bending (S5), and beam flange tension–compression (S6) springs.

(2) By analyzing the mechanical properties of each fundamental component comprising the beam–to–column connections, the accurate load–displacement curve of a single component can be obtained. Accordingly, the overall component analysis model of the connections can be constructed. This model can be employed to investigate further the overall mechanical characteristics of the connections of structures.

(3) A numerical analysis model for the collapse behavior of the beam–column assemblies with different stiffness connections was established based on the parameters of each fundamental component derived from the calculation examples. Behaviors, such as the load–displacement responses and failure modes, were consistent with the test results, satisfying the accuracy requirements of engineering calculations.

(4) Simplified component models with different connections based on the component method are highly accurate and efficient. The test results indicate that the proposed methods can predict structural resistance and progressive collapse performance, which was beneficial for research on structural anti-progressive collapse.

Acknowledgments

This research was supported by the National Natural Science Foundation of China [grant numbers 51678476, 51908449] and the Scientific Research Plan Projects of the Shaanxi Education Department [grant numbers 20JY033, 20JK0713]. All opinions, findings, conclusions, and recommendations expressed in this paper are those of the authors and do not necessarily reflect the views of the sponsors.

References

[1] Meng B., Li L.D., Zhong W.H., et al., “Improving anti-progressive collapse capacity of welded connection based on energy dissipation cover-plates”, Journal of Constructional Steel Research, 188, 107051, 2022.

[2] Meng B., Hao J.P. and, Zhong W.H., “Numerical study on the anti-progressive collapse performance of steel frame-steel plate shear wall structures”, Journal of Building Engineering, 35, 102049, 2021.

[3] Tan Z., Zhong W.H., Meng B., et al., “Effects of the numbers of stories and spans on the collapse-resistance performance of multi-story steel frame structures with reduced beam section connections”, Advanced Steel Construction, 18(2), 616-628, 2022.

[4] Zhong W.H., Tan Z., Song X.Y., et al., “Anti-collapse analysis of unequal span steel beam–column substructure considering the composite effect of floor slabs”, Advanced Steel Construction, 15(4), 377–385, 2019.

[5] Ahmadi E. and Hosseini S.A., “Capacity evaluation of eight bolt extended endplate moment connections subjected to column removal scenario”, Advanced Steel Construction, 17(3), 273–282, 2021.

[6] Zhong W.H., Tan Z., Tian L.M., et al., “Collapse resistance of composite beam-column assemblies with unequal spans under an internal column-removal scenario”, Engineering Structures, 206, 110143, 2020.

[7] Tan Z., Zhong W.H., Meng B., et al., “Numerical evaluation on collapse-resistant performance of steel-braced concentric frames ”, Journal of Constructional Steel Research, 193, 107268, 2022.

[8] Li G.Q., Zhang J.Z. and Jiang J., “Multi-story composite framed-structures due to edge-column loss”, Advanced Steel Construction, 16(1), 20–29, 2020.

[9] Tan Z., Zhong W.H., Tian L.M., et al., “Quantitative assessment of resistant contributions of two-bay beams with unequal spans”, Engineering Structures, 242, 112445, 2021.

[10] Adam J.M., Parisi F., Sagaseta J., et al., “Research and practice on progressive collapse and robustness of building structures in the 21st century”, Engineering Structures, 173, 122–149, 2017.

[11] Tan Z., Zhong W.H., Tian L.M., et al., “Numerical study on collapse-resistant performance of multi-story composite frames under a column removal scenario”, Journal of building Engineering, 44, 102957, 2021.

[12] Zheng L. and Wang W.D., “Multi-scale numerical simulation analysis of CFST column-composite beam frame under a column-loss scenario”, Journal of Constructional Steel Research, 190, 107151, 2022.

[13] Sarraj M., “The behavior of steel fin plate connections in fire”, Sheffield : University of Sheffield, 2007.

[14] Liu C., Tan K.H. and Fung T.C., “Component-based steel beam–column connections modelling for dynamic progressive collapse analysis”, Journal of Constructional Steel Research, 107(1), 24-36, 2015.

[15] Yang B. and Tan K.H., “Experimental tests of different types of bolted steel beam-column joints under a central-column-removal scenario”, Engineering Structures, 54, 1112-1130, 2013.

[16] Tan Z., Zhong W.H., Tian L.M., et al., “Research on the collapse-resistant performance of composite beam-column substructures using multi-scale models”, Structures , 27, 86–101, 2020.

[17] EN1993-1-8. Eurocode 3: Design of Steel Structure, Part 1-8: Design of joints. Brussels: European Committee for standardization; 2005.

[18] Elsalti M.K. and Richard R.M., “Derived moment rotation curves for partially restrained connections”, Development in Structural Engineering Computing, 18: 55-62, 2009.

[19] Fisher J.W, and Struik J.K., “Guide to design criteria for bolted and riveted joints”, New York: Wiley Interscience Press, 1974.

[20] Rex C.O, and Easterling S.W., “Behavior and modeling of a bolt bearing on a single plate”, Journal of Structural Engineering, 129(6), 792-88, 2003.

[21] Ramberg W. and Osgood W.R., “Description of stress–strain curves by three parameters”, Washington DC: National Advisory Committee for Aeronautics, 1943.

[22] Hayes M.D., “Structural analysis of a pultruded composite beam: shear stiffness determination and strength and fatigue life predictions”, Blacksburg: Faculty of the Virginia Polytechnic Institute and State University, 2003.

[23] Faella C., Piluso V. and Rizzano G., “Structural steel semirigid connections: theory, design and software”, Florida: Chemical Rubber Company Press, 2000.

[24] Yang B. and Tan K.H., “Robustness of bolted-angle connections against progressive collapse: mechanical modeling of bolted-angle connections under tension”, Engineering Structures, 547(12), 153-168, 2013.

[25] Yim H.C, and Krauthammer T., “Mathematic-mechanical model of WUF-B connection under monotonic load”, Engineering Journal, 2(1), 71-90, 2010.

[26] Sadek F., Main J.A., and Lew H.S., “An experimental and computational study of steel moment connection under a column removal scenario”, Gaithersburg: National Institute of Standards and Technology, 2010.

Advanced Steel Construction – Vol. 19 No. 1 (2023) 9–16
DOI:10.18057/IJASC.2023.19.1.2
(**Special Issue:** *10th International Conference on Advances in Steel Structures, ICASS'2020, Chengdu, China*)

EXPERIMENTAL INVESTIGATION ON MECHANICAL PROPERTIES OF GRADE 1670 STEEL WIRES UNDER AND AFTER ELEVATED TEMPERATURE

Er-Feng Du [1, *], Xiao-Bo Hu [2], Zhong Zhou [2] , Qian Li [2], Xiao Lyu [3] and Yi-Qun Tang [2]

[1] *China-Pakistan Belt and Road Joint Laboratory on Smart Disaster Prevention of Major Infrastructures, Southeast University, Nanjing, China*
[2] *School of Civil Engineering, Southeast University, Nanjing, China*
[3] *School of Civil Engineering, Shandong Jianzhu University, Ji'nan, China*
* *(Corresponding author: E-mail: erfengdu@seu.edu.cn)*

ABSTRACT

Grade 1670 steel wires were selected for elevated-temperature and post-elevated-temperature tensile tests. The test data were analyzed through comparison with the results in existing literatures. The elevated-temperature test results indicate that, mechanical properties of the steel wires degraded with the increase of temperature. The mechanical behaviors of the steel wires degraded rapidly at the temperature exceeding 300°C, and the load-carrying ability was substantially lost when the temperature increased up to 700°C. In the post-elevated-temperature test, the modulus of the steel wire was almost completely recovered after cooling from the elevated temperatures. The nominal yield strength and ultimate strength degraded obviously after cooling from the temperature exceeding 400°C. Based on the test data, the reduction factors of the mechanical properties at and after elevated temperatures are fitted as a function of the temperature, and constitutive models of the steel wires are established. The results can provide technical supports for the analysis of fire performance of prestressed cable support structures, and their post-fire repair.

ARTICLE HISTORY

Received:	20 July 2022
Revised:	22 August 2022
Accepted:	10 January 2023

KEYWORDS

Steel wires;
Elevated temperatures;
Mechanical properties;
Experimental research;
Stress-strain curve

1. Introduction

Steel cables are the key members of long-span prestressed steel structures such as cable domes, string domes and tension beams, as shown in Fig. 1. However, mechanical properties of the steel cables are significantly degraded at elevated temperatures, thereby seriously influencing the safety of the overall structure. The steel cable is mainly composed of steel wires, and thus the study on the elevated-temperature and post-elevated-temperature mechanical properties, such as the elastic modulus, proportional limit, yield strength, and ultimate strength of the steel wire, is of great significance to the fire resistance analysis and post-fire evaluation of large-span prestressed steel structures.

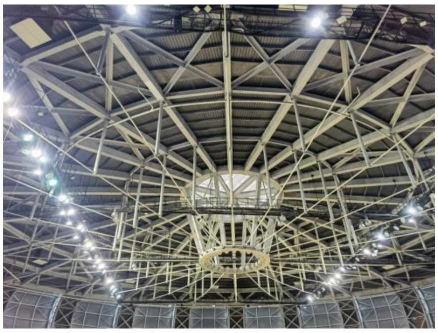

(a) String dome structure

(b) Tension beam structure

Fig. 1 Long-span prestressed steel structures

Mechanical properties of steel cables at elevated temperatures have been investigated by scholars. Zhou et al.[1] tested mechanical behaviors of 27 Grade 1860 prestressed steel cables from ambient temperatures to 700°C, and obtained stress-strain curves of the steel cables at different temperatures. Zong et al.[2,3] conducted experimental research on mechanical performances of Grade 1860 prestressed steel cables at elevated temperatures, and obtained the degradation law and mechanical model of the steel cables. Fontanari et al.[4] studied mechanical properties of C80 high-carbon steel cables at elevated temperatures, and provided a numerical analysis method to study the fire resistance of steel cables. Conor et al.[5] performed tensile tests on ASTM A416-12a steel cables composed of 7 steel wires at elevated temperatures, and as compared with Eurocodes, the results showed that the Eurocodes cannot accurately predict the stress-strain relationship of the steel cable. Shakya et al.[6] studied the mechanical performance of steel cables composed of 7 Grade 1860 steel wires at elevated temperatures, and gave an empirical equation for the mechanical properties of steel cables as a function of the temperature. Du et al.[7-10] carried out tensile tests at elevated temperatures on a Grade 1670 steel cable, a Grade 1670 parallel steel wire strand, and a Grade 1860 steel cable, and revealed the relationship between the reduction factor of mechanical behaviors and the temperature. Sun et al. [11-13] conducted tensile tests at elevated temperatures on a Grade 1500 stainless steel cable, a Grade 1670 high-vanadium cable, and a Grade 1770 steel wire coated with 5% zinc-aluminum alloy, and obtained a reduction factor equation for mechanical properties of steel cables and steel wires.

In view of the mechanical properties of steel cables after exposure to elevated temperatures, Fan et al.[14] studied the mechanical properties of Grade 1570 high-strength prestressed steel wires after cooling to ambient temperature from elevated temperatures, and obtained variation laws of mechanical behaviors of steel wires. Lu et al.[15,16] tested the post-fire mechanical performances of a Grade 1670 steel cable and prestressed steel wires of different grades, and investigated effects of different cooling methods on the mechanical behaviors of steel cables and steel wires. Zheng et al.[17] and Atienza et al.[18] performed tensile tests on Grade 1770 prestressed steel wires after cooling from elevated temperatures, and obtained the degradation law of mechanical properties of steel wires after high temperature. Zong et al.[19] conducted experimental research on a Grade 1860 prestressed steel cable after heating, and reveled the relationship between the mechanical properties of the steel cable and the exposure temperature. Zhang et al.[20] carried out experimental research on the post-fire mechanical properties of a Grade 1670 cold-drawn steel wire used in suspension bridges, and analyzed the influence of the exposure temperature on the mechanical behaviors of the steel wire after cooling.

Though aforementioned scholars have performed a series of studies on the mechanical performance of steel wires, and accumulated a lot of test data, due to the continuous improvement in performance of steel wires, mechanical behaviors of the newly emerging steel cables in engineering are less investigated. Therefore, this paper conducts an experimental study on elevated-temperature and post-elevated-temperature mechanical properties of Grade 1670 prestressed steel wires, and provides a reference for the property evaluation of prestressed steel structures under and after fire.

2. Test program

2.1. Test equipment

The test equipment for elevated-temperature and post-elevated-temperature mechanical properties of steel wires is shown in Fig. 2. The loading device was an electronic universal testing machine, with a maximum tensile force of 300kN. The specimen was heated by an electronic elevated-temperature furnace. The furnace was equipped with multi-layer resistance wires. The furnace had a diameter of 24cm and a height of 46cm. The maximum temperature in the furnace could reach 1200°C. The strain of the steel wire was measured by an elevated-temperature strain extensometer with a gauge length of 50mm. During the measurement, the knife edge at the end of the extensometer was closely contacting the specimen. Data such as the strain and temperature were automatically collected by a computer.

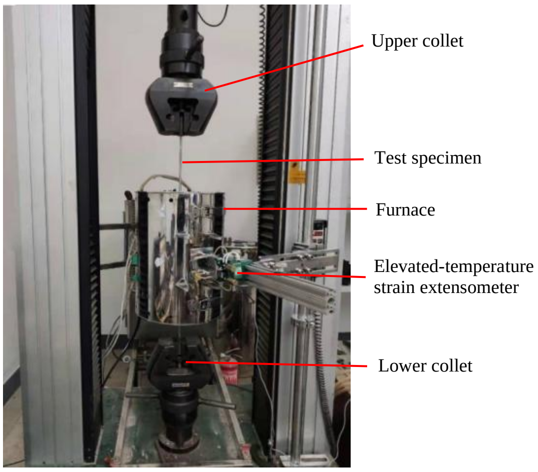

Fig. 2 Electronic universal testing machine

2.2. Test specimens

The steel wires used in the elevated-temperature and post-elevated-temperature tests had a strength grade of 1670MPa, a diameter of 7mm, and a length of 80cm. Due to the high strength and hardness of the prestressed steel wire, it is easy for the wire to slip when directly clamped by the testing machine. Therefore, pier heads and clip anchors were set at both ends of the specimen for effective clamping. The clamping device is shown in Fig. 3. The diameter of the pier head was 14mm, and the diameter and length of the clip anchor were 25mm and 80mm, respectively. A length of 15cm at the upper and lower ends of the steel wire outside the elevated-temperature furnace was set aside to cool in the air, so as to avoid the influence of high temperatures on the collets of the testing machine.

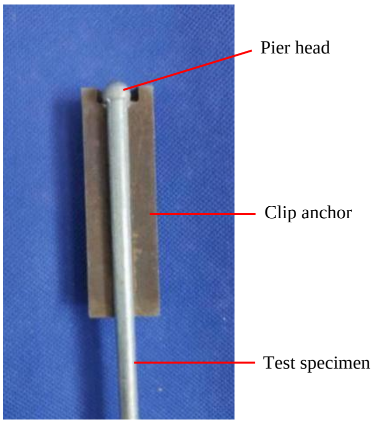

Fig. 3 Clamping device for specimen

2.3. Loading procedure

8 temperature levels were set for the tests of elevated-temperature mechanical properties, including 20°C (ambient temperature), 100°C, 200°C, 300°C, 400°C, 500°C, 600°C, and 700°C, respectively. Tests were conducted according to the test methods specified in “Metallic materials - Tensile testing - Part 1: Method of test at room temperature” (GB/T228.1-2010)[21] and “Metallic materials - Tensile testing - Part 2: Method of test at elevated temperature” (GB/T228.2-2015)[22]. The specimens were heated to a specified temperature and then kept for 30 min, to ensure the temperature evenly distributed in the specimens. During the heating and isothermal processes, no tension was applied on the test specimen. Stretching was performed after the temperature distributed uniformly and stably, at a constant rate of 3 mm/min.

5 temperature levels were set for the tests of post-elevated-temperature mechanical properties, including 300°C, 400°C, 500°C, 600°C, and 700°C, respectively. According to the same heating method as that in the elevated-temperature test, the specimens were firstly heated to the target temperature, subsequently kept constant at that temperature for 30 min, and then naturally cooled to ambient temperature followed by stretching. The stretching method was the same as that in the elevated-temperature test.

3. Results and analysis of the elevated-temperature test

3.1. Visual observations

Apparent characteristics of the specimens after the elevated-temperature tensile test are shown in Fig. 4. The heating temperatures of various specimens from left to right were 20°C, 100°C, 200°C, 300°C, 400°C, 500°C, 600°C and 700°C, respectively. At 20°C (ambient temperature), the specimen broke near the pier head, due to the damage at the pier head caused during cold rolling. While at other temperatures, the specimens broke in the heated area. At 20°C, the specimen was damaged at an oblique angle of 45°. At 200°C ~ 400°C, the metallic luster of the specimen became darker, and the fracture was cup-shaped with serrations. At 500°C, the metallic luster on the surface of the specimen completely faded, and the fracture began to be tapered. At 600°C, the specimen was light yellow, and the fracture was more tapered. When the temperature was 700°C, the specimen was yellowish brown.

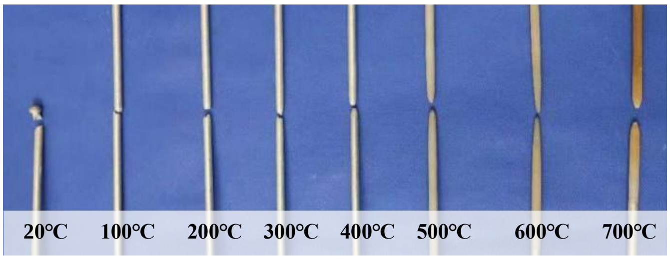

Fig. 4 Failure modes of steel wires after elevated-temperature test

3.2. Analysis of test results

According to the strain data obtained in the test, stress-strain curves of the specimens at different temperatures are plotted in Fig. 5. At the same time, reduction factors of mechanical properties of the steel wires under various temperatures can be calculated, as shown in Table 1. It can be seen from the

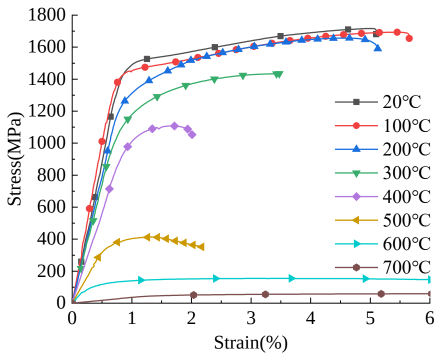

Fig. 5 Stress-strain curves of steel wires at elevated temperatures

figure and the table that, with the increase of temperature, the mechanical properties such as the elastic modulus, nominal yield strength (i.e., the yield strength corresponding to the strain level of 0.2%), and ultimate strength of the specimens all degraded. The elastic modulus of the specimen remained unchanged at 100°C, and decreased at 200°C to 89% of that at ambient temperature. Above 300°C, the rate of decrease of the elastic modulus was accelerated with the temperature increase. At 500°C, the elastic modulus was 37% of that at ambient temperature, and the elastic modulus at 700°C was only 2% of that at room temperature. As the temperature increased, the nominal yield strength and ultimate strength of the specimens decreased slowly below 200°C, within a range of 10%, and decreased rapidly above 400°C. At 500°C, the nominal yield strength and the ultimate strength decreased by 74% and 76%, respectively. At 700°C, the nominal yield strength and ultimate strength were less than 10% of those at ambient temperature.

Table 1

Mechanical properties of steel wires at elevated temperatures

T (°C)	$E_s(T)$ (GPa)	$E_s(T)/E_s$	$\sigma_{0.2}(T)$(MPa)	$\sigma_{0.2}(T)/\sigma_{0.2}$	$\sigma_b(T)$(MPa)	$\sigma_b(T)/\sigma_b$
20	180	1.00	1500	1.00	1703	1.00
100	180	1.00	1449	0.97	1693	0.99
200	160	0.89	1295	0.86	1656	0.97
300	148	0.82	1180	0.79	1434	0.84
400	115	0.64	1010	0.67	1108	0.65
500	66	0.37	383	0.26	414	0.24
600	31	0.17	123	0.08	155	0.09
700	3.5	0.02	40	0.04	47	0.03

Notes: T is the temperature; $E_s(T)$ and E_s are the elastic modulus of steel wires at temperature T and ambient temperature, respectively; $\sigma_b(T)$ and σ_b are the ultimate strength of steel wires at temperature T and ambient temperature, respectively; $\sigma_{0.2}(T)$ and$\sigma_{0.2}$ are the yield strength of steel wires at temperature T and ambient temperature, respectively.

In general, the mechanical performances of the prestressed steel wires changed little with the temperature below 300°C and degraded significantly at 300°C ~ 600°C, and the load-carrying ability was substantially lost when the temperature reached 700°C.

3.3. Comparison and discussion

Reduction factors of the elastic modulus, nominal yield strength and ultimate strength obtained by test results of this paper are compared with those of a Grade 1860 prestressed steel wire of Shakya et al. [6], a Grade 1770 prestressed steel wire of Zheng et al. [16], a Grade 1860 steel cable of Du et al. [7], and a Grade 1670 high-vanadium cable of Sun et al. [12], as shown in Figures 6 ~ 8. In the figures, the reduction factors in this paper, Shakya et al. [6], Zheng et al. [16], Du et al. [7] and Sun et al. [12] are marked with DW1670, SW1860, ZW1770, DC1860 and SC1670, respectively.

(1) Comparison of reduction factors of elastic modulus

As shown in Fig. 6, in terms of the steel wires, the reduction factors of elastic modulus obtained by test results of this paper (DW1670) and ZW1770 are generally lower than SW1860, and except for 700°C, the test results of this paper are very close to ZW1770. As compared with the test results of steel cables, DW1670 is close to DC1860 at 100°C, 500°C and 600°C, and lower than DC1860 at other temperatures. DW1670 is close to SC1670 below 400°C, and lower than SC1670 when the temperature is above 500°C.

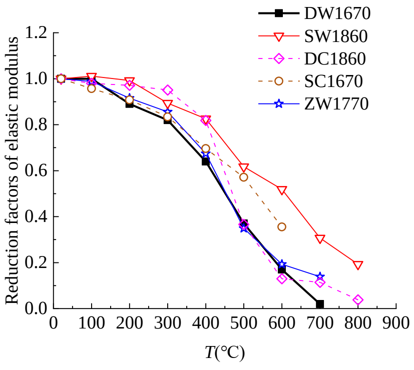

Fig. 6 Comparison of reduction factors of elastic modulus

(2) Comparison of reduction factors of nominal yield strength

As can be seen in Fig. 7, DW1670 and SW1860 are generally higher than ZW1770. DW1670 is close to SW1860 below 200°C, higher than SW1860 at 300°C and 400°C, and lower than SW1860 above 500°C; close to DC1860 except for 400°C at which DW1670 is higher than DC1860. The reduction factors of this paper (DW1670) are lower than SC1670 except for 100°C at which DW1670 is close to SC1670.

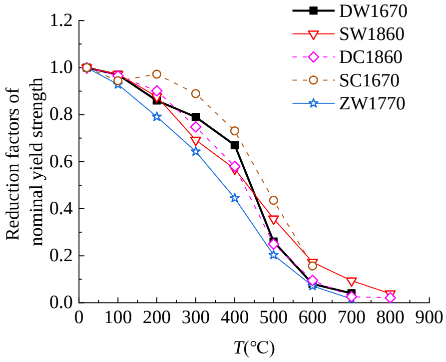

Fig. 7 Comparison of reduction factors of nominal yield strength

(3) Comparison of reduction factors of ultimate strength

As exhibited in Fig. 8, the reduction factors of ultimate strength obtained by test results of this paper (DW1670) are higher than SW1860 and ZW1770 from 200°C to 400°C, and close to ZW1770 but lower than SW1860 above 500°C. DW1670 is higher than SC1670 and DC1860 at 300°C and 400°C, and close to SC1670 and DC1860 from 500°C to 700°C except for 500°C at which DW1670 is lower than SC1670.

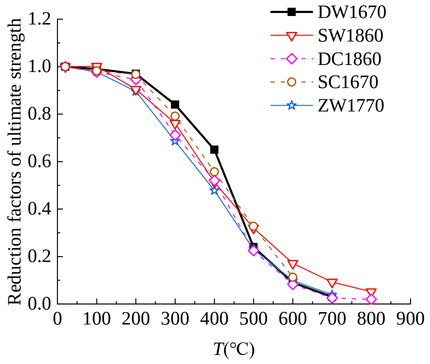

Fig.8 Comparison of reduction factors of ultimate strength

In general, though the reduction factors of mechanical properties of prestressed steel wires and cables of different strength grades are discrete to a certain extent, their variation laws are basically the same. The mechanical properties of steel cables under elevated temperature can be approximately represented by those of steel wires.

3.4. Fitting equation for reduction factors

According to the test data, fitting equations for reduction factors of mechanical properties of steel wires at high temperatures are obtained as follows,

3.4.1. Elastic modulus

$$\frac{E_S(T)}{E_S}=\frac{1}{1+e^{0.0101(T-550)}} \tag{1}$$

where, $E_S(T)$ and E_S are the elastic modulus of steel wires at temperature T and ambient temperature, respectively.

Fig. 9 gives the fitting curve of Eq. (1).

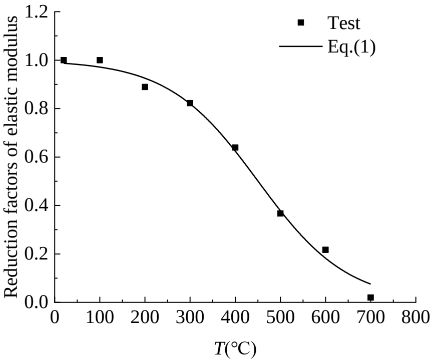

Fig. 9 Reduction factor of elastic modulus-temperature curve

3.4.2. Proportional limit

$$\frac{\sigma_p(T)}{\sigma_p}=7.46\times10^{-9}T^3-8.94\times10^{-6}T^2+1.23\times10^{-3}T+0.97 \tag{2}$$

where, $\sigma_p(T)$ and σ_p are the proportional limit of steel wires at temperature T and ambient temperature, respectively.

The fitting curve of Eq. (2) is plotted in Fig. 10.

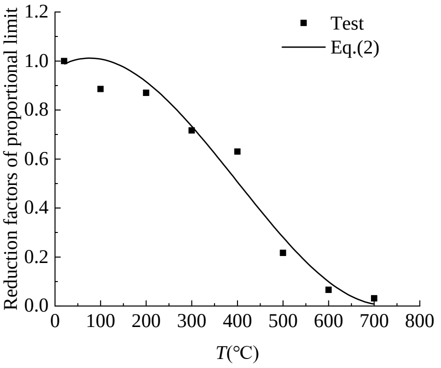

Fig. 10 Reduction factor of proportional limit-temperature curve

3.4.3. Ultimate strength

$$\frac{\sigma_b(T)}{\sigma_b}=\frac{1}{1+e^{0.0147(T-432)}} \tag{3}$$

where, $\sigma_b(T)$ and σ_b are the ultimate strength of steel wires at temperature T and ambient temperature, respectively.

Fig. 11 shows the fitting curve of Eq. (3).

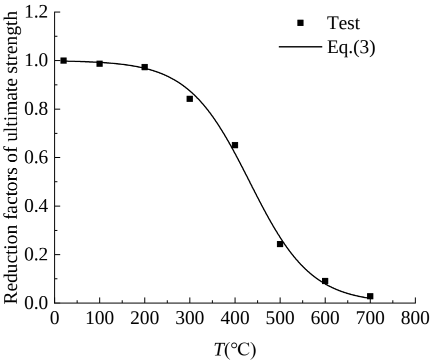

Fig. 11 Reduction factor of ultimate strength-temperature curve

3.4.4. Strain at ultimate strength

The strain corresponding to the maximum stress of the specimen reaching the ultimate strength is the strain at ultimate strength. The reduction factor of the strain at ultimate strength at elevated temperature is obtained as follows,

$$\frac{\varepsilon_b(T)}{\varepsilon_b}=\begin{cases}1 & 20^\circ\mathrm{C}\le T\le180^\circ\mathrm{C}\\ -3.30\times10^{-3}T+1.57 & 180^\circ\mathrm{C}\le T\le400^\circ\mathrm{C}\\ 3.40\times10^{-4}T+9.67\times10^{-2} & 400^\circ\mathrm{C}\le T\le500^\circ\mathrm{C}\\ 5.80\times10^{-3}T-2.62 & 500^\circ\mathrm{C}\le T\le700^\circ\mathrm{C}\end{cases} \tag{4}$$

where, $\varepsilon_b(T)$ and ε_b are the strain at ultimate strength of steel wires at temperature T and ambient temperature, respectively.

The fitting curve of Eq. (4) is shown in Fig. 12.

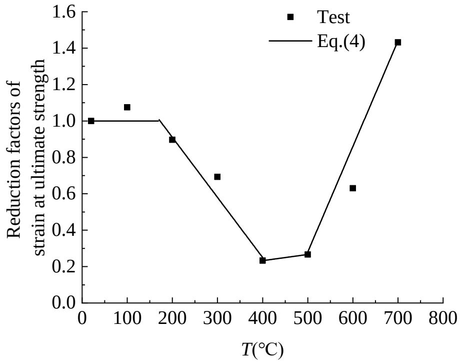

Fig. 12 Reduction factor of strain at ultimate strength-temperature curve

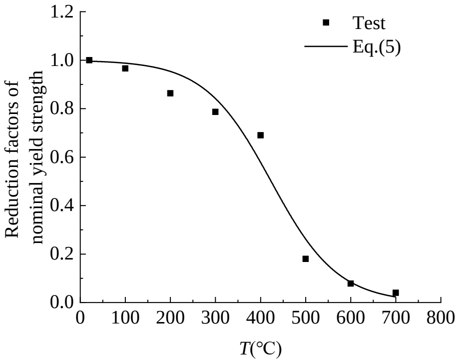

Fig. 13 Reduction factor of nominal yield strength-temperature curve

3.4.5. Nominal yield strength

$$\frac{\sigma_{0.2}(T)}{\sigma_{0.2}}=\frac{1}{1+e^{0.0135(T-424)}} \tag{5}$$

where, $\sigma_{0.2}(T)$ and $\sigma_{0.2}$ are nominal yield strength of steel wires at temperature T and ambient temperature, respectively.

The fitting curve of Eq. (5) is shown in Fig. 13.

3.4.6. Strain at nominal yield strength

$$\frac{\varepsilon_{0.2}(T)}{\varepsilon_{0.2}}=\begin{cases}1 & 20^{\circ}\mathrm{C}\le T\le 380^{\circ}\mathrm{C}\\ -2.40\times10^{-3}T+1.9161 & 380^{\circ}\mathrm{C}\le T\le 600^{\circ}\mathrm{C}\end{cases} \tag{6}$$

where, $\varepsilon_{0.2}(T)$ and $\varepsilon_{0.2}$ are strain at nominal yield strength of steel wires at temperature T and ambient temperature, respectively.

The fitting curve of Eq. (6) is presented in Fig. 14.

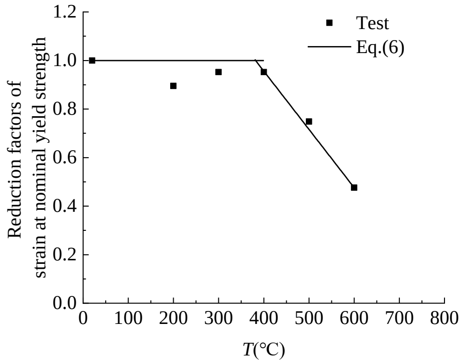

Fig. 14 Reduction factor of strain at nominal yield strength-temperature curve

3.5. Constitutive equation

The constitutive equation of the steel wires at elevated temperatures is fitted with a trilinear line. The trilinear line includes a segment from the origin to the proportional limit point, a segment from the proportional limit point to the nominal yield strength point, and a segment from the nominal yield strength point to the ultimate strength point. The fitting equation is shown as follows,

$$\sigma=\begin{cases}E_{\mathrm{S}}(T)\times\varepsilon & 0\le\varepsilon\le\dfrac{\sigma_{\mathrm{p}}(T)}{E_{\mathrm{S}}(T)}\\[2ex] \dfrac{\sigma_{0.2}(T)-\sigma_{\mathrm{p}}(T)}{\varepsilon_{0.2}(T)-\dfrac{\sigma_{\mathrm{p}}(T)}{E_{\mathrm{S}}(T)}}\times\left[\varepsilon-\dfrac{\sigma_{\mathrm{p}}(T)}{E_{\mathrm{S}}(T)}\right]+\sigma_{\mathrm{p}}(T) & \dfrac{\sigma_{\mathrm{p}}(T)}{E_{\mathrm{S}}(T)}\le\varepsilon\le\varepsilon_{0.2}(T)\\[2ex] \dfrac{\sigma_{\mathrm{b}}(T)-\sigma_{0.2}(T)}{\varepsilon_{\mathrm{b}}(T)-\varepsilon_{0.2}(T)}\times\left[\varepsilon-\varepsilon_{0.2}(T)\right]+\sigma_{0.2}(T) & \varepsilon_{0.2}(T)\le\varepsilon\le\varepsilon_{\mathrm{b}}(T)\end{cases} \tag{7}$$

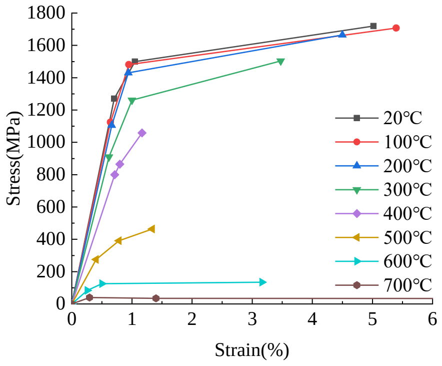

Fig. 15 Stress-strain fitting curves of steel wires at elevated temperatures

Stress-strain curves at various temperatures obtained by the equation are shown in Fig. 15.

4. Results and analysis of post-elevated-temperature test

4.1. Visual observations

Fig. 16 shows the failure modes of the specimens after the tensile test. The maximum temperatures experienced by various specimens from left to right were 300°C, 400°C, 500°C, 600°C and 700°C, respectively. When the specimen was experiencing a temperature of 300°C, it was broken near the pier head, with a fracture along the 45° direction, which phenomenon was the same as the specimen broken at ambient temperature. The specimens that had been exposed to a temperature above 400°C were all broken in the heated area after cooling, and their fractures were all tapered and necked. After exposure to 500°C, the metallic luster on the surface of the specimen faded. The surface of the specimen turned light yellow after exposure to 600°C, and yellowish - brown after exposure to 700°C.

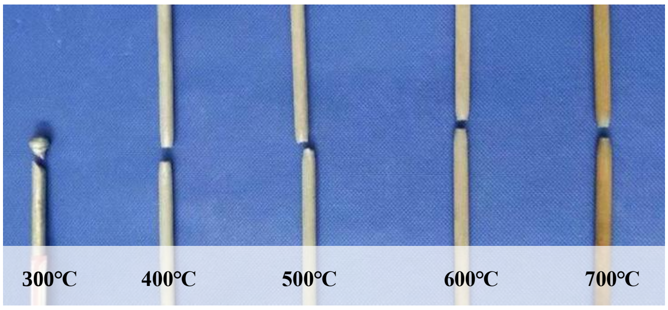

Fig. 16 Failure modes of steel wires after post-elevated-temperature test

4.2. Analysis of test results

Stress-strain curves of the specimens cooled from different temperatures are presented in Fig. 17. According to the test data, reduction factors of mechanical properties of the steel wires after exposure to elevated temperatures can be obtained, as tabulated in Table 2. It can be found from the figure and table that, the elastic modulus of the specimens did not change obviously after cooling from the elevated temperatures, and their reduction factors were all within 10%. Therefore, the specimens could recover the initial elastic modulus after fire. After cooling from the temperature below 400°C, the nominal yield strength and ultimate strength of the specimens had no evident degradation, and the reduction factor was within 10%. The nominal yield strength and ultimate strength of the specimens began to degrade significantly after cooling from the temperature above 400°C. The nominal yield strength decreased by 22% and the ultimate strength decreased by 23% after exposure to 500°C. With the increase of the maximum exposure temperature, the degradation of the nominal yield strength and ultimate strength of the specimen became more obvious. After cooling from the temperature up to 700°C, the nominal yield strength and the ultimate strength had decreased to 32% and 40% of that at the ambient temperature, respectively.

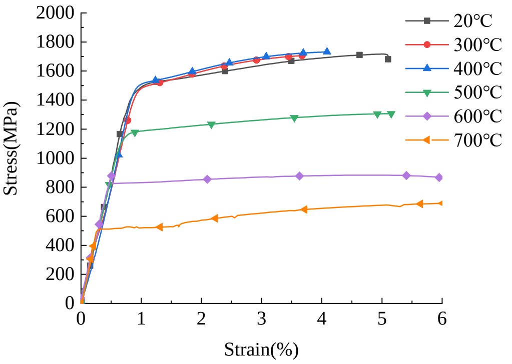

Fig. 17 Stress-strain curves of steel wires after cooling from elevated temperatures

4.3. Comparison and discussion

Since the elastic modulus of the steel wires changed very little after cooling from elevated temperatures, only the reduction factors of the nominal yield strength and ultimate strength of the steel wires are compared. Reduction factors of the nominal yield strength and ultimate strength obtained in this paper are compared with those of a Grade 1570 prestressed steel wire of Fan *et al.* [14], a Grade 1670 galvanized prestressed steel wire of Lu *et al.* [15], and a Grade 1770 prestressed steel wire of Zheng *et al.* [17] and Atienza *et al.* [18], as exhibited in Figures 18 and 19. In the figures, the reduction factors in this paper, Fan *et al.* [14], Lu *et al.* [15], Zheng *et al.* [17] and Atienza *et al.* [18] are marked with DW1670, FW1570, LW1670, ZW1770 and AW1770, respectively.

(1) Comparison of nominal yield strength

As can be seen in Fig. 18, the reduction factors of this paper (DW1670) are close to those of LW1670, ZW1770 and AW1770 after exposure to temperatures below 300°C; close to LW1670 and higher than others after cooling from 400°C. DW1670 is close to LW1670 and AW1770 and higher than ZW1770 and FW1570 after cooling from 500°C, and is only lower than LW1670 after exposure to 600°C. DW1670 decreases more quickly after cooling from 600°C and 700°C, and is obviously lower than LW1670 and close to the others after exposure to 700°C.

Table 2

Mechanical properties of steel wires after cooling from elevated temperatures

T(°C)	$E_S^{\#}(T)$(GPa)	$E_S^{\#}(T)/E_S$	$\sigma_{0.2}^{\#}(T)$(MPa)	$\sigma_{0.2}^{\#}(T)/\sigma_{0.2}$	$\sigma_b^{\#}(T)$(MPa)	$\sigma_b^{\#}(T)/\sigma_b$
20	180	1	1500	1	1703	1
300	175	0.97	1490	0.99	1705	1.00
400	185	1.03	1503	1.00	1731	1.02
500	173	0.96	1175	0.78	1306	0.77
600	171	0.95	929	0.62	961	0.56
700	190	1.06	485	0.32	683	0.40

Notes: T is the maximum exposure temperature, $E_S^{\#}(T)$ is the elastic modulus of steel wires after cooling from T, $\sigma_{0.2}^{\#}(T)$ is the nominal yield strength of steel wires after cooling from T, $\sigma_b^{\#}(T)$ is the ultimate strength of steel wires after cooling from T.

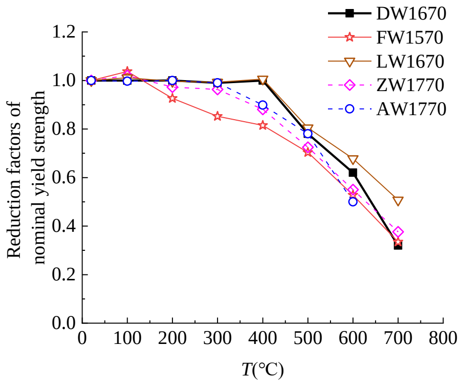

Fig. 18 Comparison of reduction factors of nominal yield strength

(2) Comparison of ultimate strength

As shown in Fig. 19, the reduction factors of FW1570 are visibly low. DW1670 is close to the others after cooling from temperatures below 300°C; close to LW1670 and higher than the others after exposure to 400°C. DW1670 is slightly lower than LW1670, close to AW1770, and slightly higher than ZW1770 after cooling from 500°C. When the maximum temperatures experienced by the specimens are above 600°C, DW1670 is close to ZW1770 and AW1770 and lower than LW1670.

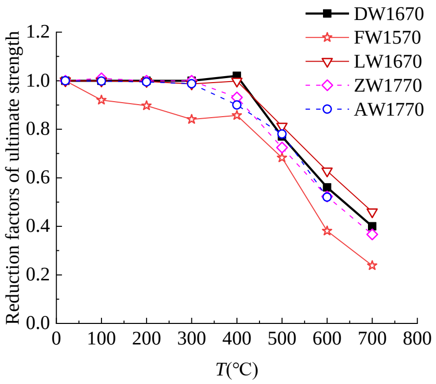

Fig. 19 Comparison of reduction factors of ultimate strength

In general, except for FW1570, the nominal yield strength and ultimate strength of different grades of steel wires begin to degrade significantly when the exposure temperature reaches above 400°C, and the decay trends are essentially consistent.

4.4. Fitting equation for reduction factors

According to the test data, fitting equations for reduction factors of mechanical properties of steel wires after exposed to elevated temperature are given as follows,

4.4.1. Elastic modulus

$$\frac{E_S^{\#}(T)}{E_S}=1 \tag{8}$$

where, $E_S^{\#}(T)$ and E_S are the elastic modulus of the steel wire after cooling from temperature T and at ambient temperature, respectively.

4.4.2. Proportional limit

$$\frac{\sigma_p^{\#}(T)}{\sigma_p}=\begin{cases}1 & 20°\mathrm{C}\le T\le 400°\mathrm{C}\\ -0.0019T+1.7591 & 400°\mathrm{C}\le T\le 700°\mathrm{C}\end{cases} \tag{9}$$

where, $\sigma_p^{\#}(T)$ and σ_p are the proportional limit of the steel wire after cooling from temperature T and at ambient temperature, respectively.

The fitting curve of Eq. (9) is plotted in Fig. 20.

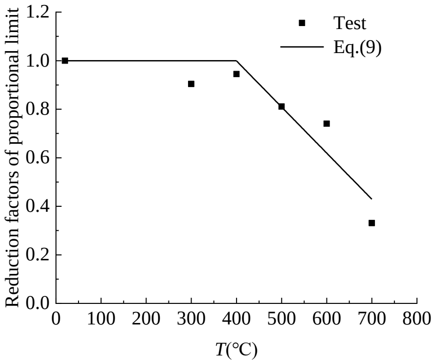

Fig. 20 Reduction factor of proportional limit-temperature curve

4.4.3. Ultimate strength

$$\frac{\sigma_b^{\#}(T)}{\sigma_b}=\begin{cases}1 & 20°\mathrm{C}\le T\le 400°\mathrm{C}\\ -0.002T+1.814 & 400°\mathrm{C}\le T\le 700°\mathrm{C}\end{cases} \tag{10}$$

where, $\sigma_b^{\#}(T)$ and σ_b are the ultimate strength of the steel wire after cooling from temperature T and at ambient temperature, respectively.

The fitting curve of Eq. (10) is shown in Fig. 21.

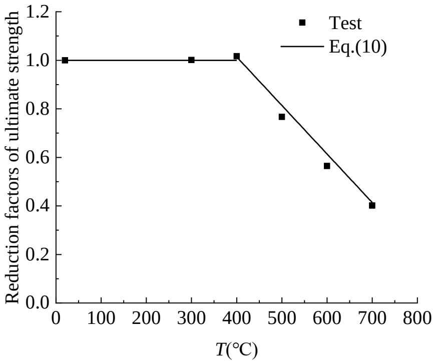

Fig. 21 Reduction factor of ultimate strength-temperature curve

4.4.4. Nominal yield strength

$$\frac{\sigma_{0.2}^{\#}(T)}{\sigma_{0.2}}=\begin{cases}1 & 20^{\circ}\mathrm{C}\le T\le 400^{\circ}\mathrm{C}\\ -0.0022T+1.892 & 400^{\circ}\mathrm{C}\le T\le 700^{\circ}\mathrm{C}\end{cases} \tag{11}$$

where, $\sigma_{0.2}^{\#}(T)$ and $\sigma_{0.2}$ are the nominal yield strength of the steel wire after cooling from temperature T and at ambient temperature, respectively.

Fig. 22 presents the fitting curve of Eq. (11).

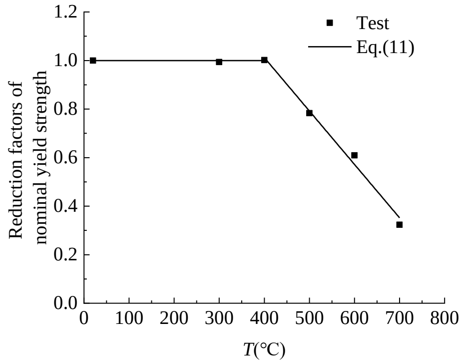

Fig. 22 Reduction factor of nominal yield strength-temperature curve

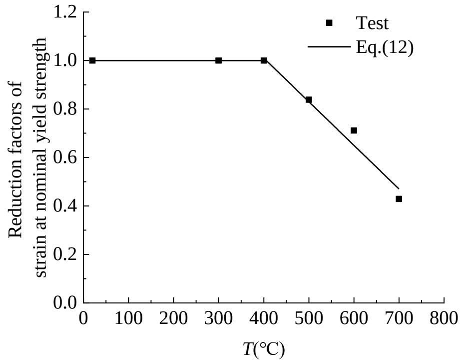

Fig. 23 Reduction factor of strain at nominal yield strength-temperature curve

4.4.5. Strain at nominal yield strength

$$\frac{\varepsilon_{0.2}^{\#}(T)}{\varepsilon_{0.2}}=\begin{cases}1 & 20^{\circ}\mathrm{C}\le T\le 400^{\circ}\mathrm{C}\\ -0.0018T+1.7591 & 400^{\circ}\mathrm{C}\le T\le 700^{\circ}\mathrm{C}\end{cases} \tag{12}$$

where, $\varepsilon_{0.2}^{\#}(T)$ and $\varepsilon_{0.2}$ are the strain at nominal yield strength of the steel wire after cooling from temperature T and at ambient temperature, respectively.

The fitting curve of Eq. (12) is plotted in Fig. 23.

4.5. Constitutive equation

By the same method as that at elevated temperatures, the constitutive equation of the steel wire after exposed to high temperatures is fitted with a trilinear line. The fitting equation is shown as follows,

$$\sigma=\begin{cases}E_S^{\#}(T)\times\varepsilon & 0\le\varepsilon\le\dfrac{\sigma_p^{\#}(T)}{E_S^{\#}(T)}\\ \dfrac{\sigma_{0.2}^{\#}(T)-\sigma_p^{\#}(T)}{\varepsilon_{0.2}^{\#}(T)-\dfrac{\sigma_p^{\#}(T)}{E_S^{\#}(T)}}\times\left[\varepsilon-\dfrac{\sigma_p^{\#}(T)}{E_S^{\#}(T)}\right]+\sigma_p^{\#}(T) & \dfrac{\sigma_p^{\#}(T)}{E_S^{\#}(T)}\le\varepsilon\le\varepsilon_{0.2}^{\#}(T)\\ \dfrac{\sigma_b^{\#}(T)-\sigma_{0.2}^{\#}(T)}{\varepsilon_b^{\#}(T)-\varepsilon_{0.2}^{\#}(T)}\times\left[\varepsilon-\varepsilon_{0.2}^{\#}(T)\right]+\sigma_{0.2}^{\#}(T) & \varepsilon_{0.2}^{\#}(T)\le\varepsilon\le\varepsilon_b^{\#}(T)\end{cases} \tag{13}$$

Stress-strain curves of steel wires cooling from various temperatures obtained by the equation are exhibited in Fig. 24.

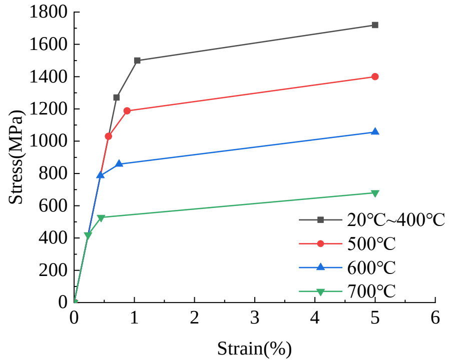

Fig. 24 Stress-strain fitting curves of steel wire after cooling from elevated temperatures

5. Conclusions

In this paper, elevated-temperature and post-elevated-temperature tensile tests were performed on Grade 1670 steel wires with a diameter of 7mm. The test results were compared with the existing test results of prestressed steel wires and steel cables. The following conclusions are obtained,

(1) At elevated temperatures, mechanical properties of the prestressed steel wire changed little with the temperature below 300°C and degraded significantly at 300°C ~ 600°C. The load-carrying ability was substantially lost when the temperature reached 700°C.

(2) After elevated temperatures, the elastic modulus of the steel wires had no obvious change with the exposure temperature. The nominal yield strength and ultimate strength of the steel wires remained unchanged after exposed to temperatures below 400°C, and tended to decrease after cooling from higher exposure temperatures.

(3) Equations of elevated-temperature and post-elevated-temperature mechanical behaviors of steel wires are fitted as a function of the temperature, and constitutive models of the steel wire at elevated temperatures and after exposed to elevated temperatures are obtained.

Acknowledgments

The research work described in this paper is sponsored by the Nation Natural Science Foundation of China (Grant No. 51808117). The financial support is highly appreciated.

References

[1] Zhou H.T., Li G.Q. and Jiang S.C., “Experimental studies on the properties of steel strand at elevated temperatures”, Journal of Sichuan University, 40(5), 106-110, 2008.

[2] Zong Z.L., He Y.F. and Li S.G., “Analysis of the fire-resistance of prestressed steel structure based on mechanical properties of steel strands under the high temperature”, Sichuan Building Science, 39(5), 47-51, 2013.

[3] Zong Z.L., Zhang J., Jiang D.W. and Yao J.W., “Experimental research on the mechanical properties of steel strand wire at elevated temperature”, Build Science, 32(1), 43-47, 2016.

[4] Fontanari V., Benedetti M., Monelli B.D. and Degasperi F., “Fire behavior of steel wire ropes: Experimental investigation and numerical analysis”, Engineering Structures, 84(1), 340-349, 2015.
[5] Conor T., “Mechanical properties of cold-drawn steel strand at elevated temperatures”, Lehigh University, 2015.
[6] Shakya A.M. and Kodur V., “Effect of temperature on the mechanical properties of low relaxation seven-wire prestressing strand”, Construction and Building Materials, 124(15), 74-84, 2016.
[7] Du Y., Peng J.Z., Liew R. J.Y. and Li G.Q., “Mechanical properties of high tensile steel cables at elevated temperatures”, Construction and Building Materials, 182(10), 52-65, 2018.
[8] Du Y., Sun Y.K. and Li G.Q., “Mechanical properties of high tensile steel cables at elevated temperature”, Engineering Mechanics, 36(4), 231-238, 2019.
[9] Du Y., Qi H.H., Jiang J., Liew R. J.Y. and Li G.Q., “Mechanical properties of 1670MPa parallel wire strands at elevated temperatures”, Construction and Building Materials, 263(8), 1-16, 2020.
[10] Du Y., Xiao L.P., Li G.Q. and Wang X.C., “Mechanical properties of high tensile parallel wire cables at elevated temperatures”, Journal of Building Materials, 23(1), 114-121, 2020.
[11] Sun G.J., Li X.H. and Xue S.D., “Mechanical properties of stainless-steel cables at elevated temperature”, Journal of Materials in Civil Engineering, 31(7), 1-10, 2019.
[12] Sun G.J., Li X.H., Xue S.D. and Chen R.H., “Mechanical properties of Galfan-coated steel cables at elevated temperatures”, Journal of Constructional Steel Research, 155(4), 331-341, 2019.
[13] Sun G.J., Li Z.H., Wu J.Z. and Ren J.Y., “Investigation of steel wire mechanical behavior and collaborative mechanism under high temperature”, Journal of Constructional Steel Research, 188(10), 1-14, 2022.
[14] Fan J. and Lu Z.T., “Experimental study on materials properties of prestressed steel wire post high temperatures”, Industrial Building, 32(9), 30-31, 2002.
[15] Lu J., Liu H.B. and Chen Z.H., “Post-fire mechanical properties of low-relaxation hot-dip galvanized prestressed steel wires”, Journal of Constructional Steel Research, 136, 110-127, 2017.
[16] Lu J., Liu H.B. and Liu J.D., “Post-fire mechanical properties of Galfan-coated steel cables with extruded anchorages”, Journal of Tianjin University(Science and Technology), 50, 7-17, 2017.
[17] Zheng W.Z., Hu Q. and Zhang H.Y., “Experimental research on the mechanical properties of prestressing steel wire at and after high temperature”, Journal of Building Structures, 27(2), 120-128, 2006.
[18] Atienza J.M. and Elices M., “Behavior of prestressing steels after a simulated fire: Fire-induced damages”, Construction and Building Materials, 23(8), 2932-2940, 2009.
[19] Zong Z.L., Zhang J., Jiang D.W. and Yao J.W., “Experimental research on the mechanical properties of steel strand after high temperature”, Fire Science and Technology, 34(3), 311-314, 2015.
[20] Zhang Z.L., Guo T., Wang S.Y., Liu J. and Wang L.B., “Experimental study on post-fire properties of steel wires of bridge suspender”, Structures, 33(21), 1252-1262, 2021.
[21] Metallic materials-Tensile testing-Part 1: Method of test at room temperature (GB/T 228.1-2010), General Administration of Quality Supervision, Inspection and Quarantine of the People's Republic of China Beijing, China, 2010.
[22] Metallic materials-Tensile testing-Part 2: Method of test at elevated temperature (GB/T 228.2-2015), General Administration of Quality Supervision, Inspection and Quarantine of the People's Republic of China Beijing, China, 2015.

Advanced Steel Construction – Vol. 19 No. 1 (2023) 17–22
DOI:10.18057/IJASC.2023.19.1.3
(**Special Issue:** *10th International Conference on Advances in Steel Structures, ICASS'2020, Chengdu, China*)

ULTIMATE STRENGTH, DUCTILITY, AND FAILURE MODE OF HIGH-STRENGTH FRICTIONAL BOLTED JOINTS MADE OF HIGH-STRENGTH STEEL

Zi-Ce Qin [1], H. Moriyama [2, *], T. Yamaguchi [3], M. Shigeishi [4], Yu-Yue Xing [1] and A. Hashimoto [5]

[1] *Graduate School of Science and Technology, Kumamoto University, Kumamoto, Japan*
[2] *Graduate School of Technology, Industrial and Social Sciences, Tokushima University, Tokushima, Japan*
[3] *Department of Civil Engineering, Osaka Metropolitan University, Osaka, Japan*
[4] *Department of Civil and Architectural Engineering, Kumamoto University, Kumamoto, Japan*
[5] *Technical Division, Faculty of Engineering, Kumamoto University, Kumamoto, Japan*
* *(Corresponding author: E-mail: moriyama.hitoshi@tokushima-u.ac.jp)*

ABSTRACT

Further structural rationalization of steel bridges such as weight reduction of members can be realized by using high-strength steel. However, owing to the high yield-to-tensile strength ratio, failure of connected members occurs before the members in the gross area are plastic-deformed sufficiently. In this study, tensile tests of frictional bolted joints with various geometrical configurations and grades of plates and bolts were conducted to compare the failure modes of high-strength and mild steel joints and to investigate the relationship among ultimate strength, ductility, and failure mode. The results indicate that the failure modes of high-strength steel joints were the same as those of mild steel joints and can be almost classified with the respective ratios of net cross-section failure resistance and plate shear failure resistance to bolt shear failure resistance. Ultimate resistance and ductility were maximum in the case of split failure mode where these ratios were approximately 1.0; they increased as the ratios decreased. Therefore, it can be concluded that these ratios should be less than 1.0 to induce the split failure mode to enable the breaking of a high-strength steel joint after the member is plastic-deformed sufficiently.

ARTICLE HISTORY

Received: 20 July 2022
Revised: 22 August 2022
Accepted: 10 January 2023

KEYWORDS

High strength steel;
High-strength frictional bolted joints;
Ultimate strength;
Ductility;
Failure modes

1. Introduction

Further structural rationalization of steel bridges such as weight reduction of members can be realized by using the strength of high-strength steel (hereafter called as HSS) and it improves the productivity and constructability of bridges. However, as the yield-to-tensile strength ratio (hereafter called the yield ratio) of HSS is greater than 0.90, failure of members connected by bolted joints can occur before members in the gross area are sufficiently plastic-deformed. Moreover, Eurocode 3, in which the limit state design is adopted, restricts the yield ratio to 0.72, which restricts the use of HSS [1,2,3]. The resistance relationship of a connected member at a general part and bolted joint part is expressed by eqs. (1)–(3) without considering any partial factors. As shown in these equations for the current design, it is difficult to complete the relationship of HSS members such as truss members, whose axial force is constant in the longitudinal direction.

$$P_{ygd} = A_g \sigma_y \tag{1}$$

$$P_{tnd} = A_n \sigma_t \tag{2}$$

$$P_{ygd} < P_{tnd} \Longleftrightarrow A_g \sigma_y < A_n \sigma_t \Longleftrightarrow \frac{\sigma_y}{\sigma_t} (= YR) < \frac{A_n}{A_g} < 1.0 \tag{3}$$

Here, P_{ygd} is the gross cross-section yield resistance, P_{tnd} is the net cross-section failure resistance, A_g is the gross cross-sectional area, σ_y is the yield strength, A_n is the net cross-sectional area, σ_t is the tensile strength, and YR is the yield ratio.

On the other hand, some researchers report that a HSS joint has the same ductility as a mild steel joint when the connected plate is broken but the bolts are unbroken [4,5,6]. Therefore, if the effect of the yield ratio on the after-slip mechanical behavior is elucidated, structural rationalization with HSS can be realized by controlling the failure mode of the joints and securing the same ductility as a mild steel joint. Recently, a HSS called "steels for bridge high performance structure (SBHS)" was fabricated in Japan; it has high strength and weldability by applying thermos-mechanical control processes [7,8]. Additionally, SBHS has already been specified in Japanese Industrial Standards [9] and various research has been conducted [10,11].

In this study, tensile tests of high-strength frictional bolted joints with SBHS, with various geometrical configurations and grades of steel plate and bolts, were conducted to compare the failure modes of HSS and mild steel joints and to investigate the relationship among ultimate strength, ductility, and failure modes.

2. Tensile tests

2.1. Specimens

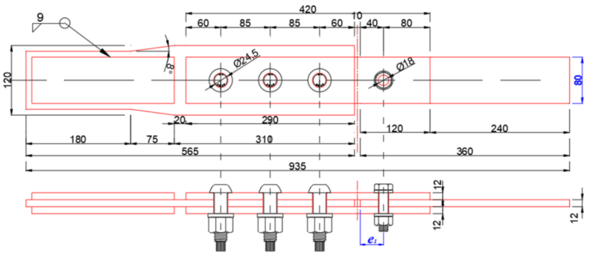

(a) Series "*n*=1, *w*/*d*=5.0"

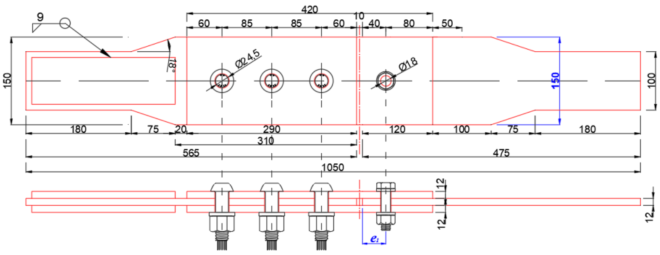

(b) Series "*n*=1, *w*/*d*=9.4"

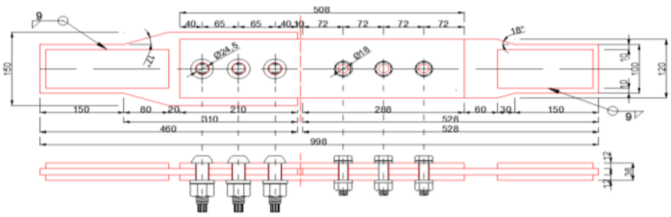

(c) Series "*n*=3"

Fig. 1 Geometrical dimensions of specimens (unit: mm)

Table 1
Structural configurations and bolt arrangement (M16 bolt)

Experimental Case	Number of Bolts	Steel Grade	Bolt Grade	End Distance e_1 (mm)	Bolt Pitch p (mm)	Width w (mm)
n1-B508-ed25-wd50	1	SBHS 500	F8T	40	-	80
n1-B508-ed25-wd94						150
n1-B510-ed25-wd50	1	SBHS 500	F10T	40	-	80
n1-B510-ed25-wd94						150
n1-B510-ed35-wd50				56	-	80
n1-B510-ed35-wd94						150
n1-B512.9-ed35-wd50	1	SBHS 500	12.9 Class	56	-	80
n1-B512.9-ed35-wd94						150
n1-B512-ed25-wd50	1	SBHS 500	12G	40	-	80
n1-B512-ed25-wd94						150
n1-B512-ed35-wd50				56	-	80
n1-B512-ed35-wd94						150
n1-B514-ed25-wd50	1	SBHS 500	S14T	40	-	80
n1-B514-ed25-wd94						150
n1-B514-ed35-wd50				56	-	80
n1-B514-ed35-wd94						150
n1-B710-ed25-wd50	1	SBHS 700	F10T	40	-	80
n1-B710-ed25-wd94						150
n1-B710-ed35-wd50				56	-	80
n1-B710-ed35-wd94						150
n1-B712.9-ed25-wd50	1	SBHS 700	12.9 Class	40	-	80
n1-B712.9-ed25-wd94						150
n1-B712.9-ed35-wd50				56	-	80
n1-B712.9-ed35-wd94						150
n1-B712-ed25-wd50	1	SBHS 700	12G	40	-	80
n1-B712-ed25-wd94						150
n1-B712-ed35-wd50				56	-	80
n1-B712-ed35-wd94						150
n1-B714-ed25-wd50	1	SBHS 700	S14T	40	-	80
n1-B714-ed25-wd94						150
n1-B714-ed35-wd50				56	-	80
n1-B714-ed35-wd94						150
n3-B510-ed45-wd75	3	SBHS 500	F10T	72	72	120
n3-B512-ed45-wd75			12G			
n3-B514-ed45-wd75			S14T			
n3-B712.9-ed45-wd75	3	SBHS 700	12.9 C.	72	72	120
n3-B712-ed45-wd75			12G			
n3-B714-ed45-wd75			S14T			

Fig.1 shows the geometrical dimensions of the specimens. M16 bolts were used on the slip-side because of the limitation of the capacity of the loading machine although it is desirable to use M22 bolts, which are commonly used in steel structures. SHTB-M22 bolts, whose tensile strength is 1400 MPa, were used on the fixed-side.

Table 1 shows the structural configurations and bolt arrangement. As shown in Fig.1 and Table 1, the parameters considered are number of bolts n, steel grades, bolt grades, end distance e_1, and width w. In cases of series "n = 3", structural configurations such as end/edge distance and bolt pitch are not changed. If bolt shear failure occurred and the plastic strain and deformation of connected plate was not confirmed based on the residual stress and bearing deformation after the test, the original bolt hole of cases corresponding to that was expanded to 24.5 mm in diameter to obtain more data by conducting re-tests. Re-tests were conducted with M22 bolts. As shown in Table 2, bolt grades and bolt tensions were varied in the re-test.

Table 2
Structural configurations and bolt arrangement of re-test specimens (M22 bolt)

Experimental Case	Number of Bolts	Steel Grade	Bolt Grade	End Distance e_1 (mm)	Width w (mm)	Designed Bolt Tensions N_d (kN)
n1-B510-ed35-wd50-N100	1	SBHS 500	F10T	56	80	205
n1-B510-ed35-wd50-N150						308
n1-B510-ed35-wd94-N100					150	205
n1-B510-ed35-wd94-N150						308
n1-B710-ed25-wd50-N100	1	SBHS 700	F10T	40	80	205
n1-B710-ed25-wd50-N150						308
n1-B710-ed25-wd94-N100					150	205
n1-B710-ed25-wd94-N150						308
n1-B714-ed35-wd50-N025	1	SBHS 700	S14T	56	80	75
n1-B714-ed35-wd50-N050						150
n1-B714-ed35-wd50-N075						224
n1-B714-ed35-wd50-N100						299
n1-B714-ed35-wd94-N025	1	SBHS 700	S14T	56	150	75
n1-B714-ed35-wd94-N050						150
n1-B714-ed35-wd94-N075						224
n1-B714-ed35-wd94-N100						299

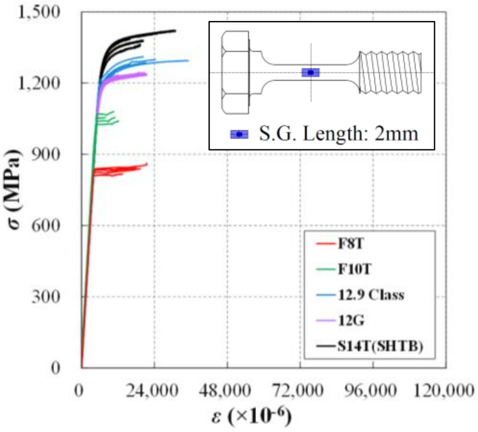

(a) Bolt

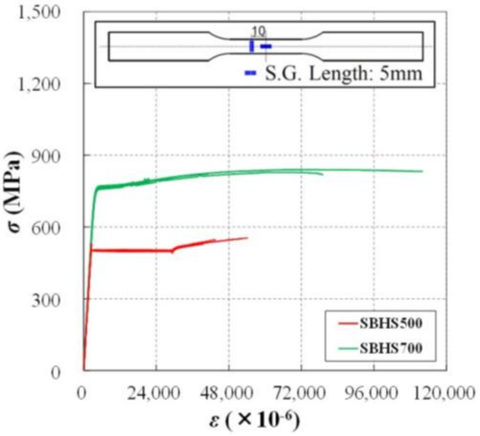

(b) Plate

Fig. 2 Mechanical properties of used steels and bolts based on material tests

Mechanical properties of plates and high-strength bolts obtained by material tests are shown in Table 3 and Fig.2. The number of material test coupons is five in every steel grade and bolt glade. Young's modulus and Poisson's ratio were calculated using the least squares method with strain gauges attached to the bolts at locations illustrated in Fig.2. When a clear yield point was not confirmed because of high yield ratio, 0.2% offset yield strength adopted to calculate the designed yield resistance of all specimens. It can be observed from Table 3 that the yield ratios of all materials are greater than 0.9. The mechanical properties of M22 bolts were quoted from the inspection certificate.

Table 3
Mechanical properties of plates and bolts

Objects	Nominal Thickness t (mm)	Bolt Diameter d (mm)	Steel /Bolt Grade	Nominal Length L (mm)	Young's Modulus E (MPa)	Poisson's Ratio ν	Upper Yield Stress σ_y (MPa)	0.2% Offset Y.S. $\sigma_{y0.2}$ (MPa)	Tensile Strength σ_t (MPa)	Yield Strain $\varepsilon_y = (\sigma_y, \sigma_{y0.2}) / E$ ($\times 10^{-6}$)	Yield Ratio $\gamma = (\sigma_y, \sigma_{y0.2}) / \sigma_t$	Elongation after Fracture (%)	Reduction of Area after Fracture (%)
Plate	12	-	SBHS500	-	205,939	0.269	527.4	-	585.4	2,561	0.901	38.6	-
			SBHS700		214,728	0.261	-	765.1	835.5	3,563	0.916	30.6	-
Bolt	-	16	F8T	65	209,623	0.283	829.1	830.2	885.8	3,955	0.936	25.5	73.9
			F10T	65	214,062	0.286	1,050.9	1,047.7	1,093.9	4,909	0.961	21.3	65.5
			12.9 Class	65	212,719	0.283	-	1,215.6	1,307.6	5,714	0.930	15.5	54.7
			12G	75	211,268	0.279	-	1,202.9	1,282.4	5,694	0.938	20.1	56.5
			S14T(SHTB)	75	208,240	0.278	-	1,316.4	1,430.0	6,321	0.921	19.2	54.4
		22*	F10T	75	-	-	-	1,037.0	1,092.0	-	0.950	20.0	71.0
			S14T(SHTB)	75	-	-	-	1,337.0	1,438.0	-	0.930	15.0	54.0

Note: Underlined data is used for calculation of yield strain ε_y and yield ratio γ. The mechanical properties of M22* bolts are quoted from the mill test certificate.

2.2. Designed resistances

Tables 4 and 5 show a summary of the designed resistance of the specimens. The designed slip resistance P_{sd} and net cross-section yield resistance P_{ynd} are calculated using eqs. (4) and (5), respectively. The ratio of these resistances β_d, which is related to the slip behavior, is obtained from eq. (6). The net cross-section failure resistance P_{tnd} and plate shear failure resistance P_{esd} are calculated using eqs. (7) and (8), respectively. The bolt shear resistance P_{bod} is calculated from eq. (9), considering the positional relationship between the shear plane and bolt thread. Only when a 12.9 Class bolt is used, the thread is included in the shear plane.

$$P_{sd} = nm\mu_d N_d \tag{4}$$

$$P_{ynd} = (w - d_0) t_m \times \sigma_y \tag{5}$$

$$\beta_d = \frac{P_{sd}}{P_{ynd}} \tag{6}$$

$$P_{tnd} = (w - d_0) t \times \sigma_t \tag{7}$$

$$P_{esd} = 2 \times \{e_1 + (n-1)p\} t_m \times \frac{\sigma_t}{2} \tag{8}$$

$$P_{bod} = nmA_{b\_sh}\tau_{tb} = n \times 2 \times \frac{\pi d^2}{4} \times \frac{\sigma_{tb}}{\sqrt{3}} \tag{9a}$$

$$P_{bod} = n \times (A_{b\_sh} + A_{b\_th})\tau_{tb} = n \times (A_{b\_sh} + A_{b\_th}) \frac{\sigma_{tb}}{\sqrt{3}} \tag{9b}$$

Here, n is the number of bolts, m (=2) is the number of faying surfaces, μ_d (=0.65) is the designed slip coefficient, N_d is the designed bolt tension, w is the width, t_m is the thickness of the connected plate, d_0 is the bolt hole diameter, σ_y is the yield strength of the connected plate, σ_t is the tensile strength of the connected plate, e_1 is the end distance on the slip-side, A_{b_sh} is the effective cross-sectional area of the bolt shank, d is the bolt diameter, A_{b_th} is the effective cross-sectional area of the bolt threaded part, and σ_{tb} is the tensile strength of the bolt. For the re-test, the designed slip coefficient μ_d was set at the minimum 0.20, the coefficient of surfaces as rolled [12], considering the wear of zinc-rich paint coating.

2.3. Measuring items and methods

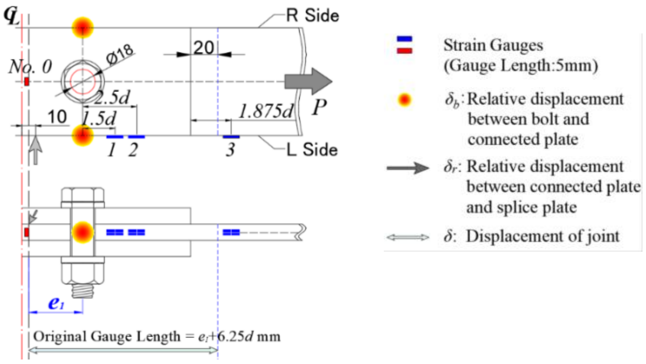

(a) Series "n=1, w/d=5.0"

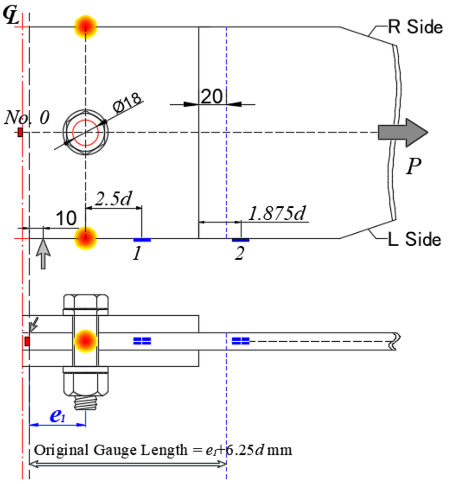

(b) Series "n=1, w/d=9.4"

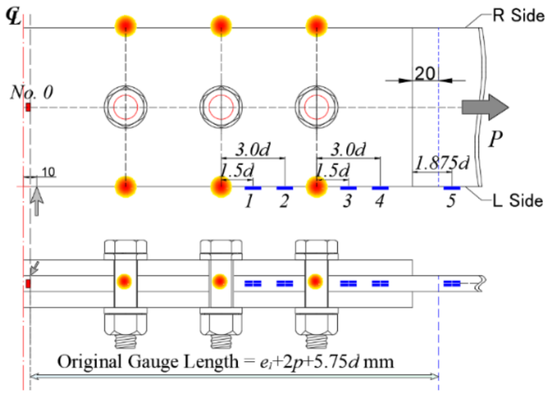

(c) Series "n=3"

Fig. 3 Measuring items and their measuring points

Table 4
Designed resistance of the specimens (M16 bolt, $\mu_d = 0.65$)

Experimental Case	P_{sd} (kN)	P_{ynd} (kN)	β_d	P_{bod} (kN)	P_{tnd} (kN)	P_{esd} (kN)	Expected Failure Mode
n1-B508-ed25-wd50	111	392	0.282	206	436	281	BO
n1-B508-ed25-wd94		835	0.133		927		BO
n1-B510-ed25-wd50	138	392	0.351	254	436	281	BO
n1-B510-ed25-wd94		835	0.165		927		BO
n1-B510-ed35-wd50		392	0.351		436	393	BO
n1-B510-ed35-wd94		835	0.162		927		BO
n1-B512.9-ed35-wd50	165	392	0.421	270	436	393	BO
n1-B512.9-ed35-wd94		835	0.198		927		BO
n1-B512-ed25-wd50	173	392	0.441	298	436	281	S
n1-B512-ed25-wd94		835	0.207		927		S
n1-B512-ed35-wd50		392	0.441		436	393	BO
n1-B512-ed35-wd94		835	0.207		927		BO
n1-B514-ed25-wd50	202	392	0.514	332	436	281	S
n1-B514-ed25-wd94		835	0.241		927		S
n1-B514-ed35-wd50		392	0.514		436	393	BO
n1-B514-ed35-wd94		835	0.214		927		BO
n1-B710-ed25-wd50	138	569	0.242	254	622	401	BO
n1-B710-ed25-wd94		1,212	0.114		1,323		BO
n1-B710-ed35-wd50		569	0.242		622	561	BO
n1-B710-ed35-wd94		1,212	0.114		1,323		BO
n1-B712.9-ed25-wd50	165	569	0.291	270	622	401	BO
n1-B712.9-ed25-wd94		1,212	0.136		1,323		BO
n1-B712.9-ed35-wd50		569	0.291		622	561	BO
n1-B712.9-ed35-wd94		1,212	0.136		1,323		BO
n1-B712-ed25-wd50	173	569	0.304	298	622	401	BO
n1-B712-ed25-wd94		1,212	0.143		1,323		BO
n1-B712-ed35-wd50		569	0.304		622	561	BO
n1-B712-ed35-wd94		1212	0.143		1,323		BO
n1-B714-ed25-wd50	202	569	0.354	332	622	401	BO
n1-B714-ed25-wd94		1,212	0.166		1,323		BO
n1-B714-ed35-wd50		569	0.354		622	561	BO
n1-B714-ed35-wd94		1,212	0.166		1,323		BO
n3-B510-ed45-wd75	413	646	0.640	762	716	1,517	N
n3-B512-ed45-wd75	519		0.804	893			N
n3-B514-ed45-wd75	605		0.836	995			N
n3-B712.9-ed45-wd75	496	936	0.530	811	1,023	2,166	BO
n3-B712-ed45-wd75	519		0.554	893			BO
n3-B714-ed45-wd75	605		0.646	995			BO

Fig.3 shows the measuring items and their measuring points. To evaluate the entire behavior of the joint, its displacement and relative displacement between the connected and splice plates were measured. The strain of the side surface of the connected plate was measured to investigate the strain distributions after a major slip. The bolt tension was measured and controlled by the strain gauge attached to the bolt shank. The bolt tension of bolts used in the re-test was controlled by the torque control based on eq. (10). The tightened tensions were 1.1 times the design bolt tensions, considering the creep phenomenon of zinc-rich paint coating after tightening. The relaxation measurement period was more than a week.

$$T = 1.1T_d = 1.1 \times kdN_0 \tag{10}$$

Table 5
Designed resistance of the re-test specimens (M22 bolt, $\mu_d = 0.20$)

Experimental Case	P_{sd} (kN)	P_{ynd} (kN)	β_d	P_{bod} (kN)	P_{tnd} (kN)	P_{esd} (kN)	Expected Failure Mode
n1-B510-ed35-wd50-N100	82	351	0.233	479	390	393	N
n1-B510-ed35-wd50-N150	123		0.350				N
n1-B510-ed35-wd94-N100	82	794	0.103		882	393	S
n1-B510-ed35-wd94-N150	123		0.155				S
n1-B710-ed25-wd50-N100	82	510	0.161	479	556	401	S
n1-B710-ed25-wd50-N150	123		0.241				S
n1-B710-ed25-wd94-N100	82	1,152	0.071		1,258		S
n1-B710-ed25-wd94-N150	123		0.107				S
n1-B714-ed35-wd50-N025	30	510	0.059	631	556	561	S
n1-B714-ed35-wd50-N050	60		0.117				S
n1-B714-ed35-wd50-N075	90		0.176				S
n1-B714-ed35-wd50-N100	120		0.235				S
n1-B714-ed35-wd94-N025	30	1,152	0.026	631	1,258	561	S
n1-B714-ed35-wd94-N050	60		0.052				S
n1-B714-ed35-wd94-N075	90		0.078				S
n1-B714-ed35-wd94-N100	120		0.104				S

Here, T_d is the designed torque, k is the torque coefficient of bolts quoted from the inspection certificate, and d is the bolt diameter.

The applied loading rate was controlled at 1 kN/s by manual operation, as much as practically possible. The sampling time is approximately once per second. In cases of plate failure modes, the applied load was removed at 95% of the maximum load after the peak to observe the peeled area for coating and bearing deformation of the bolt hole. In cases of bolt shear failure mode, loading was continued until bolt breakage occurred due to brittle failure.

3. Results

3.1. Failure modes

As shown in Fig.4, the failure modes confirmed in the test were shear failure (SH), split failure (SP), net cross-section failure (N), bolt shear failure (BO), bolt shear failure and plate shear yielding (BO(SH)), bolt shear failure and net cross-section yielding (BO(N)). These modes are the same as those of mild steel joints [13,14,15], as well as HSS joints in other countries [4,5,6].

Fig.5 shows the definition of failure modes in this paper. Shear failure mode (SH) is the state when only plate shear yielding occurs, followed by tear-out failure. Similarly, for net cross-section failure mode (N) and bolt shear failure mode (BO), only the corresponding yielding and failure occur. Split failure mode (SP) is the state when both plate shear and net cross-section yielding occurs, followed by tear-out failure. The modes BO(SH) and BO(N) induce plate shear yielding and net cross-section yielding, respectively in addition to bolt shear failure. Figs. 4 and 5 show that the zinc-rich paint coating peeled, and the extent of this peeling depended on the plastic area of the connected plate.

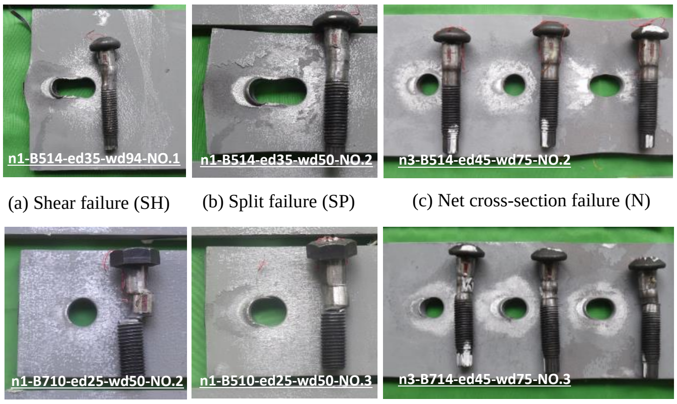

(a) Shear failure (SH) (b) Split failure (SP) (c) Net cross-section failure (N)

(d) Bolt shear failure (BO) (e) Bolt shear failure and plate shear yielding ((BO(SH)) (f) Bolt shear failure and net cross-section yielding ((BO(N))

Fig. 4 Failure modes confirmed in the test

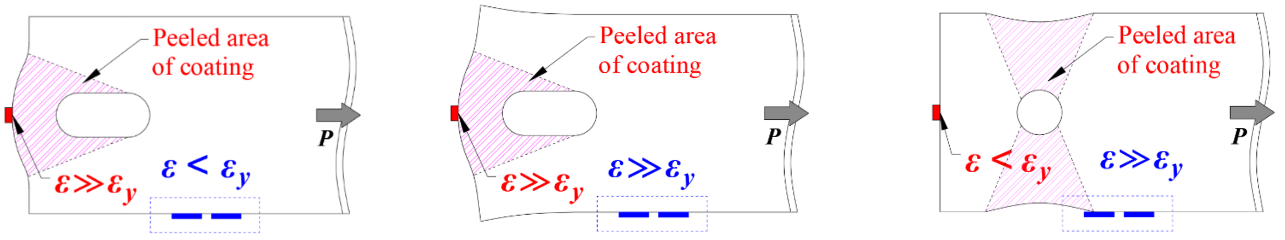

(a) Shear failure (SH)

(b) Split failure (SP)

(c) Net cross-section failure (N)

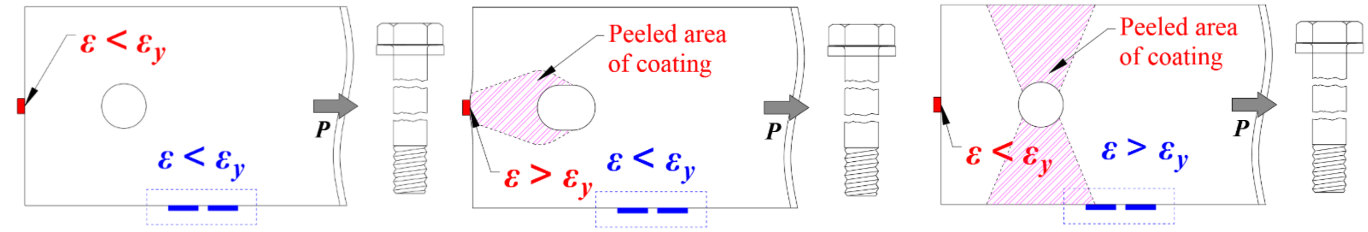

(d) Bolt shear failure (BO)

(e) Bolt shear failure and plate shear yielding ((BO(SH))

(f) Bolt shear failure and net cross-section yielding ((BO(N))

Fig. 5 Definition of failure modes

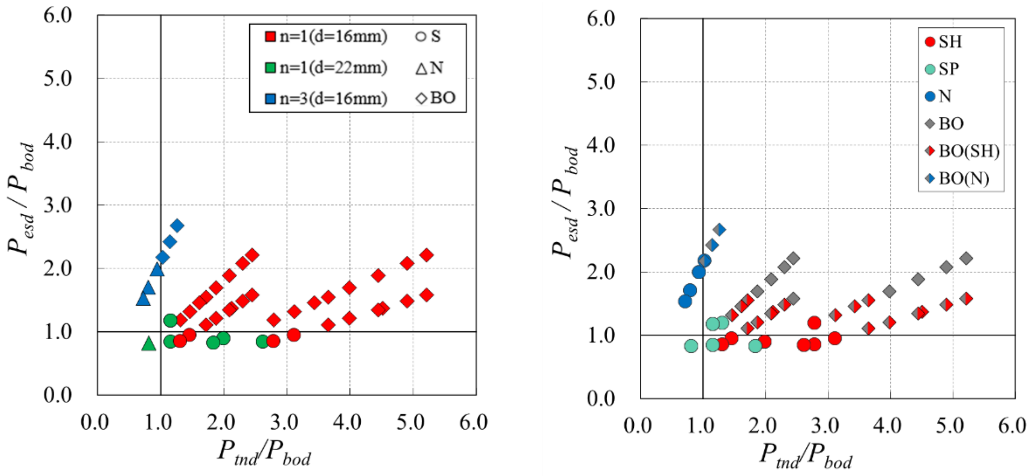

(a) Expected failure modes

(b) Actual failure modes

Fig. 6 Classification of the failure modes by P_{tnd}/P_{bod} and P_{esd}/P_{bod}

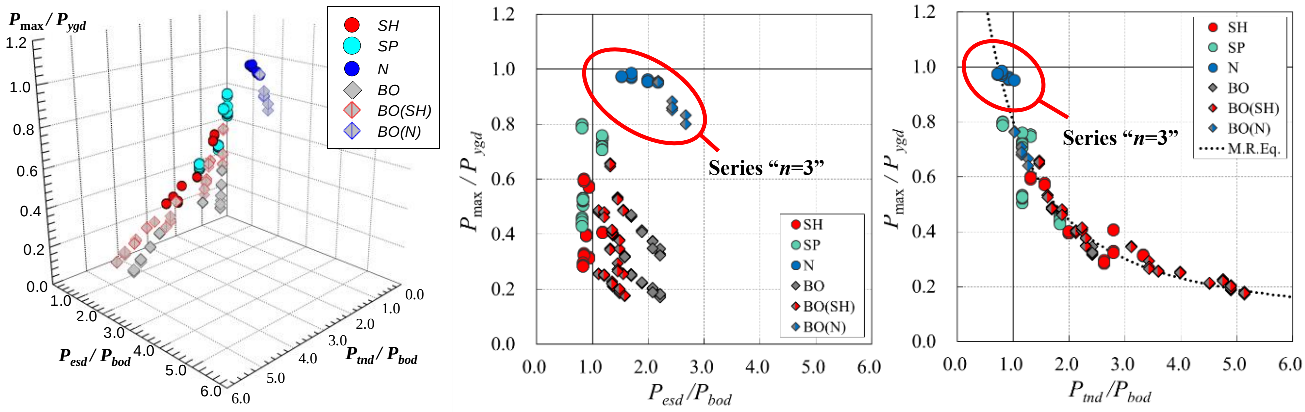

(a) Bird's view

(b) P_{max}/P_{ygd} vs P_{esd}/P_{bod} plane

(c) P_{max}/P_{ygd} vs P_{tnd}/P_{bod} plane

Fig. 7 Relationship among P_{max}/P_{ygd}, P_{esd}/P_{bod}, and P_{tnd}/P_{bod}

3.2. Comparison of the expected and actual failure modes

The expected and actual failure modes classified by P_{tnd} / P_{bod} and P_{esd} / P_{bod} are shown in Fig.6. Mode SH, N, and BO can be almost classified using the aforementioned conventional equations developed for mild steel joints. Coupled modes such as SP, BO(SH), and BO (N) occurred as P_{tnd}/P_{bod} and P_{esd}/P_{bod} decreased. Especially in the case of SP, P_{esd}/P_{bod} and P_{tnd}/P_{bod} were both approximately 1.0.

3.3. Relationship among ultimate strength, structural configurations, and failure modes

To use the plastic deformation capacity of the connected member, the maximum load of the joint P_{max} must be larger than the gross cross-section yield resistance P_{ygd}. Fig.7 shows the relationship among the ratios P_{max}/P_{ygd}, P_{esd}/P_{bod}, and P_{tnd}/P_{bod}. The maximum load of the joint gradually became larger than the gross cross-section yield resistance as these ratios decreased or the number of bolts increased. In cases of series "$n = 1$", mode SP shows the highest ultimate resistance. However, there is no case in this study whose P_{max}/P_{ygd} is higher than 1.0. Focused on the distribution tendency of the plotted data, P_{max}/P_{ygd} was inversely proportional to P_{esd}/P_{bod}. Therefore, multiple regression analysis was performed to obtain the approximate curve shown in Fig.7(c). The considered approximate equation is expressed as eq. (11). The results of multiple regression analysis are shown in Table 6. The adjusted coefficient of deter-mination R^2_{adj} of this equation is 0.908, indicating a strong correlation.

Table 6

Statistical results of multiple regression analysis

R	R^2	Adjusted R^2_{adj}	Standard Error of the Estimate SE_e	Partial Regression Coefficients	Estimate	95% Confidence Level Lower Limits	95% Confidence Level Upper Limits	Standard Error SE	t-Statistic	P-Statistic
0.953	0.909	0.908	0.07	a	0.051	0.019	0.082	0.016	3.141	0.002
				b	10.006	4.535	15.477	2.770	3.612	0.0004
				c	2.632	1.462	3.802	0.592	4.443	<0.0001

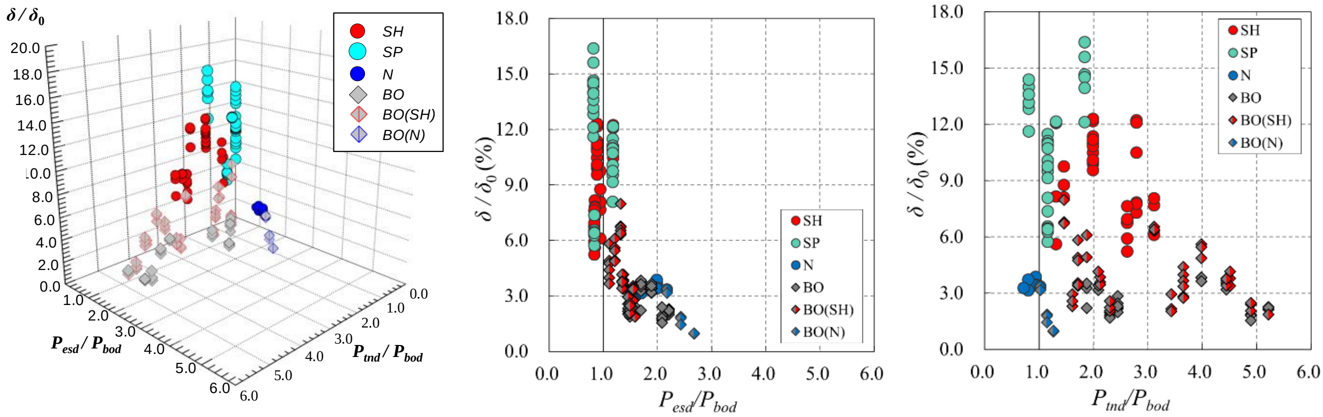

(a) Bird's view (b) δ/δ_0 vs P_{esd}/P_{bod} plane (c) δ/δ_0 vs P_{tnd}/P_{bod} plane

Fig. 8 Relationship among δ/δ_0, P_{esd}/P_{bod}, P_{tnd}/P_{bod}

$$\frac{P_{\max}}{P_{ygd}} = a\exp\left(\frac{b}{P_{tnd}/P_{bod}+c}\right) \tag{11}$$

Here, a, b, and c are partial regression coefficients.

3.4. Relationship among ductility, structural configurations, and failure modes

Similarly, the relationship among elongation δ/δ_0, P_{esd}/P_{bod}, and P_{tnd}/P_{bod} is shown in Fig.8. The elongation δ/δ_0 is the ratio of the entire displacement of the joint at maximum load δ to the original gauge length δ_0. As P_{esd}/P_{bod} and P_{tnd}/P_{bod} decreased, the elongation δ/δ_0 increased. In cases of series "n = 1", mode SP shows the highest ductility and the highest ultimate resistance.

4. Conclusions

In this study, tensile tests of high-strength frictional bolted joints with HSS developed in Japan were conducted to compare the failure modes of HSS and conventional mild steel joints and to investigate the relationship among ultimate strength, ductility, and failure mode. The following conclusions can be drawn.

(1) Failure modes of HSS joints can be assumed to be the same as those of mild steel joints and can be almost classified using the designed ultimate resistance ratios of the plate and bolt such as P_{esd}/P_{bod} and P_{tnd}/P_{bod}, which have already been developed for mild steel joints and widely used in some design codes. For instance, when a coupled failure mode occurred, the corresponding resistance ratio related to the mode was approximately 1.0. Especially, in the case of split failure mode of the connected plate, these ratios were both approximately 1.0.

(2) The maximum load of the joint gradually became larger than the gross cross-section yield resistance these ratios P_{esd}/P_{bod} and P_{tnd}/P_{bod} decreased or the number of bolts increased. There is no case in this paper whose $P_{\max}/P_{ygd}$ is greater than 1.0. As $P_{\max}/P_{ygd}$ was inversely proportional to P_{esd}/P_{bod}, the approximate equation that can precisely estimate $P_{\max}/P_{ygd}$ was obtained, considering only P_{tnd}/P_{bod}. The adjusted coefficient of determination R^2_{adj} of the proposed equation is 0.908.

(3) The entire elongation of the joint δ/δ_0 increased as P_{esd}/P_{bod} and P_{tnd}/P_{bod} decreased and the number of bolts increased along with the maximum load.

(4) In cases of series "n = 1", the split failure mode (SP) exhibits the highest ultimate resistance and ductility. Considering (1)–(3), the ratios P_{esd}/P_{bod} and P_{tnd}/P_{bod} should be less than 1.0 to induce mode SP to enable the breakage of the HSS joint after the member is plastic-deformed sufficiently.

For joints consisting of multiple bolts in the longitudinal and transverse direction, other failure modes such as block shear failure occur easily, which could not be confirmed in this test. Therefore, future work will be devoted to conducting tensile tests on mutiple-bolted joints. Numerical analysis will be also conducted to investigate the influence of various structural configurations and bolt arrangement on the relationship among $P_{\max}/P_{ygd}$, P_{esd}/P_{bod}, and P_{tnd}/P_{bod}.

Acknowledgment

This work was supported by The Japan Iron and Steel Federation. The authors would like to express their gratitude.

References

[1] Eurocode 3: Design of Steel Structures - Part 1-1: General Rules and Rules for Buildings, EN1993-1-1, European Committee for Standardization (CEN), 2005.
[2] Eurocode 3: Design of Steel Structures - Part 1-8: Design of Joints, EN1993-1-8, European Committee for Standardization (CEN), 2005.
[3] Eurocode 3: Design of Steel Structures - Part 1-12: Additional Rules for the Extension of EN 1993 up to Steel Grades S700, EN1993-1-12, European Committee for Standardization (CEN), 2007.
[4] Može P., Beg D. and Lopatič J., "Net cross-section design resistance and local ductility of elements made of high strength steel", Journal of Constructional Steel Research, 63(11), 1431-1441, 2007.
[5] Može P. and Beg D., "High strength steel tension splices with one or two bolts", Journal of Constructional Steel Research, 66(8-9), 1000-1010, 2010.
[6] Wang Y.B., Lyu Y.F., Li G.Q. and Liew J.Y.R., "Behavior of single bolt bearing on high strength steel plate", Journal of Constructional Steel Research, 137, 19-30, 2017.
[7] Homma, K., Tanaka, M., Matsuoka, K., Kasuya, T. and Kawasaki, H., "Development of application technologies for bridge high-performance steel, BHS", Nippon Steel Technical Report, 97, 51-57, 2008.
[8] Miki, C., Ichikawa, A., Kusunoki, T. and Kawabata, F., "Proposal of new high-performance steels for bridges (BHS500, BHS700)", Journal of Japan Society of Civil Engineers, ser. 1, 738(64), 1-10, 2003. (in Japanese)
[9] JIS G 3140: Higher yield strength steel plates for bridges, Japanese Industrial standards, 2011. (in Japanese)
[10] Duc, D.V., Okui, Y., Hagiwara, K. and Nagai, M., "Probabilistic distributions of plate buckling strength for normal and bridge high-performance steels", International Journal of Steel Structures, 13(3), 557-567, 2013.
[11] Rahman, M., Okui, Y., Shoji, T. and Komuro, M., "Probabilistic ultimate buckling strength of stiffened plates, considering thick and high-performance steel", Journal of Constructional Steel Research, 138, 184-195, 2017.
[12] Execution of Steel Structures and Aluminum Structures -Part 2: Technical Requirements for Steel Structures, EN1090-2, European Committee for Standardization (CEN), 2008.
[13] Može P. and Beg D., "A complete study of bearing stress in single bolt connections", Journal of Constructional Steel Research, 95, 126-140, 2014.
[14] Može P., "Bearing strength at bolt holes in connections with large end distance and bolt pitch", Journal of Constructional Steel Research, 147, 132-144, 2018.
[15] Toda Y., Yamaguchi T., Mineyama Y., and Naoe K., "Experimental study of bearing strength of frictional bolted connection based on bolt hole deformation", Journal of Japan Society of Civil Engineers, ser. A1, 70(3), 333-345, 2014. (in Japanese)

Advanced Steel Construction – Vol. 19 No. 1 (2023) 23–30
DOI:10.18057/IJASC.2023.19.1.4
(**Special Issue:** *10th International Conference on Advances in Steel Structures, ICASS'2020, Chengdu, China*)

A PRELIMINARY STUDY OF DEPOSITION RATE, MATERIAL PROPERTY AND STABILITY OF WAAM STAINLESS STEEL PLATES

Siân I. Evans and Jie Wang *

Department of Architecture and Civil Engineering, University of Bath, Bath, BA2 7AY United Kingdowm
** (Corresponding author: E-mail: j.wang@bath.ac.uk)*

ABSTRACT

Wire arc additive manufacturing (WAAM) has significant potential to produce freeform, but structurally efficient geometries out of stainless steel, for use in the construction industry, however, there is currently no standardisation of the manufacturing parameters used to produce WAAM structures. This paper discusses an experimental programme carried out on WAAM 316L stainless steel plated structures to assess the effects of the deposition rate, which is directly associated with productivity. This programme comprises tensile tests on coupons extracted along different printing directions, geometric imperfection measurement (including surface roughness, waviness and overall out-of-straightness), and stub column tests designed to determine the local stability of unstiffened plates manufactured with different deposition rates. The applicability of current Eurocode design rules for stainless steel structures, including the ductility requirements and effective width equations, have been assessed based on the obtained experimental data.

ARTICLE HISTORY

Received: 20 July 2022
Revised: 22 August 2022
Accepted: 10 January 2023

KEYWORDS

Wire arc additive manufacturing (WAAM);
Advanced steel construction;
3D printing;
Local buckling;
Material proterties;
Unstiffened plates

1. Introduction

The construction industry accounts for 30% of the world's greenhouse gas emissions, 30% of raw material use worldwide, and 36% of global energy usage [1] and so it is under a lot of pressure to become more sustainable. Improving material utilization through use of additive manufacturing (AM) may help to achieve this. Large metal structures are required in the construction industry and wire arc additive manufacturing (WAAM, a form of direct energy deposition) has the capability to produce these [2] at a viable rate of production due to its rapid deposition rate [1]. Unfortunately, this rapid deposition rate may compromise the surface quality and dimensional accuracy of the part [3] and introduce further potential defects including high residual stress, distortion, porosity and anisotropic material properties [4].

Numerous variables can be adjusted to alter the properties of the build, including the deposition rate, the heat input, the interpass temperature, and the direction of the build. It is not yet fully understood how these variables affect the structural response of WAAM builds. The only experiments [5]–[7] currently available that have investigated the overall structural stability performance of WAAM structures have been carried out on specimens produced with invariant and manufacturer-determined parameters.

Previous material tests on WAAM builds have given inconsistent results, with some authors finding that the Young's modulus (E) of machined samples was higher for those extracted at 45° to the substrate, than for those extracted at 0° or 90° [6], [8], whilst others have found no significant differences in E across samples extracted from different angles [9]. Previous literature also indicates that E is generally 20% less for as-built samples than machined samples due to their undulating geometry [10]. The ultimate tensile strength (σ_u) has been found to be highest at 45° to the substrate because this is where there is the highest density of cell boundaries along the main slip direction [9], and it has been found to be lowest at 90° to the substrate because here the part is loaded across its layers [6].

This paper aims to detail the results from a series of experiments undertaken to assess the effects of the deposition rate and the build direction on key material properties, geometric accuracy and structural stability. The experiments comprise tensile coupon tests, stub column tests and geometric imperfection measurements on 316L stainless steel parts made by WAAM. 316L stainless steel was chosen because it has high strength, high ductility, relatively low cost, and excellent corrosion resistance [4]. The applicability of current Eurocode design rules for stainless steel structures, including the ductility requirements and effective width equation have been assessed based on the obtained test data.

2. Sample fabrication

2.1. WAAM rig and selecting printing parameters

All samples for these experiments have been manufactured on a WAAM rig comprised of an ESAB Aristo 4004i pulse system welding power supply (in MIG set up), a three-axis cartesian motion system (comprised of three servo-drives), an extractor, an enclosure, an Omron controller, and a computer to program the rig on (Fig. 1). The welding torch is located on the Z-axis and is controlled using motion instructions sent using Trajexia software.

The builds employed a wire diameter of 0.8 mm to ensure a thin weld bead was produced. The wire feed speed (WFS) also affects the thickness of a build so a suitable range of 8-10 m/min was chosen to again ensure that slender parts could be manufactured. These combinations of wire diameter and WFS led to a high deposition rate of 2.42 kg/hr and a low deposition rate of 1.93 kg/hr. The specimens produced using these two deposition rates were denoted with 'H' (high deposition) and 'L' (low deposition), respectively.

The control manufacturing parameters used were a heat input of 0.415 kJ/mm, an interpass temperature of 150°C, the welding technology (MIG), the shield gas flow rate and composition, the contact tip distance (7 mm), the feedstock (0.8 mm diameter 316L stainless steel wire), the substrate design and fixture, and the motion system. The voltages used were 29.2 V for the H-specimens and 29.0 V L-specimens because the voltage varies slightly with WFS. A heat input of 0.415 kJ/mm was chosen as it gave stable bead geometry. In order to achieve this heat input, the travel speed was 10.313 mm/s and 12.917 mm/s for the L-specimens and H-specimens, respectively.

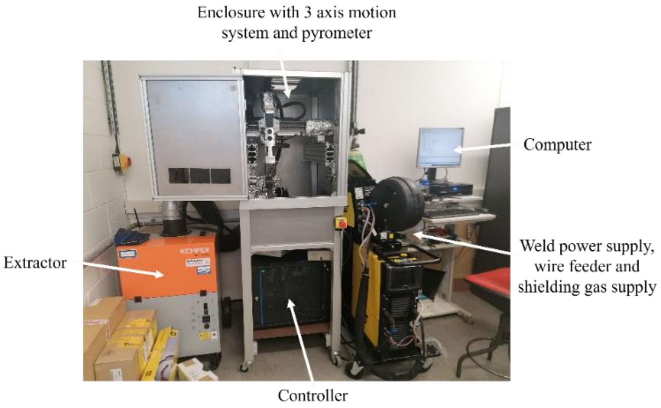

Fig. 1 Labelled photograph of the rig

2.2. Fabrication and preparation of tensile coupons

The coupons were extracted from two plates (each 150 mm wide by 100 mm tall, with a nominal thickness of 3 mm) produced using the two different deposition rates (2.42 kg/hr and 1.93 kg/hr), which were denoted as PH and PL (Plate with High (or Low) deposition rate), respectively. The plates were made in layers on 50×200×6 mm 316L stainless steel substrates. Each layer was deposited, before the height of the welding torch was updated manually on the welding program, with the increase in height being measured using a Vernier calliper. This process was repeated until the plates were 100 mm tall.

Once PH and PL were produced, they were sawn from the substrates (reducing the height of each plate to approximately 80 mm), and six coupons were cut from each plate by water jetting cutting. The dimensions of the coupons are based on the sub-size rectangular specimens specified in the ASTM E8/E8M-13 [11] and were scaled down by a ratio of 0.75:1 to ensure the coupons would fit on the plate. This scaling allowed the gauge length-to-width ratio to remain at 4, required by this standard. The coupons were extracted at different angles to the build direction, as shown in Fig.2b, with the spacing between coupons being flexible. Unfortunately, only one coupon could be extracted from each plate at 0° to the substrate due to constraints on the size of the plates.

Each tensile coupon is named using the following convention: TH or TL (depending on if the coupon is from PH or PL) – angle to the substrate – coupon number as indicated in Fig.2b. After extraction, the coupons were machined to a nominal thickness of 2 mm (or 1.6 mm where the surface waviness required this) to ensure a uniform thickness across their lengths. TL-90-3 had a surface waviness too great for it to be machined flat, so it was not tested.

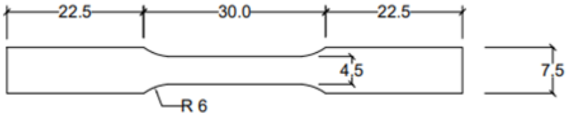

(a) Coupon dimensions

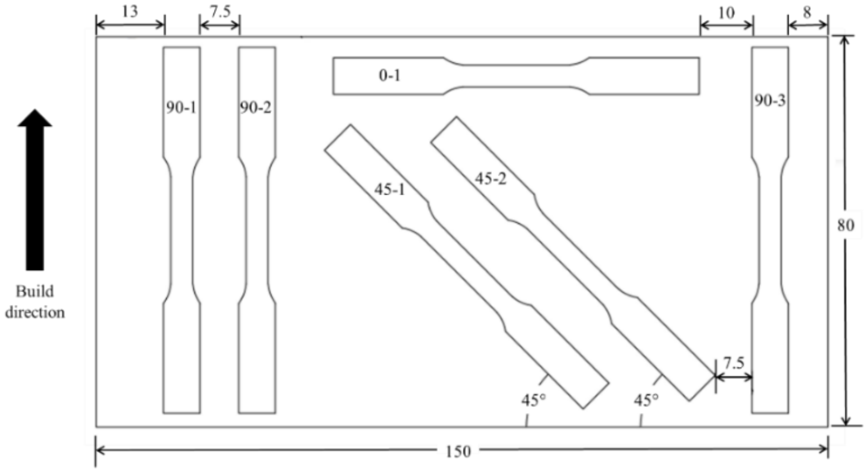

(b) Coupon locations on plate (mm)

Fig. 2 Tensile coupon dimensions and locations

2.3. Fabrication and preparation of EAS stub columns

Four equal angle section (EAS) stub columns were manufactured, with two using the higher deposition rate (labelled as EH1 and EH2), and two using the lower deposition rate (labelled as EL1 and EL2). The substrates used were 75×100×6 mm and the EAS had nominal dimensions Width×Width×Height of 50×50×100 mm. The fabrication of these EAS stub columns followed the same process as the corresponding PL or PH specimens, with the samples being built such that they are compressed in the 90° direction during testing.

Once built, the samples were sawn off the substrates and large welding drops caused by balling were roughly removed from the surface, preventing their noise on the measured geometries while ensuring that the waviness and roughness remained (Fig. 3). Next, the ends were hand filed to be parallel with each other and perpendicular to the longitudinal direction. They were then sanded with wet and dry paper, before being lapped with lapping paste to ensure that the load would be distributed across the entire cross-section of each column from the very beginning of the compression tests.

Fig. 3 The stub column samples after being removed from the substrates and with balling roughly removed (from left to right, samples EL1, EL2, EH1 and EH2)

3. Tensile tests and results

The coupons were tested at room temperature using an Instron 3369 50 kN testing frame which measured the load, and an 8 mm clip gauge extensometer to measure the strain. Displacement control (calculated from the estimated strain rates over the parallel length required in EN ISO 6892-1 [12] ($\leq$0.00007 s^{-1} in the elastic range and $\leq$0.00024 s^{-1} in the plastic range)) was used. There was no clearly defined yield point for any of the tests, so the strain rate was changed when it was clear that the stress-strain graph had started to curve. This occurred at displacements between 0.75 mm and 1.5 mm depending on sample.

Despite all surface undulations being removed before testing, the coupons exhibited surface deformations which corresponded to their building directions (as shown in Fig. 4). This has previously been found by other authors as well [8].

Fig. 4 The sample TH-45-2 after testing. It has been placed back together and there are surface deformations visible at 45° to the length of the coupon, corresponding to the fact that the coupon was extracted from the WAAM build at 45°.

The obtained stress-strain curves are shown in Fig. 5 and the key material properties including the Young's modulus (E), the 0.2% proof stress ($\sigma_{0.2}$), the ultimate tensile strength (σ_u), the strain at ultimate tensile strength (ε_u), the percentage elongation after fracture (ε_f) measured according to [12], and strain hardening parameters n and m (from the modified O-R model [13]) are given in Table 1. These are compared to benchmark values for conventionally produced 316L stainless steel in Fig. 6 and an assessment of the ductility of each sample is shown in Fig. 7.

Samples extracted from the same plate and at the same angle were expected to have similar E, however, E for sample TH-45-2 is 22.1% less than that of sample TH-45-1. Similarly, coupon TH-90-3 has a much lower E than samples TH-90-1 and TH-90-2. This variation could indicate that E varies across the build, however, there is not yet enough data to conclude this. The greatest E is found for coupons extracted at 45° for both plates, whilst the E at 0° and 90° are on average 40.3% and 46.4% less than the average benchmark value respectively [14]. Both of these points reinforce findings by in [6], where E for machined samples taken at 0° or 90° were lower than conventionally produced material by about 30-55%. All samples have E below the benchmark values, indicating that WAAM samples are less stiff than traditionally produced parts.

WAAM parts are expected to have a lower failure strain when compared to wrought and annealed counterparts because internal defects and surface roughness act as stress locations and the fine microstructure makes the part less ductile as dislocation motion is limited [15]. Only three coupons had ε_f values greater than the lower benchmark value [16], which shows an agreement with this hypothesis.

All samples have $\sigma_{0.2}$ greater than the benchmark average and all coupons except TH-0-1 have σ_u values between the upper and lower benchmark values [16], indicating that WAAM is capable of producing parts of equal strength to those produced by conventional methods, but not necessarily demonstrating the increase in strength expected from the fine grains [15]. As only one coupon was extracted at 0° for each plate, this result is likely accidental. The greatest σ_u is seen at 90° for both plates, however, it is expected to be greatest at 45° [9] and lowest at 90° [6].

The three ductility requirements stated in EN 1993-1-1 [17] are all met by all coupons tested (Fig. 7), suggesting that WAAM is capable of producing parts which have acceptable ductility. It should be noted that four samples (TH-90-1, TH-90-2, TH-45-1 and TH-45-2) failed outside of the clip gauge so the strains measured from the onset of necking may be inaccurate. This could be why the former three samples all appeared to report low strains at failure.

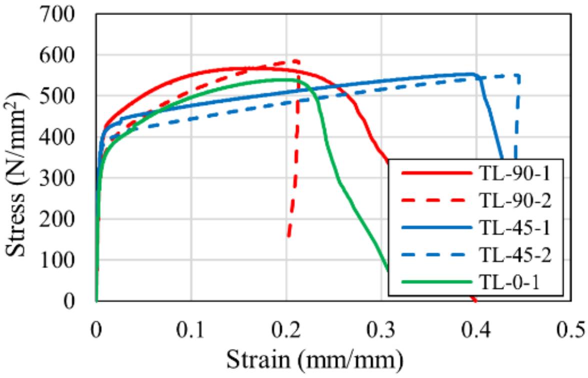

(a) Lower deposition rate

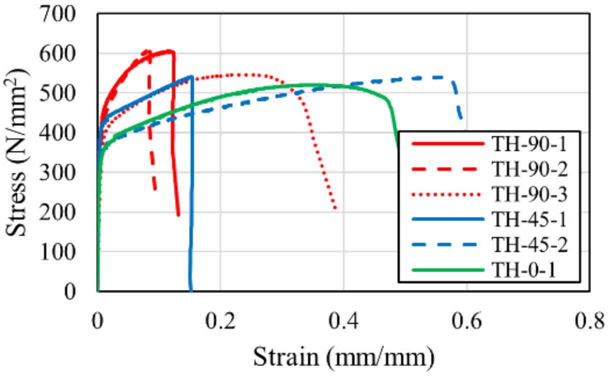

(b) Higher deposition rate

Fig. 5 The stress-strain relationships of tensile coupons

Table 1
Results of tensile coupon tests

Sample	E (N/mm^2)	$\sigma_{0.2}$ (N/mm^2)	σ_u (N/mm^2)	ε_u (mm/mm)	ε_f (mm/mm)	n	m
TL-90-1	107436	370	567	0.165	0.318	6.05	3.28
TL-90-2	103559	313	586	0.209	0.271	7.64	2.87
TL-45-1	155854	361	553	0.393	0.391	4.43	3.27
TL-45-2	182207	338	550	0.441	0.438	2.55	3.15
TL-0-1	112008	308	539	0.197	0.340	6.73	3.00
TH-90-1	122627	395	605	0.118	0.267	6.95	3.29
TH-90-2	116825	360	610	0.084	0.203	5.67	3.07
TH-90-3	78808	324	546	0.240	0.353	5.48	3.08
TH-45-1	180844	381	541	0.152	0.269	5.72	3.47
TH-45-2	140918	325	539	0.558	0.567	4.06	3.11
TH-0-1	123797	311	520	0.353	0.473	6.95	3.10

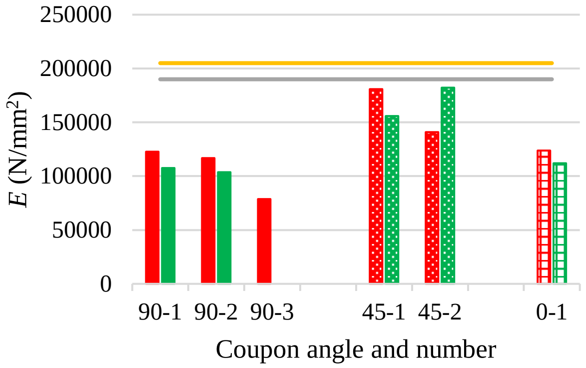

(a) Young's modulus

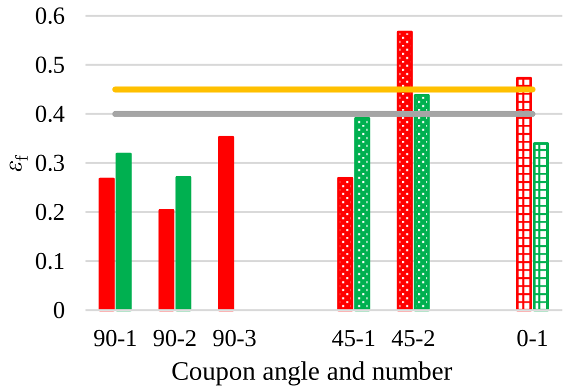

(b) percentage elongation after fracture

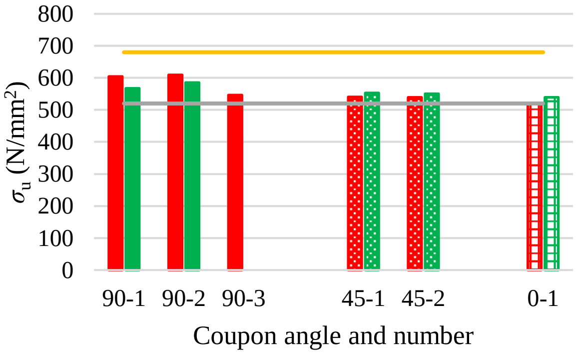

(c) Ultimate tensile strength

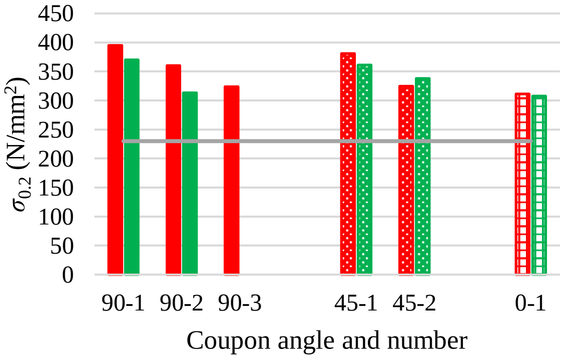

(d) 0.2% proof strength

🟥 High deposition rate 🟩 Low deposition rate

— Benchmark low — Benchmark high

Fig. 6 Comparison of material properties of each tensile coupon, categorised by deposition rate and angle of extraction

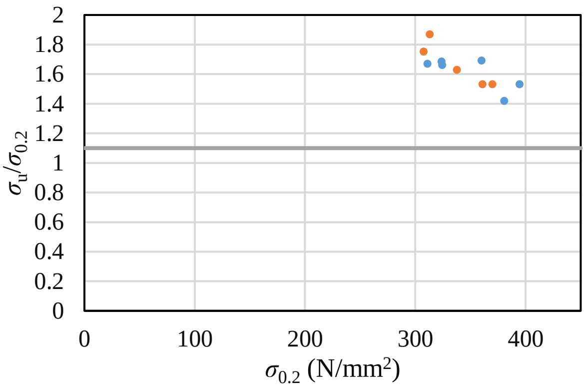

(a) Ultimate to yield strengh ratio

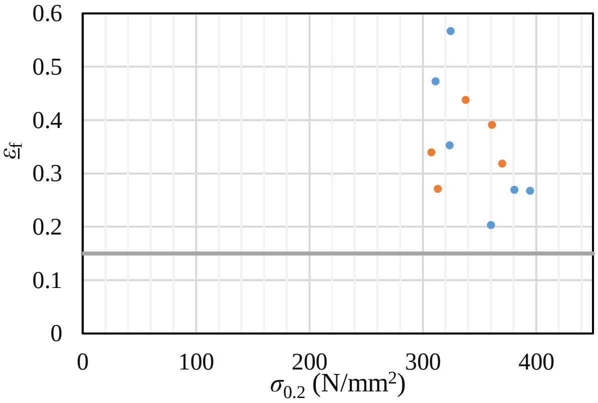

(b) Fracture strain

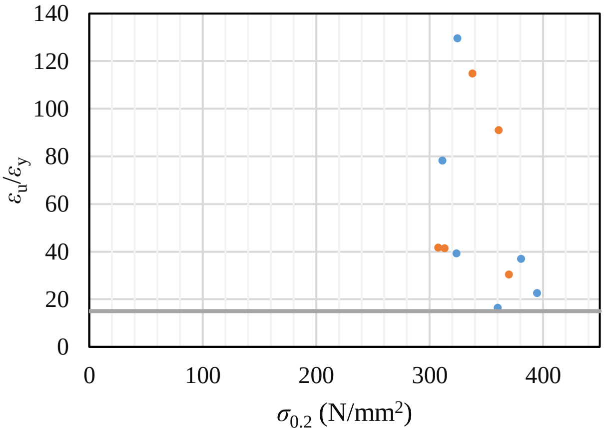

(c) Ultimate to yield strain ratio

● High deposition rate ● Low deposition rate

— Ductility Requirement

Fig. 7 The ductility requirements [17] and results from the tensile coupon tests

4. Geometric imperfection measurement

All four stub columns were 3D scanned using a Hexagon CMS 108AP laser line scanner (30 μm accuracy), attached to a Hexagon ROMER arm, and the data was outputted to SpatialAnalyzer as point clouds. These point clouds were then analysed using MATLAB. The use of Archimedes' Principle was not deemed necessary to obtain the volume of each sample as this can be found using the results of the 3D scans, and other researchers have found the values calculated from each of these methods to be essentially identical [10].

It was observed that for all the samples, the cross-section varies across the height and width of the build, as shown in Fig. 8. Based on the obtained geometric data clouds, the average flange thickness (t_{av}), minimum thickness (t_{min}), average of minimum thicknesses between layers ($t_{av,min}$), average cross-sectional area (A_{av}), part height (L), maximum deviation of the mid-thickness from the average mid-thickness (γ), average layer height (h_{av}), slenderness ($\bar{\lambda}_p$), surface waviness (ω) (Eq. (1), where $t_{av,max}$ is the average of maximum thickness of each layer), and surface roughness S_a (Eq. (2) where f_n is the height of a peak or depth of a valley, measured at N locations), were calculated and are reported in

Table. The values for surface waviness and surface roughness were similar for all columns, so the deposition rate had no clear effect here. It was expected the EH1 and EH2 would be thicker as they were made employing a faster WFS [18], however, the measured data revealed that EL1 and EL2 have a larger minimum and average thickness than EH1 and EH2. The location of the minimum thickness varies for each column and for each flange of each column, as does the location of maximum deviation from the central line.

$$\omega = \frac{t_{av,max} - t_{av,min}}{2} \tag{1}$$

$$S_a = \frac{1}{N} \sum_{n=1}^{N} |f_n| \tag{2}$$

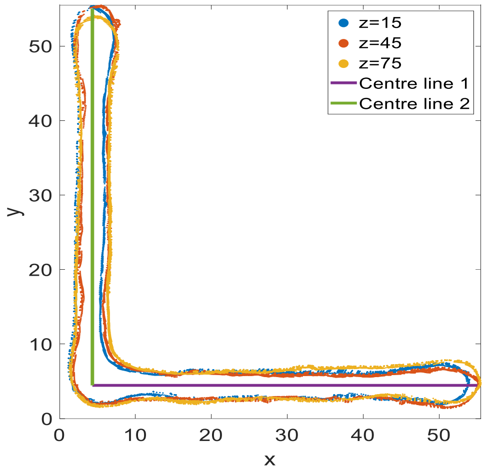

(a) Across different heights

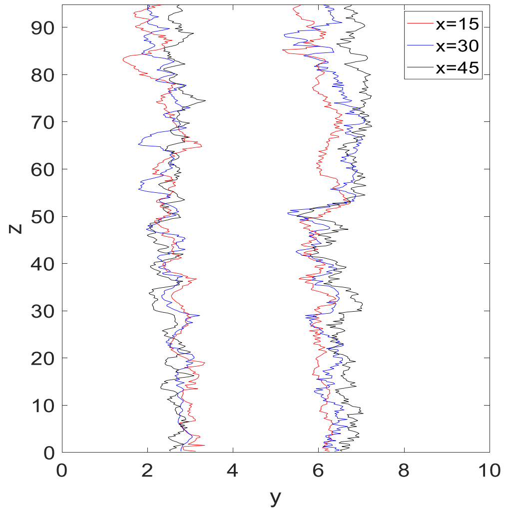

(b) Across different widths

Fig. 8 Variation in the cross-section of sample EL2 across a) different heights, and b) different widths. All units are in mm

Table 2

Measurements and material properties of the stub columns

Sample	t_{av} (mm)	t_{min} (mm)	$t_{av,min}$ (mm)	A_{av} (mm^2)	L (mm)	γ (mm)	h_{av} (mm)	ω (mm)	S_a (mm)	N_u (kN)	k_{theo} (kN/mm)	k (kN/mm)	δ_u (mm)
EL1	4.15	2.29	3.68	418	94.7	1.83	2.38	0.28	0.57	98.9	466	106	4.52
EL2	3.63	2.00	3.38	414	97.6	1.88	2.57	0.27	0.34	92.1	448	60	4.50
EH1	3.40	1.40	2.93	389	95.8	2.39	2.46	0.37	0.50	80.8	431	93	4.45
EH2	3.61	1.58	2.99	383	99.1	1.92	2.61	0.30	0.40	96.7	410	114	4.04

5. Stub column tests

5.1. Testing procedure

The tests on EAS stub columns were carried out to evaluate the stability performance of external plated elements (with only one longitudinal edge supported) manufactured by WAAM. The stub column tests were conducted on a 2000 kN loading machine, with a 9 mm thick end plate placed on top of each sample to ensure equal distribution of the applied compressive stresses. Four vertical LVDTs were set up between the upper and lower plates, along with two horizontal LVDTs on the inside faces of the EASs at approximately mid-height and mid-width (Fig. 9) to monitor the lateral displacements of the flanges. In previous work by other authors, the horizontal LVDTs have been positioned at the geometric centre of the EASs [19], however, the geometry of these EASs is imperfect so here they are placed at the centre of each flange instead.

The load was applied to each sample using displacement control (0.15 mm/min), with the load being read directly from the loading machine and the displacements being read from the LVDTs (at 0.5 Hz). Testing was concluded when a clear decline in axial load had occurred, and excessive end shortening had been observed, in line with the experimental procedures chosen by other authors [20].

5.2. Test results

The failure modes of the tested EAS stub columns are displayed in Fig. 10. It can be seen that the EL2, EH1 and EH2 stub columns all displayed a single wave of flange buckling occurring at the same height on the two flanges; however, this height was different for each column and did not necessarily occur at the mid-height. The EL1 stub column displayed two buckling waves along the length, which is very unlikely to happen in traditional rolled EAS members with "near-perfectly" flat geometries [19]. This may be caused by the manufactured imperfection, where a clear thickness offset was presented towards the upper half of the EL1 stub column, as can be seen in Fig. 3.

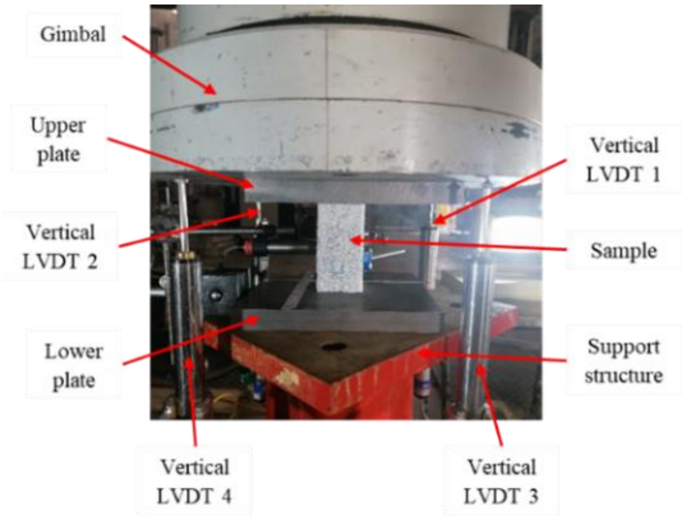

(a) Photograph of the stub column test setup

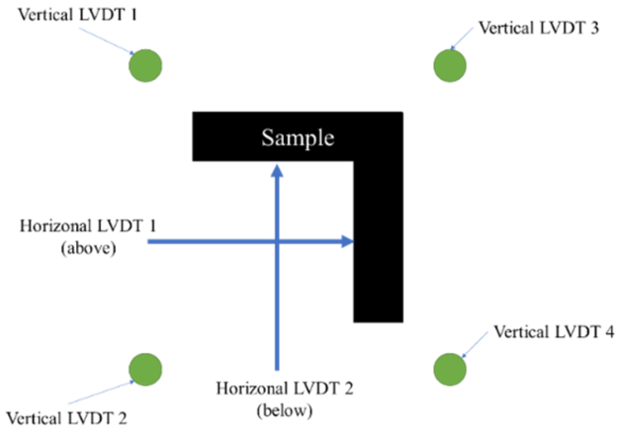

(b) Schematic plan view of the test setup

Fig. 9 a) Photograph of the setup of the LVDTs, plates and supporting structure, and b) schematic of the LVDT setup

The ultimate load (N_u), stiffness (k), and the end shortening (δ_u) of each stub column are shown in Table 1. The theoretical stiffness, k_{theo}, calculated based on the averaged cross-sectional area is also included in Table 2 for comparison purposes. For each stub column, the experimental stiffness, k, was between 13-28% of the predicted stiffness and this can be attributed to the undulating geometry of the builds and the consequence that the stiffness may not be uniform across the height of each sample. Moreover, the axial stiffness of EH specimens was expected to be less than that of EL specimens as EH specimens report greater averaged thicknesses and cross-sectional areas Table 2. However, the opposite is observed in this study, as shown in Fig. 11a where axial load vs end shortening curves of the stub columns are plotted. Therefore, predicting the stiffness using the average cross-sectional area may not be an appropriate approach and the deformability, stability and other stiffness related structural behaviour of WAAM plates needs to be carefully assessed. Further investigation may be carried out to explain this observation.

Fig. 11b shows the horizontal displacements measured during the test on EH1, with one flange buckling outward and one inward (as seen in Fig. 10). Similar results were found for the other stub columns, except for EL1 (Fig. 11c). Here, the horizontal displacements at the measured locations show that both flanges moved inwards in the initial loading stage. This may be cause by the higher order (two-buckling wave) mode of failure developed in this specimen and the measurements close to the mid-height location were not necessarily representative.

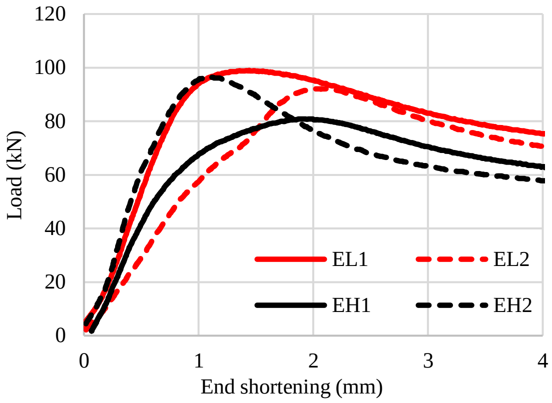

(a) Load vs end-shortening curves

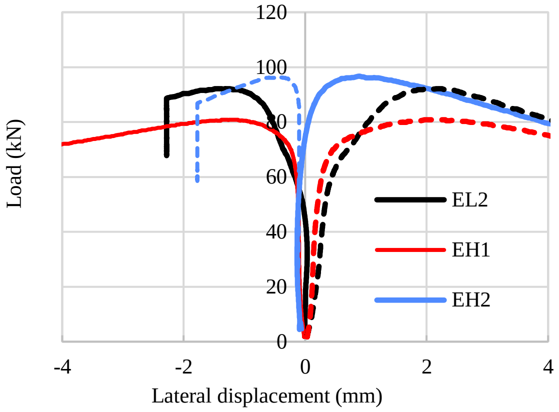

(b) Load vs lateral displacement at mid height of flanges of EL2, EH1 and EH2 stub columns

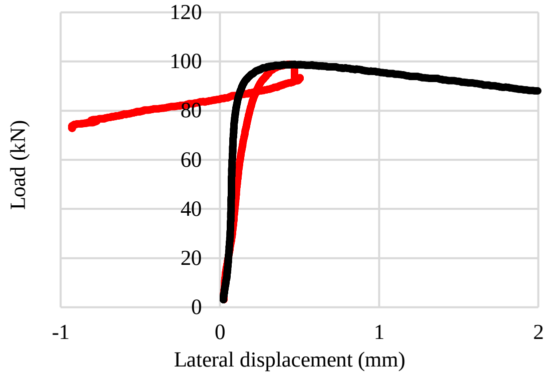

(c) Load vs lateral displacement at mid height of flanges of EL1

Fig. 11 Load displacement curves from stub column tests

Fig. 10 The buckled stub columns after testing (from left to right, samples EL1, EL2, EH1 and EH2)

5.3. Applicability of effective width equation

The buckling resistance of each column is compared with the Eurocode prediction [21] for external plate elements in Fig. 12. In Fig. 12, the vertical axis is the ultimate load N_u normalised by the plastic load $N_y = A\sigma_{0.2}$ (where A is the cross-sectional area calculated using t_{av} or $t_{av,min)}$ of each cross-section, and the horizontal axis is the average plate slenderness $\bar{\lambda}_p$ of the flanges of the EAS stub columns. The equation deriving $\bar{\lambda}_p$ is given in Eq. (3), where c is the entire flange width, t is t_{av} or $t_{av,min}$, $\varepsilon = [(235/\sigma_{0.2})(E/210000)]^{0.5}$ (with $\sigma_{0.2}$ and E based on the measured properties from the machined tensile coupons in the 90° direction), and k_σ is the buckling coefficient. $k_\sigma = 1.3$ as obtained according to the aspect ratio and boundary condition of the flange of the EAS stub columns [22]. Based on the $\bar{\lambda}_p$ values, all the samples are classified as Class 4 [17].

$$\bar{\lambda}_p = \frac{c/_{t}}{28.4\varepsilon\sqrt{k_\sigma}} \qquad (3)$$

The comparison in Fig. 12 shows that the tested samples presented significantly lower buckling resistances (calculated using t_{av}) compared to the codified prediction. However, the results calculated using $t_{av,min}$ are much closer to the prediction, suggesting that this may be a more appropriate measurement to use. Selecting the most appropriate dimensions to use in predictions of behaviour is an important issue for WAAM steel structures due to their non-uniform thickness across both the cross-section and the height. Based on the results presented in this study, it is clear that the averaged cross-sectional dimensions are not the best parameters to be used to estimate the structural performance of WAAM builds. More representative geometric parameters are sought, and a standardisation of this step is needed, which would require a large data pool and should be determined in conjunction with any modification of the local buckling equation to produce a reliable prediction of the stability performance of WAAM structures.

Another point to consider is that the properties of the stub column may be different to those of a larger column because heat accumulation may cause the top and bottom to have different microstructures. The geometry may also vary more substantially from the ideal EAS as geometric errors in printing add up, so the applicability of these results to larger columns must be considered carefully.

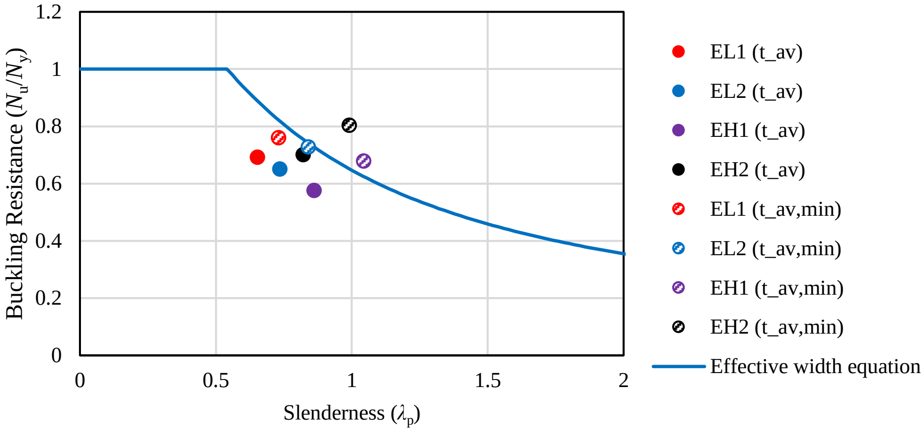

Fig. 12 The buckling resistances of each stub column (ultimate load from stub column tests/yield load from tensile coupon tests), plotted against their slenderness (calculated using t_{av} or $t_{av,min)}$ along with the effective width equation [21]

6. Conclusions

This paper has investigated the effect of the deposition rate and build direction on the material, geometric and stability performance of 316L stainless steel plated structures made by WAAM. The following conclusions have been identified:

1. The Young's moduli of the tensile coupons extracted at 45° to the substrate were found to be the greatest, indicating that this direction of the build is stiffest.
2. Although the failure strain of the WAAM parts was found to be less than those of wrought and annealed parts, all tensile coupons meet the ductility requirements stated in EN 1993-1-1 [17].
3. The deposition rate was found to have no effect on the surface roughness or surface waviness. However, a lower deposition rate was found to be associated with thicker builds.
4. The buckling modes of the EAS stub columns made by WAAM were different from those of traditionally rolled steel angle sections, as can be attributed to the combined effect of their high out-of-straightness and surface waviness.
5. The average thickness and average cross-sectional area may not be the best parameters to characterize the local buckling resistance of WAAM plates under compression. Instead, the average value of the minimum thickness for each layer of the builds was found to present a better characterization of their stability performance, resulting in predictions close to the effective width equation given in EN 1993-1-4 [21]. However, a standardization of this step will require a large experimental data pool.

References

[1] C. Buchanan and L. Gardner, 'Metal 3D printing in construction: A review of methods, research, applications, opportunities and challenges', *Engineering Structures*, no. 180, pp. 332–348, Feb. 2019.

[2] S. W. Williams, F. Martina, A. C. Addison, J. Ding, G. Pardal, and P. Colegrove, 'Wire + Arc Additive Manufacturing', *Materials Science and Technology*, vol. 32, no. 7, pp. 641–647, May 2016, doi: 10.1179/1743284715Y.0000000073.

[3] Q. Wu, Z. Ma, G. Chen, C. Liu, D. Ma, and S. Ma, 'Obtaining fine microstructure and unsupported overhangs by low heat input pulse arc additive manufacturing', *Journal of Manufacturing Processes*, no. 27, pp. 198–206, 2017.

[4] C. R. Cunningham, J. Wang, V. Dhokia, A. Shrokani, and S. T. Newman, 'Characterisation of Austenitic 316LSi Stainless Steel Produced by Wire Arc Additively Manufacturing with Interlayer Cooling', presented at the Solid Freeform Fabrication 2019, Austin, USA, 2019.

[5] V. Laghi, M. Palermo, G. Gasparini, V. Girelli, and T. Trombetti, 'Experimental results for structural design of Wire-and-Arc Additive Manufactured stainless steel members', *Journal of Constructional Steel Research*, vol. 167, 2020, [Online]. Available: https://doi.org/10.1016/j.jcsr.2019.105858

[6] C. Buchanan, W. Wing, and L. Gardner, 'Testing of Wire and Arc Additively Manufactured Stainless Steel Material and Cross-Sections', Hong Kong, China, Dec. 2018.

[7] P. Kyvelou, C. Huang, L. Gardner, and C. Buchanan, 'Structural Testing and Design of Wire Arc Additively Manufactured Square Hollow Sections', *Journal of Structural Engineering*, vol. 147, no. 12, 2021.

[8] P. Kyvelou *et al.*, 'Mechanical and microstructural testing of wire and arc additively manufactured sheet material', *Materials & Design*, no. 192, p. 108675, 2020.

[9] V. Laghi, M. Palermo, L. Tonelli, G. Gasparini, L. Ceschini, and T. Trombetti, 'Tensile properties and microstructural features of 304L austenitic stainless steel produced by wire-and-arc additive manufacturing', *The International Journal of Advanced Manufacturing Technology*, no. 106, pp. 3693–3705, 2020.

[10] L. Gardner, P. Kyvelou, G. Herbert, and C. Buchanan, 'Testing and initial verification of the world's first metal 3D printed bridge', *Journal of Constructional Steel Research*, no. 172, p. 106233, 2020.

[11] ASTM International, 'ASTM E8/E8M-13, Standard Test Methods for Tension Testing of Metallic Materials'. 2013.

[12] BS EN ISO 6892, 'BS EN ISO 6892-1:2019 Metallic materials, tensile testing, method of test at room temperature'. 2020.

[13] P. Hradil, A. Talja, E. Real, E. Mirambell, and B. Rossi, 'Generalized multistage mechanical model for nonlinear metallic materials', *Thin-Walled Structures*, vol. 63, pp. 63–69, Feb. 2013, doi: 10.1016/j.tws.2012.10.006.

[14] 'Properties: Stainless Steel - Grade 316 (UNS S31600)', *AZoM.com*. https://www.azom.com/properties.aspx?ArticleID=863 (accessed Apr. 27, 2021).

[15] D. Bourell *et al.*, 'Materials for additive manufacturing', *CIRP Annals - Manufacturing Technology*, no. 66, pp. 659–681, 2017.

[16] BS EN 10088-2, 'BS EN 10088-2:2014 Stainless Steels Part 2: Technical delivery conditions for sheet/plate and strip of corrosion resisting steels for general purposes'. 2014.

[17] European Committee for Standardization (CEN), 'Eurocode 3: Design on steel structures. Part 1-1: General rules and rules for buildings', Brussels, Belgium, EN 1993-1-1:2005/A1:2014, 2015.

[18] M. Dinovitzer, X. Chen, J. Laliberte, X. Huang, and H. Frei, 'Effect of wire and arc additive manufacturing (WAAM) process parameters on bead geometry and microstructure', *Additive Manufacturing*, vol. 26, pp. 138–146, Mar. 2019.

[19] G. Shi, Z. Liu, H. Y. Ban, Y. Zhang, Y. J. Shi, and Y. Q. Wang, 'Tests and finite element analysis on the local buckling of 420 MPa steel equal angle columns under axial compression', *Steel and Composite Structures*, vol. 12, no. 1, pp. 31–51, 2011.

[20] H. X. Yuan, Y. Q. Wang, Y. J. Shi, and L. Gardner, 'Stub column tests on stainless steel built-up sections', *Thin-Walled Structures*, vol. 83, pp. 103–114, Oct. 2014.

[21] European Committee for Standardization (CEN), 'Eurocode 3: Design of steel structures. Part 1-4: General rules - Supplementary rules for stainless steels', Brussels, Belgium, EN 1993-1-4, 2006.

[22] N. S. Trahair, M. A. Bradford, D. A. Nethercot, and L. Gardner, *The Behaviour and Design of Steel Structures to EC3*, Fourth. 2008.

Advanced Steel Construction – Vol. 19 No. 1 (2023) 31–37
DOI:10.18057/IJASC.2023.19.1.5
(**Special Issue:** *10th International Conference on Advances in Steel Structures, ICASS'2020, Chengdu, China*)

ELASTIC BUCKLING OF OUTSTAND STAINLESS-CLAD BIMETALLIC STEEL PLATES

Yi-Xiao Mei and Hui-Yong Ban *

Department of Civil Engineering, Tsinghua University, Beijing, PR China
** (Corresponding author: E-mail: banhy@tsinghua.edu.cn)*

ABSTRACT

The application of stainless-clad (SC) bimetallic steel in various conditions such as offshore and marine environment requires members designed in different cross-sectional shapes, which consist of both internal and outstand elements. To form a comprehensive understanding of buckling behaviour of the SC bimetallic steel members, the behaviour of outstand compression plates needs to be investigated. In this study, the theoretical elastic buckling stress of outstand SC bimetallic steel plates subjected to uniformly distributed uniaxial compression is derived. Considering the position of neutral surface, the energy method and Ritz formulation are used to solve the buckling stress. Adaptation of the first-order shear deformation plate theory (FSDT) is used to modify the solution, which is further compared with finite element analyses. The influence of different parameters such as cladding configuration, clad ratio, elastic modulus ratio, aspect ratio and width-to-thickness ratio on the elastic buckling behaviour of the SC bimetallic plates is analysed. The simplified design formulae and design requirements are summarized to form a comprehensive design method.

ARTICLE HISTORY

Received:	20 July 2022
Revised:	22 August 2022
Accepted:	10 January 2023

KEYWORDS

Stainless-clad bimetallic steel plate;
Elastic buckling;
Uniaxial compression;
First-order shear deformation plate theory (FSDT);
Outstand plates

1. Introduction

As an advanced high-performance laminated steel, stainless-clad (SC) bimetallic steel has been increasingly utilised in engineering structures in recent years. The SC bimetallic steel consists of two types of metallurgically bonded layers, i.e., the cladding layer made of stainless steel and the substrate layer made of conventional mild (CM) steel, which can provide remarkable corrosion resistance and economic efficiency, respectively. By virtue of these overwhelming advantages, the SC bimetallic steel has already been successfully applied in high-rise buildings and steel bridges and is considered as a new solution for infrastructures against environmental corrosion, such as offshore and marine structures.

The research advances of SC bimetallic steel structures have been previously reviewed by the authors [1]. A series of comprehensive studies on full-life cycle material properties of SC bimetallic steel hitherto have been reported, in which different service conditions including fire [2], post-fire loading [3], marine atmospheric corrosion [4], cyclic loading [5] and impact loading [6] are considered. On the topic of mechanical performance of structural members, limited but increasing attention has been paid to SC bimetallic steel members such as plates [7], columns [8] and connections [9].

Compression is one of the major types of loads applied to steel structures, and for steel structure members under compression, buckling is one of the most essential failure modes of engineering design. For a novel structural material such as SC bimetallic steel, there is very limited research addressing the buckling mechanism. Therefore, a series of basic studies looking into the stability of SC bimetallic steel members, from plates to columns, have been conducted by the authors. Combining theoretical analyses ranging from elastic to inelastic stages [7] as well as experimental investigations of stub and long columns [8], the authors aim at establishing a set of buckling design methods which can provide a solid foundation for the future application of SC bimetallic steel in structures.

A previous paper presented by the authors [7] addresses the elastic buckling of internal SC bimetallic steel plates in hollow section columns or I-section columns, which can be also refereed to simply supported plates. The nominal elastic buckling stress of such plates is derived using two different theories, i.e., the classical plate theory (CPT) and the first-order shear deformation plate theory (FSDT). Validated by finite element models, the FSDT solutions are adopted to carry on parametric studies on the effects of key factors such as cladding configuration, clad ratio, elastic modulus ratio and width-to-thickness ratio on the elastic buckling stress. Furthermore, a simplified design method to calculate elastic buckling stress in an efficient and accurate way has been proposed, along with the design requirements for bonding interface shear strength.

Since the previous studies on SC bimetallic steel structures mainly focus on the hollow section members and simply supported plates in these sections, there is a lack of attention paid to the outstand (three edges simply supported and one edge free of support) plates shown in Fig. 1(a). Although the hollow sections such as square hollow sections (SHS), rectangular hollow sections (RHS) and circular hollow sections (CHS) are the most suitable sections for SC bimetallic steel because it can allow the cladding layer whose corrosion resistance is excellent to be put on the outside, while the substrate layer made of CM steel to be protected inside. However, in practice many structures have to be designed with columns or beams using open sections such as I-sections or C-sections. In such sections, there are not only simply supported boundary conditions, but also plates with three edges simply supported and one edge free of support. Therefore, the need for studying the elastic buckling of outstand plates is of the same importance as that for internal plates.

In the present work, on the basis of the previous study, the elastic buckling behaviour of outstand plates subjected to uniaxial compression is thoroughly investigated. The comparison of internal and outstand plates in a common I-section column is illustrated in Fig. 1(a). With consideration of the position of neutral surface as well as the first-order shear deformation plate theory, the energy method is utilised to derive the closed-form analytical solution of the buckling stress, which is further compared with finite element analyses results. Effects of cladding configuration, clad ratio, elastic modulus ratio, aspect ratio and width-to-thickness ratio on the elastic buckling behaviour are investigated by parametric study. A set of simplified formulae for the calculation of buckling stress is proposed in order to establish a complete design method.

2. Theoretical derivation

2.1. Basic assumptions

The theoretical analysis is based on the following assumptions for simplification and generalization: (1) The materials are homogeneous and linear elastic; (2) The plate is ideally flat without geometric imperfections or residual stresses; (3) Membrane stresses due to the small deflection can be neglected; (4) The load is uniformly distributed on the edge of the plate.

For the reason that the outstand plates may be adopted in structural members with different cross-sections, two cladding configurations are considered in this study: plates with singly-sided cladding metal (denoted by SP) and plates with doubly-sided cladding metal (denoted by DP), as illustrated in Fig. 1(b). The boundary conditions and buckling mode are also included in Fig. 1(b). The clad ratio β is defined as a ratio of the thickness of the cladding layer(s) to the overall thickness of the plate t. Accordingly, the thickness of the cladding layer in SP is βt; the DP are simplified to be symmetrically laminated herein, thus the two cladding layers are both $0.5\beta t$ thick.

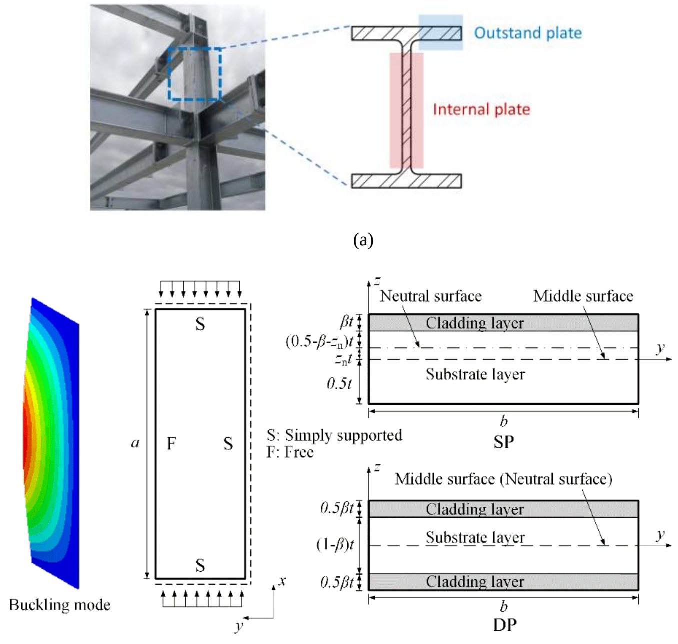

(a)

(b)

Fig. 1 Illustration of (a) internal and outstand plates in an I-section column; (b) boundary conditions and cladding configurations of outstand plates.

As discussed in many studies [10,11], the middle surface may not coincide with the physical neutral surface due to the unsymmetrical configuration of plate. To eliminate the coupling phenomenon between transverse bending and in-plane stretching during deformation as well as to avoid additional moment caused by eccentricity, the uniformly distributed load is considered to be applied within the neutral surface. In the case of SP, the relative position of neutral surface from the middle one can be calculated by [7]:

$$z_{\mathrm{n}}=\frac{\beta(1-\beta)(E_{\mathrm{c}}-E_{\mathrm{s}})}{2[\beta E_{\mathrm{c}}+(1-\beta)E_{\mathrm{s}}]}, \tag{1}$$

in which E_s and E_c are the elastic moduli of substrate and cladding materials, respectively.

Eq. (1) shows that the relative position of neutral surface from the middle one z_n depends on clad ratio as well as the elastic moduli of the two component metals. When the elastic modulus of the substrate material is larger than that of the cladding material, which is the case of SC bimetallic steel or other common bimetallic steel such as titanium-clad (TC) bimetallic steel, z_n is always no larger than zero. As the clad ratio increases, the absolute value of z_n grows until a certain value of clad ratio is reached, this value is usually around 0.5 and depends on the ratio of elastic moduli $E_\mathrm{c}/E_\mathrm{s}$. For SC bimetallic steel, the highest absolute value of z_n is 0.008, which is relatively moderate, while for TC bimetallic steel, this value can rise to 0.086, which is quite considerable for plate analysis. In order to ensure the accuracy and maintain consistency with the previous work, z_n will be taken into consideration in the following analysis.

2.2. Ritz formulation and solution for the buckling stress

The buckling stress of a homogeneous outstand plate can be solved by the energy method with Ritz formulation [12]. Based on the boundary conditions of outstand plate and coordinate system shown in Fig. 1(b), the deflection ω can be expressed by the Ritz approximation of rectangular plates:

$$\omega=fy\sin\frac{m\pi x}{a} \tag{2}$$

The strain energy Π_i and external potential energy Π_e can be written as:

$$\Pi_\mathrm{i}=\frac{D}{2}\int_0^a\int_0^b\left\{\left(\frac{\partial^2\omega}{\partial x^2}+\frac{\partial^2\omega}{\partial y^2}\right)^2-2(1-\nu)\left[\frac{\partial^2\omega}{\partial x^2}\times\frac{\partial^2\omega}{\partial y^2}-\left(\frac{\partial^2\omega}{\partial x\partial y}\right)^2\right]\right\}\mathrm{d}x\mathrm{d}y \tag{3}$$

$$\Pi_\mathrm{e}=-\frac{1}{2}\int_0^a\int_0^b\sigma_x t\left(\frac{\partial\omega}{\partial x}\right)^2\mathrm{d}x\mathrm{d}y \tag{4}$$

where D is the bending stiffness of the plate, which will be discussed later.

The principle of minimum total potential energy requires that the first variation of total potential energy equals to zero:

$$\delta\Pi=\delta(\Pi_\mathrm{i}+\Pi_\mathrm{e})=0 \tag{5}$$

Because $f\neq0$ when buckling occurs, by substituting Eqs. (2)-(4) into Eq. (5) and setting constant m=1 and ν=0.3, the buckling stress σ_cr can be expressed as:

$$\sigma_\mathrm{cr}=\left(0.425+\frac{b^2}{a^2}\right)\frac{\pi^2 D}{b^2 t} \tag{6}$$

The bending stiffness D is denoted as D_sp for SP and D_dp for DP, which is identical between internal and outstand SC bimetallic steel plate and has been derived in the previous study [7] as follows:

$$D_\mathrm{sp}=\int_{-t/2}^{t/2}Q_{11}(z-z_\mathrm{n}t)^2\,dz=\frac{t^3}{12(1-\nu^2)}E_\mathrm{sp} \tag{7}$$

$$E_\mathrm{sp}=[E_\mathrm{c}(4\beta^3-6\beta^2+3\beta)+E_\mathrm{s}(-4\beta^3+6\beta^2-3\beta+1)]+12z_\mathrm{n}\beta(\beta-1)(E_\mathrm{c}-E_\mathrm{s})+12z_\mathrm{n}^2[\beta E_\mathrm{c}+(1-\beta)E_\mathrm{s}] \tag{8}$$

$$D_\mathrm{dp}=\int_{-t/2}^{t/2}Q_{11}z^2\,dz=\frac{t^3}{12(1-\nu^2)}E_\mathrm{dp} \tag{9}$$

$$E_\mathrm{dp}=E_\mathrm{c}(\beta^3-3\beta^2+3\beta)+E_\mathrm{s}(-\beta^3+3\beta^2-3\beta+1) \tag{10}$$

The main difference between the expression of E_sp and E_dp is that the former one involves z_n so it is more complicated. On the contrary, because the laminar structure of DP is symmetric (i.e. $z_\mathrm{n}=0$), the expression of is E_dp simple.

2.3. Influence of transverse shear deformation

Due to the difficulty of establishing and solving the FSDT-based governing equations of outstand SC bimetallic steel plates, a simplified method has been adopted herein to consider the influence of transverse shear deformation independently. The buckling stress is modified by introducing the shear deformation effect factor k_FSDT [7]:

$$\sigma_\mathrm{cr,FSDT}=k_\mathrm{FSDT}\times\left(0.425+\frac{b^2}{a^2}\right)\frac{\pi^2 D}{b^2 t} \tag{11}$$

$$k_\mathrm{FSDT}=1-\frac{2\chi}{2\chi+1-\nu} \tag{12}$$

$$\chi=\frac{\pi^2}{12K_\mathrm{s}}\left(\frac{t}{b}\right)^2\left(\frac{1}{(a/b)^2}+1\right) \tag{13}$$

where K_s is the shear correction factor.

The derivation of the shear deformation effect factor k_FSDT and the shear correction factor K_s can be found in literature [7]. In this study, in order to keep the concision and to avoid repetition, the whole expression of K_s is not presented herein due to its extraordinarily complicated form. The mathematical software MATLAB is employed to calculate K_s in the validation and parametric analyses while specific values are listed in tables for engineering design.

3. Validation and parametric analyses

3.1. Validation against numerical results

The theoretical solution of the buckling stress $\sigma_\mathrm{cr,FSDT}$ expressed by Eq. (11) is validated in two ways through FE analyses, i.e., MATLAB and ABAQUS. The MATLAB codes developed by Ferreira [13] have been modified by the authors to include the boundary condition of outstand plates. The bending stiffness and transverse shear stiffness have also been modified to the equivalent ones of bimetallic steel plates. The FE models of bimetallic steel plates are developed in ABAQUS for eigenvalue buckling analysis. The shell offset calculated by Eq. (1) has been incorporated in the models so that the uniformly distributed load is applied exactly within the neutral surface. Since the first order buckling mode for outstand plates subjected to uniaxial compression is known to be symmetric, only half of the plate is modelled to save the computing time. With proper consideration for the influence of transverse shear deformations, the codes used in MATLAB and the models developed in ABAQUS can both calculate the buckling stress of bimetallic steel outstand plates under the assumption of FSDT.

To ensure the consistency of the two methods, the four-node quadrilateral element Q4 defined by Ferreira [13] is used in MATLAB while the four-node quadrilateral shell element with reduced integration S4R is used in ABAQUS. In both ways of FE analyses, the number of elements on the loaded edges is set as twenty while the number of elements on the other two edges changes with the aspect ratio *a*/*b* to make sure the elements are square. The elastic moduli of the cladding and substrate materials are taken as E_c=1.93×10^{5}MPa and E_s=2.06×10^{5}MPa, respectively, according to the Chinese standards [14,15].

Two cladding configurations illustrated in Fig. 1(b) are considered while different clad ratios, width-to-thickness ratios, aspect ratios and cladding materials are used for the purpose of validation. The theoretical solutions $\sigma_{cr,FSDT}$ are compared with the FE analysis results $\sigma_{cr,MATLAB}$ and $\sigma_{cr,ABAQUS}$ in Table 1 through 12 groups of data. In each group, 11 clad ratios between 0 and 1 are considered, while one typical group of results is plotted in Fig. 2. In Table 1, the cladding type consists of two parts; the first part represents the cladding configuration (i.e. SP and DP) while the second part represents the cladding material. SC is the stainless-clad bimetallic steel defined above while TC is the titanium-clad bimetallic steel, whose cladding material is replaced by titanium with an elastic modulus of 1.03×10^{5}MPa.

The comparison of FE analysis results $\sigma_{cr,MATLAB}$ and $\sigma_{cr,ABAQUS}$ suggests that the FE analysis methods have complete consistency with each other, which can verify the adequacy of the FE models. It can be seen from Table 1 and Fig. 2 that, the theoretical solutions derived herein agree well with both MATLAB and ABAQUS analysis results, which means the proposed theory herein is particularly accurate for elastic buckling analysis of outstand SC bimetallic steel plates in a wide range of parameters.

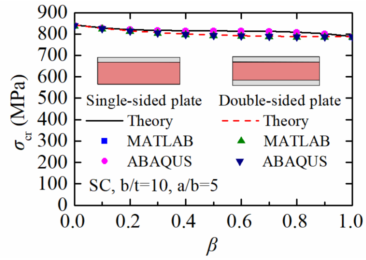

Fig. 2 Comparison of two typical groups of results (SP and DP, SC, *b*/*t*=10, *a*/*b*=5)

Table 1
Comparison between theoretical solutions with FE analysis results

Group	Cladding Type	*b*/*t*	*a*/*b*	$\sigma_{cr,ABAQUS}$ /$\sigma_{cr,FSDT}$		$\sigma_{cr,ABAQUS}$ /$\sigma_{cr,MATLAB}$	
				Mean	COV	Mean	COV
1	SP, SC	10	5	0.998	0.000	1.003	0.000
2	SP, SC	15	5	0.993	0.000	1.001	0.000
3	SP, SC	20	5	0.993	0.000	1.001	0.000
4	SP, SC	50	5	0.996	0.000	1.001	0.000
5	SP, SC	20	3	0.990	0.000	1.001	0.000
6	SP, SC	20	1	0.987	0.000	1.003	0.000
7	SP, TC	10	5	0.999	0.001	1.003	0.000
8	SP, TC	20	5	0.993	0.001	1.001	0.000
9	DP, SC	10	5	0.998	0.000	1.003	0.000
10	DP, SC	20	5	0.993	0.000	1.001	0.000
11	DP, TC	10	5	1.000	0.001	1.003	0.000
12	DP, TC	20	5	0.994	0.001	1.001	0.000

3.2. Parametric analyses

Based on the validated theoretical solutions, a series of parametric analyses have been carried out, in which the effects of clad ratio, width-to-thickness ratio, aspect ratio, cladding configuration and cladding material are clarified. The buckling stress $\sigma_{cr,FSDT}$ is calculated according to Eqs. (11)-(13), in which K_s is computed with the help of MATLAB.

3.2.1. Influence of clad ratio

The influence of clad ratio on the buckling stress $\sigma_{cr,FSDT}$ is already shown in Fig. 2 that with an increase of clad ratio, the buckling stress decreases. Although the start and end points are the same, the downward trends of SP and DP are distinctly different. There is a plateau in the middle section of the SP curve and steep slopes in the edge sections, while the slope of the DP curve is gradually descending as the clad ratio increases. While the overall downward trend can be explained by the smaller elastic modulus of the cladding material compared to that of the substrate one, the cause of difference between SP and DP curves should be further clarified.

It can be known from Eqs. (11)-(13) that for plates with identical dimensions, the buckling stress is influenced by the bending stiffness *D* and the shear deformation effect factor k_{FSDT}. The variation of both parameters with the clad ratio is shown in Fig. 3. It can be found that the shapes of bending stiffness curves are quite similar to those of buckling stress curves , while the shear deformation effect factor curves have different shapes from the buckling stress curves and their variation is slight. Hence, it can be concluded that the influence of clad ratio is predominately reflected in the bending stiffness.

The difference between the bending stiffness *D* between SP and DP can be explained by Eqs. (7) and (9). Since the bending stiffness is calculated by integration, for one specific point within the plate, the further it is from the neutral axis through the thickness direction, the greater its influence on the integral result will be. For the unsymmetric structure possessed by SP, when the clad ratio is very small or very large, the variation of clad ratio can be regarded as substituting the material near the external surface. For such position, since its distance from the neutral surface is large, the influence on the integration result of bending stiffness is significant. On the other hand, when the clad ratio is around 0.5, the change of clad ratio means replacing the material in the middle, which can hardly change the bending stiffness since z_n is very small. Whilst for the symmetric DP, since the cladding layers are placed on the outside, as the clad ratio increases, the material is changed from substrate material into cladding material, and this change takes place from outside to inside, resulting in the gradually descending slope of bending stiffness curve.

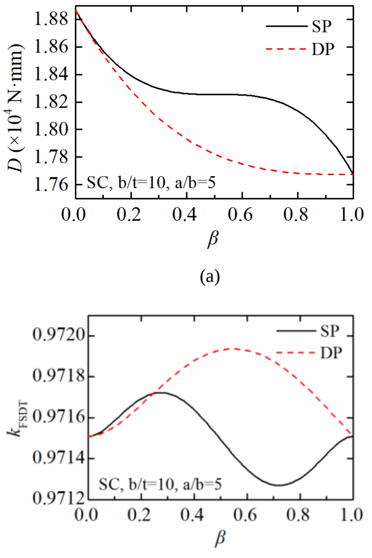

(a)

(b)

Fig. 3 Influence of clad ratio on (a) bending stiffness; (b) shear deformation effect factor

3.2.2. Influence of width-to-thickness ratio

Fig. 4 shows the influence of width-to-thickness ratio *b*/*t* on the buckling stress, in which different cladding configurations, clad ratios and cladding materials are also taken into consideration. The range of *b*/*t* is between 10 and 80 to cover both moderately thick plates and thin plates. It can be concluded from the Fig. 4 that when the width-to-thickness ratio is below 30, the buckling stress decreases with *b*/*t* rapidly; the descending rate slows as *b*/*t* becomes larger. This trend is in accordance with the expression of plate buckling stress Eq. (11).

It can also be seen that for SC bimetallic steel plates, the variation of clad ratio has very limited influence on the buckling stress comparing to the variation of width-to-thickness ratio. In comparison, the difference between curves of different clad ratio is clear when the cladding material is changed from stainless steel into titanium, as illustrated in Figs. 4(c) and 4(d). This phenomenon can be explained by the elastic modulus. Since the substrate material is fixed, when the cladding material is stainless steel whose elastic modulus is similar to that of CM steel, the difference between the two metals is slight and the influence of clad ratio is thus insignificant. However, when the cladding material is titanium, its elastic modulus is only half of that of CM steel, which leads logically to a more considerable effect.

It should be noticed that in Fig. 4(d), when the clad ratio is small (from 0.1 to 0.5), the difference between curves is visible, but as the clad ratio continues to grow, the curves of β=0.5, 0.7 and 0.9 have rather limited distinction. This can be clarified by the DP curve shown in Fig. 3(a), when clad ratio is small the variation of clad ratio has a strong impact on the buckling stress, whilst the impact is considerably diminished when the clad ratio becomes larger.

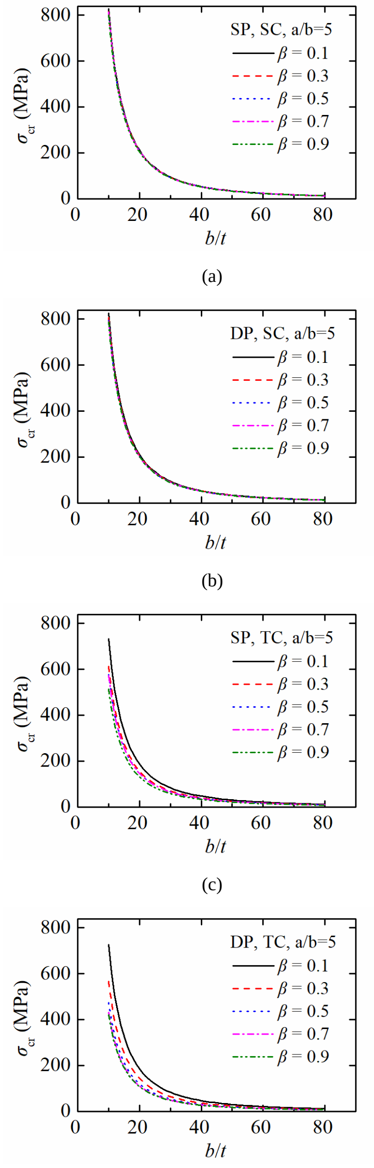

(a)

(b)

(c)

(d)

Fig. 4 Influence of width-to-thickness ratio on the buckling stress of (a) SP, SC; (b) DP, SC; (c) SP, TC; (d) DP, TC.

3.2.3. Influence of aspect ratio

A similar trend can be observed in Fig. 5 with respect of the influence of the aspect ratio *a*/*b*. Several factors such as cladding configurations, clad ratios and cladding materials are considered as well. From 1 to 10, the range of aspect ratio *a*/*b* covers both square plate and long rectangular plate. When the aspect ratio is below 4, the buckling stress decreases with *a*/*b* rapidly; the descending rate goes down as *a*/*b* grows. The expression of plate buckling stress Eq. (11) can once again be used to explain this trend, as the reciprocal of the aspect ratio has been squared and placed in bracket. Similar to what we have found in the study of width-to-thickness ratio, the variation of clad ratio has very limited influence on the buckling stress compared with the variation of aspect ratio for SC bimetallic steel plates, and the gap between curves of different clad ratios is wider when stainless steel is replaced by titanium as the cladding material. This phenomenon can be also explained by the elastic modulus the same way as it has been clarified in last section.

Fig. 5(c) shows that the difference between curves changes with the clad ratio, when the clad ratio is rather small or large, the gap between curves is visible. For clad ratios between 0.3 and 0.7, the curves are very close to each other. In Fig. 5(d), it has been also found that when the clad ratio is small (0.1~0.3), the difference between curves is visible, while the curves of larger clad ratio show minor difference. The SP and DP curves shown in Fig. 3(a) can offer a reasonable explanation, as the influence of clad ratio on the buckling stress varies for different clad ratios and cladding configurations.

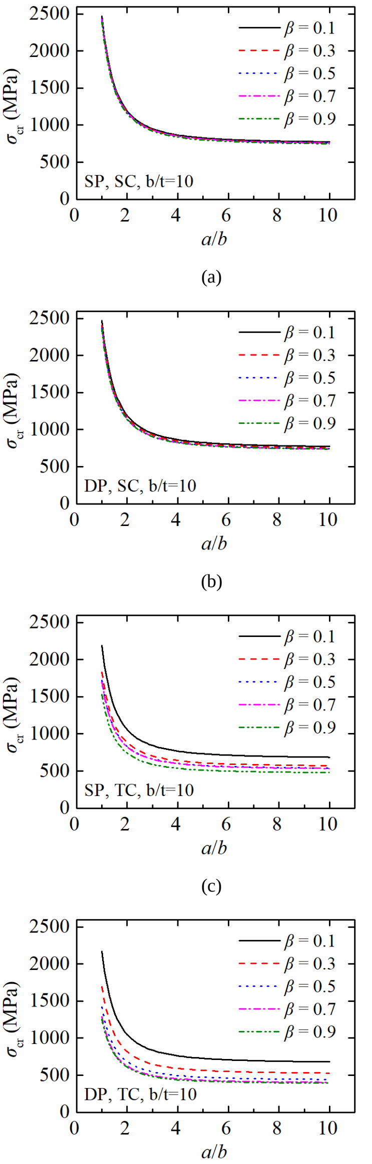

(a)

(b)

(c)

(d)

Fig. 5 Influence of aspect ratio on the buckling stress of (a) SP, SC; (b) DP, SC; (c) SP, TC; (d) DP, TC.

3.2.4. Influence of cladding metal

If the cladding metal is replaced by others, the elastic modulus E_c will become different and thus the elastic buckling stress will be influenced. In Fig. 6, the elastic modulus ratio E_c/E_s is selected as the abscissa to demonstrate the influence of cladding metal. It can be seen that as the elastic modulus of the cladding metal increases, the buckling strength grows in a quasi-linear way. For SP with clad ratios around 0.5, when the elastic modulus of the cladding metal reduces to a substantial degree, i.e. below 60% of that of the substrate metal, the buckling strength of plates drops a little bit more quickly. The influence of clad ratio on the buckling stress decreased as the elastic modulus ratio gradually approaches 1 due to the similarity of cladding and substrate materials. Three different combinations of with-to-thickness ratio and aspect ratio as well as five different clad ratios has been used to conduct a more comprehensive analysis of the influence of cladding material. Through Figs. 6(a)~6(e), it can be found that the shapes of curves in different figures are very similar albeit the width-to-thickness ratio and aspect ratio are different.

Generally, for SP, the curves of β=0.3, 0.5 and 0.7 are similar to each other, while the curves of β=0.1 and 0.9 show considerable difference. For DP, the curves of β=0.5, 0.7 and 0.9 are similar to each other, while the curves of β=0.1 and 0.3 show considerable difference. As analysed in the previous section, this phenomenon can be explained by the influence of clad ratio on the buckling stress shown in Fig. 2 and Fig. 3(a).

In engineering application, the clad ratio used for bimetallic steel is small in most cases due to the consideration of cost and efficiency. For example, the

SC bimetallic steel built-up square hollow section stub columns studied in literature [8] were designed to have clad ratios of 0.207 and 0.391. Hence, more attention should be addressed to the range of small clad ratios. Within the clad ratio ranging from 0.1 to 0.5, the influence of cladding metal suggests that for SC bimetallic steel plates whose elastic modulus ratio E_c/E_s is around 0.94, the effect of parameters is subtle and thus the design method of stainless steel plates can be adopted with necessary slignt modification. . For TC bimetallic steel, a small change of important parameters will lead to a substantial difference in buckling stress, so more attention should be paid when considering the influence of different factors such as clad ratio and width-to-thickness ratio.

To summarize, the cladding metal is critical to the buckling stress of bimetallic steel plates. When the material properties of the cladding and substrate materials such as elastic moduli have significant difference, the slight change of other parameters such as clad ratio and width-to-thickness ratio will cause a big change to the buckling stress.

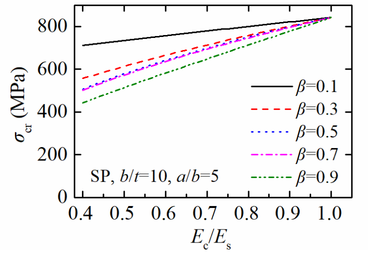

(a)

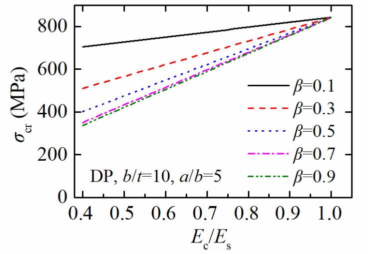

(b)

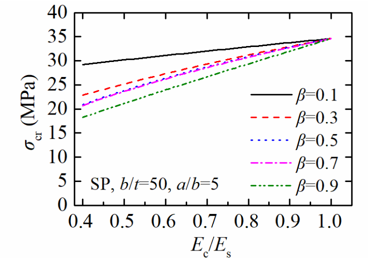

(c)

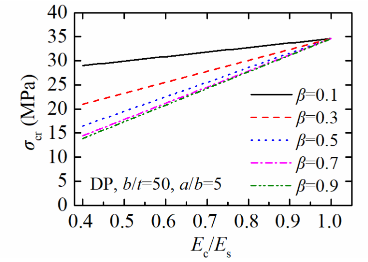

(d)

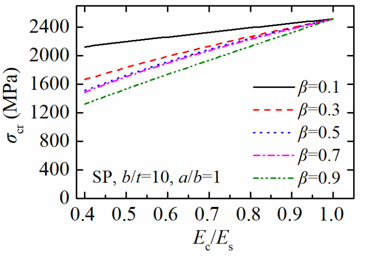

(e)

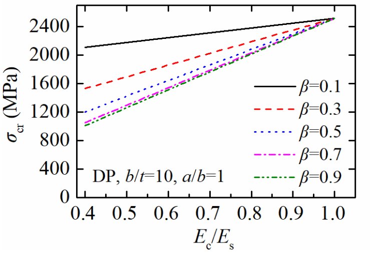

(f)

Fig. 6 Influence of cladding metal on the buckling stress of (a) SP, *b*/*t*=10, *a*/*b*=5; (b) DP, *b*/*t*=10, *a*/*b*=5; (c) SP, *b*/*t*=50, *a*/*b*=5; (d) DP, *b*/*t*=50, *a*/*b*=5; (e) SP, *b*/*t*=10, *a*/*b*=1; (f) DP, *b*/*t*=10, *a*/*b*=1.

3.2.5. Influence of boundary condition

Since the elastic buckling of simply supported (internal) bimetallic steel plates has been investigated in a previous study [7], it is worthwhile to compare the buckling stresses of outstand plates with those of internal plates to find out the influence of boundary condition, and thus to gain a deeper knowledge of the elastic buckling of bimetallic steel plates.

The data of simply supported bimetallic steel plates given in [7] are compared with those of outstand plates herein. The parameters of plates are determined in accordance to the previous study, as the three clad ratios 0.2, 0.5 and 0.8 and two cladding configurations SP and DP are considered. Figs. 7(a) and 7(b) show the results with various elastic modulus ratios E_c/E_s while the width-to-thickness ratio is set as 10 and the shape of the plates is square. Figs. 7(c) and 7(d) demonstrate the results with different width-to-thickness ratios while the material is TC bimetallic steel and the shape of the plates is also square.

It can be seen from Fig. 7 that due to the different boundary conditions, the elastic buckling stress of outstand plates is significantly smaller than that of the internal plates. It needs to be noted that the curves of internal and outstand plates in Fig. 7 have similar shape, which means the variation of buckling stress with both elastic modulus ratio E_c/E_s and width-to-thickness ratio is not profoundly influenced by the change of boundary conditions.

In recognition of the similarity of internal and outstand plates with regard to the variation of buckling stress, the design method of outstand plates can be established on this basis. For the simplicity and convenience of engineering application, a similar way can be applied with only a few key parameters to be updated.

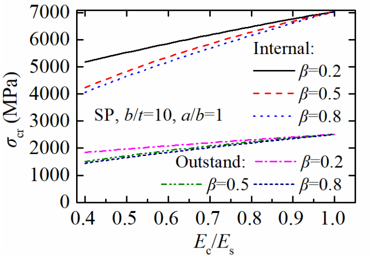

(a)

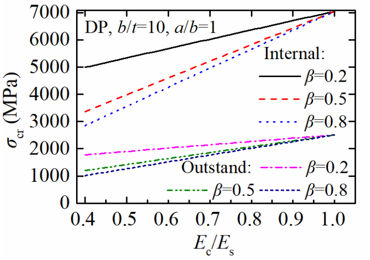

(b)

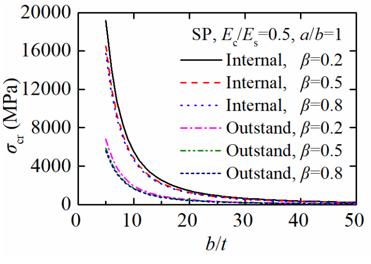

(c)

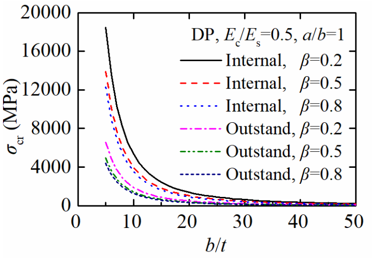

(d)

Fig. 7 Influence of boundary condition on the buckling stress of (a) SP, b/t=10, a/b=1; (b) DP, b/t=10, a/b=1; (c) SP, E_c/E_s=0.5, a/b=1; (d) DP, E_c/E_s=0.5, a/b=1;

4. Design methods

Since the theoretical derivation has been validated against numerical analyses and the influence of critical parameters has been clarified, the design methods for the elastic buckling of outstand SC bimetallic steel plates can be provided. In the authors' previous study on the internal (simply supported) plates, the simplified solution of critical buckling stress has been proposed along with the design requirements for interface shear strength. However, for outstand plates, the transverse shear stresses can't be explicitly expressed by any formula because the buckling stress is solved by the energy method with Ritz formulation.

Therefore, the design methods proposed herein will focus on the calculation of critical buckling stress of bimetallic steel plates. Given that the design methods to calculate the buckling stress of simply supported plates have already been provided in literature [7], they can be combined with the research findings hereinto form a set of integrated and generall design formulae for both oustand and interal elastic buckling of bimetallic steel plates.

By substituting the shear deformation effect factor k_{FSDT} (expressed as Eq. (12)) into the expression of the buckling stress $\sigma_{\mathrm{cr,FSDT}}$ (expressed as Eq. (11)), the buckling stress of internal and outstand plates can be expressed by a unified equation as shown in Eq. (14):

$$\sigma_{\mathrm{cr}}=\frac{\left(1-\frac{2\chi_{\mathrm{int(out)}}}{2\chi_{\mathrm{int(out)}}+1-\nu}\right)k_{\mathrm{int(out)}}\pi^2 D}{b^2 t} \tag{14}$$

In Eq. (14), the parameters $k_{\mathrm{int(out)}}$ and $\chi_{\mathrm{int(out)}}$ varies with the boundary conditions.

For internal plates:

$$k_{\mathrm{int}}=(\frac{mb}{a}+\frac{n^2 a}{mb})^2 \tag{15}$$

$$\chi_{\mathrm{int}}=\frac{t^2\pi^2}{12K_s}(\frac{m^2}{a^2}+\frac{n^2}{b^2}) \tag{16}$$

in which the coefficients m and n are positive integers that results in a lowest k_{int}, which is determined by the aspect ratio of the plates.

For outstand plates:

$$k_{\mathrm{out}}=\left(0.425+\frac{b^2}{a^2}\right) \tag{17}$$

$$\chi_{\mathrm{out}}=\frac{\pi^2}{12K_s}(\frac{t}{b})^2\left(\frac{1}{(a/b)^2}+1\right) \tag{18}$$

The shear correction factor K_s and bending stiffness D are different for two cladding configurations. The expressions of bending stiffness have been given in Eqs. (7)~(10), and the expressions of are K_s as follows:

For plates with singly-sided cladding metal (SP):

$$K_s=\frac{t^5 E_{\mathrm{sp}}^2}{144E_{\mathrm{eq}}h_s(z)} \tag{19}$$

in which E_{sp} is the integral elastic modulus of SP, as shown in Eq. (8); $h_d(z)$ is a complicated parameter whose expanded form is too long to be introduced here. The expanded form can be found in the Appendix A of literature [7]. Another parameter appears in Eq. (19) is the equivalent elastic modulus of the plate E_{eq}, which is same for both SP and DP plates:

$$E_{\mathrm{eq}}=\beta E_{\mathrm{c}}+(1-\beta)E_{\mathrm{s}} \tag{20}$$

For plates with doubly-sided cladding metal (DP):

$$K_s=\frac{t^5 E_{\mathrm{dp}}^2}{144E_{\mathrm{eq}}h_{\mathrm{d}}(z)} \tag{21}$$

in which E_{dp} is the integral elastic modulus of DP, as shown in Eq. (10); E_{eq} is the equivalent elastic modulus of the plate as expressed in Eq. (20); $h_d(z)$ is a complicated parameter whose expanded form can be also found in the Appendix A of literature [7].

Although it is hard to establish a simplified expression or a fitting function for the shear correction factor K_s, the authors have suggested a solution for engineering application, that is to use tables for engineers to look up from, as shown in Table 2 for common paraters in practice, while more tables corresponding to different elastic modulus ratios and clad ratios can be provided in the design code to cover the whole range of engineering application. With the help of such tables, one can conveniently find the approximate shear correction factor value of a specific bimetallic steel plate using the tables and linear interpolation.

Table 2

The shear correction factor K_s for different bimetallic steel types and cladding configurations

	Shear correction factor K_s			
Clad ratio	SC bimetallic steel		TC bimetallic steel	
	SP	DP	SP	DP
0	0.8333	0.8333	0.8333	0.8333
0.05	0.8340	0.8337	0.8367	0.8351
0.10	0.8355	0.8347	0.8456	0.8405
0.15	0.8372	0.8361	0.8572	0.8490
0.20	0.8386	0.8378	0.8676	0.8602
0.25	0.8394	0.8395	0.8727	0.8730

5. Conclusions

A comprehensive study into the elastic buckling of outstand SC bimetallic plates subjected to uniaxial compression has been presented. Taking the neutral surface and transverse shear deformation into consideration, the energy method is adopted to derive the analytical solutions of the buckling stress. The FE models are developed in both MATLAB and ABAQUS to verify the accuracy of theoretical solutions, in which different combinations of parameters like clad ratios, width-to-thickness ratios, aspect ratios and cladding materials are used for the purpose of validation. The validated formulae have been used to carry out a series of parametric analyses to further clarify the influence of critical parameters. Finally, in combination of the previous research findings, a comprehensive design method for SC bimetallic plates has been proposed, including a set of formulae to calculate the elastic buckling stress. Detailed findings are outlined as follows:

(1) The energy method with Ritz formulation can be adopted to solve the buckling stress of outstand SC bimetallic steel plates, while the relative position of neutral surface from the middle one z_n, the bending stiffness D and the first-order shear deformation effect have been considered to improve the accuracy;

(2) Numerical analyses based on two FE analysis tools (MATLAB and ABAQUS) have been conducted, and the results obtained through these two methods show complete consistency with each other as well as with the theoretical solutions;

(3) The influence of clad ratio on the buckling stress is mainly controlled by the bending stiffness, and the patterns of SP and DP are different;

(4) The influence of width-to-thickness ratio on the buckling stress is more significant compared to that of the clad ratio;

(5) When the aspect ratio is small, the change of the plate shape can lead to a considerable variation of buckling stress;

(6) When the material properties of the cladding and substrate materials are significantly different such as the case of TC bimetallic steel, the slight change of other parameters can cause a big change in the buckling stress;

(7) For internal and outstand bimetallic steel plates, the boundary conditions can significantly affect the buckling stress, but the influence of parameters is similar;

(8) Combining the design formulae of internal and outstand bimetallic stel plates, an integrated design method have been proposed to calculate the elastic buckling stress of bimetallic steel plates.

References

[1] Ban H. Y., Mei Y. X., Shi Y. J., “Research advances of stainless-clad bimetallic structures”, Engineering mechanics, 38(6), 1-23, 2021 (in Chinese).
[2] Ban H. Y., Bai R. S. Yang L., Bai Y., “Mechanical properties of stainless-clad bimetallic steel at elevated temperatures”, Journal of Constructional Steel Research, 162, 105704, 2019.
[3] Ban H. Y., Bai R. S., Chung K. F., Bai Y., “Post-fire material properties of stainless-clad bimetallic steel”, Fire Safety Journal, 112, 102964, 2020.
[4] Ban H. Y., Yang K. H., Mei Y. X., “Experimental study of corrosion resistance of stainless-clad bimetallic steel and welded connections”, Journal of Tianjin University (Science and Technology), 54(2), 111–121, 2021 (in Chinese).
[5] Ban H. Y., Zhu J. C., Shi G., Zhang Y., “Tests and modelling on cyclic behaviour of stainless-clad bimetallic steel”, Journal of Constructional Steel Research, 166, 105944, 2020.
[6] Mei Y. X., Ban H. Y., “High strain rate behaviour of stainless-clad bimetallic steel”, Engineering Structures, 207, 110219, 2020.
[7] Mei Y. X., Ban H. Y., Shi Y. J., “Elastic buckling of simply supported bimetallic steel plates”, Journal of Constructional Steel Research, 198, 107581, 2022.
[8] Ban H. Y., Mei Y. X., “Local buckling behaviour of stainless-clad bimetallic steel built-up square hollow section stub columns”, Thin-Walled Structures, 182, 110207, 2023.
[9] Ban H. Y., Zhu J. C., Shi G., “Cyclic loading tests on welded connections of stainless-clad bimetallic steel and modelling”, Journal of Constructional Steel Research, 171, 106140, 2020
[10] Zhang D. G., Zhou Y. H., “A theoretical analysis of FGM thin plates based on physical neutral surface”, Computational Materials Science, 44, 716–720, 2008.
[11] Karamanli A., Aydogdu M., “Bifurcation buckling conditions of FGM plates with different boundaries”, Composite Structures, 245, 112325, 2020.
[12] Chen J., Stability of Steel Structures: Theory and Design (6th Edition), Science Press, Beijing, 2011 (in Chinese).
[13] Ferreira A. J. M., Fantuzzi N., MATLAB Codes for Finite Element Analysis, Springer, 2020
[14] Standard for Design of Steel Structures (GB 50017-2017), China Architecture & Building Press, Beijing, 2018 (in Chinese).
[15] Code for Technical specification for stainless steel structures (CECS 410:2015), China Planning Press, Beijing, 2015 (in Chinese).

Acknowledgement

This study was financially supported by the National Natural Science Foundation of China (No. 52078272, 51778329), which is gratefully acknowledged.

Advanced Steel Construction – Vol. 19 No. 1 (2023) 38–45
DOI: 10.18057/IJASC.2023.19.1.6
(**Special Issue:** *10th International Conference on Advances in Steel Structures, ICASS'2020, Chengdu, China*)

ANALYSIS AND DESIGN OF AXIALLY LOADED SQUARE CFST COLUMN TO RC BEAM JOINTS STIFFENED BY DIAGONAL RIBS

Dan Gan [1], Hua-Xuan Tang [1], Wen Li [1], Zheng Zhou [2, *], Xu-Hong Zhou [1] and Zhen-Ming Chen [3]

[1] *School of civil engineering, Chongqing University, Chongqing , China*
[2] *College of civil engineering, Hunan University, Changsha , China*
[3] *China Construction Steel Structure Engineering Corp., LTD, Shenzhen 518118, China*
* *(Corresponding author: E-mail:* zhouzhengchn@126.com*)*

ABSTRACT

This work proposes a partially through-beam joint system to connect square concrete-filled steel tubular (CFST) columns and reinforced concrete (RC) beams. In the system, the holes in the steel tube allow longitudinal beam reinforcements to be continuous through the joint zone to achieve direct load-transfer of the beam, and the square steel tube with holes is strengthened by welding diagonal ribs located at the corners of the steel tube. Finite element (FE) analyses on joints with RC beams were carried out based on verified models. The analysis results showed that diagonal ribs welded to the joint tube confined the concrete in the joint zone efficiently and made up for the reduction in axial load capacity caused by the holes of the steel tube, so the joint system can meet the requirements of strong-joint weak-component under axial compression with ease. Finally, mechanics-based models and axial strength equations of joints were proposed, and the predicted results agreed well with the FE results. These results proved that the square CFST column to RC beam joints stiffened by diagonal ribs were feasible and can be applied in engineering practice based on reasonable design.

ARTICLE HISTORY

Received:	20 July 2022
Revised:	22 August 2022
Accepted:	10 January 2023

KEYWORDS

Concrete-filled steel tube;
RC beam;
Steel-concrete composite joint;
Diagonal ribs;
Axial compression behavior

1. Introduction

Concrete-filled steel tubular (CFST) columns get more and more applications as the main structural elements for resisting both vertical and lateral loads in multistory and high-rise buildings [1–4]. Compared with the circular CFST columns, the square CFST column has relatively large bending stiffness, high bending capacity and convenient construction, and has been well applied in engineering. Square CFST columns are usually connected to steel beams or reinforced concrete (RC) beams. In consideration of the cost, square CFST column to RC beam joints are widely used in China [5].

Various joint systems connecting CFST columns with RC beams have been proposed. Generally, there are two types of joint systems, namely through-column and through-beam joints, as shown in Fig. 1. In the through-column joint (Fig. 1 (a)), the column steel tube is continuous through the joint zone, and the longitudinal reinforcements of RC beams are usually connected to steel corbels or stiffening rings which stiffen the joint zone and transfer both the shearing forces and bending moments [6,7]. In the through-beam joint (Fig. 1 (b)), the column steel tube is discontinuous, and the beam longitudinal reinforcements pass through the joint zone directly. Besides, the ring beam and column longitudinal reinforcements are used to strengthen the joint zone and to compensate for the reduction in axial load capacity caused by the discontinuous column tube [8–13]. Nevertheless, for through-column joints various stiffeners such as stiffening rings are needed to transfer the force from the reinforcements and welding on site cannot be avoided, and for through-beam joints the details for ring beams are complex and the protruded ring beams are architecturally undesirable.

(a) Through-column joint [7]

(b) Through-beam joint [10]

Fig. 1 Typical CFST column to RC beam joints

In recent years, a new kind of joint system, namely partially through-beam joints, was proposed due to the practical engineering demands, as shown in Fig. 2. In the partially through-beam joints, the holes in the hollow steel tube allowed beam longitudinal reinforcements to be continuous through the joint zone to transfer the bending moment and shearing force of the RC beam directly and effectively. Besides, the additional outer steel tube [14] or internal diaphragms [15] were welded to the joint steel tube to make up for the reduction in axial load capacity caused by the holes. The experimental and analytical results showed that these joint systems showed good axial and cyclic performance [14–16].

On the basis of previous research, a novel, more simplified and reliable partially through-beam joints was proposed in this work. As shown in Fig. 3, diagonal ribs were welded to the edge of the hole to confine concrete in the joint zone and to co-carry the axial load. The square CFST columns stiffened by diagonal ribs were experimentally and analytically evaluated by the authors [17,18]. The results showed that: 1) the diagonal ribs changed the buckling mode and effectively delayed the local buckling of the square steel tube; 2) the diagonal ribs not only confined the steel tube and concrete, but also co-carried the axial load; 3) in comparison to square CFST columns with other stiffeners, the columns with diagonal ribs had higher strength, better ductility and larger energy dissipation capacity under the same steel ratio. Consequently, the newly proposed square CFST column to RC beam joints stiffened by diagonal ribs are anticipated to possess good mechanical properties.

(a) Joint with rectangular holes [14]

(b) Stiffened interior joint [15]

Fig. 2 Typical partially through-beam joints

However, it remains questionable that whether the proposed joint system can meet the requirements of the strong-joint weak-component under axial compression due to the holes in the joint steel tube. In this work, the feasibility of square CFST column to RC beam joints stiffened by diagonal ribs was carried out, and the axial compression behavior of the joints was studied through finite element (FE) analyses using ABAQUS. The FE models were verified by the test results in relevant literature, followed by extensive parametric analyses. Finally, based on the analytical results, the mechanics-based models and axial strength equations for the joints were proposed.

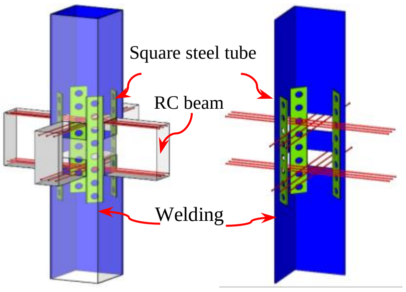

Fig. 3 Square thin-walled CFST column to RC beam joints

2. Finite element model

2.1. Model description

(1) Benchmark model

Fig. 4 shows the details of the benchmark model. The width (B_c) and height (H_c) of the column were 300 mm and 1400 mm, respectively. The width (B_b) and height (H_b) of the beam were 150 mm and 300 mm, respectively. The width of the end sub-plate (b) was 75mm, namely the diagonal ribs were welded at 1/4 of the column width (i.e., b=1/4B_c). The thickness of the diagonal rib (t_s) and steel tube (t_t) were taken as 8mm. The spacing between two adjacent holes (s), the diameter of holes in the diagonal ribs (d) and the width of diagonal ribs (b_s) were 75mm, 25mm and 106.07mm, respectively. The ratio of hole area to the beam cross-sectional area was defined as the hole ratio of joint steel tube (ρ) (i.e., ρ=2b_h/H_b), which was 0.5 in the benchmark model. The concrete compressive strength (f_c) was 40MPa and the steel yield strength (f_y) was 345MPa. The yield strength of beam longitudinal reinforcements was 400MPa. The studied parameters are listed in Table 1.

(2) Modeling method

The concrete was modeled by solid element (type C3D8R). For concrete under compression, the Concrete Damaged Plasticity (CDP) model was used to model concrete, and the stress-strain relationships proposed by Han et al.[1] and GB50010 2010 [19] were applied for the column and beam concrete, respectively. For concrete under tension, the stress-strain model was obtained by defining the tensile stress and tensile fracture energy presented in CEB-FIP MC90 [20]. The elastic modulus and Poisson's ratio of concrete were 4730*sqrt(f_c) and 0.2 [21], respectively.

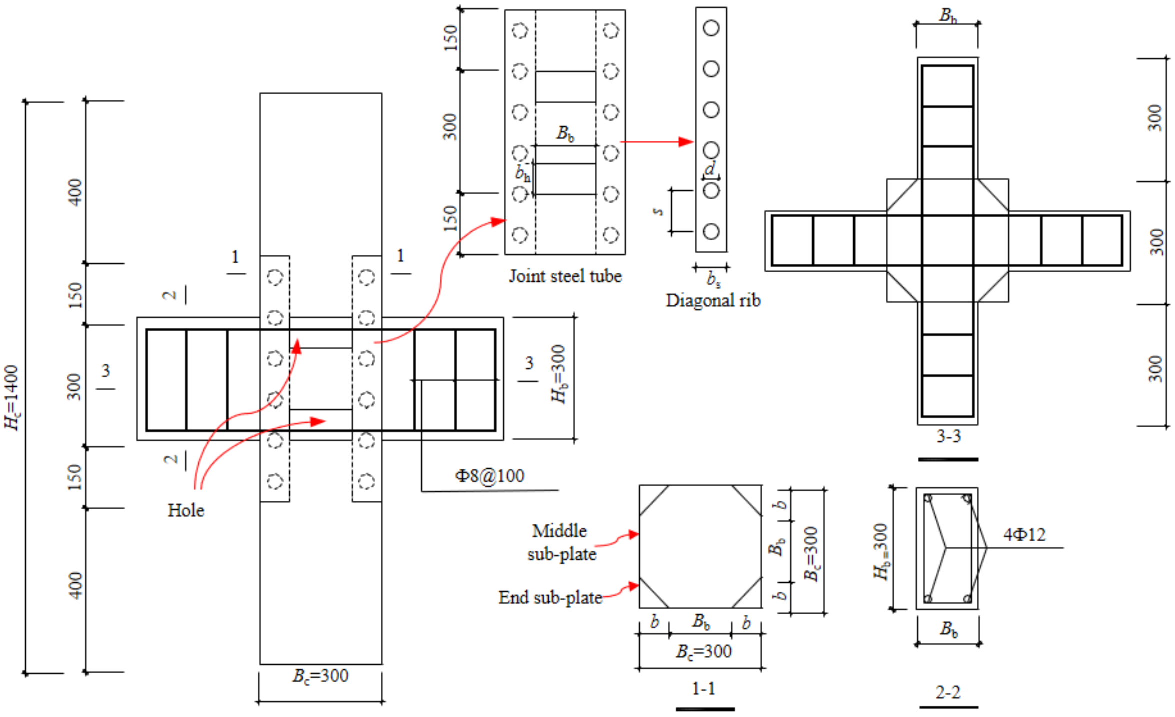

Fig. 4 Details of the benchmark model (units: mm)

Table 1
Joint parameters

Parameter	Variables	Fixed values
Width of end sub-plate (*b*)	$0.25B_c$, $0.27B_c$, $0.28B_c$, $0.30B_c$, $0.32B_c$, $0.33B_c$	$1/4B_c$
Width-to-thickness ratio of steel tube (B_c/t_t)	18.75, 21.43, 25, 30, 37.5, 50	37.5
Ratio of diagonal rib thickness to tube thickness (t_s/t_t)	0, 0.25, 0.50, 0.75, 1.00, 1.25, 1.50	1.00
Diameter of hole in diagonal rib (*d*)	$0b_s$, $0.20b_s$, $0.24b_s$, $0.40b_s$, $0.60b_s$,$0.70b_s$	$0.24b_s$
Spacing between two adjacent holes (*s*)	3*d*, 4*d*, 5*d*, 6*d*, 9*d*	3*d*
Hole ratio of joint steel tube (*ρ*)	0.5, 0.6, 0.7, 0.8, 0.9, 1.0	0.5
Concrete compressive strength (f_c: MPa)	30, 40, 50, 60, 70, 80	40
Steel yield strength (f_y: MPa)	235, 345, 460, 550, 600, 700, 800	345

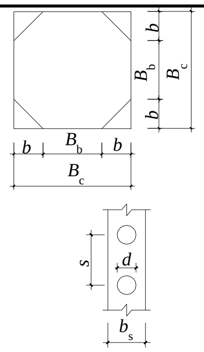

Steel tubes and diagonal ribs were simulated by shell element (type S4R), and reinforcements were simulated by truss element (type T3D2). The elastic-perfectly plastic stress-strain model was adopted for steel. The elastic modulus and Poisson's ratio of steel were selected as 206GPa and 0.3, respectively.

In the FE model, diagonal ribs and beam reinforcements were embedded in the concrete. The interface between the steel tube and concrete was modeled by surface-to-surface contact interaction, where the hard contact was used for the normal behavior and Mohr-Coulomb friction model with a fiction coefficient of 0.6 was used for the tangential behavior. The column end was fixed, and only the vertical degree of freedom of the column top was released.

As shown in Fig. 5, the mesh size was 1/10 of the column width based on sensitivity study.

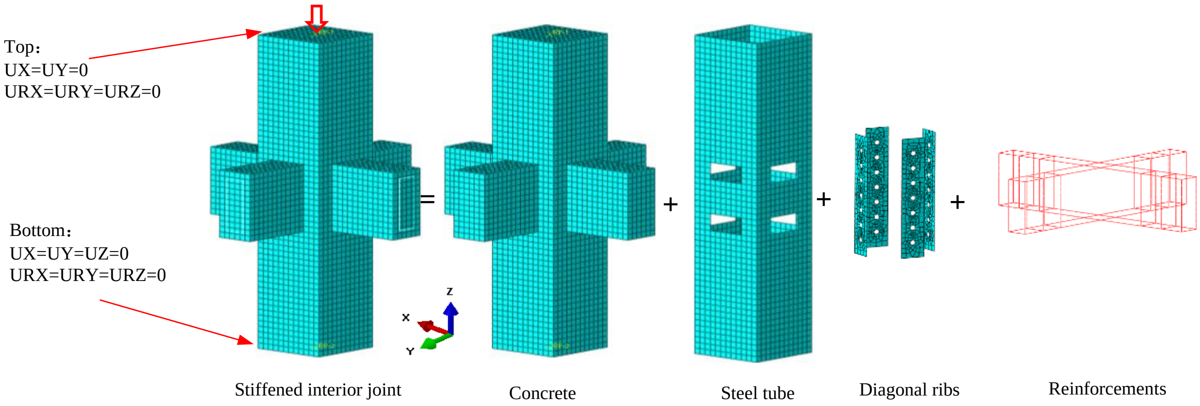

Fig. 5 FE model of joints

2.2. Model verification

(1) Square CFST column stiffened by diagonal ribs

Typical square CFST columns stiffened by diagonal ribs in previous tests [18] were simulated. As shown in Fig. 6, the FE model well predicted the initial stiffness and peak strength.

(2) TRC column to RC beam joints

Similar joint specimens in the literature [11,12] were simulated. As shown in Fig. 7 and Fig. 8, the failure modes, initial stiffness and peak strength were in good agreement with test results. Based on these verifications, the proposed model can be used for further analyses.

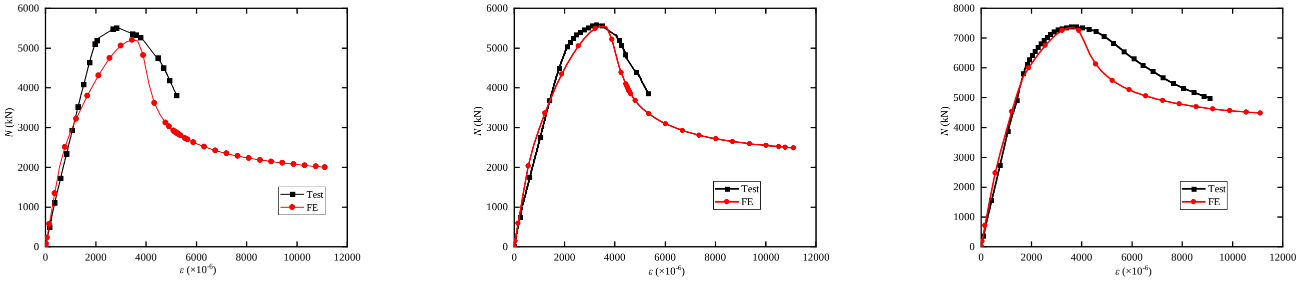

(a) SS-2-2-B (b) SS-2-3-B (c) SS-6-2-B

Fig. 6 Comparison on FE and experimental results for square CFST columns stiffened by diagonal ribs

(a) B-240-120-2

(b) B-240-120-3

(c) B-240-120-4

Fig. 7 Comparison on FE and experimental results for circular TRC column to RC beam joints

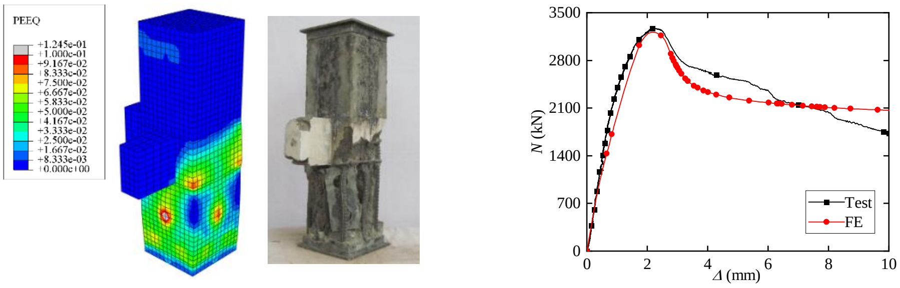

(a) SC(GS)-140-2-S

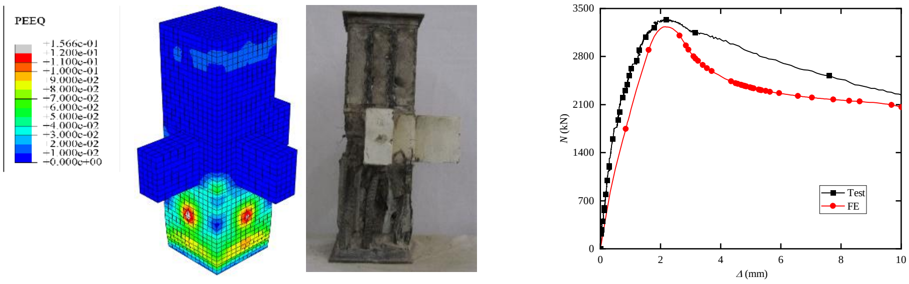

(b) SC(GS)-140-3-S

(c) SC(GS)-140-4-S

Fig. 8 Comparison on FE and experimental results for square TRC column to RC beam joints

3. Parametric study

As shown in Fig. 9, two failure modes for the interior joints stiffened by diagonal ribs were observed based on the strain distribution of the concrete, namely the joint failure and column failure.

(1) Effect of end sub-plate width (*b*) and hole ratio of joint steel tube (*ρ*)

Fig. 10(a) shows the effect of *b*. The failure mode and peak strength remained almost unchanged with *b* increased from $1/4B_c$ to $1/3B_c$, and the requirements of the strong-joint weak-component under axial compression were satisfied. Consequently, the end sub-plate width was suggested to be $1/4\ B_c$ - $1/3B_c$ (i.e., $b = 1/4B_c - 1/3B_c$). Note that the beam width also changed with variation of *b*, since the diagonal ribs were welded to the edge of the hole.

As shown in Fig. 10(b), the peak strength was unchanged due to the same column failure with *ρ* smaller than 0.9. However, the strength was reduced obviously and the failure mode was changed to joint failure due to larger *ρ* of 1.0. Therefore, *ρ* should be no larger than 0.9 to avoid excessively weakening the joint steel tube and to achieve the strong-joint weak-component. Additionally, the potential direct shear failure of the interface between the column and beam would occur when *ρ* was smaller than 0.5 [22]. Consequently, it is recommended the hole ratio lager than 0.5 while smaller than 0.9 (i.e., ρ = 0.5-0.9).

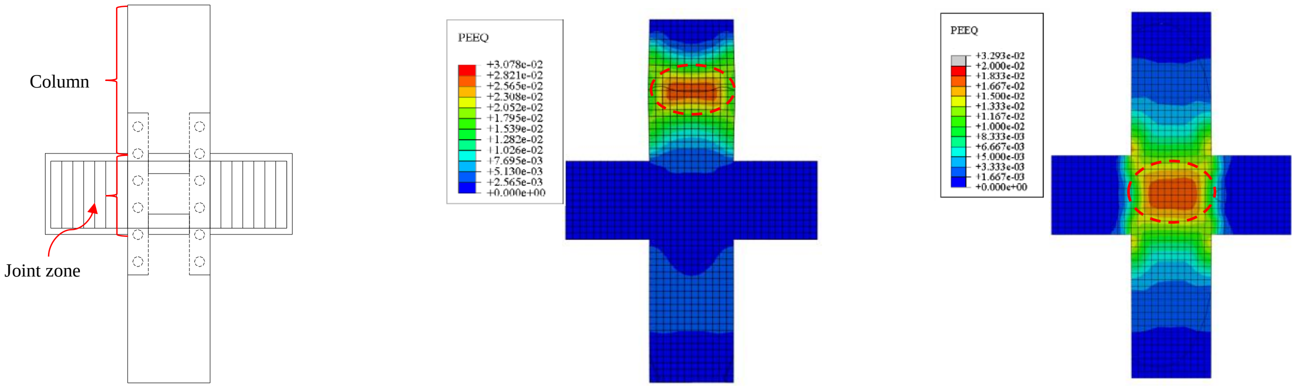

(a) Column failure (b) Joint failure

Fig. 9 Failure modes of joints stiffened by diagonal ribs

(2) Effect of thickness of joint steel tube (t_t) and thickness of diagonal rib (t_s)

As shown in Fig. 11(a), the peak strength was increased with larger t_t, whereas the failure mode remained unchanged, as the load capacity provided by the column and joint zone varied simultaneously.

As shown in Fig. 11(b), thicker t_s increased the load capacity of the joint zone, and thus the peak strength was enhanced significantly for specimens with joint failure. However, the strength enhancement was slight after the value of t_s/t_t larger than 0.75, as the failure mode was changed to the column failure and the load capacity was provided by the unstiffened CFST column. For ease of design, the thickness of the diagonal rib was suggested to be the same as that of the steel tube (i.e., t_s/t_t =1.0).

(3) Effect of concrete strength (f_c) and steel yield strength (f_y)

As showed in Fig. 12, the strength increased linearly with larger f_c and f_y, as f_c and f_y didn't change difference of the confinement stress between different zones, and thus the failure mode was unchanged.

(4) Effect of spacing between two adjacent holes (*s*) and diameter of holes (*d*)

As shown in Fig. 13(a), the spacing of holes affected the strength little and the failure mode was unchanged. This was attributed to fact that the effective cross-sectional areas of diagonal ribs were unchanged. According to Zhou et al. [23], the spacing was recommended at least 2.25 times the hole diameter (i.e., $s \geq 2.25d$) to avoid the potential highly stressed regions between two adjacent concrete dowels.

Fig. 13(b) showed that the strength of specimens decreased with *d* increased from 0 to $0.7b_s$, but the strength reduction was within 3%, and the failure mode was also unchanged. A larger *d* could facilitate concreting, increase the anchorage and improve the load transfer between the steel and concrete, while also weak the diagonal ribs. Therefore, the hole diameter (*d*) is recommended to be with the range of $0.2\text{-}0.7b_s$ (i.e., $d = 0.2\text{-}0.7b_s$).

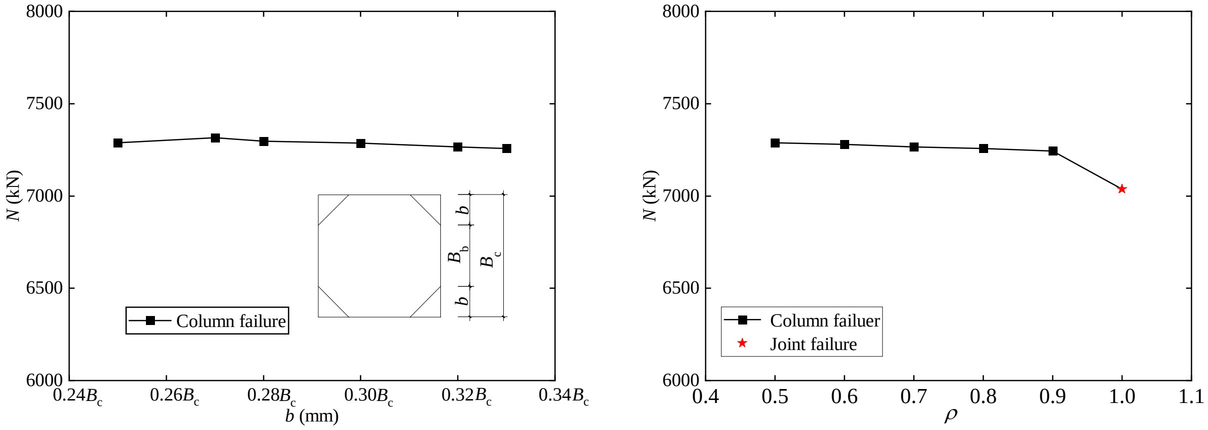

(a) Effect of *b* (b) Effect of *ρ*

Fig. 10 Effect of *b* and hole ratio of joint steel tube

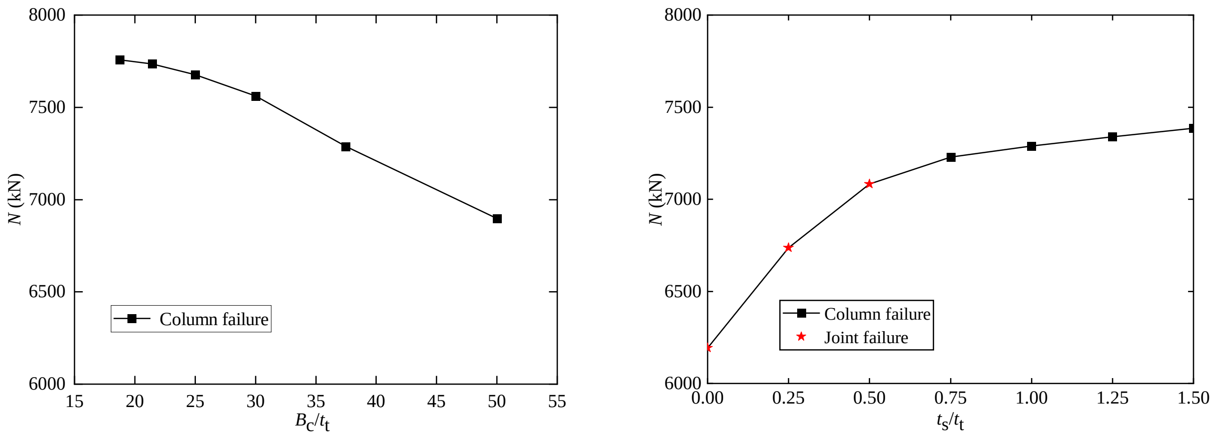

(a) Effect of b/t_t

(b) Effect of t_s/t_t

Fig. 11 Effect of t_s and t_t

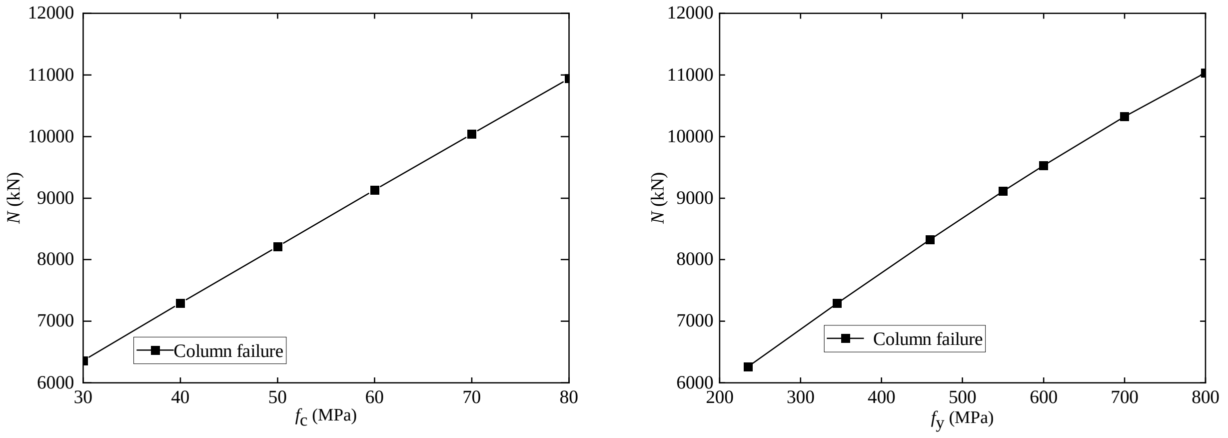

(a) Effect of f_c

(b) Effect of f_y

Fig. 12 Effect of f_c and f_y

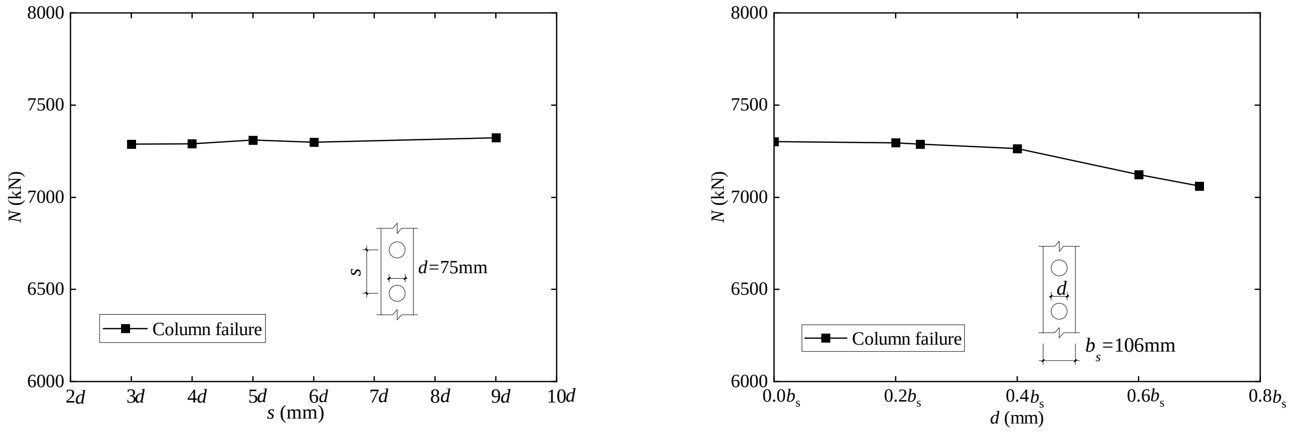

(a) Effect of *s*

(b) Effect of *d*

Fig. 13 Effect of *s* and *d*

4. Prediction for axial load capacity of joint zone

4.1. Plastic stress distribution method

In this section, the plastic stress distribution (PSD) method was firstly used to predict the axial load capacity of the joint zone, as the PSD method was widely used as the primary method for calculating the strength of steel-concrete composite members [24,25]. In the PSD method, steel components are assumed to have attained their yield stress in either tension or compression and the concrete is assumed to have attained their compressive stress in compression [24]. Tension strength of the concrete is neglected. Note that neglecting the local buckling of the steel tube was reasonable, as the column steel tubes were designed to meet the width-to-thickness ratio limitations in typical standards [26].

The axial load capacity of the joint zone depended on the minimum load capacity provided by Zones I and II, as shown in Fig. , and thus the load capacity of Zone I was focused on due to the holes. Consequently, the axial load capacity of joint zone (N_j) was calculated as

$$N_j = A_c f_c + A_{tj} f_{ty} + A_{sj} f_{sy} \tag{1}$$

Where A_c, A_{tj} and A_{sj} are the net cross-sectional areas of the concrete, joint steel tube and diagonal rib, respectively. f_c, f_{ty} and f_{sy} are the concrete compressive strength, and yield strength of the steel tube and diagonal rib, respectively.

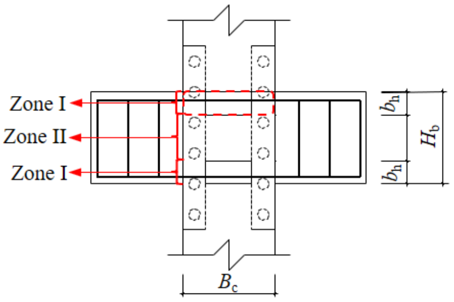

Fig. 14 Diagram of joint zone

As shown in Fig. 15, the average ratio and standard deviation of the calculated to the FE predicted were 0.827 and 0.045, respectively, indicating that the PSD method was very conservative .

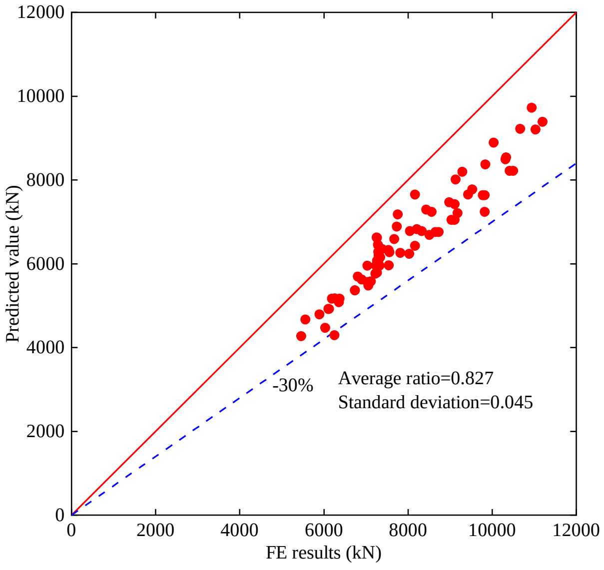

Fig. 15 Comparison between FE results and computation results from PSD method

4.2. Proposed model

Based on the above-mentioned calculation results, the PSD method was too conservative due to the unconsidered confinement from the steel tube and diagonal ribs to the concrete. Therefore, in this section, the axial load capacity for the joint zone was calculated based on the confined concrete theory [27]. It was assumed that the arching action acted in the form of second-degree parabolas with an initial tangent angle of 45° both in the horizontal and vertical directions. Both diagonal ribs and steel tubes were considered to not only confine the concrete through horizontal tensile stress, but also carry vertical forces through longitudinal compressive stress.

The axial load capacity of the joint zone (N_j) was calculated as:

$$N_j = A_c\sigma_{cc} + A_{tj}\sigma_{tv} + A_{sj}\sigma_{sv} + N_{jb} \tag{2}$$

$$\sigma_{cc} = \begin{cases} f_c'\left(-1.254 + 2.254\sqrt{1 + 7.94\dfrac{f_r'}{f_c'}} - 2\dfrac{f_r'}{f_c'}\right), & f_c' \le 50\text{MPa}^{[24]} \\ f_c'\left(-0.413 + 1.413\sqrt{1 + 11.4\dfrac{f_r'}{f_c'}} - 2\dfrac{f_r'}{f_c'}\right), & f_c' \ge 50\text{MPa}^{[25]} \end{cases} \tag{3}$$

$$f_r' = k_e f_r \tag{4}$$

Where σ_{cc} is the compressive strength of confined concrete. σ_{cc}, σ_{tv} and σ_{sv} are the compressive strength of confined concrete and the vertical compressive stress of the steel tube and diagonal rib, respectively. N_{jb} is the load capacity provided by the RC beam. f_r' and f_r are the effective confinement stress and confinement stress, respectively. k_e is the confinement effectiveness coefficient.

For Zone I, the confinement stress was provided by the joint steel tube with holes and diagonal ribs. The effectively confined zones were shown in Fig. 16. Note that the beam longitudinal reinforcements were mainly used to resist the bending moment and thus their confining effect was ignored. Therefore, the effective confinement stress was calculated by

$$f_r' = k_{ev}k_{eh} f_r \tag{5}$$

Where k_{ev} is the vertical confinement effectiveness coefficient of Zone I. k_{eh} is the horizontal confinement effectiveness coefficient for the square steel tube with diagonal ribs.

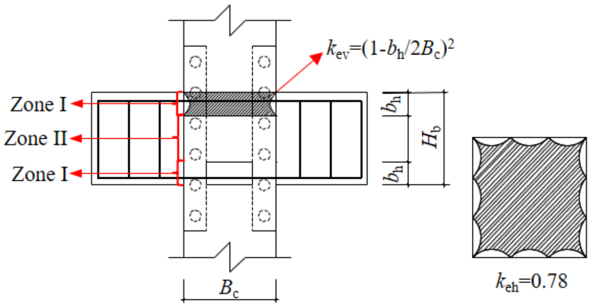

Fig. 16 Effectively confined zones

The confinement stress f_r from the diagonal ribs stiffened square steel tube with holes was calculated by:

$$2\sigma_{th}t_t(1-\rho) + 2\sigma_{sh}\cos 45^\circ t_s\left(1-\frac{d}{s}\right) = f_r\left(B_c - 2t_t\right) \tag{6}$$

Where σ_{th} and σ_{sh} are horizontal tensile stress of the steel tube and diagonal rib. d and s are the diameter and spacing of the holes on one diagonal rib, respectively. ρ is the hole ratio.

According to Sakino et al. [28], the vertical compressive stress (σ_{tv}) and horizontal tensile stress (σ_{th}) of the steel tube were taken as $0.89f_{yt}$ and $0.19f_{yt}$, respectively, which satisfied the von Mises criteria since the steel tube yielded at the peak load. Analogously, the vertical compressive stress of diagonal ribs σ_{sv} and σ_{sh} were respectively taken as $0.89f_{ys}$ and $0.19f_{ys}$ due to no local buckling.

The load capacity provided by the RC beams was [16]

$$N_{jb} = \beta f_c' \alpha n b_h B_b \tag{7}$$

Where β is the uneven distribution coefficient of the concrete compressive stress of the diffusion cross-section and is taken as 0.33. α is the diffusion angle of local compression and is taken as 0.5. n is the number of orthogonal beams. B_b and b_h is the beam width and hole height.

As shown in Fig. 17, the average ratio and standard deviation of the calculated to the tested and FE predicted is 0.988 and 0.064, respectively. Therefore, the proposed axial load capacity equations well predicted the strength of the joint zone stiffened by diagonal ribs.

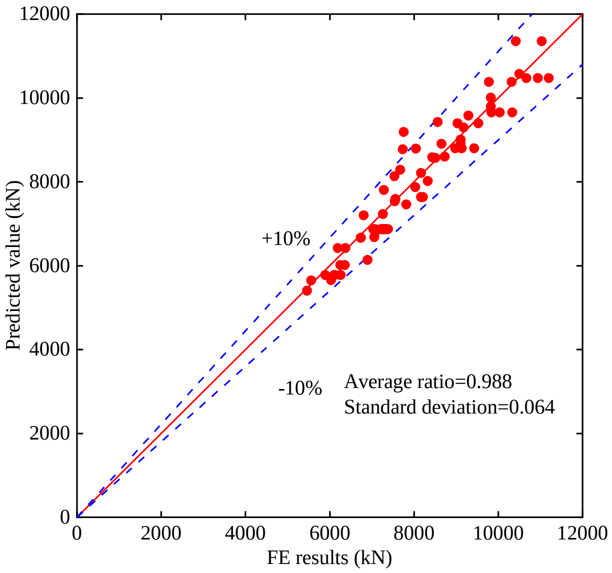

Fig. 17 Comparison between FE results and predicted results from proposed model

5. Conclusions

In this work, the feasibility of square CFST column to RC beam joints stiffened by diagonal ribs was carried out, and the axial compression behavior of the joints was studied through FE analyses. The following conclusions can be drawn:

(1) Two failure modes, namely joint failure and column failure, were observed based on parametric analyses. The results showed that the increase of material strength enhanced the joint strength linearly, while not affected the failure mode; the thickness of the diagonal rib and hole ratio affected both the joint strength and the failure mode.

(2) The strong-joint weak-componen can be achieved without conducting calculation once the following joint details were satisfied, namely the diagonal rib was welded at 1/4 to 1/3 times the column width (i.e., b =1/4B_c-1/3B_c), the hole ratio was larger than 0.5 while smaller than 0.9 (i.e., the hole area to the beam cross-sectional area ratio ρ = 0.5-0.9), the thickness of the diagonal rib was the same as that of the steel tube, the spacing between two adjacent holes was no less than 2.25 times of the hole diameter (i.e., $s \geq 2.25d$), and the hole diameter was within 0.2-0.7 times the diagonal ribs width (i.e., d = 0.2-0.7b_s).

(3) The plastic stress distribution (PSD) method was found to be very conservative with the average ratio and standard deviation of 0.827 and 0.045, respectively, as the confinement from the steel tube and diagonal ribs to the concrete was ignored. Based on the confined concrete theory, the mechanics-based models were proposed and agreed well with the FE results with the average ratio and standard deviation of 0.98 and 0.064, respectively.

Acknowledgements

The authors greatly appreciate the financial support provided by the National Natural science Foundation of China (Nos. 51878097 and 52208167). However, the opinions expressed in this article are solely the authors' own.

References

[1] Han L.H., Li W, Bjorhovde R., "Developments and advanced applications of concrete-filled steel tubular (CFST) structures: Members", Journal of Constructional Steel Research. 100, 211–228, 2014.

[2] Kang X.J., Liu Y.H., Zhao L., Yu Z.X., Zhao S.C. and Tang H., "Dynamic response analysis method for the peak value stage of concrete-filled steel tube beams under lateral impact", Advanced Steel Construction. 15, 329–337,2019.

[3] Liu S.W., Liu Y.P., Chan S.L., "Advanced analysis of hybrid steel and concrete frames: Part 1: Cross-section analysis technique and second-order analysis", Journal of Constructional Steel Research. 70, 326–336, 2012.

[4] Liu S.W., Liu Y.P., Chan S.L., "Advanced analysis of hybrid steel and concrete frames: Part 2: Refined plastic hinge and advanced analysis", Journal of Constructional Steel Research. 70, 337–349, 2012.

[5] Wang D.S. and Zhou J.L., "Development and prospect of hybrid high-rise building structures in China", Journal of Building Structures (in Chinese). 31, 62–70, 2010.

[6] Yu H. and Zha X.X., "Seismic behavior of CFST column to beam joint without welding in construction field: experiment and FE analysis", Industrial Construction (in Chinese). 41, 15–19, 2011.

[7] Nie J.G., Wang Y.H., Tao M.X., "Research and optimization on laminated steel tube column-concrete beam joints with outer stiffening ring", Sci. China Technol. Sci. 56, 1282–1293, 2013.

[8] Nie J.G., Bai Y., Cai C.S., "New Connection System for Confined Concrete Columns and Beams. I: Experimental Study", Journal of Structural Engineering. 134, 1787–1799, 2008.

[9] Tang X.L., Cai J., Chen Q.J., Liu X.P. and He A., "Seismic behaviour of through-beam connection between square CFST columns and RC beams", Journal of Constructional Steel Research. 122, 151–166, 2016.

[10] Chen Q.J, Cai J., Bradford M.A., Liu P.X. and Wu Y., "Axial Compressive Behavior of Through-Beam Connections between Concrete-Filled Steel Tubular Columns and Reinforced Concrete Beams", Journal of Structural Engineering. 141, 04015016, 2015.

[11] Zhou X.H., Li B.Y., Gan D., Liu J.P.and Chen Y.Frank., "Connections between RC beam and square tubed-RC column under axial compression: Experiments", Steel and Composite Structures. 23, 453–464, 2017.

[12] Zhou X.H., Cheng G.Z., Liu J.P., Gan D. and Chen Y.Frank, "Behavior of circular tubed-RC column to RC beam connections under axial compression", Journal of Constructional Steel Research. 130, 96–108 ,2017.

[13] Chen. F., Li G.C., Zhang L. and Yang Z.J., "Experimental and numerical investigation on seismic performance of ring-beam connection to gangue concrete filled steel tubular columns", Advanced Steel Construction. 18, 506–516, 2022.

[14] Yuan H.X., Wu Z.K., Du X.X., Guo J.C., Wen S.Q. and Wen Y.J., "Experimental study on structural performance of joint between RC beam with continuous reinforced bars and CFST column with rectangular openings", Engineering Journal of Wuhan University (in Chinese). 55, 356–365, 2022.

[15] Gan D., Zhou Z., Zhou X.H. and Tan K.H., "Seismic Behavior Tests of Square Reinforced Concrete–Filled Steel Tube Columns Connected to RC Beam Joints", Journal of Structural Engineering. 145, 04018267,2019.

[16] Gan D., Zhao Z.X., Zhou Z. and Zhou X.H, "Axial compression behavior of reinforced concrete beam to square thin-walled concrete-filled steel tube column joints stiffened by internal diaphragms", Structural Concrete. 18, 2022.

[17] Zhou Z., Gan D., Zhou X.H, "Cyclic-shear behavior of square thin-walled concrete-filled steel tubular columns with diagonal ribs", Engineering Structures. 259, 114177, 2022.

[18] Zhou Z., Gan D., Zhou X.H., "Improved Composite Effect of Square Concrete-Filled Steel Tubes with Diagonal Binding Ribs", Journal of Structural Engineering. 145, 04019112,2019.

[19] GB 50010-2010: Code for design of concrete structures 2010., Minstry of Housing and Urban-Rural Development of the People's Republic of China, Beijing, China, 2016.

[20] CEB: CEB-FIP Model Code 1990., Thomas Telford Services Lt, Lausanne, Switzerland, 1993.

[21] ACI 318M-08: Building Code Requirements for Structural Concrete, American Concrete Institute, Detriot(Michigan), America, 2019.

[22] Gan D., Zhou Z., Yan F. and Zhou X.H., "Shear Transfer Capacity of Composite Sections in Steel Tubed-Reinforced-Concrete Frames", Structures. 12, 54–63, 2017.

[23] Zhou X.H., Zhou Z., Gan D., "Analysis and design of axially loaded square CFST columns with diagonal ribs", Journal of Constructional Steel Research. 167, 105848, 2020.

[24] Eurocode 4: Design of composite steel and concrete structures. Part 1.1: General rules and rules for building.European Committee for Standardization, Brussels: CEN, 2004.

[25]Specification for structural steel buildings, American Institute of Steel Construction, Chicago, USA, 2016.

[26] Yang C., Yu Z.X., Sun Y.P., Zhao L. and Zhao H., "Axial residual capacity of circular concrete-filled steel tube stub columns considering local buckling", Advanced Steel Construction. 14, 18, 2017.

[27] Mander J.B., Priestley M.J.N., Park R., "Theoretical Stress-Strain Model for Confined Concrete", Journal of Structural Engineering. 114, 1804–1826,1988.

[28] Sakino K., Nakahara H., Morino S. and Nishiyama I., "Behavior of Centrally Loaded Concrete-Filled Steel-Tube Short Columns", Journal of Structural Engineering. 130, 180–188, 2004.

Advanced Steel Construction – Vol. 19 No. 1 (2023) 46–51
DOI:10.18057/IJASC.2023.19.1.7
(**Special Issue:** *10^{th} International Conference on Advances in Steel Structures, ICASS'2020, Chengdu, China*)

STUDY ON FIRE RESISTANCE OF BOX-TYPE COMPOSITE WALLS

Yan-Qing Fu [1, 2], Qing-Qing He [3], Guang-Chong Qin [3], Tao Lan [3, *] and Ran Li [3]

[1] Southwest Jiaotong University, Sichuan, China
[2] Central Research Institute of Building and Construction Co., Ltd, MCC Group, Beijing, China
[3] China Shipbuilding Industry Corporation International Engineering Co., Ltd., Beijing, China
[*] (Corresponding author: E-mail: qd_lantao@163.com)

ABSTRACT

The fire resistance limit value of box-type composite walls is one of the important parameters for applying this system. To this end, this article selects different refractory structural measures for the composite wall and analyzes the parameters in each part of the fire-resistant structure, including rock wool thickness, keel spacing, number of opening rows in the keel, gypsum board layers and thickness, etc. The results show that the thickness of rock wool, gypsum board layers and thickness, type of cladding plates and the number of layers, the axial compression ratio have significant influence on the fire endurance. The keel distance and the number of openings rows are almost unaffected. Based on the above analysis, the fire resistance optimization design method and fire resistance calculation formulas of the composite wall are proposed to provide theoretical support for the fire protection design of the box-type steel structural system.

ARTICLE HISTORY

Received:	20 July 2022
Revised:	22 August 2022
Accepted:	10 January 2023

KEYWORDS

Box-type steel structure;
Fire resistance;
Parametric analysis;
Fire resistant optimization design

1. Introduction

In the seismic structural system, steel plate shear walls, as the lateral force-resisting member, have advantages of lightweight, good ductility and powerful energy consumption capability, which play a pivotal role in the safety of structural system. To follow the development trend of the construction industry, combining the design concept of assembled steel structure and steel plate walls, the box-type assembled steel structural system emerges as the times require, the structural system is shown in Fig.1. The box-type assembled steel structural system consists of the stiffening plate which is not constrained by the peripheral frame, with advantages of production industrialization, assembled construction, etc. In particular, as a novel type of assembled steel structural system, this structure can give full play to the advantage of steel material and assembled structure, reduce the construction time greatly, and has been applied to the practical engineering.

Through the experimental study of module units and shaking table of box-type assembled steel structural system, it has been found that this structural system has good ductility and seismic performance under seismic load by Lan and Men [1]~[3]. In the module unit experiment, when the corners of the structure are reinforced, the ductility and bearing capacity of the structure is improved greatly. In the shaking table experiment, the maximum elastic-plastic story drift angle of this structure is 1/52 under the 9th intensity rare earthquake, which meets the requirement of the code of seismic design for buildings (GB 50011-2010) [4], indicating the excellent seismic performance. However, this structural system is a pure steel structure with poor fire resistance, for the popularization and application of this structure system, the effect of fire on buildings can't be ignored.

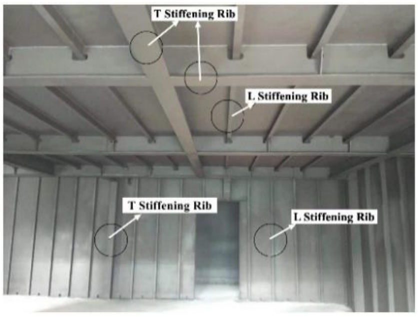

Fig. 1 Box-type assembled steel structural system

For these reasons, this paper will conduct the relevant analysis and research on the fire-resistance of box-type assembled composite walls, including the design of fire-resistance structure and finite element analysis of the fire resistance. Finally, based on the analysis result, a method for designing the fire-resistant of composite walls is presented, which provides the basis for the application of the box-type steel structural system.

2. Structural design for fire resistance

2.1. Structural design and stress mechanism

2.1.1. Structural design for composite walls

This paper mainly analyzes the fire-resistance of the box-type assembled composite wall under the one-side fire, the specimen is shown in Fig. 2.In the figure, a joist steel beam with large stiffness is set at the top of the wall, which is used to simulate the uniform load transferred by the floor. Additionally, considering the effect of partial fixing, the box-section ground beam is set at the bottom of the wall.

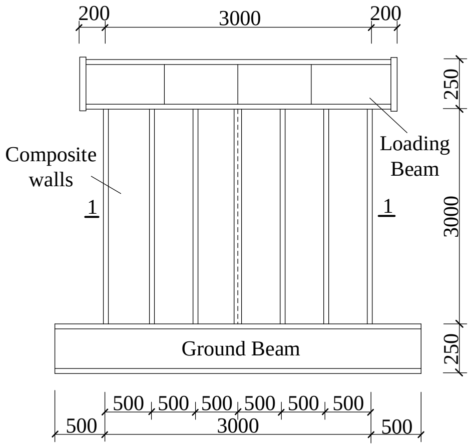

(a) Front elevation of specimens

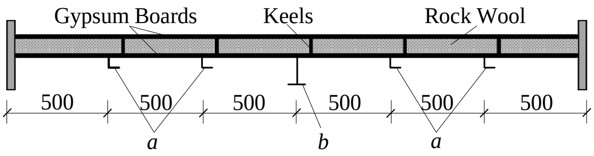

(b) 1-1 Section

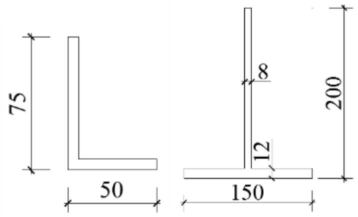

(c) Size of stiffeners (a and b)

Fig. 2 Fire-resistance structure of box-type assembled composite walls.

2.1.2. Stress mechanism of composite walls

Steel plate walls are divided into thick steel plate walls and thin steel plate walls. In literature [5], Zhao provided the stress mechanism of steel plate walls, for thick steel plate walls, it occurred shear deformation under seismic load, and formed the tensile band. The effect of stiffeners is to restrict the deformation of steel plate, until the tensile band reached the ultimate strength. Thick steel plate walls occurred shear failure, the failure deformation is shown in Fig. 3(a). For thin steel plate walls, its failure mode is the same as thick steel plate walls, when concrete slabs are covered on the steel plate wall. The tensile band is mainly distributed in the area enclosed by the concrete slab and the stiffener, the failure deformation is shown in Fig. 3(b).

(a) Thick steel plate walls (b) Thin steel plate walls

Fig. 3 Failure modes of specimens

2.2. Proposal for fire-resistant structure

The fire-resistant structural design of composite walls mainly includes: the covering thickness, the keel distance and row numbers of openings, types of cladding plates, the thickness of walls and the number of stiffeners. The details are as follows:

(1) Design of covering thickness. The covering thickness is mainly related to the layer numbers and thickness of the filling material and the cladding plate. If the covering thickness is too thin, the protective layer is easy to fall off under fire condition, leading to contact directly between steel and fire, and reducing the safety of members. Therefore, in designing the fire-resistant structure, the thickness and layer numbers of rock wool and gypsum board, which are used as filling material and cladding plates, should be chosen reasonably.

(2) Keel distance and row numbers of openings. In the fire-resistant structure, the presence of lightgage steel joist can keep the stability of walls under fire load, but the fire resistance of composite wall is greatly reduced. To reduce this influence on the fire resistance, opening in the keel reasonably is crucial.

(3) Types of cladding plates. When selecting the cladding plate, the fire resistance, applicability and economy of the material must be considered. Common materials include fire-retardant gypsum boards (FRGB), glass magnesium boards (GMB), as well as calcium silicate boards (CSB). Analyze the fire resistance of composite walls of the three-faced board, and select the appropriate cladding plates.

(4) Depth-thickness ratio and number of stiffeners. The load of the box-type composite wall is mainly subjected by steel plates and stiffeners. Stiffeners limit the deformation of the steel plate, but also bear horizontal shear force. Therefore, determining the appropriate depth-thickness ratio and the number of stiffeners is critical to the fire resistance of composite wall.

3. Analysis of fire resistance

3.1. Judgment standard for fire resistance

According to "The Fire Resistance Design Of Steel Structure And Steel-concrete Composite Structure" [6], there are two judgment standard for reaching the fire resistance of composite wall[7]. The first is the out-plane deformation rate of the wall exceeds the specified limit l2/15hx; the second is the out-plane displacement of the wall reaches l/800hx, which l is the length of the wall(mm); hx is the section height of the wall(mm).

3.2. Establishment of finite element model

In the establishment of finite element models, the C3D8R element was used for rock wool plate, cladding plate and steel plate, S4R element was used for keel, and the calculation model proposed by Lie and Chabot[8]was used for constitutive relation of steel. The test method refers to "The Fire-resistance Tests-elements Of Building" (GB/T 9978-2008)[9], two analysis steps are set up in the finite element analysis. In the first step, the constant axial load N at the top of the wall is applied to the rigid beam in the form of equivalent uniformly distributed load. In the second analysis step, the ODB result file obtained from the temperature field analysis was imported into the mechanical model for thermodynamic coupling calculation, and the fire resistance limit was solved. The bottom of the specimen was completely consolidated; the initial temperature was set at 20°C.

In order to verify the reliability of the above model, finite element simulation was carried out on some specimens of the fire resistance test[10] and the simulated values were obtained and compared with the experimental values, as shown in Table 1. The maximum deviation was 8.1%, and the minimum deviation was 4.3%, which was small enough to indicate that the above model could be used in subsequent fire resistance research.

Table 1

Comparison of fire resistance with simulated value and test value

Specimen number	Construction measures（from the fire surface to the backfire surface）					Fire resistance（min）		
	B1 layer	B2 layer	Keel	B3 layer	B4 layer	Test value	Simulated value	Deviation
S1	FRGB	FRGB	C89	FRGB	FRGB	71	67	-5.6%
S2	FRGB	GMB	C140	GMB	FRGB	94	90	-4.3%
S3	FRGB	GMB	C89	GMB	FRGB	98	90	-8.1%
S5	CSB	CSB	C89	CSB	CSB	58	62	6.8%

3.3. Stress distribution and failure mechanism

To study the stress distribution and failure mechanism of composite walls under fire condition. According to the technical specification for concrete structures of tall buildings (JGJ 3-2010)[11], the shear wall was designed with an axial compression ratio limit of 0.5. It was compared with axial compression ratio of 0.2 and 0.8. Specimen parameters were shown in Table 2, which a1, a2 is the thickness of FRGB on the fire surface and the backfire surface, respectively; n is the axial compression ratio.

Table 2

Parameters of specimens

Specimen number	Thickness of rock wool(mm)	Keel distance(mm)	Thickness of FRGB		Axial compression Ratio, n
			a1(mm)	a2(mm)	
Q1	100	60	10	10	0.2
Q2	100	60	10	10	0.5
Q3	100	60	10	10	0.8

The stress distribution of specimens with different axial compression ratio is shown in Fig. 4. When the axial compression ratio n is 0.2 (Fig. 4a), the deformation of the entire steel plate is like a pumpkin, the plastic yield mainly distributes symmetrically in the four corners. Stress concentration occurs in the area near the loading beam and the bottom fixed end. The stress of the steel plate, L-type and T-type stiffeners is relatively small. For the edge constrained steel plate, since the constrained steel plate is not a load-bearing member, and the model only considers the internal heat conduction effect, the stress in the area near the edge restrained steel plate not closed to the end is little.

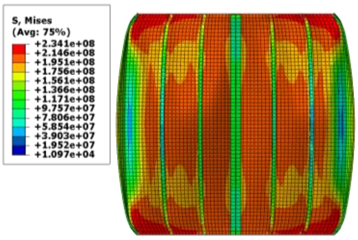

(a) n=0.2

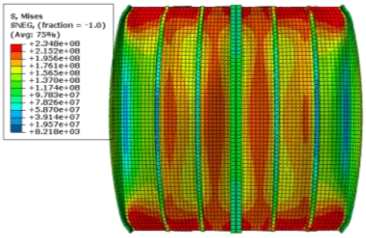

(b) n=0.5

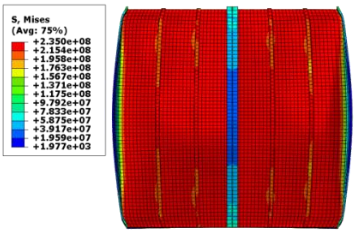

(c) n=0.8

Fig. 4 Stress distribution of composite walls

When the axial compression ratio n is 0.5 (Fig. 4b), the stress concentration area at the upper and lower end of the wall increases, and gradually extends from the corner to the middle of the steel plate. The stress in the middle of the wall is great, but the stress of the L-type and T-type stiffener is still little.

When the axial compression ratio n is 0.8 (Fig. 4c), the stress concentration area of the specimen develops from the end to the whole wall, the stress of the T-type stiffener is still small, but the stress of steel plate and L-type stiffeners increases and the yield is uniform. The edge steel plate is mainly deformed by expansion, but the stress near the edge steel plate increases greatly, and the whole wall almost reaches the yield strength.

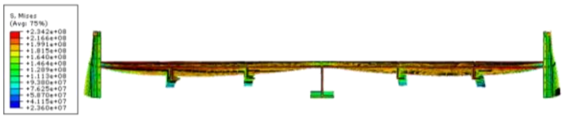

(a) n=0.2

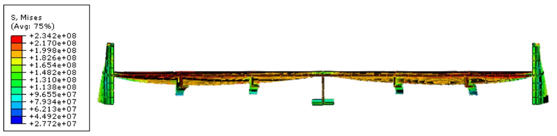

(b) n=0.5

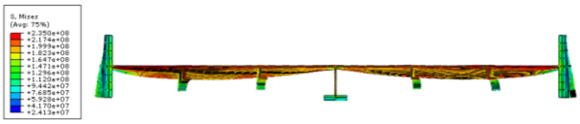

(c) n=0.8

Fig. 5 Deformation of composite walls with different axial compression ratio

The deformation of composite walls with different axial compression ratio as shown in Fig. 5, the deformation of the steel plate was symmetrically distributed along the axis of T-type stiffener. On the initial heating stage, the steel plate of composite walls bulged, the L-type stiffener bent, but the T-type stiffener had almost no distortion. With the increase of heating time, the lateral displacement in the upper end of steel plates increased. Finally, the deformation of the steel plate reached the limit, the composite wall was damaged.

3.4. Parametric analysis

The fire resistance of composite wall is affected by various parameters, such as the thickness of rock wool and keel distance, etc. In order to research the influence of various parameters on the fire resistance of composite walls, select the main parameters to analyze the fire resistance. The values of the main parameters are shown in table 3, which a1, a2 is the thickness of cladding plates on the fire surface and the backfire surface, respectively; b1, b2 is the layer number of FRGB on the fire surface and the backfire surface, respectively.

Table 3
The value of specimen parameters

The main parameters	The value
Thickness of rock wool（mm）	50, 100, 150
Keel distance（mm）	No keel, 1000, 600
Layer numbers of FRGB b1+b2（layer）	1+1, 1+2, 2+1, 2+2
Row numbers of opening(row)	1, 3, 5, 7
Thickness of cladding plates a1+a2（mm）	10+10, 10+12, 10+15, 12+10, 15+10
Types of cladding plates	FRGB、GMB、CSB
Depth-thickness ratio	300, 400, 500, 600

3.4.1. Thickness of rock wool

The relationship between the thickness of rock wool and fire resistance is shown in Fig. 8. As the thickness of rock wool increases, the fire resistance of composite walls increases. When the thickness of rock wool exceeds 100mm, the straight slope increases from 0.62 to 1.62, and the fire resistance increases more. Increasing the thickness of rock wool can effectively improve fire resistance. When the thickness of rock wool exceeds 100mm, the effect of increasing the fire resistance is better.

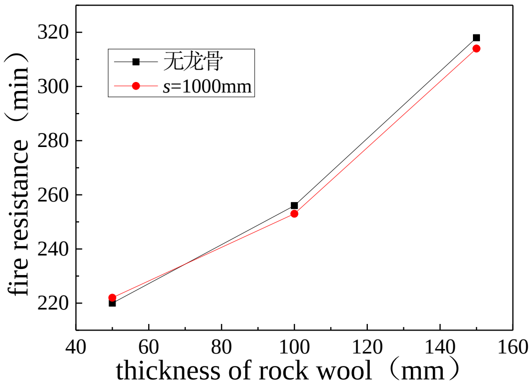

Fig. 6 Relationship between thickness of rock wool and fire resistance

3.4.2. Keel distance

The relationship between keel distance and fire resistance is shown in Fig. 7. With the increase of keel distance, the fire resistance gradually decreases, but the range is little, which means that the influence of keel distance on the fire resistance is little. In practical engineering, considering the convenience of construction and the size of walls, the recommended value for keel distance is 600 mm, which does not affect the use of the building but also can meet the requirements of fire resistance.

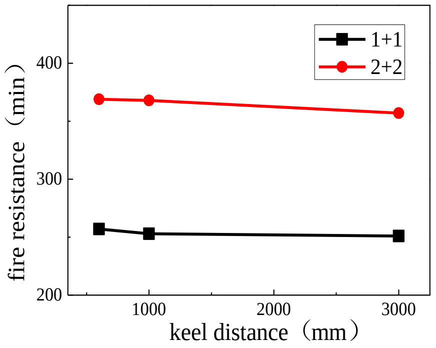

Fig. 7 Relationship between the keel distance and fire resistance

3.4.3. Layer numbers of gypsum boards

The fire resistance of specimens with different layer numbers of gypsum boards is shown in table 4, which b1, b2 is the layer number of cladding boards on the fire surface and the backfire surface, respectively, and c is the thickness of rock wool. It can be seen that as the layer number of gypsum boards increases, the fire resistance of specimens increases. When the total layers of gypsum boards are unchanged, The more gypsum boards layers on the fire surface, the more improvement of fire resistance. Therefore, it can be seen that increasing layer numbers of gypsum boards is economic and effective measures to improve fire resistance.

Table 4

The fire resistance of specimens with different layer numbers of gypsum boards

Layer numbers of FRGB b1+b2（layer）	Fire resistance（min）	
	c=100mm	c=150mm
1+1	257	359
1+2	309	363
2+1	335	387
2+2	368	483

3.4.4. Row numbers of keel openings

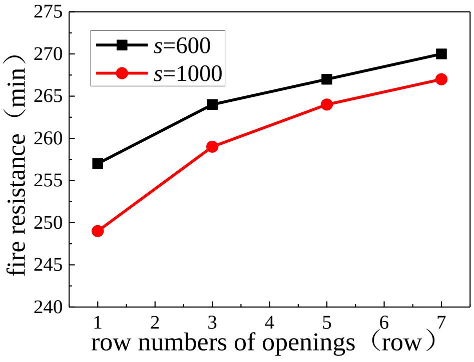

Fig. 8 Relationship between row numbers of openings and fire resistance

The relationship between row numbers of keel openings and the fire resistance is shown in Fig. 8. As the row number of keel openings increases, the fire resistance of specimens increases. When the keel distance s is 600mm, and the row number of keel openings m exceeds 5, the effect on the fire resistance is not obvious, although the heat conduction path of the keel is extended. When the keel distance s is 1000mm, the fire resistance is the same as when keel distance is 600mm. Therefore, in the practical application, we should pay attention to the selection of appropriate keel opening row, avoid too much keel opening.

3.4.5. Thickness of gypsum boards

The relationship between the gypsum board thickness and fire resistance is shown in Fig. 9. Regardless of the fire surface and the backfire surface, with the thickness of gypsum boards increasing, the fire resistance of specimens increases. When the thickness of rock wool is 50 mm and 100mm, the thickness of gypsum board on backfire surface increases by 5mm, the fire resistance of specimens increases by 3.0% and 6.0% on average. When the thickness of plasterboard on fire surface increases by 5mm, the fire resistance of specimens increases by 7.0% and 9.0% on average, indicating that the thickness of plasterboard has a great influence on the fire resistance of specimens.

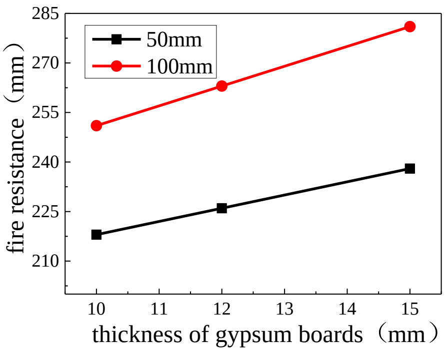

(a) the backfire surface

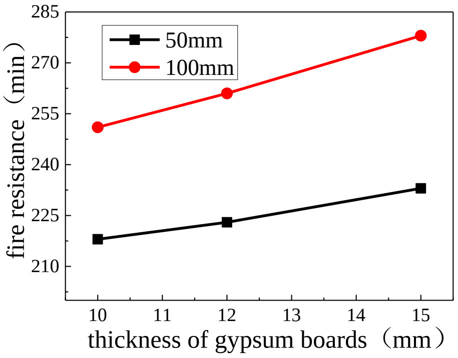

(b) the fire surface

Fig. 9 Relationship between thickness of gypsum boards and fire resistance

3.4.6. Types of cladding plates

The fire resistance of composite walls with different cladding plate is shown in table 6, which b1, b2 is the layer number of cladding boards on the fire surface and the backfire surface, respectively. It can be seen that under different layer numbers of cladding plates, the fire resistance of glass magnesium boards is greater than the other two kinds of boards, indicating that the fire resistance of glass magnesium boards is better, calcium silicate boards is second, gypsum boards is the worst.

Table 3

The fire resistance of specimens with different kinds of cladding boards

Layer numbers of cladding plates b1+b2（layer）	Fire resistance（min）		
	FRGB	GMB	CSB
1+1	257	313	261
2+1	335	367	282

In general, the fire resistance of composite walls can be effectively and economically improved by selecting high-quality cladding plates, appropriate layer numbers, and thickness of cladding plates.

3.4.7. Axial compression ratio

The relationship between the axial compression ratio and the fire resistance is shown in Fig. 12. With the axial compression ratio increases, the fire resistance of composite walls decreases. When the number of layers of gypsum boards on the fire surface and the backfire surface respectively is 1 layer and the axial compression ratio is 0.3 and 0.8, the fire resistance of specimens is 283min and 207min respectively, falling about 36%. When the numbers of layers of gypsum boards on the fire surface and the backfire surface respectively is 2 layers and 1 layer, the other situations are the same, the fire resistance of specimens is 347min and 307min respectively, falling about 13%. It can be seen that the axial compression ratio has a great influence on the fire resistance of walls, and the influence of the axial compression ratio on the fire resistance limit is weakened when layer numbers of gypsum boards increase. Therefore, in designing the fire resistance, the influence of the axial compression ratio can be reduced by increasing layer numbers of gypsum boards.

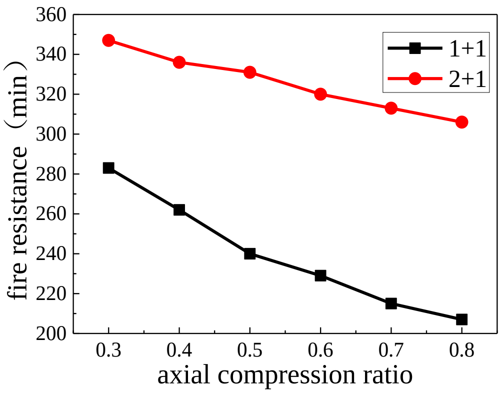

Fig. 10 Relationship between axial compression ratio and fire resistance

3.4.8. Depth-thickness ratio

The relationship between the depth-thickness ratio and the fire resistance of composite walls is shown in Fig. 11. When the depth-thickness ratio is less than 400, the fire resistance increases with the increase of depth-thickness ratio. When the depth-thickness ratio is more than 400, the fire resistance decreases with the increase of depth-thickness ratio. When the number of L-type stiffeners is 4, the influence is more obvious. It can be seen that the fire resistance can be improved by optimizing the design for the structure.

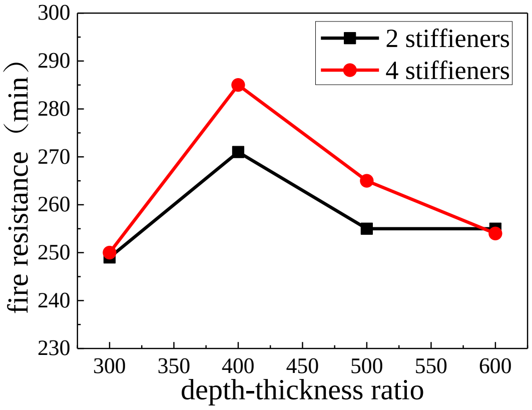

Fig. 11 Relationship between depth-thickness ratio and fire resistance

3.5. Summary analysis

As a basic specimen, its parameters are: rock wool thickness of 100mm, keel distance of 600mm, fire surface gypsum board layer number for a layer, backfire surface gypsum board layer number for a layer, thickness of 10mm, deep ratio of 375, fire resistance for 256min. The simulated value of parameter analysis was compared with the calculated value of the basic specimen to analyze the influence of different parameters on the fire resistance of the specimen, as shown in Fig. 12.

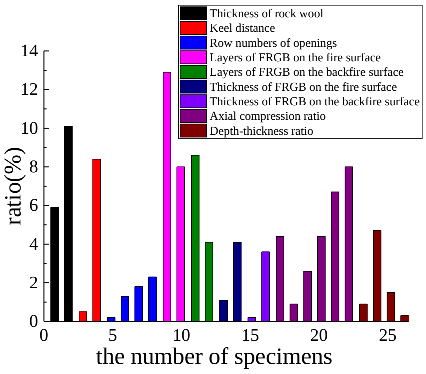

Fig. 12 The influence degree of different parameters on fire resistance

It can be seen from Fig. 12 that the thickness of rock wool, the number and thickness of plasterboard layers, and the axial compression ratio have a greater impact on the fire resistance, and the keel distance also has a certain impact. However, considering the use of building space, the number and thickness of plasterboard layers are mainly considered in the design of fire resistance, and the thickness of rock wool can be considered as appropriate.

4. Design method of fire-resistant structure

4.1. Design formula for fire resistance

The analytical result of the fire resistance of composite walls is shown in table 7. The fire-resistance design formula was proposed. According to the fire-resistance simulation values of different specimens, the fire-resistance regression equation was obtained by polynomial superposition regression analysis, as follows:

$$T_e = 113.95 + 0.92 \times h - 121.72 \times n - 0.02 \times \lambda + 65.89 \times b_1 + 39.89 \times b_2 \qquad (1)$$

which h is the thickness of rock wool, n is the axial compression ratio, λ is the depth-thickness ratio, b1 is layer numbers of gypsum boards on the fire surface, b2 is layer numbers of gypsum boards on the backfire surface; the thickness of rock wool ranges from 50mm to150mm, the axial compression ratio ranges from 0.3 to 0.8, and the depth-thickness ratio ranges from 300 to 600.

Table 7
The analytical results of the fire resistance of composite walls

Specimen number	Thickness of rock wool (mm)	Layer numbers of FRGB b1+b2 (layer)	Axial compresion ratio	Depth-thickness ratio	Fire resistance（min）		
					Simulated value	Test value	Deviation
1	50	1+1	0.3	400	222	219.66	-1.1%
2	100	1+1	0.3	400	285	265.66	4.8%
3	150	1+1	0.3	400	314	311.66	-0.7%
4	100	1+2	0.3	400	309	305.55	-1.1%
5	100	2+1	0.3	400	335	331.55	-1.0%
6	100	2+2	0.3	400	368	371.45	0.9%
7	100	1+1	0.5	400	240	241.32	0.5%
8	100	1+1	0.6	400	229	229.15	0.1%
9	100	1+1	0.7	400	215	216.98	0.9%
10	100	1+1	0.8	400	207	204.80	-1.1%
11	100	1+1	0.3	300	250	268.05	6.7%
12	100	1+1	0.3	500	265	263.28	-0.7%
13	100	1+1	0.3	600	251	260.89	2.6%

The formula is used to recalculate the fire resistance of the wall to verify the correctness. The calculated values are shown in Table 7, and the deviation is shown in Table 7 when compared with the finite element simulation values. This comparison shows that the calculated value agrees well with the simulated value, because the maximum deviation is only 6.7%. Therefore, the formula can be used to predict the fire resistance of composite walls well.

4.2. Design method for fire resistance

According to the "Code For Fire Protection Design Of Building"(The 2018 Edition) (GB 50016-2014) [12], when the fire-resistance rating is 3, the fire resistance of composite walls is not less than 120min; when the fire-resistance rating is 1, the fire resistance is not less than 180min. Therefore, in this section, based on the analytical result of the finite element, the structural design method of fire resistant is proposed, which meets the fire resistance requirement of 120min and 180min.

4.2.1. The fire resistance is 120min

Firstly, according to the "Technical Specification For Concrete Structures Of Tall Building" (JGJ 3-2010) [11], the axial compression ratio of walls in the reinforced bottom zone is 0.5, and that in other zone is 0.3, the choice of depth-thickness ratio and stiffeners must meet the serviceability limit state. Hence, 4 L-shaped stiffener ribs are selected, and the depth-thickness ratio is 400. The gypsum board is used as the wall cladding board, and the fire surface and backfire surfaces are covered with a cladding board with a thickness of 10mm. With the rock wool as the filling material, the thickness of that is 50mm. Through the above measures, the fire resistance requirement of 120min can be met. When the axial compression ratio is 0.5, the fire resistance limit calculated by formula (1) is 195min, meeting the requirement of fire resistance limit of 120min. In addition, the keel distance and row numbers of openings have little effect on the fire resistance, which can be determined according to the actual requirements.

4.2.2. The fire resistance is 180min

According to the fire-resistant structure design idea proposed in this paper, the concrete form and construction measures of fire-resistant 180min composite wall are refined. The load level, depth ratio and reinforcement design are the same as those of fire-resistant 120min.

In the design of the thickness of the cladding board, the gypsum board is used as the cladding board of the wall, and the fire surface and the backfire surface are covered with a layer of cladding board with a thickness of 10mm.With the rock wool as the filling material, its thickness is 50mm. Through the above measures, it can meet the fire resistance requirement of 180 min. When the axial compression ratio is 0.5, through increasing the layer numbers of gypsum boards on the fire surface, or using glass magnesium plates as cladding plates, it can also meet the requirements of fire resistance with 180min.

5. Conclusions

In this paper, the fire resistance structure of box-type assembled composite walls is designed and its fire resistance is analyzed by the finite element method. The effects of parameters on fire resistance were studied, such as the thickness of rock wool, the keel distance and rows of openings, the layer number and thickness of gypsum boards, types of cladding plates, the depth-thickness ratio and the axial compression ratio. The conclusions are as follows:

(1)According to the finite element analysis, among the factors affecting the fire performance, the thickness of rock wool, the number and thickness of gypsum board, and the axial compression ratio have a greater impact on the fire performance; the keel distance also has a certain influence. However, considering the use of building space, the thickness of rock wool can also be considered as appropriate when designing fire resistance. Increasing the thickness of gypsum board on fire surface can effectively improve the fire resistance limit of wall; and changing the type of covering plate is also an economic and effective measure.

(2) In this paper, the fire resistance design method of composite wall is summarized, and the formula of fire resistance calculation of wall is put forward according to the result of finite element analysis. Through the verification, the proposed formula can be used for practical engineering.

References

[1] Men J.J., He Q.Q., Lan T., Guo C.L., Jiang Z.Q., "Shaking table model test design for box-type steel structure residence", Industrial Architecture, 2018, 48(09), 9-14+82.

[2] Lan T., Guo C.L., Men J.J., He Q.Q., Zhao T., Wang L.Y., "Shake table model test of prefabricated box-type steel structure house", Industrial Architecture, 2018, 48(09), 1-8.

[3] Lan T., Song Z., Men J.J., Zhao T.Z., Zhao T., Wang L.Y., "Experimental study on seismic performance of box-type steel structure modules reinforced with reinforced corners", Industrial architecture, 2018, 48 (09), 15-21.

[4] GB 50011-2010, Code of seismic design for buildings 2016, Ministry of Housing and Urban-Rural Development of the People's Republic of China, Beijing, China, 2016.

[5] Zhao T.T., "Study on seismic performance of wall in bottom reinforced area of box-plate steel structure residence", Xi'an University of Architecture & Technology, 2018.

[6] Li G.Q., Han L.H., Lou G.B., Jiang S.C., Fire resistance design of steel structure and steel-concrete composite structure, China, 2006.

[7] Li G.Q.et al, Steel structure resistance calculation and design, China, 1999.

[8] T. T. Lie, M. Chabot, "Method to predict the fire resistance of circular concrete filled hollow steel columns", Journal of Fire Engineering, 1990, 2(4), 111-126.

[9] GB/T 9978-2008, Fire-resistance tests-elements of building, Ministry of Housing and Urban-Rural Development of the People's Republic of China, Beijing, China, 2008.

[10] Chen W., "Fire resistance test and theoretical research of cold-formed steel bearing composite wall", Southeast University, 2014.

[11] JGJ 3-2010, Technical specification for concrete structures of tall building, Ministry of Housing and Urban-Rural Development of the People's Republic of China, Beijing, China,2010.

[12] GB 50016-2014, Code for Fire Protection Design of Building 2018, Ministry of Housing and Urban-Rural Development of the People's Republic of China, Beijing, China, 2018.

Advanced Steel Construction – Vol. 19 No. 1 (2023) 52–69
DOI:10.18057/IJASC.2023.19.1.8
(**Special Issue:** *10^{th} International Conference on Advances in Steel Structures, ICASS'2020, Chengdu, China*)

BEHAVIOR OF WEB PERFORATED COLD-FORMED STEEL BEAMS UNDER COMBINED BENDING AND SHEAR ACTION

Li-Ping Wang [1, 2, *], Jian Li [1], Xing-Xing Cao [1], Dong-Hui Wen [3] and Hai-Bo Wang [4]

[1] *School of Civil Engineering, Central South University, Changsha 410075, PR China*
[2] *Engineering Technology Research Center for Prefabricated Construction Industrialization of Hunan Province, Changsha, 410075, PR China*
[3] *Department of Architecture and Environmental Engineering, Taiyuan University, Taiyuan 030032, PR China*
[4] *Hunan Tieyuan Civil Engineering Testing Co., Ltd, Changsha 410075, PR China*
* *(Corresponding author: E-mail: wlp2016@csu.edu.cn)*

ABSTRACT

To cater engineering application needs, cold-formed steel (CFS) members often have some web openings which could influence bearing capacity of the steel beam under combined bending and shear action. This paper presents tests on 20 groups of thin-walled web-perforated lipped C-shaped CFS beams, which were conducted under single point loading mode at mid-span. Besides, detailed finite element parameter analysis on the high shear-span ratio (a/h= 1.5 ~ 4.0) specimens was conducted by ABAQUS after the model was verified, which was mainly focused on the influences of different hole depth-to-web height ratios (d_h/h) and web height-to-thickness ratios (h/t) on the bearing capacity and failure modes of the beams. Based on the results of test and FEA, the mechanical behavior and failure rules of thin-walled web perforated lipped C-shaped CFS beams under combined bending and shear action were deeply studied.

ARTICLE HISTORY

Received: 20 July 2022
Revised: 22 August 2022
Accepted: 10 January 2023

KEYWORDS

Cold-formed steel;
Combined action of bending and shear;
Web openings

1. Introduction

The thin-walled web-perforated CFS members are commonly used in practical engineering applications to provide convenience for the installation of pipeline facilities and to achieve efficient use of story height. However, the web opening will result in an unfavorable effect in the mechanical performance of the members. A series of research had been done on the behavior of web-perforated CFS members. From 1994 to 1997, Langan et al. [1-3] carried out experimental and theoretical research on web perforated flexural CFS members, a series of shear capacity design formulas for CFS members with web perforations (including circular holes and non-circular holes) were proposed, which have been adopted in AISI S100 [4] and AS/NZS 4600 [5]. Through experimental and theoretical research on thin-walled CFS flexural and compression members, Schafer et al. [6-9] put forward a new method taking interactive buckling of plates into consideration to calculate the bearing capacity of thin-walled CFS members, namely the direct-strength-method (DSM). In 2004, the direct-strength-method (DSM) was adopted by the AISI S100 [4]. In 2008, Moen et al. [10-13] proposed the modified DSM formula for CFS beams with web openings after experimental and theoretical research on web-perforated CFS flexural members. In 2012, on the basis of test results of plain lipped CFS members with C-shaped and Supa-Cee section, Pham and Hancock [14] proposed specific DSM for C-shaped steel beams in shear and in combined bending and shear action, in which the influence of tension field action was considered. In 2014, Keerthan et al. [15,16] conducted test and FEA on the hollow flange channel beams under combined bending and shear action, and proposed the lower bound equation applicable to the section form. In 2015, by means of test and FEA, Faridmehr [17] et al. studied behavior of C-channel stiffened CFS beams subjected to the bending and the primarily shear conditions, verified the effectiveness of the stiffening design, and pointed out the conservatism of M-V interaction design method in AISI. For double limb built-up section CFS bending members, Young and Wang [18,19] carried out series of tests and FEA studies during 2015 to 2017, and extended the rules of DSM for these members with the effect of openings and screws considered. During 2018 to 2019, Pham [20,21] et al. used a new experiment setup to minimize effect of applied bending moment in shear span, so as to study shear capacity of CFS beams in higher aspect ratios, and the results from test were recalibrated with the theoretical calculation results of the DSM in AISI and AS/NZS. Degtyareva et al. [22] conducted FEA on thin-walled CFS bending members with staggered slotted web perforations under combined bending moment and shear force action in 2019, and put forward specific equations for the bearing capacity of this kind of members. For C-shaped web perforated beams, Lawson et al. [23] proposed a derived formula for calculating the additional deflection, and compared the calculating results with those of tests and FEA. In 2020, based on the test results of rectangular and slotted web perforations of high-strength CFS beams, Pham et al. [24] proposed a modified formula for the DSM design for this kind of members. In 2022, Wang et al. [25] conducted tests on 26 groups of thin-walled web-perforated CFS members with low shear-span ratio (1.0 and 1.5) and presented detailed finite element analysis, and the study was focused on the influence of holes on the shear performance of such members.

In this paper, to study the behavior of thin-walled web perforated lipped C-shaped CFS beams under combined bending moment and shear force action, tests on 20 groups of specimens were carried out, in which the single-point loading mode at mid-span section was adopted. And FEA was conducted by means of ABAQUS. The results of FEA and test were compared together, from which the accuracy of FEA model was validated. After that, by changing the hole depth-to-web height ratio and the web height-to-thickness ratio of the steel beams in relatively higher shear-span ratio (1.5 ~ 4.0), the parameter analysis was presented, and the effect of each parameter on the bending and shear performance of thin-walled web perforated lipped C-shaped CFS beams was deeply studied.

2. Experimental investigation of beams in bending and shear

2.1. Specimen design

The material of the 20 groups of specimens was all high strength zinc-coated cold-formed steel (G550), and section thickness was all 1.9 mm. Fig.1 (a) shows the dimension definition of the specimen. The specific meanings of each letter are as follow: the nominal web height is h, the nominal flange width is b_f, and the nominal lip width is b_l. Three different shear-span ratios of 2.0, 2.5 and 3.0 were designed in the test. The position of circular holes were all set at the half height of the specimen web within the shear zone, as shown in Fig.1 (b). The range of the value of d_h/h was 0 to 0.8. The label defining rules of specimen is presented in Fig. 2, in which repeated specimens are marked with R at the end of label. The dimensions of the specimen are presented in Table 1.

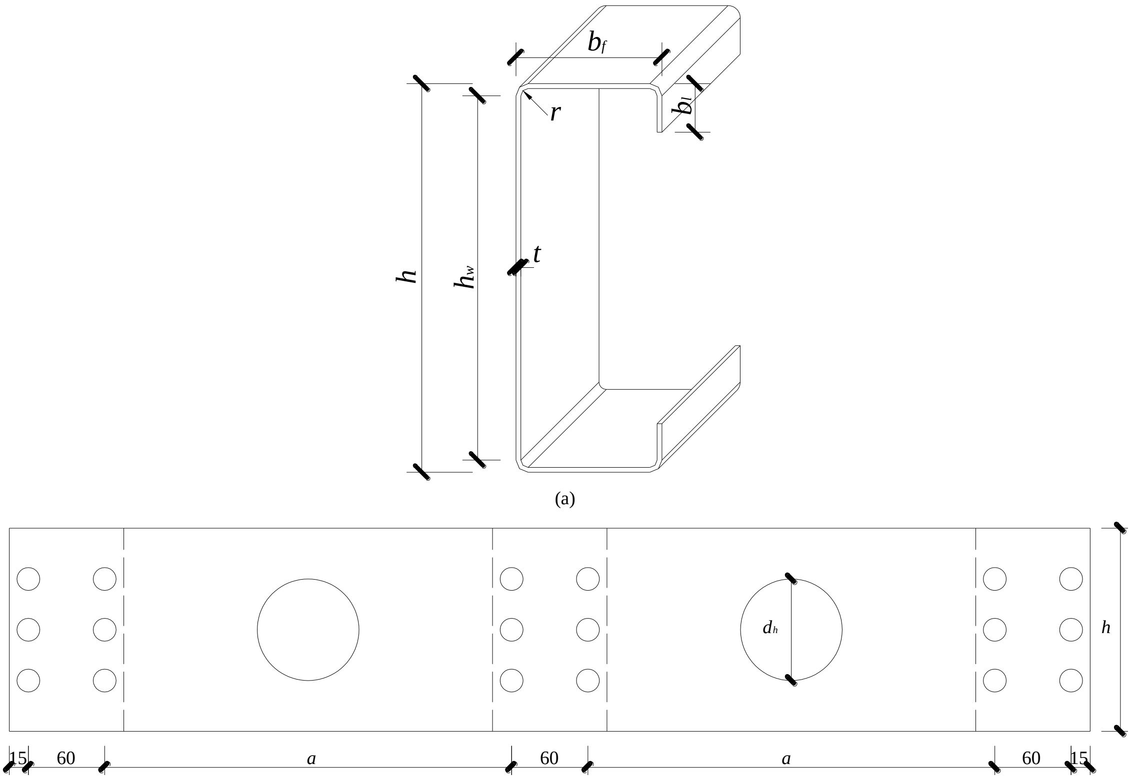

(a)

(b)

Fig. 1 Geometrical parameter definition (a) Section (b) Specimen

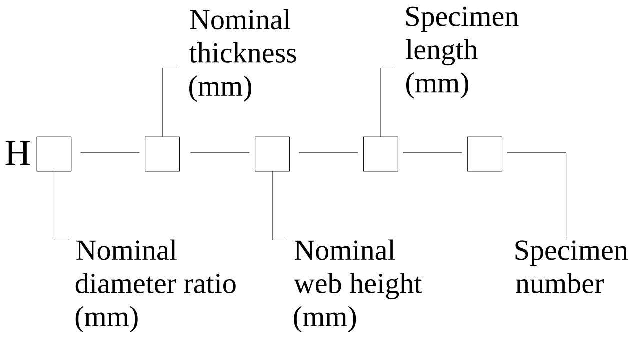

Fig. 2 Specimen labelling rules

Table 1
Geometric dimensions of specimen

Specimen	Web	Flange	Lip	Thickness	Diameter	The hole depth-to-web height ratio	The shear-span ratio	The web height-to-thickness ratio
	h_w/mm	b_f/mm	b_l/mm	t/mm	d_h/mm	dh/h	a/h	h/t
H0-1.9-160-850-a	150.09	60.46	20.21	1.93	\	\	2.0	82.91
H0-1.9-160-850-b	150.17	60.39	20.38	1.92	\	\		83.34
H0-1.9-160-850R-a	150.30	60.73	20.45	1.93	\	\		82.95
H0-1.9-160-850R-b	151.36	60.59	20.46	1.91	\	\		83.66
H0.35-1.9-160-850-a	150.21	60.55	20.50	1.91	55.95	0.35		83.75
H0.35-1.9-160-850-b	149.97	60.57	20.42	1.90	55.83	0.35		84.13
H0.5-1.9-160-850-a	150.03	60.57	20.46	1.92	80.02	0.50		83.21
H0.5-1.9-160-850-b	150.40	60.66	20.45	1.91	79.97	0.50		83.58
H0.8-1.9-160-850-a	150.79	60.42	20.39	1.91	127.92	0.80		83.66
H0.8-1.9-160-850-b	149.85	60.56	20.26	1.91	127.92	0.80		83.52
H0-1.9-160-1010-a	150.47	60.69	20.37	1.92	\	\	2.5	83.48
H0-1.9-160-1010-b	150.76	60.49	20.46	1.90	\	\		84.28
H0.35-1.9-160-1010-a	150.74	60.73	20.33	1.95	55.88	0.35		82.23
H0.35-1.9-160-1010-b	150.60	60.45	20.61	1.94	55.89	0.35		82.47
H0.5-1.9-160-1010-a	150.36	60.44	20.45	1.91	80.03	0.50		83.66
H0.5-1.9-160-1010-b	150.04	60.35	20.40	1.93	80.01	0.50		83.08

H0.8-1.9-160-1010-a	150.72	60.80	20.96	1.88	128.03	0.81		84.35
H0.8-1.9-160-1010-b	150.63	61.44	20.92	1.91	128.02	0.81		83.18
H0-1.9-160-1170-a	150.68	60.55	20.44	1.96	\	\	3.0	81.96
H0-1.9-160-1170-b	152.56	60.59	19.94	1.93	\	\		83.29
H0-1.9-160-1170R-a	150.28	60.66	20.35	1.95	\	\		82.28
H0-1.9-160-1170R-b	150.40	60.72	20.30	1.96	\	\		81.76
H0.5-1.9-160-1170-a	151.23	61.61	19.80	1.94	79.98	0.49		83.57
H0.5-1.9-160-1170-b	151.24	60.77	19.82	1.92	79.97	0.50		83.48
H0.65-1.9-160-1170-a	150.53	60.66	21.22	1.90	104.04	0.65		83.93
H0.65-1.9-160-1170-b	151.04	60.56	20.47	1.95	104.05	0.65		82.02
H0.8-1.9-160-1170-a	150.86	60.65	19.91	1.99	127.92	0.80		80.73
H0.8-1.9-160-1170-b	151.18	60.73	19.95	1.97	127.91	0.80		81.61
H0-1.9-200-1010-a	193.69	74.67	24.43	1.93	\	\	2.0	103.48
H0-1.9-200-1010-b	193.94	74.66	24.24	1.94	\	\		103.06
H0.2-1.9-200-1010-a	193.41	74.69	25.00	1.92	39.98	0.20		104.22
H0.2-1.9-200-1010-b	193.59	74.67	24.77	1.90	39.89	0.20		105.32
H0.35-1.9-200-1010-a	193.85	74.65	24.95	1.92	69.92	0.35		104.41
H0.35-1.9-200-1010-b	1.93.40	74.74	24.91	1.91	69.90	0.35		105.03
H0.5-1.9-200-1010-a	193.91	74.67	24.49	1.93	99.87	0.50		103.96
H0.5-1.9-200-1010-b	194.32	74.64	24.89	1.89	99.95	0.50		106.37
H0.65-1.9-200-1010-a	193.15	74.63	24.88	1.90	129.92	0.65		105.20
H0.65-1.9-200-1010-b	193.35	74.90	25.32	1.92	129.91	0.65		104.21
H0.8-1.9-200-1010-a	194.25	74.76	24.62	1.90	159.95	0.80		104.98
H0.8-1.9-200-1010-b	193.68	74.71	24.92	1.91	159.87	0.80		104.61

2.2. Test program

In the test, the method of single-point loading at the load connector at the mid-span of a pair of specimens was adopted, which can avoid possible lateral deformation during loading. Fig. 3 shows the loading device of test. To adapt to loading needs of different-length specimens, two supports will move according to the specimen length, while reaction frame and reaction beam stayed at the original position.

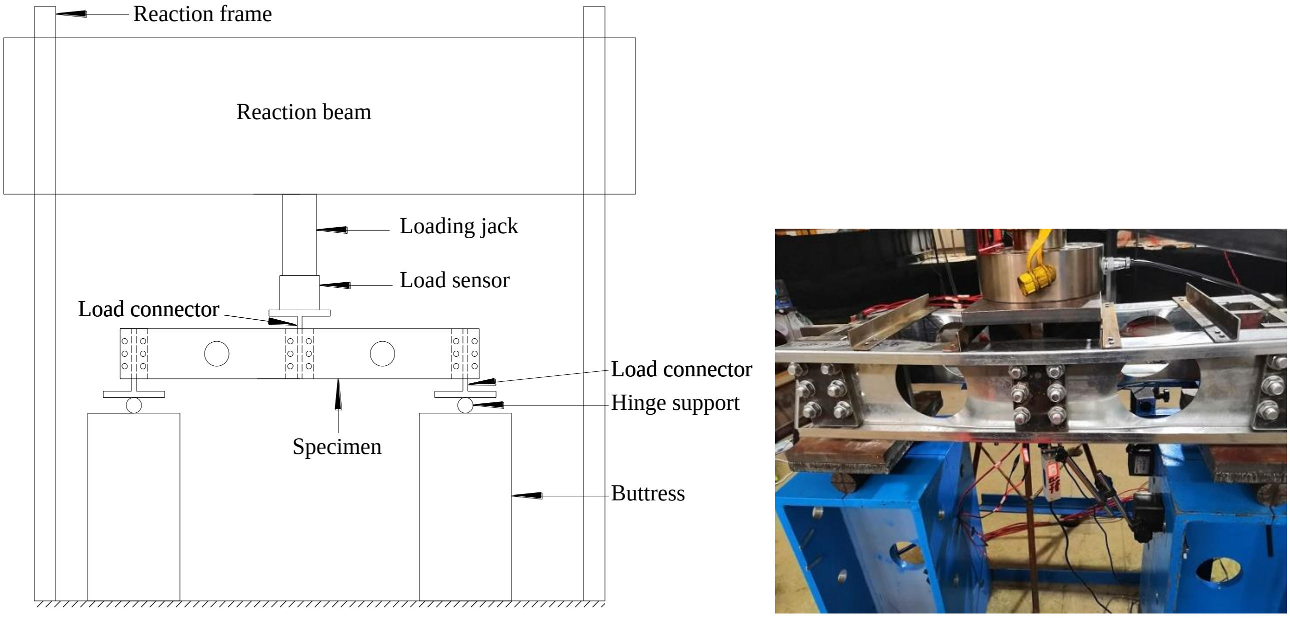

(a) (b)

Fig. 3 Test loading device (a) sketch (b) Test photo

As shown in Fig. 4, for the alignment check before loading stage and the stress monitoring during the test, 5 strain gauges were set at compression flange and lip at mid-span of specimen and junction part of flange and web in tension. As can be seen in Fig. 5, to monitor the mid-span deflection, the out-of-plane bending deformation, the shear deformation and the distortional deformation, different transducers of displacement were set respectively.

For the purpose of evenly distributing the load to the two specimens, geometric alignment and physical alignment were all carried out before the tests. After the alignment was checked, the preloading was conducted, from which effect of inaccuracy specimen installation on the results can be eliminated. After 3 times of preloading, the formal loading was carried out. During the initial formal loading, the mode was controlled by force, then it was transformed into the displacement-control mode until the end of test. With safety ensured, the test was carried on after the maximum value of load to get complete load-displacement results.

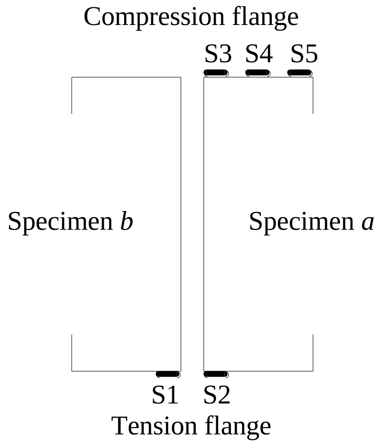

Fig. 4 Strain gauge arrangements

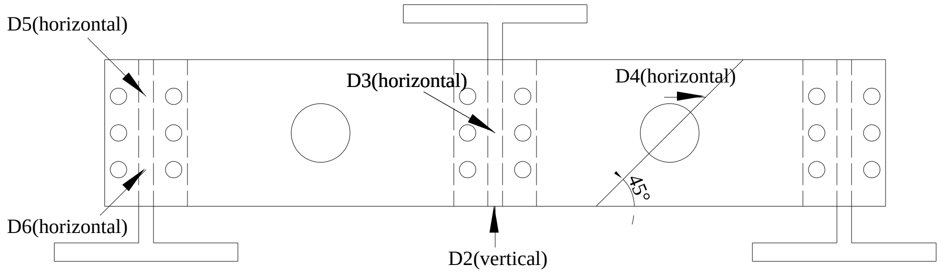

Specimen *a*

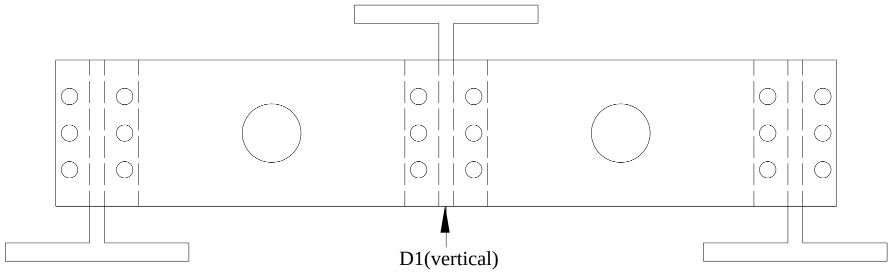

Specimen *b*

Fig. 5 Displacement meter arrangements

Table 2
Results from test and FEA

	Test results							
Specimen	Ultimate bearing capacity	Mid-span moment	Shear force of central section of circular hole	Failure mode	The shear -span ratio	Reduction coefficient of F_u	Finite element results	V_{EXP}/V_{FEA}
	F_u/kN	M_u/kN·m	V_{EXP}/kN		a/h	Δ	V_{FEA}/kN	
H0-1.9-160-850	87.41	15.30	43.71	D+L	2.0	1.00	39.45	1.11
H0-1.9-160-850R	87.54	15.32	43.77	D+L		1.00	39.45	1.11
H0.35-1.9-160-850	82.99	14.53	41.50	S+D+L		0.95	39.98	1.04
H0.5-1.9-160-850	65.54	11.47	32.77	S+D		0.75	32.47	1.01
H0.8-1.9-160-850	28.03	4.90	14.01	S		0.32	14.09	0.99
H0-1.9-160-1010	72.12	15.51	36.06	D+L	2.5	1.00	33.87	1.06
H0.35-1.9-160-1010	71.48	15.37	35.74	S+D+L		0.99	34.37	1.04
H0.5-1.9-160-1010	65.26	14.03	32.63	S+D		0.90	31.58	1.03
H0.8-1.9-160-1010	25.51	5.48	12.75	S		0.35	14.00	0.91
H0-1.9-160-1170	64.00	16.32	32.00	D+L	3.0	1.00	29.16	1.10
H0-1.9-160-1170R	63.64	16.23	31.82	D+L		1.00	29.16	1.09
H0.5-1.9-160-1170	61.87	15.78	30.94	S+D+L		0.97	29.99	1.03
H0.65-1.9-160-1170	44.93	11.46	22.47	S		0.70	22.32	1.01

H0.8-1.9-160-1170	27.76	7.08	13.88	S		0.43	13.93	1.00
H0-1.9-200-1010	94.99	20.43	47.50	D+L	2.0	1.00	44.79	1.06
H0.2-1.9-200-1010	91.60	19.69	45.80	D+L		0.96	45.37	1.01
H0.35-1.9-200-1010	93.37	20.07	46.68	S+D+L		0.98	44.26	1.05
H0.5-1.9-200-1010	73.52	15.81	36.76	S		0.77	35.65	1.03
H0.65-1.9-200-1010	49.73	10.69	24.87	S		0.52	25.36	0.98
H0.8-1.9-200-1010	29.73	6.39	14.87	S		0.31	15.19	0.98
							Average	1.03
							COV	0.048

2.3. Test results and discussion

2.3.1. Ultimate bearing capacity

Ultimate bearing capacity of specimen is listed in Table 2. Since stress condition and failure mode are the same for specimen in the same group, only results of specimen a were listed in the table.

By comparing with solid web specimen with the same value of *a*/*h*, the reduction coefficient in Fig. 6 of bearing capacity of web perforated specimen is obtained and shown in the column of *Δ* in Table 2. As can be seen from Fig. 6, variation of bearing capacity is inversely proportional to variation of the size of the opening. As the value of d_h/h increases from 0 to 0.8, for specimen with the value of *a*/*h* of 2.0, the bearing capacity of specimen decreases by 68% (*h*/*t* = 84.2) and 75% (*h*/*t* = 105.3), respectively. For specimen with the value of *a*/*h* of 2.5, the ultimate bearing capacity decreases by 65% (*h*/*t* = 84.2). And for specimen with the value of *a*/*h* of 3.0, the ultimate bearing capacity decreases by 57% (*h*/*t* = 84.2).

The relation of bearing capacity with the value of *h*/*t* is shown in Fig. 7. It can be seen from the figure, when the value of *a*/*h* and d_h/h of the specimen are constant, the higher the value of *h*/*t* is (the larger the effective shearing web area is), the greater the bearing capacity is. Under same conditions, the degree of effect of the value of *h*/*t* on the bearing capacity decreases as the hole diameter increases.

2.3.2. Load-deflection curves

The symmetrically set up pair of specimens and had basically same stress conditions and displacements, to facilitate the presentation and analysis, only load-deflection curves of specimen *a* are presented, as shown in Fig. 8. When the value of d_h/h is relatively smaller ($d_h/h \leq 0.5$), the curve has a rapid decrease after the maximum point. When the value of d_h/h is relatively larger ($d_h/h \geq 0.65$), the curve decreases more gently after the maximum point.

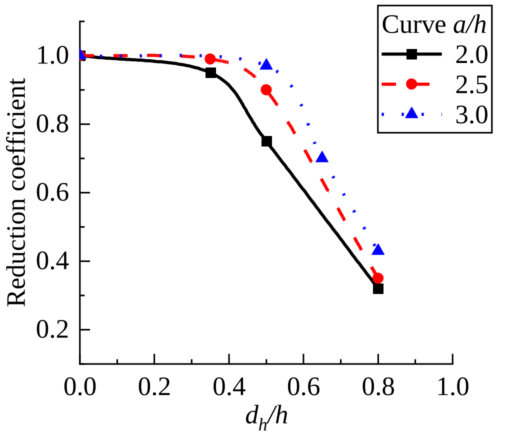

Fig. 6 Reduction coefficient of bearing capacity with the value of d_h/h

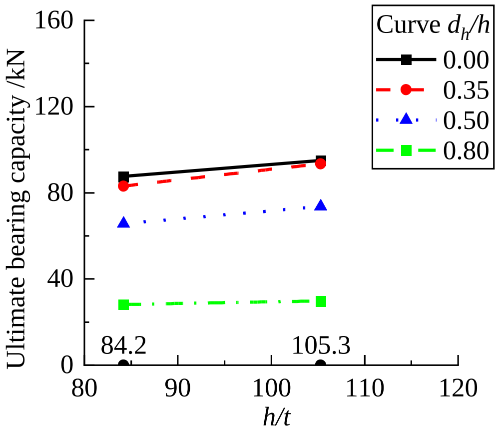

Fig. 7 Bearing capacity with the value *h*/*t* (*a*/*h*=2.0)

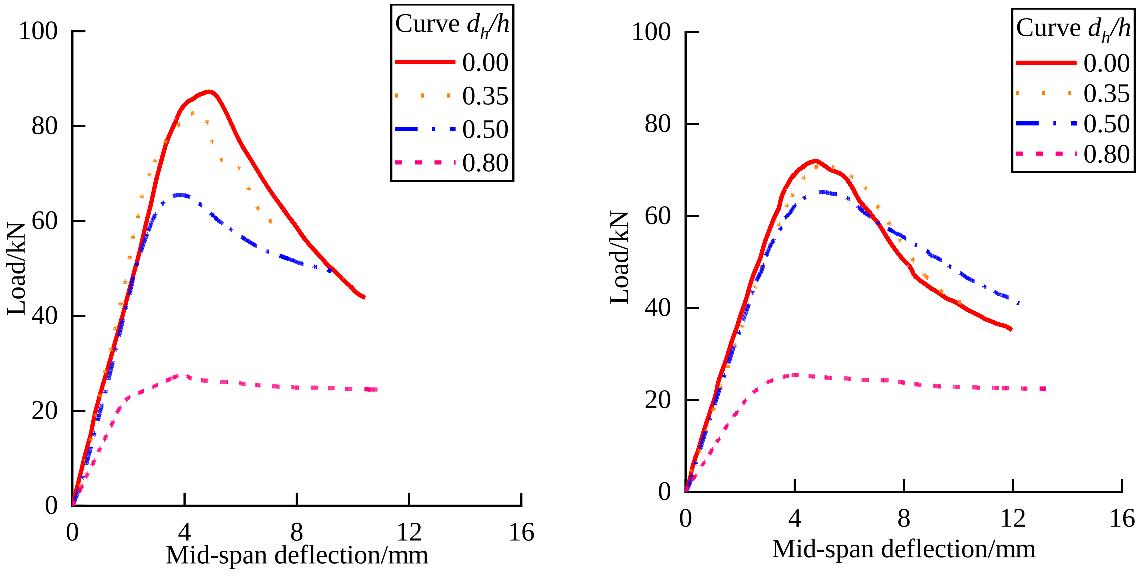

(a) Section H160-850 series

(b) Section H160-1010 series

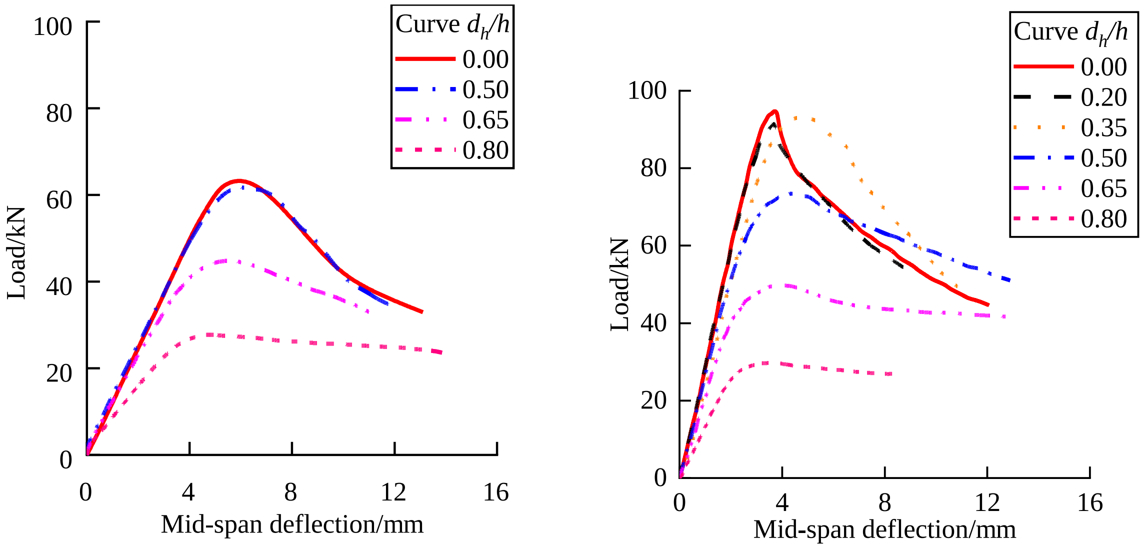

(c) Section H160-1170 series

(d) Section H200-1010 series

Fig. 8 Load-deflection curves of specimen at mid-span

2.3.3. *Failure mode*

Since the specimens were under combined of bending moment and shear force action, there would be the bending failure mode dominated by local buckling deformation and distortional buckling deformation or shear failure mode dominated by the shear buckling deformation appear in the specimens. The failure mode is listed in Table 3 and shown in Fig 9.

Table 3
Failure mode of specimen

The value of *a/h*	Range of the value of d_h/h	Failure mode
$a/h = 2.0$	$d_h/h < 0.35$	The coupled failure of local buckling deformation and flange distortional buckling deformation.
$a/h = 2.5$		
$a/h = 3.0$	$d_h/h < 0.5$	
$a/h = 2.0$	$d_h/h = 0.35$	The shear buckling failure in web, accompanied by the coupled failure of local buckling deformation and flange distortional buckling deformation.
$a/h = 2.5$	$0.35 \le d_h/h \le 0.5$	
$a/h = 3.0$	$d_h/h = 0.5$	
$a/h = 2.0$	$d_h/h \ge 0.5$	The dominating web shear buckling failure.
$a/h = 2.5$	$d_h/h > 0.5$	
$a/h = 3.0$		

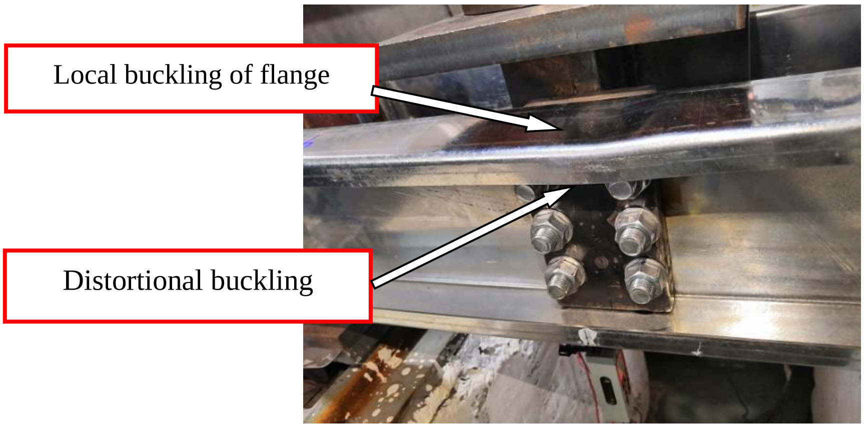

(a) Failure mode of specimen “H0-1.9-160-850”

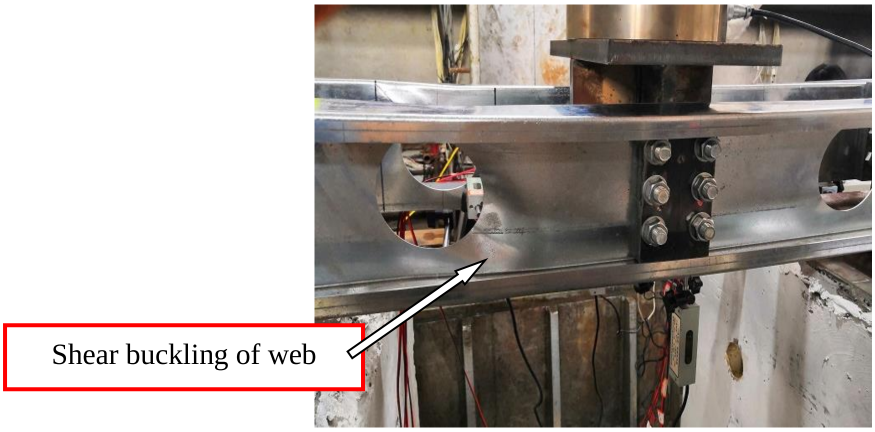

(b) Failure mode of specimen " H0.65-1.9-160-1170"

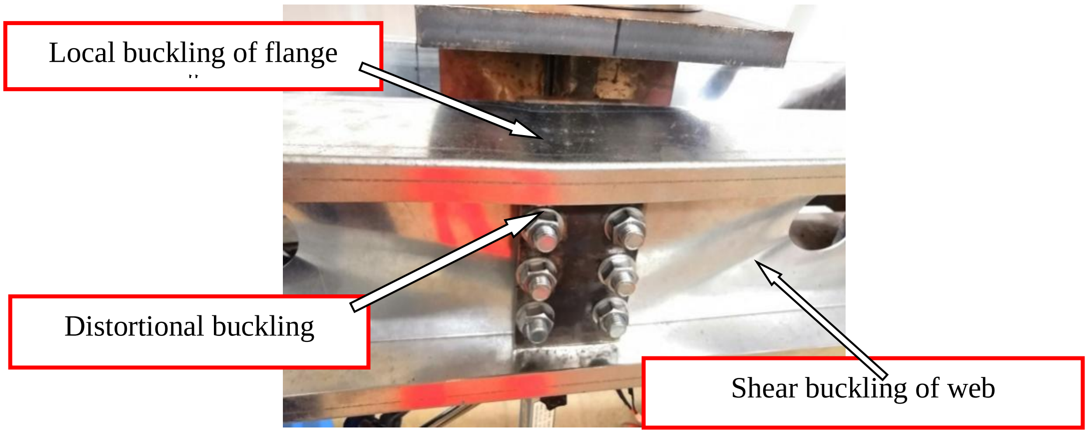

(c) Failure mode of specimen "H0.35-1.9-200-1010"

Fig. 9 Typical failure modes of specimens

3. Finite element analysis

3.1. Finite element model

The FEA model of specimen was established by means of ABAQUS. According to the test loading method, the model for FEA could be simplified by establishing only the model of specimen *a*.

3.1.1. Element and mesh

Due to that plate of lipped C-shaped CFS member is thin-walled shell, which is prone to produce buckling deformation, S4R shell element was adopted. The FEA models were divided into the meshing scale of 5×5 mm. For the model of web perforated specimens, area partition was conducted near the web hole in order to apply the quadrilateral mapped mesh, so as to ensure the convergence of calculation. Finally, the global mesh was divided.

3.1.2. Boundary conditions and loading mode

In response to the actual conditions in test, the setting of boundary condition in FEA model was as follows: at both ends of beam, where the supports were, coupling point was taken below the beam section to couple with the contact part between web and connector. At mid-span section, another point at the upper web (loading position) of the specimen was also taken to couple with the contact part. The displacement loading mode was adopted in FEA, and mid-span coupling point was adopted as load applying point, and Y direction displacement was applied at the point.

3.1.3. Material properties and initial imperfections

The specimen could obtain initial imperfections due to the effect of manufacture or other factors, which can affect the mechanical performance of specimen. The material properties of the specimen obtained through the tensile test are shown in Table 4, and it was applied in the finite element model according to setting rules of ABAQUS. For the specimens with value of h/t of 52.6, 84.2 and 105.3, the measured initial imperfection was 0.588 mm, 0.892 mm and 0.887 mm, respectively.

Table 4
Material properties

Nominal strength of yield point	Other parameters			
$\sigma_{0.2}$/ MPa	E/ GPa	$\sigma_{0.2}$/ MPa	σ_u/ MPa	ε_f/ %
550.00	200.90	574.30	607.00	12.28

3.1.4. Analysis method

The overall finite element analysis process used a two-step approach, namely the eigenvalue buckling analysis step and the nonlinear analysis step. During first one step, the required buckling modes were extracted. And on basis of that, in the second step, the measured initial imperfections were added and applied in analysis. To achieve smooth convergence of nonlinear analysis process, it was further divided into halves. Number one was to ensure the smooth operation of boundary conditions and contact relations by appliance of small value of displacement, and number two was to apply all the displacements to the specimen.

3.2. Model validation against test results

For the FEA model validation, it was conducted by comparing results of FEA and test together, respectively from the following aspects: the failure mode, the ultimate bearing capacity and the load-deflection curve.

3.2.1. Failure characteristics

The failure mode of specimen from FEA and test are compared in Fig. 10. As seen from the figure that the failure mode of the FEA is generally consistent with that of test.

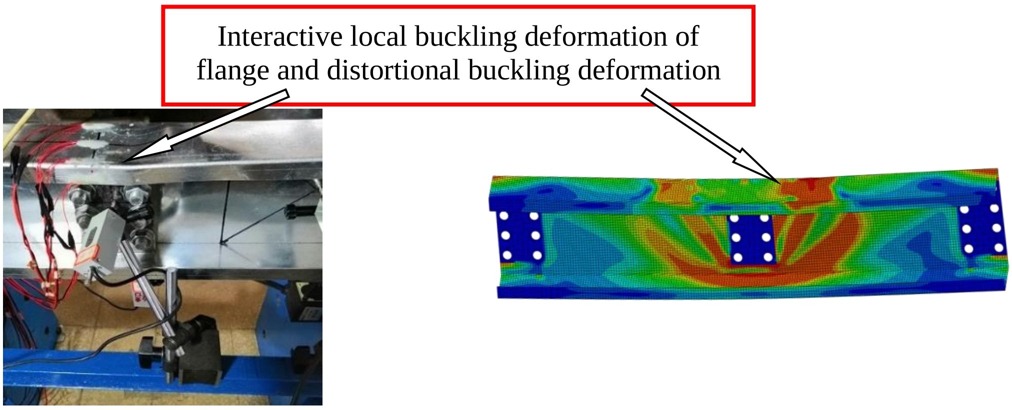

(a) Test result

(b) FEA result

(1) Specimen H0-1.9-200-1010

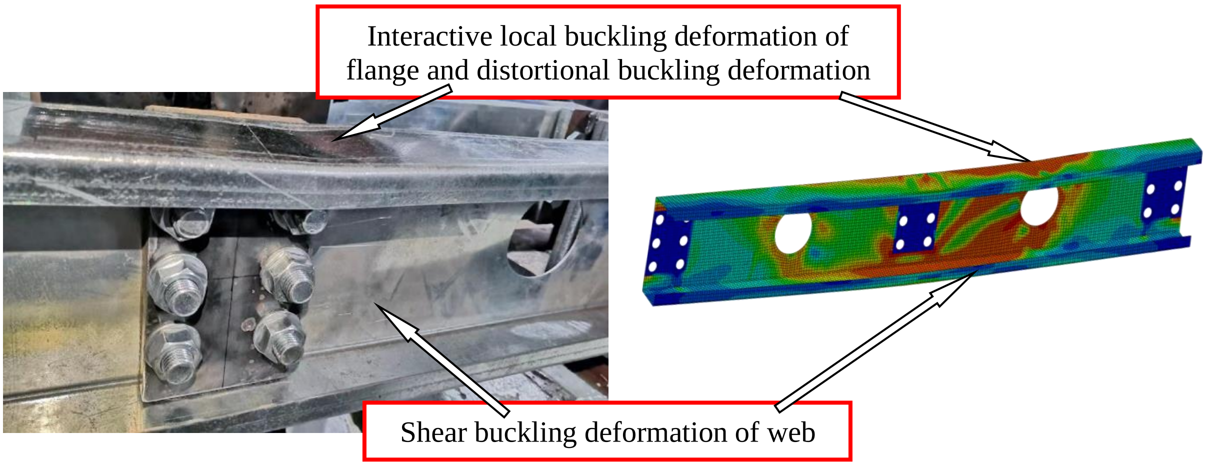

(a) Test result

(b) FEA result

(2) Specimen H0.5-1.9-160-1170

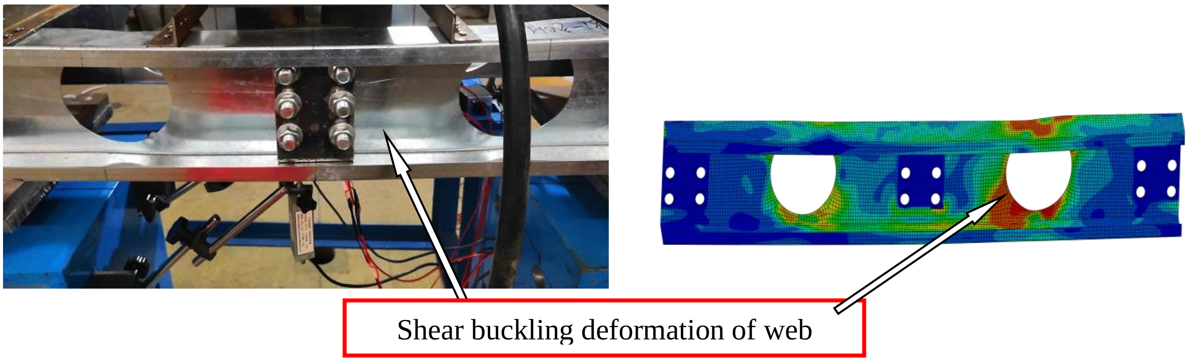

(a) Test result

(b) FEA result

(3) Specimen H0.8-1.9-160-1010

Fig. 10 Comparison on failure mode of specimen from test and FEA

3.2.2. Ultimate bearing capacity

The results of the bearing capacity of specimen from FEA and test are presented in Table 2. It can be seen, the value of V_{EXP}/V_{FEA} is between 0.91 and 1.11, whose average value and coefficient of variation are 1.03 and 0.048, respectively, which shows that the FEA model adopted in this paper has high accuracy.

3.2.3. Load-deflection curves

The load-deflection curves of Hd_h/h-1.9-160-850 series and Hd_h/h-1.9-160-1010 series in test are compared with FEA results in Fig. 11. It can be seen, when the value of d_h/h is relatively smaller (0.35), the elastic stiffness of load-deflection curve in test is relatively smaller than that of FEA, and curve of specimen in test has a higher strength after buckling than that of FEA. When the value of d_h/h increases (0.50), the curves of FEA are in better agreement with those of test, which verifies rationality of FEA again.

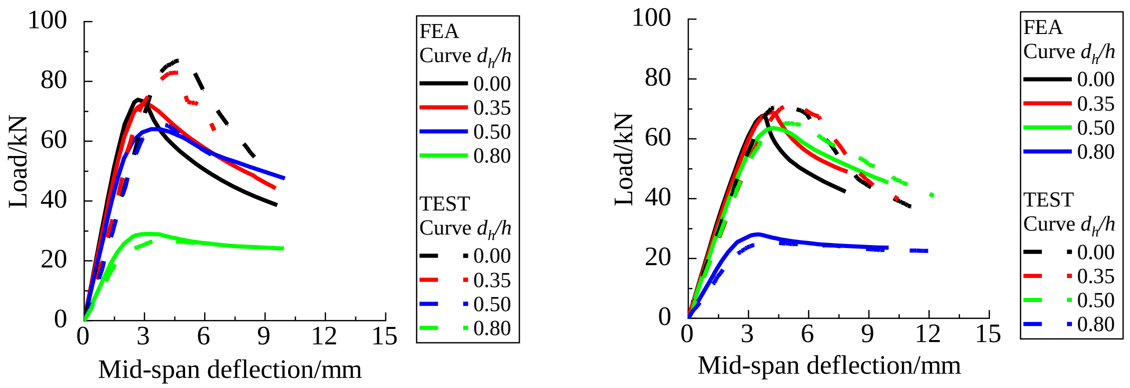

(a) Hd_h/h-1.9-160-850

(b) Hd_h/h-1.9-160-1010

Fig. 11 Load-deflection curves from test and FEA

4. Parametric study

4.1. Design of parameters

To conduct further research on the comprehensive performance of thin-walled web-perforated lipped C-shaped CFS beams under combined bending moment and shear force action, series of models verified above were adopted for further nonlinear parameter analysis. It is found from the test results that the two main factors that affect bearing capacity and failure mode of specimen are, respectively, the value of d_h/h and the value of a/h, and the value of h/t also affects the bearing capacity to a certain degree. Combined with tests design, h of the specimen for parameter analysis is designed as 100 mm, 120 mm, 140 mm, 160 mm, 180 mm, 200 mm and 300 mm, respectively, and the section thickness (t) of specimen was 1.9 mm, from which different value of h/t can be obtained. In addition, specimens with the h of 100 mm and 160 mm, additional specimens with t = 1.0 mm were designed. Due to that this paper mainly studies performance of web-perforated beams under combined bending moment and shear force action, the value of a/h of the specimens ranged from 1.5 to 4.0 with an increment of 0.5.

4.2. Influence of hole depth-to-web height ratio

The curve of the bearing capacity of specimen with the value of d_h/h is shown in Fig. 12. The curves are approximately horizontal at the beginning. When the value of d_h/h increases to a certain level, the curves drop sharply. At that time, bearing capacity shows more sensitivity to the change of the value of d_h/h.

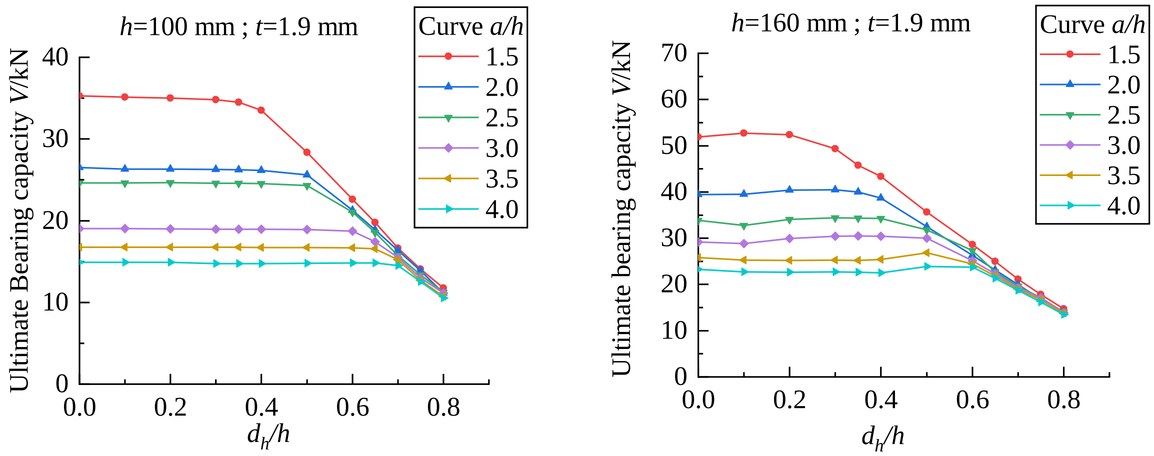

(a) h/t=52.6

(b) h/t=84.2

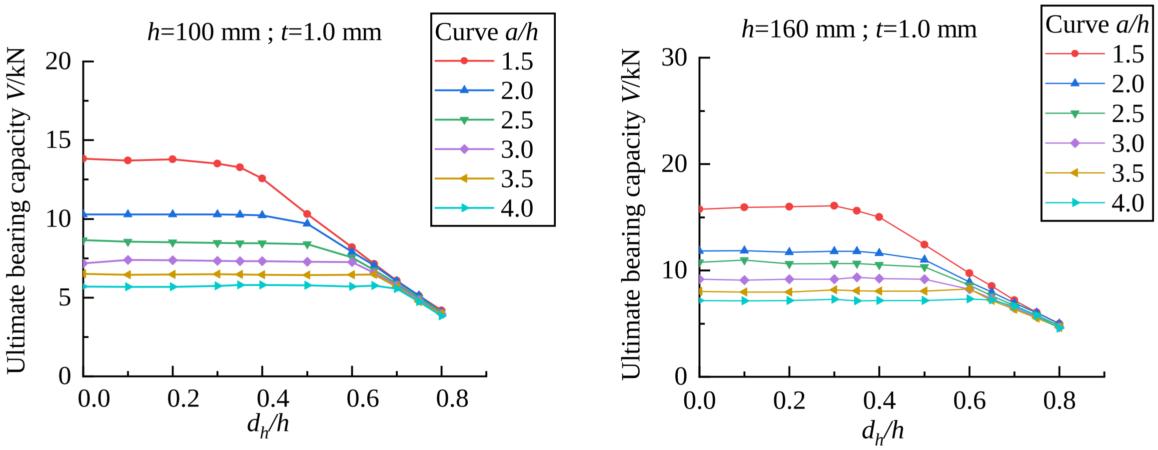

(c) h/t=100

(d) h/t=160

Fig. 12 Curves of bearing capacity with the value of d_h/h

Due to limited length, Hd_h/h-1.9-180-930 series (a/h = 2.0) are chosen for specific analysis. Fig. 13~15 shows the failure mode. For specimens with the value of $d_h/h \le 0.35$, as seen from Fig. 13-(a) ~ (b), at mid-span section, there are obvious stress concentration areas in flange and along the shear failure direction in the shear-zone. As the value of d_h/h increases, the area of stress concentration in the shear zone increases. Specimens are subjected to the coupled bending and shear failure. As seen from Fig.14 -(a)~(b), interactive local buckling deformation and distortional buckling deformation occur at mid-span section. As seen from Fig.15-(a) ~ (b), slight local buckling deformation occurs in the shear zone along shear failure direction. For specimens with the value of d_h/h of 0.35 to 0.4, the area of stress concentration in the compression flange along the flange-width direction at mid-span decreases obviously, while the area along the span direction of specimen increases, and the failure mode begins to change. For specimens with the value of $d_h/h > 0.4$, as seen from Fig. 13-(c) ~ (d), the main area of stress concentration is in the web in shear zone along shear failure direction. As seen from Fig. 14-(c) ~ (d), interactive local buckling deformation and distortional buckling deformation occur at mid-span section. As seen from Fig. 15-(c) ~ (d), obvious local buckling deformation occurs near the web opening along shear failure direction. In conclusion, when the value of a/h= 2.0, as the value of d_h/h increases, failure mode of the steel beam changes from the coupled failure of bending and shear at mid-span into the shear failure of web local buckling in shear zone.

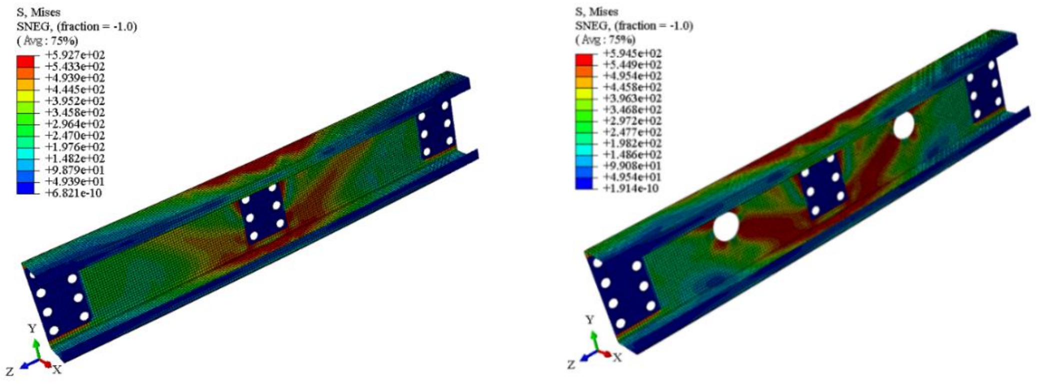

(a) H0-1.9-180-930 (b) H0.30-1.9-180-930

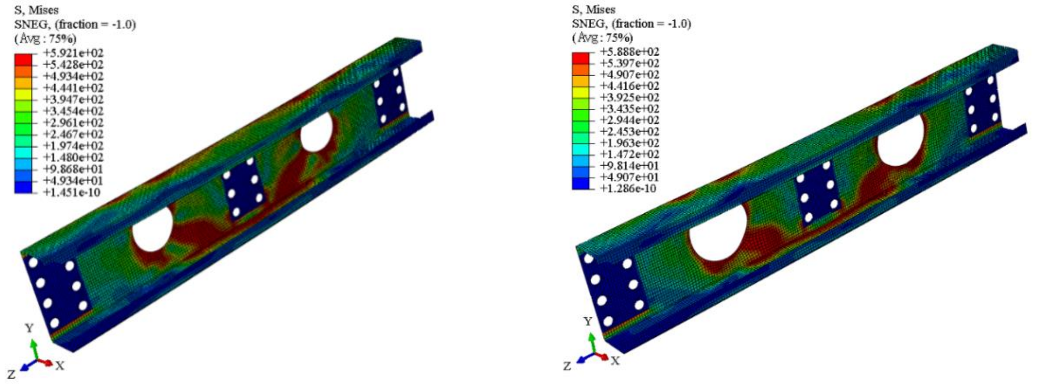

(c) H0.50-1.9-180-930 (d) H0.65-1.9-180-930

Fig. 13 Failure mode of series “Hd_h/h -1.9-180-930” with the value of d_h/h

(a) H0-1.9-180-930 (b) H0.3-1.9-180-930 (c) H0.5-1.9-180-930 (d) H0.65-1.9-180-930

Fig. 14 Buckling deformation of series “Hd_h/h-1.9-180-930” with the value of d_h/h

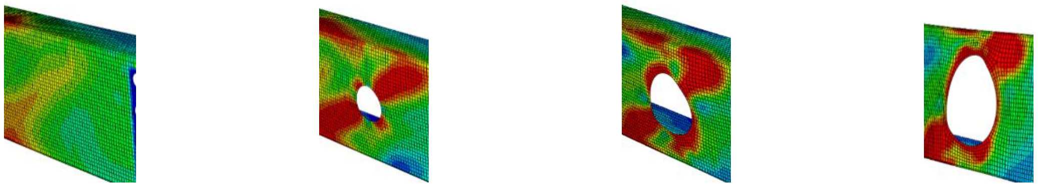

(a) H0-1.9-180-930 (b) H0.3-1.9-180-930 (c) H0.5-1.9-180-930 (d) H0.65-1.9-180-930

Fig. 15 Web buckling deformation of series “Hd_h/h-1.9-180-930” with the value of d_h/h

The mid-span load-deflection curve of Hd_h/h-1.9-180-930 series is shown in Fig. 16. When the value of $d_h/h \le 0.35$, the curve has a fast drop after the peak point, indicating that failure of steel beam shows a certain suddenness. When the value of $d_h/h > 0.35$, the curve drops slower after the maximum point, which shows that the steel beam displays certain ductility after failure. The reason for that is when the value of d_h/h is relatively larger, more significant shear bucking deformation occur in the web, and the out-of-plane shear deformation weakens the overall unloading effect of the beams.

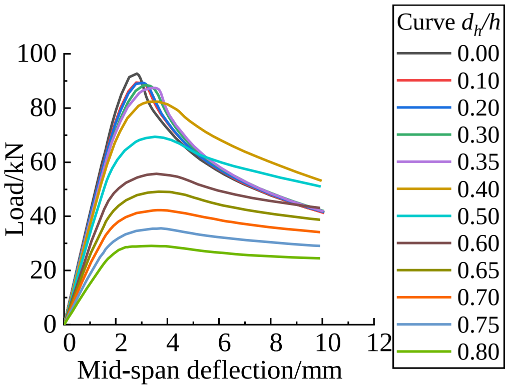

Fig. 16 Load-deflection curves of series "Hd_h/h-1.9-180-930" with the value of d_h/h (a/h=2.0)

4.3. Influence of web height-to-thickness ratio

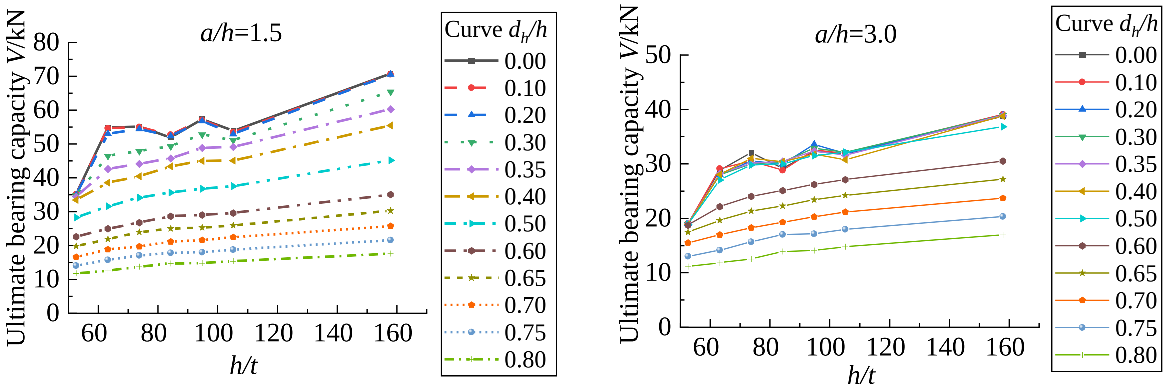

Fig. 17 Bearing capacity with the value of h/t (with different values of a/h, t=1.9 mm)

The curve of bearing capacity with the value of h/t is shown in Fig. 17. The specific analysis of bearing capacity corresponding to Fig. 17 is shown in Table 5. As seen from Fig. 18, with the value of d_h/h of 0 and 0.35, the bearing capacity shows more sensitivity to the change of the value of h/t. While with the value of d_h/h of 0.65 and 0.8, the bearing capacity is less affected by the value of h/t. The reasons can be explained that with a relatively smaller value of d_h/h, as the value of h/t increases, the ratio of plate width to plate thickness is easy to cross the critical value, thus failure mode transform from shear failure to local buckling failure. With a relatively larger value of d_h/h, area of shearing web core is deducted, and the shear stress for the remaining area above and below the web hole is smaller, which leads to that the influence of increase in the value of h/t on the bearing capacity is limited.

Table 5
Analysis of the effect of the value of h/t on bearing capacity of specimen

The value of a/h	Range of the value of d_h/h	Influence of the value of h/t on bearing capacity
1.5	$d_h/h \leqslant 0.2$	(1) High Coincidence degree of the curve ; (2) When the value of h/t is 52.6 ~ 73.7, 84.2 ~ 94.7 and 105.3 ~ 157.9, the bearing capacity increases as the increase of the value of h/t; (3) When the value of h/t is 73.7 ~ 84.2 and 94.7 ~ 105.3, bearing capacity decreases as the value of h/t increases.
3.0	$d_h/h \leqslant 0.5$	
1.5	$d_h/h > 0.2$	Bearing capacity increases with as the value of h/t increases, and the trend of the curve is similar.
3.0	$d_h/h > 0.5$	

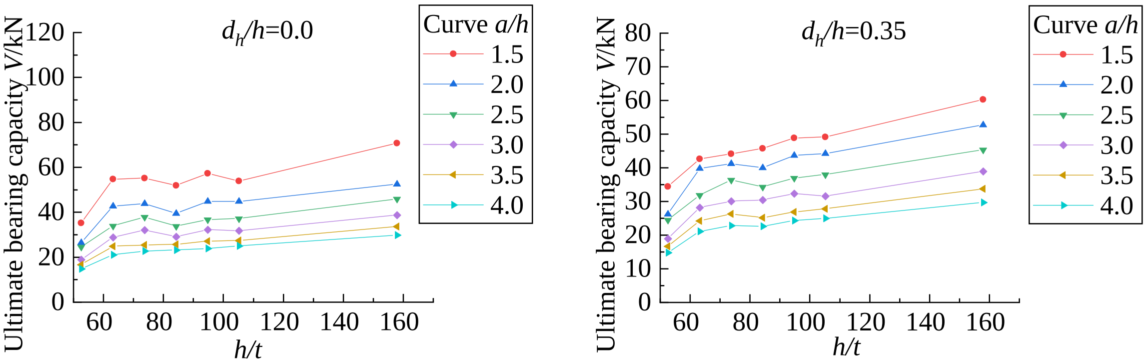

(a) (b)

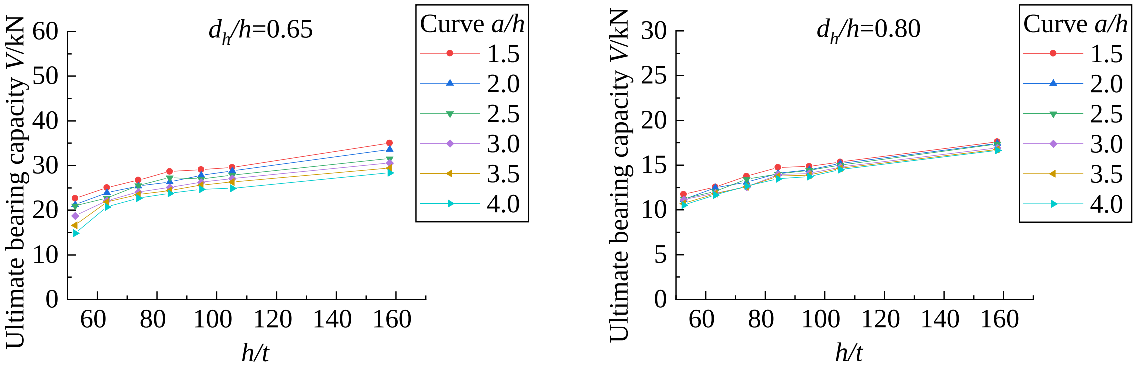

(c) (d)

Fig. 18 Bearing capacity with the value of h/t (with different values of d_h/h, t=1.9 mm)

The variation of failure mode with the value of h/t of specimen with the value of a/h of 1.5 is shown in Fig. 19. As seen from Fig. 19-(a) ~ (b), with the value of d_h/h of 0.1 and relatively smaller value of h/t (h/t= 52.6 or 63.2), an obvious stress concentration area appears in flange and the web along shear failure direction at mid-span. As seen from Fig. 19 (a), maximum value of stress of specimen H0.10-1.9-100-510 at failure can reach the yield strength, which indicates material property of specimen is fully utilized. As seen from Fig. 19-(c) ~ (d), as the value of d_h/h increases, stress concentration area in the compression flange along flange-width direction at mid-span gradually decreases, while that along length direction of the steel beam gradually increases. And the maximum stress value at failure gradually decreases, which indicates that the steel beam is more prone to buckling. As seen from Fig. 20, when the value of d_h/h is 0.65, main area of stress concentration of specimen is in web shear failure direction, failure mode majors in shear failure, and the value of h/t barely affect the failure mode.

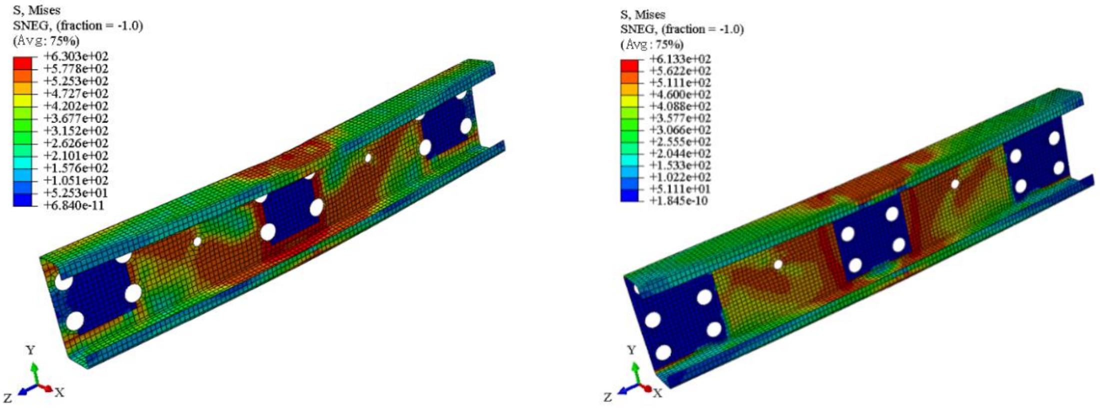

(a) H0.10-1.9-100-510 (h/t=52.6) (b) H0.10-1.9-120-570 (h/t=63.2)

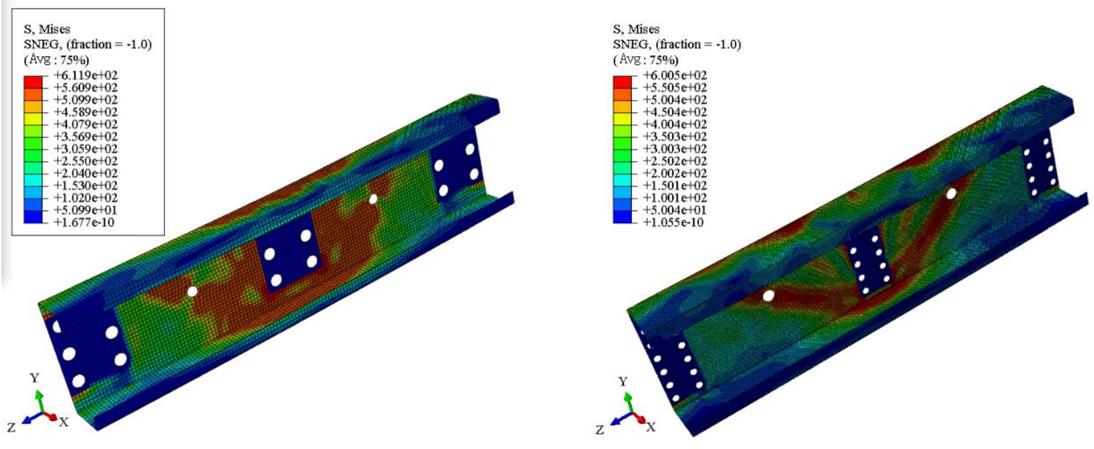

(c) H0.10-1.9-160-690 (h/t=84.2) (d) H0.10-1.9-300-1110 (h/t=157.3)

Fig. 19 Failure mode with the value of h/t (t = 1.9 mm; a/h = 1.5; d_h/h = 0.10)

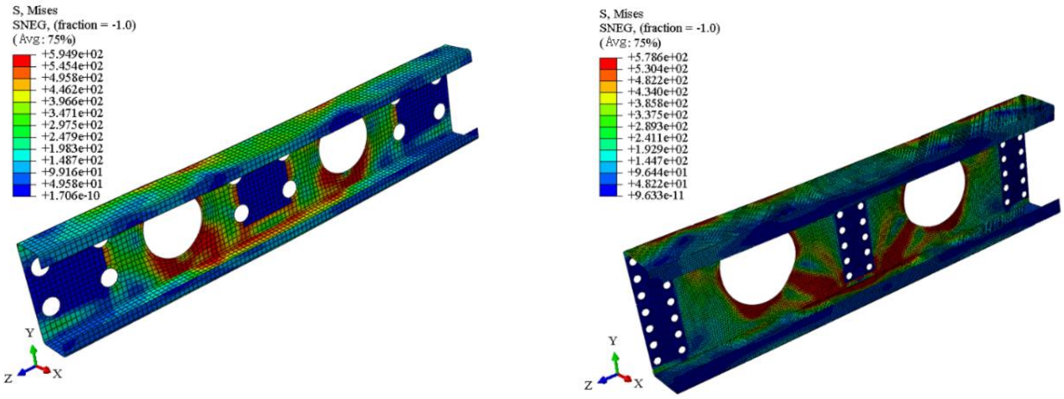

(a) H0.65-1.9-100-510(*h/t*=52.6) (b) H0.65-1.9-300-1110(*h/t*=157.3)

Fig. 20 Failure mode with the value of *h/t* (t = 1.9 mm; a/h = 1.5; d_h/h = 0.65)

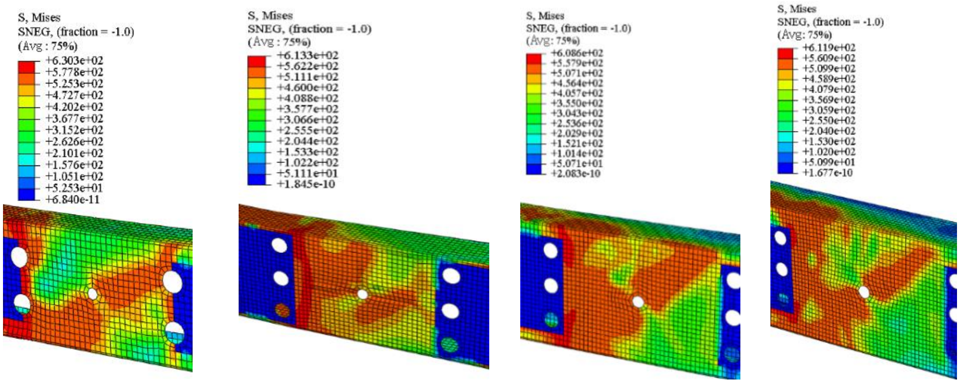

(a) *h/t*=52.6 (b) *h/t*=63.2 (c) *h/t*=73.7 (d) *h/t*=84.2

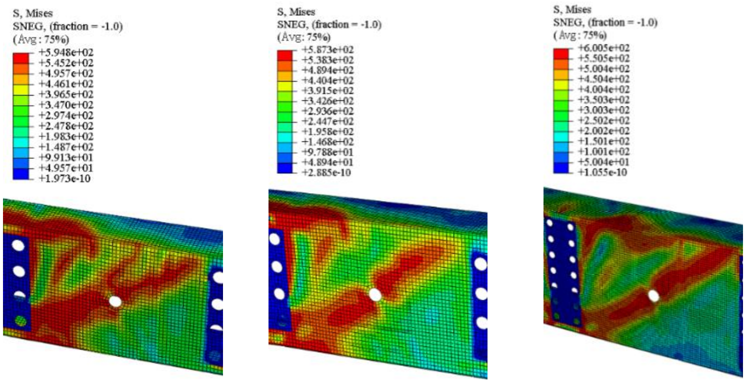

(e) *h/t*=94.7 (f) *h/t*=105.3 (g) *h/t*=157.9

Fig. 21 Web buckling deformation with the value of *h/t* (t = 1.9 mm; a/h = 1.5; d_h/h = 0.1)

Fig. 21 and Fig. 22 show that, buckling deformation in flange and the web in shear zone at mid-span with different values of *h/t*, respectively. As seen from Fig. 21, there is significant local buckling deformation in the web of steel beam with the value of *h/t* of 52.6, 84.2 and 105.3. As seen from Fig. 22, the web buckling deformation in shear zone of specimens with different values of *h/t* is similar. Combined with the above, when value of *h/t* increases from 73.7 to 84.2 and from 94.7 to 105.3, the curve of bearing capacity with value of *h/t* decreases due to flange local buckling deformation at mid-span, which shows that web local buckling has significant effect on the bearing capacity.

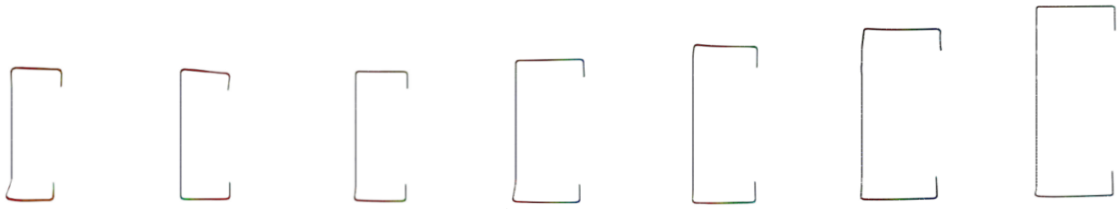

(a) *h/t*=52.6 (b) *h/t*=63.2 (c) *h/t*=73.7 (d) *h/t*=84.2 (e) *h/t*=94.7 (f) *h/t*=105.3 (g) *h/t*=157.9

Fig. 22 Flange buckling deformation with the value of *h/t* (t= 1.9 mm; a/h = 1.5; d_h/h = 0.1)

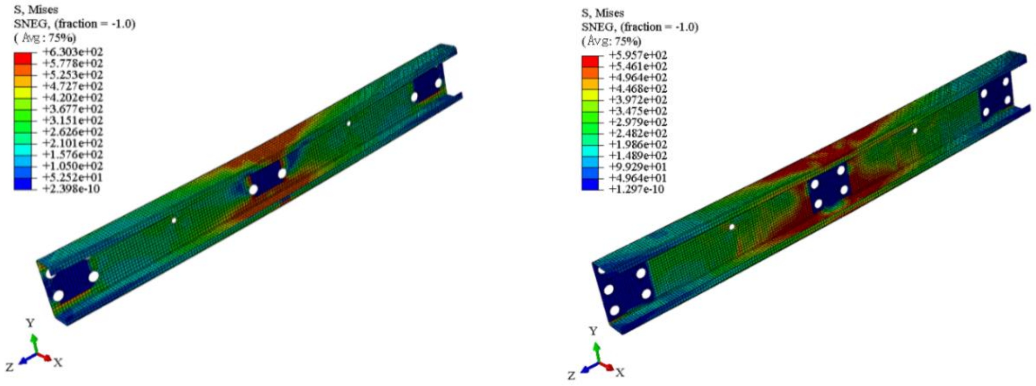

(a) H0.10-1.9-100-810 (h/t=52.6) (b) H0.10-1.9-120-930 (h/t=63.2)

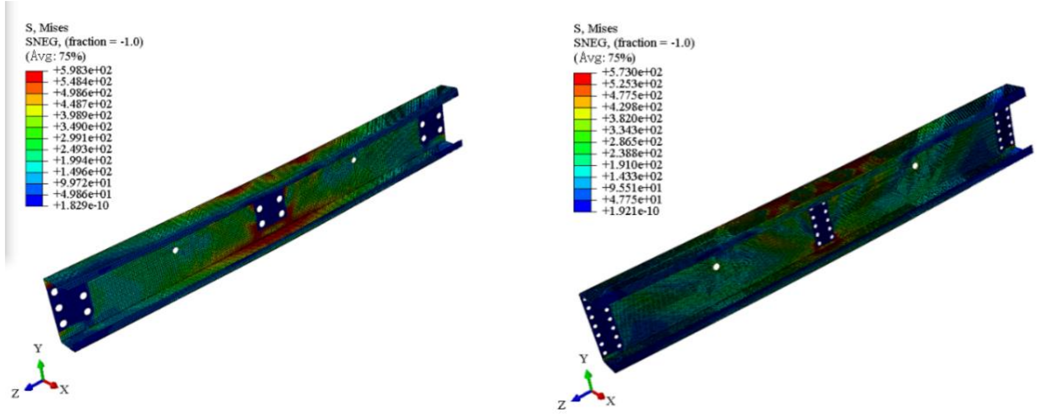

(c) H0.10-1.9-160-1170 (h/t=84.2) (d) H0.10-1.9-300-2010 (h/t=157.3)

Fig. 23 Failure mode with the value of *h/t* (*a/h* = 3.0; d_h/h = 0.10)

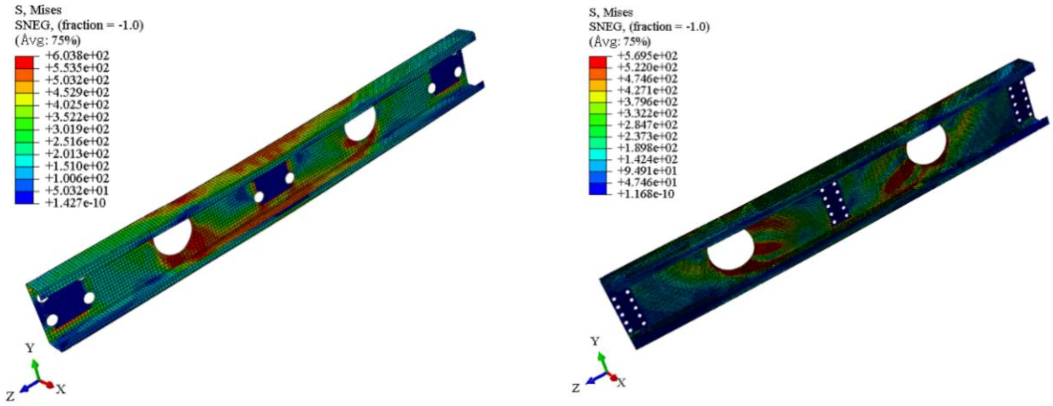

(a) H0.65-1.9-100-810 (*h/t*=52.6) (b) H0.65-1.9-300-2010 (*h/t*=157.3)

Fig. 24 Failure mode with the value of *h/t* (*a/h* = 3.0; d_h/h = 0.65)

Fig. 23 shows the failure mode with the value of *h/t* of specimen with the value of *a/h* of 3.0. As seen from the figure, with the value of d_h/h of 0.1, the failure mode of specimen with different the values of *h/t* are mainly bending failure at mid-span, the shear failure in web is not significant, and there is an obvious flange stress concentration at mid-span which decreases as the value of *h/t* increases. As seen from Fig. 24, with the value of d_h/h of 0.65, as the increase of the value of *h/t*, stress concentration area tend to be located in the web shear failure direction, and failure mode transforms from the coupled failure of bending and shear to the shear failure.

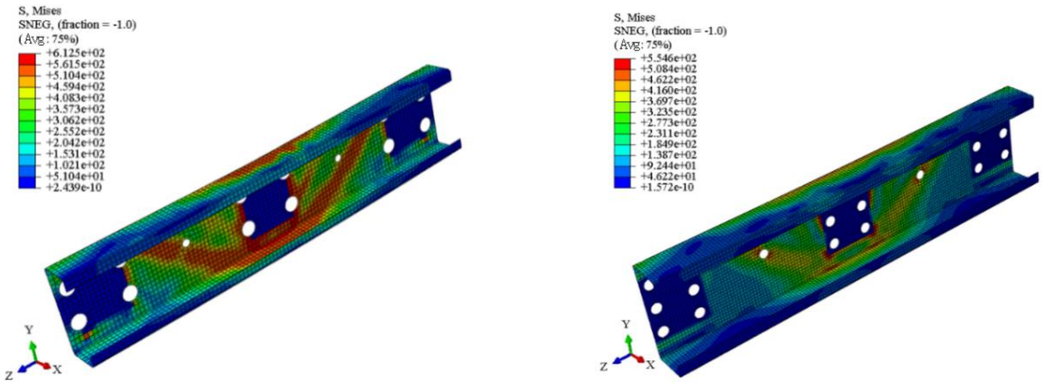

(a) H0.10-1.0-100-510 (*h*/*t*=100) (b) H0.10-1.0-160-690 (*h*/*t*=160)

Fig. 25 Failure mode with t =1.0 mm (a/h = 1.5)

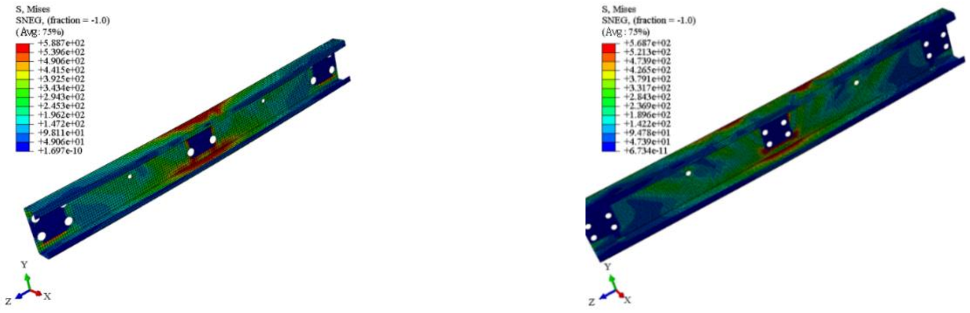

(a) H0.10-1.0-100-810 (*h*/*t*=100) (b) H0.10-1.0-160-1170 (*h*/*t*=160)

Fig. 26 Failure mode with t =1.0 mm (a/h = 3.0)

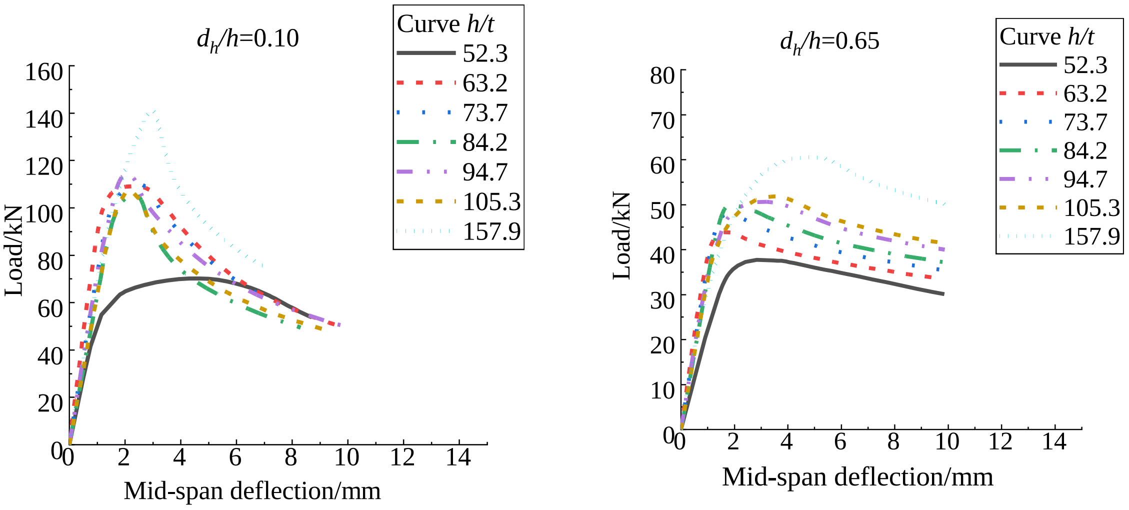

(a) d_h/h=0.10 (b) d_h/h=0.65

Fig. 27 Load-deflection curves with the value of *h*/*t* (*t*= 1.9 mm, *a*/*h*=1.5)

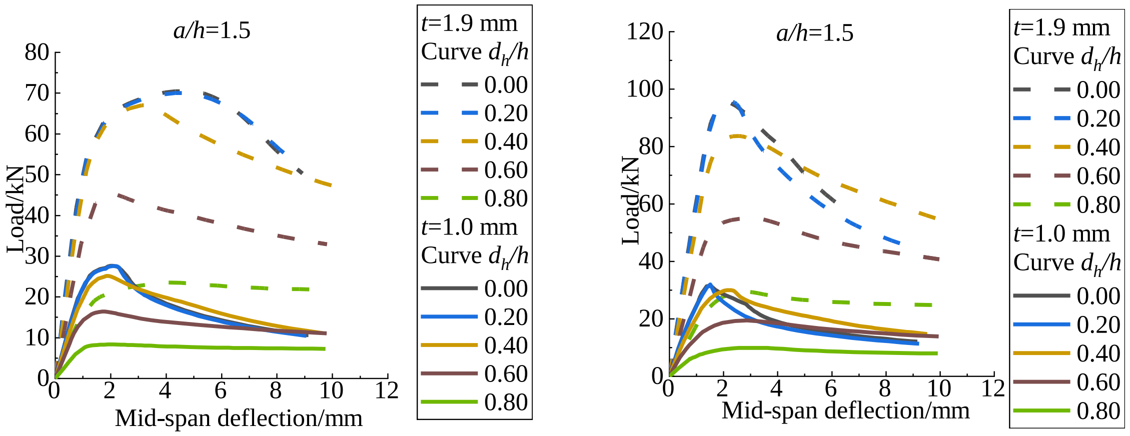

(a) *h*=100 mm (b) *h*=160 mm

Fig. 28 Load-deflection curves with the value of *h*/*t* (with same *h*)

The failure mode of specimen with t = 1.0 mm under the same conditions with those of specimens in Fig. 19 and Fig. 23 are respectively presented in Fig. 25 and Fig. 26. As seen from the figure, as t changes from 1.9 mm to 1.0 mm, the stress concentration area of the specimen decreases.

The load-deflection curve with the value of h/t is presented in Fig. 27 and Fig. 28. As seen from Fig. 27 that with same t= 1.9 mm, specimen with the value of h/t of 52.6 has the lowest stiffness, the beam with the value of h/t of 63.2 has the highest stiffness, and the stiffness increases the most as the value of h/t increases from 52.6 to 63.2. As seen from Fig. 28, when t changes from 1.9 mm to 1.0 mm, as the value of h/t increases, the stiffness decreases significantly, and the post-buckling strength of specimen with h = 100 mm also decreases.

4.4. Influence of shear-span ratio

Fig. 29 shows curve of the bearing capacity of specimen with the value of a/h, and analysis is presented in Table 6. According to Section 3.2 that when the value of d_h/h is relatively larger, the bearing capacity is determined by the value of d_h/h. In hence, for steel beam dominated by shear failure due to the opening of super large holes (d_h/h > 0.5), the value of a/h barely affect the bearing capacity.

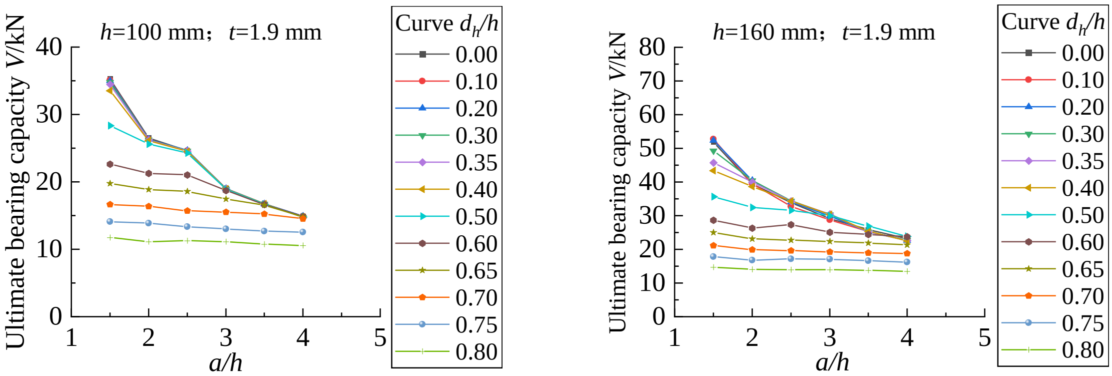

(a1) Hd_h/h-1.9-100 (a2) Hd_h/h-1.9-160

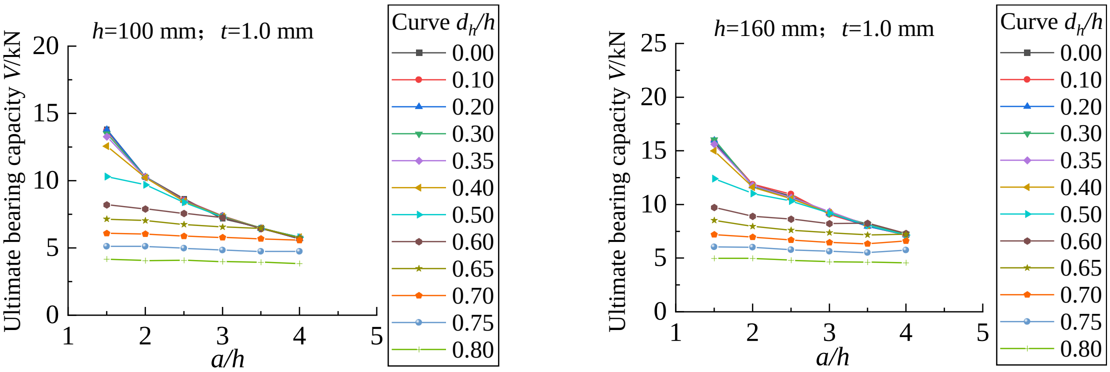

(b1) Hd_h/h-1.0-100 (b2) Hd_h/h-1.0-160

Fig. 29 Bearing capacity with the value of a/h

Table 6

Analysis of the influence of the value of d_h/h on the bearing capacity of specimen

Range of the value of h/t	Range of the value of d_h/h	Influence of the value of a/h on bearing capacity of specimen
h/t = 52.6	$d_h/h \leqslant 0.40$	The curves is highly overlapped, and bearing capacity shows sensitivity to the change of the value of a/h.
h/t > 52.6	$d_h/h \leqslant 0.20$	
h/t = 52.6	$0.4 < d_h/h \leqslant 0.65$	The curves begin to deviate, and the influence of variation of the value of a/h on bearing capacity decreases as the value of d_h/h increases.
h/t > 52.6	$0.2 < d_h/h \leqslant 0.50$	
h/t = 52.6	d_h/h > 0.65	The change of the value of a/h has the least influence on bearing capacity, the curve is close to the horizontal state.
h/t > 52.6	d_h/h > 0.50	

Take specimens with the value of h/t of 52.6 (h= 100 mm, t= 1.9 mm) and the value of d_h/h of 0.2 and 0.75 as examples, the specific analysis on the variation of failure modes of steel beams with the value of a/h is as following.

When the value of h/t of specimen is 52.6 (h= 100 mm, t= 1.9 mm), as seen from Fig. 30, with the value of d_h/h of 0.2, the variation of flange stress distribution at mid-span is less affected by the value of a/h, and the area of web stress concentration in the shear zone shrinks as the value of a/h increases, which shows that failure mode of specimen gradually changes from the coupled failure of bending and shear to the mainly bending failure as the value of a/h increases. As seen in Fig. 31, for specimens with the value of d_h/h of 0.75, the failure mode is less affected by the value of a/h, and the stress is mainly concentrated near the web opening. With the increase of the value of a/h, slight stress concentration appears in the compression flange above the hole

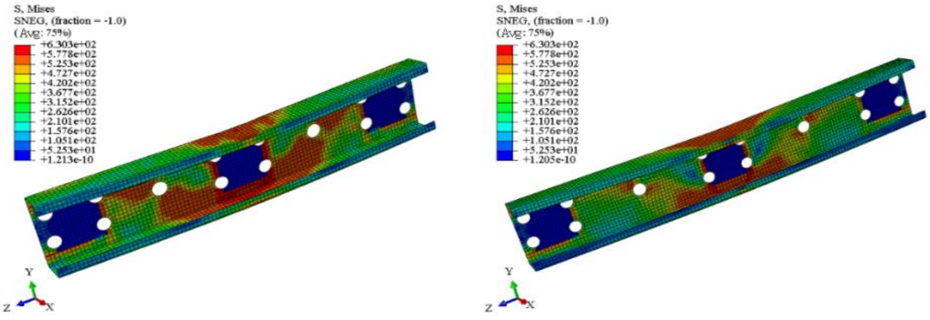

(a) H0.20-1.9-100-510 (a/h=1.5) (b) H0.20-1.9-100-610 (a/h=2.0)

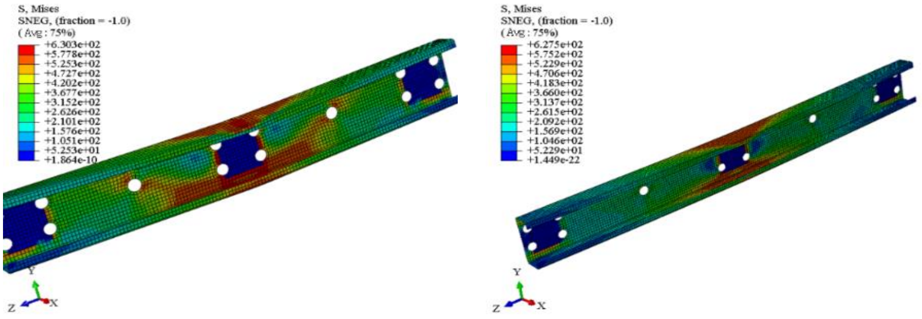

(c) H0.20-1.9-100-710 (a/h=2.5) (d) H0.20-1.9-100-910 (a/h=3.5)

Fig. 30 Failure mode with the value of a/h (h= 100 mm; t= 1.9 mm; d_h/h= 0.20)

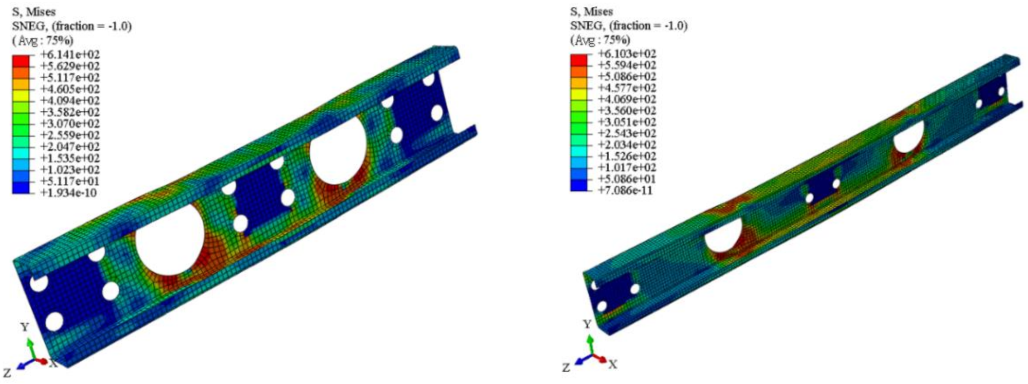

(a) H0.75-1.9-100-510 (a/h=1.5) (b) H0.75-1.9-100-910 (a/h=3.5)

Fig. 31 Failure mode with the value of a/h (h= 100 mm; t= 1.9 mm; d_h/h= 0.75)

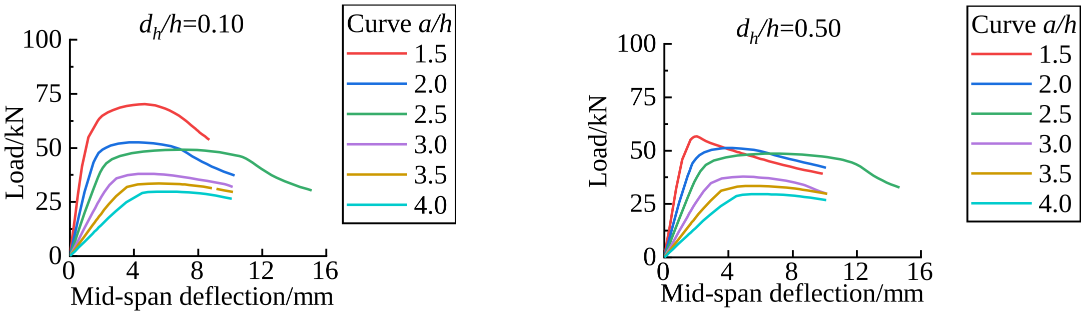

(a) (b)

Fig. 32 Load-deflection curves with the value of a/h (h/t =52.6)

Fig. 32 shows the load-deflection curve with the value of a/h, under the condition that the value of h/t is 52.6 (h= 100 mm, t= 1.9 mm) and the values of d_h/h are 0.1 and 0.5, respectively. As can be seen, stiffness of specimen drops as the increase of the value of a/h, which is due to that effect of bending moment also getting larger as the increase of the value of a/h.

4.5. Classification of failure mode of web perforated beam in combined bending and shear action

According to the analysis above, the bending-shear members studied in this paper have three types of failure modes, which are respectively the mainly shear failure, the mainly bending failure and the coupled failure of bending and shear.

The specimen subjected to mainly shear failure has the following characteristics: (1) The failure mode is dominated by local web shear buckling in the shear zone. (2) The bearing capacity shows sensitivity to the change of the value of d_h/h, and the corresponding bearing capacity is located at where the curve of bearing capacity against the value of d_h/h starts decreasing linearly.

The bearing capacity of web perforated specimen is close to that of solid-web specimen when it is subjected to mainly bending failure, thus the bearing capacity of steel beam can be mainly predicted according to the failure mode.

For beams subjected to the bending failure, flange stress concentration appears at mid-span, while web stress concentration is not significant. For beams subjected to the coupled failure of bending and shear, obvious stress concentration appears in both flange and web.

According to the characteristics of these three basic failure modes, Table 7 summarizes the classification of the failure modes of web perforated thin-walled C-shaped CFS bending-shear members with different loading conditions and geometric parameters.

Table 7

Classification of the failure mode of web perforated thin-walled C-shaped CFS beams under combined bending moment and shear force action

Failure mode	Demarcation conditions (Parameters range)
Mainly shear failure	(1) The value of a/h: $1.5 \leqslant a/h \leqslant 2.0$, and the value of d_h/h: $d_h/h \geqslant 0.60$; (2) The value of a/h: $2.0 < a/h \leqslant 4.0$, and the value of d_h/h: $d_h/h \geqslant 0.65$.
Coupled failure of bending and shear	Beams beyond the scope of parameters of steel beams with mainly shear failure and mainly bending failure in this Table.
Mainly bending failure	The value of a/h: $2.5 < a/h \leqslant 4$, and the value of d_h/h: $d_h/h \leqslant 0.2$.

5. Conclusions

This paper presents tests on 20 groups of thin-walled web perforated C-shaped CFS beams under combined bending moment and shear force action and the FEA by means of ABAQUS. The rationality of the model was verified by comparing results from test and FEA. Then refined parameter analysis was conducted on the three factors as follows: the value of d_h/h, the value of h/t and the value of a/h. On basis of that, failure modes of web perforated thin-walled C-shaped CFS beams under combined bending moment and shear force action were classified, and several conclusions were put ward as following:

(1) The value of d_h/h has a decisive effect on bearing capacity and failure mode of specimen. With the increase of the value of d_h/h, the failure mode of the steel beam transforms from the coupled failure of bending and shear to the shear failure, or from the bending failure to the coupled failure of bending and shear and then to the shear failure.

(2) The value of h/t affects failure mode of specimen mainly subjected to the bending failure and the coupled failure of bending and shear to a certain degree. With the increase of value of h/t, the stress concentration area decreases. With the same h, bearing capacity and stiffness of the specimen decrease as the value of h/t increases.

(3) The value of a/h affects failure mode of specimen mainly subjected to the bending failure and the coupled failure of bending and shear to a certain degree. With the increase of the value of a/h, web stress concentration in in shear zone and stiffness of specimen decrease. With a relatively smaller value of d_h/h ($d_h/h \leq 0.5$), bearing capacity shows more sensitivity to the change of the value of a/h, and bearing capacity drops as the increase of the value of a/h.

Acknowledgement

The authors are appreciated for the funding and support from the National Natural Science Foundation of China (Grant No. 51608538), Testing Research Funding from Hunan Tieyuan Civil Engineering Testing Co., Ltd (HNTY2021K02) and Natural Science Foundation of Hunan Province (2021JJ50029).

References

[1] Langan J E., Laboube R A., YU W., Structural behavior of perforated web elements of cold-formed steel flexural members subjected to web crippling and a combination of web crippling and bending[D]. University of Missouri-Rolla, 1994.

[2] Uphoff C, Laboube R A, YU W., Structural behavior of circular holes in web elements of cold-formed steel flexural members subjected to web crippling for End-One-Flange loading[D]. University of Missouri-Rolla, 1996.

[3] Eiler M, Laboube R, YU W., Behavior of web elements with openings subjected to linearly varying shear[D]. University of Missouri-Rolla, 1997.

[4] North American specification for the design of cold-formed steel structural members: AISI-S100-2016[S]. Washington: American Iron and Steel Institute, 2016.

[5] Standards Australia/Standards New Zealand (SA). Australia/New Zealand standard A S/NZS4600 cold-formed steel structures, Sydney, Australia; 2005.

[6] Schafer B W, Pekoz T., Laterally braced cold-formed steel flexural members with edge stiffened flanges[J]. Journal of Structural Engineering-ASCE, 1999, 125(2): 118-127.

[7] Schafer B W., Local, distortional, and Euler buckling of thin-walled columns[J]. Journal Of Structural Engineering-ASCE, 2002, 128(3): 289-299.

[8] YU C, Schafer B W., Distortional buckling tests on cold-formed steel beams[J]. Journal Of Structural Engineering, 2006, 132(4): 515-528.

[9] Schafer B.W., Direct strength method design guide[Z]. Washington. American Iron and Steel Institute, 2006.

[10] Moen C D., Direct strength design of cold-formed steel members with perforations[D]. The Johns Hopkins University, 2009.

[11] Moen C D, Schafer B W., Elastic buckling of cold-formed steel columns and beams with holes[J]. Engineering Structures, 2009, 31(12): 2812-2824.

[12] Moen C D, Schafer B W., Elastic buckling of thin plates with holes in compression or bending[J]. Thin-Walled Structures, 2009, 47(12): 1597-1607.

[13] Moen C D, Schudlich A, von der Heyden A., Experiments on cold-formed steel C-shaped joists with unstiffened web holes[J]. Journal of Structural Engineering, 2013, 139(5): 695-704.

[14] Pham C H, Hancock G J., Direct strength design of cold-formed C-shapeds for shear and combined actions[J]. Journal of Structural Engineering, 2012, 138(6): 759-768.

[15] Keerthan P, Hughes D, Mahendran M., Experimental studies of hollow flange channel beams subject to combined bending and shear actions[J]. Thin-Walled Structures, 2014, 77: 129-140.

[16] Keerthan P, Mahendran M, Hughes D., Numerical studies and design of hollow flange channel beams subject to combined bending and shear actions[J]. Engineering structures, 2014, 75: 197-212.

[17] Faridmehr I, Tahir M M, Osman M H, et al., An experimental investigation of stiffened cold-formed C-channels in pure bending and primarily shear conditions[J]. Thin-Walled Structures, 2015, 96: 39-48.

[18] Wang L, Young B., Beam tests of cold-formed steel built-up sections with web perforations[J]. Journal of Constructional Steel Research, 2015, 115: 18-33.

[19] Wang L, Young B. Design of cold-formed steel built-up sections with web perforations subjected to bending[J]. Thin-Walled Structures, 2017, 120: 458-469.

[20] Pham S H, Pham C H, Hancock G J., Experimental study of shear strength of cold-formed channels with an aspect ratio of 2.0[J]. Journal of Constructional Steel Research, 2018, 149: 141-152.

[21] Pham S H, Pham C H, Rogers C A, et al., Experimental validation of the Direct Strength Method for shear spans with high aspect ratios[J]. Journal of Constructional Steel Research, 2019, 157: 143-150.

[22] Degtyareva N, Gatheeshgar P, Poologanathan K, et al., Combined bending and shear behaviour of slotted perforated steel channels: Numerical studies[J]. Journal of Constructional Steel Research, 2019, 161: 369-384.

[23] Lawson R M, Basta A., Deflection of C section beams with circular web openings[J]. Thin-Walled Structures, 2019, 134: 277-290.

[24] Pham D K, Pham C H, Pham S H, et al., Experimental investigation of high strength cold-formed channel sections in shear with rectangular and slotted web openings[J]. Journal of Constructional Steel Research, 2020, 165: 10588.

[25] Wang L, Li J, Luo C, et al. Experimental and numerical study on the shear behavior of web perforated cold-formed steel beams[J]. Structures, 2022, 45: 2117-2136.

Advanced Steel Construction – Vol. 19 No. 1 (2023) 70–76
DOI:10.18057/IJASC.2023.19.1.9
(**Special Issue:** *10th International Conference on Advances in Steel Structures, ICASS'2020, Chengdu, China*)

MECHANICAL PROPERTIES AND SIMULATION METHOD OF STRUCTURAL STEEL AFTER HIGH CYCLE FATIGUE DAMAGE

Qi Si [1], Yang Ding [1, 2], Liang Zong [1, 2, *] and Heng Liu [1]

[1] *School of Civil Engineering, Tianjin Univ., Tianjin 300072, China.*
[2] *Key Laboratory of Coast Civil Structure Safety, Ministry of Education, Tianjin Univ., Tianjin 300072, China*
** (Corresponding author: E-mail: zongliang@tju.edu.cn)*

ABSTRACT

The steel structure will be subjected to alternating loads during its service, so the fatigue damage will gradually accumulate. Although fatigue damage may not cause immediate failure of the steel structure, the mechanical properties of the steel structure will inevitably be weakened. In this paper, the changes in mechanical properties of Q355B and Q690D steels after fatigue damage were investigated by static tensile tests. Then, a numerical simulation method for structural steel after fatigue damage was proposed. Finally, the results obtained from the finite element model were compared with the experimental results to verify the accuracy of the proposed numerical simulation method.

ARTICLE HISTORY

Received: 20 July 2022
Revised: 22 August 2022
Accepted: 10 January 2023

KEYWORDS

Steel structure;
Mechanical properties;
Simulation method;
Fatigue damage;
High cycle fatigue

1. Introduction

With the continuous development of Chinese infrastructure construction, steel structures are widely adopted in large-span space structures, bridge structures, marine engineering structures, and many other important projects with the advantages of lightweight, excellent mechanical properties, and recyclability. Steel structure engineering in its service period will be subject to long-term alternating loads such as vehicles, wind, waves, etc., which accumulate to form significant fatigue damage. Although fatigue damage may not cause immediate failure of the steel structure, the mechanical properties of the steel structure will inevitably be weakened under the effect of long-term cumulative damage, increasing the potential safety risks.

In recent years, the influence of fatigue damage on the mechanical properties of metal materials has attracted the attention of scholars at home and abroad, and related research has been carried out. In terms of experimental research, Moćko [1] studied the effects of pre-fatigue on the DP 500 steel during tensile tests at low and high strain rates. Cockings [2] studied the effect of pre-strain and pre-fatigue on the monotonic behavior of AerMet100, 300M, and MLX-17 steels. Zhang [3] studied the residual strength of Q690 high-strength steel with pre-fatigue damage through a static tensile test. Wu [4] studied the degradation mechanism of mechanical properties of 45 steel with different degrees of fatigue damage. Tang [5] investigated the influence of pre-fatigue damage on the mechanical properties of Q345 steel and studied the effects of the pre-damage levels on the ultimate bending strength of thin-walled steel columns. Sun and Guo [6] measured the high-cycle fatigue damage based on electrical resistance change. Sánchez-Santana [7] studied the effect of fatigue damage on the dynamic tensile behavior of 6061-T6 aluminum alloy and AISI 4140T steel.

In terms of numerical simulation studies, current research mainly focuses on fatigue crack initiation and propagation. Xin et al. [8,9] considered the damage accumulation under cyclic loading based on the SWT damage model and simulated the crack initiation of S355 and S690 through the extended finite element method. Zhang and Ma [10] studied the high-cycle and very-high-cycle fatigue (VHCF) behaviors of AlSi10Mg alloy produced by additive manufacturing and developed a crystal plasticity finite element model (CPFEM) with Voronoi tessellation to simulate the cyclic plastic deformation considering defect effects. Tanaka and Mura [11] first proposed the stress cycle required to calculate the fatigue crack initiation in the slip band based on the crack initiation theory. Based on the Tanaka-Mura crack initiation model, Bruckner [12] first simulated the microcrack initiation process using the finite element method. Jezernik et al. [13] considered that the formation of slip band cracks in the grain was not instantaneous but a slow change process and simulated it in stages.

To sum up, there are few studies on the degradation law and simulation method of mechanical properties of steel after fatigue damage. In this paper, Q355B steel and Q690D steel, which are the most commonly used steel grade for steel structures in China, were examined. Firstly, the changes in mechanical properties of Q355 and Q690 steels with fatigue damage were investigated by static tensile tests. Then, a numerical simulation method for structural steel with fatigue damage was proposed based on the continuous medium damage mechanics model and extended finite element method. Finally, the results obtained from the finite element model were compared with the experimental results to verify the accuracy of the proposed numerical simulation method.

2. Experimental research

In this paper, the experimental scheme is divided into the following three steps: Firstly, five specimens with polished surfaces were tested for high cycle fatigue life under the conditions that loading stress is σ0 and stress ratio is -1. The standard of fatigue failure of specimens was that the loading frequency of the test machine decreased by 5 Hz or cracks appeared on the surface of the specimens. The average value of the fatigue life of the five specimens was taken as the fatigue life Nf of the material under the loading stress of σ0 and the stress ratio of -1. Secondly, according to the linear cumulative damage criterion, high-frequency vibrations were applied to the steel coupons at different times to obtain the pre-fatigue steel specimens with specified damage degrees. Finally, the monotonic tensile loading tests were carried out on pre-fatigue steel coupons to investigate the effects of fatigue damage on the mechanical properties of Q355B and Q690D steel.

2.1. Tensile test on Q355B with pre-fatigue damage

The Q355B specimens were taken from 25 mm thick Q355B steel plates. Cylindric coupons were adopted, and the dimensions were determined according to the Chinese standards GB/T 228.1-2010 and GB/T 3075-2008, as illustrated in Fig. 1.

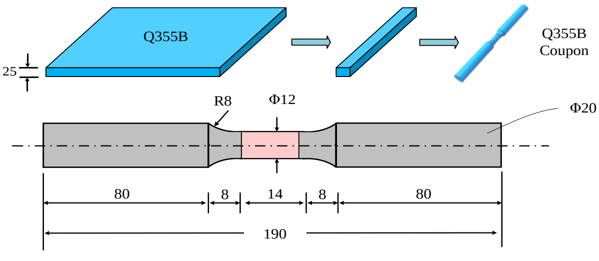

Fig. 1 Dimensional diagram of Q355B specimen (unit:mm)

Fig. 2 QBG-300

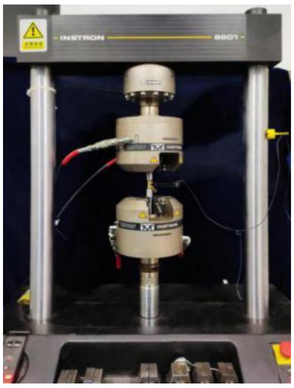

Fig. 3 Instron 8801

The high-cycle fatigue tests were carried out with the QBG-300 high-frequency testing equipment, as shown in Fig. 2. The stress amplitude σ_0 for the Q355B high-cycle fatigue tests was set to 250 MPa with the stress ratio R equal to -1, and the load form was sinusoidal. The fatigue life of five Q355B fatigue specimens was obtained, i.e., 109.5×10^4, 101.8×10^4, 112.1×10^4, 106.2×10^4, and 117.1×10^4. The average life of the five coupons 109.3×10^4 was taken as the high cycle fatigue life N_f of Q355B at this stress amplitude.

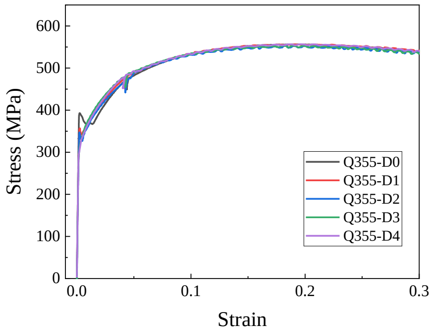

(a) Stress-strain curve

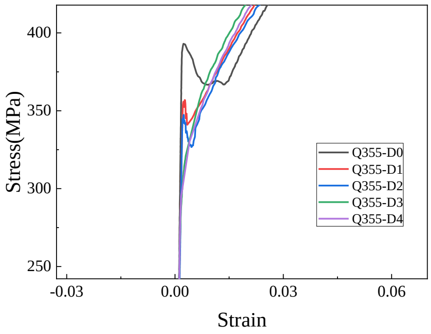

(b) Yield platform

Fig. 4 Mechanical properties of Q355 steel after fatigue damage

Table 1
Mechanical properties of Q355 steel after fatigue damage

Coupons	D	E (MPa)	f_y (MPa)	f_u (MPa)	f_u / f_y
Q355-D0	0.00	215045	388	556	1.44
Q355-D1	0.19	205138	357	556	1.56
Q355-D2	0.37	204337	346	548	1.59
Q355-D3	0.56	199664	330	558	1.69
Q355-D4	0.74	198010	304	557	1.83

With the same stress amplitude and stress ratio, 20×10^4, 40×10^4, 60×10^4, and 80×10^4 cycles of pre-fatigue loading were conducted on the specimens, respectively, and thus the specimens of Q355B steel after fatigue damage were obtained. Miner's linear fatigue accumulation methods were adopted to quantify the fatigue damage degree. Then, monotonic tensile tests were conducted on the pre-fatigued coupons with Instron model 8801, as shown in Fig. 3. The monotonic tensile tests were carried out with displacement control, and the engineering stress-strain curve obtained from the experiment is plotted in Fig. 4, and the main mechanical property parameters are listed in Table 1.

From the test results, with the increase of pre-fatigue damage, the upper yield point and yield plateau on the obtained stress-strain curves disappeared. As the degree of damage increased, the yield strength and elastic modulus tended to decrease [14].

To study the changes of Q355B steel mechanical properties with the degree of damage, the regression analysis was performed, as shown in Fig. 5, where E/E_0, f_y/f_{y0}, f_u/f_{u0} are the ratios of the yield strengths, ultimate strengths, fracture strains, and elastic moduli between the pre-fatigued and undamaged coupons, respectively.

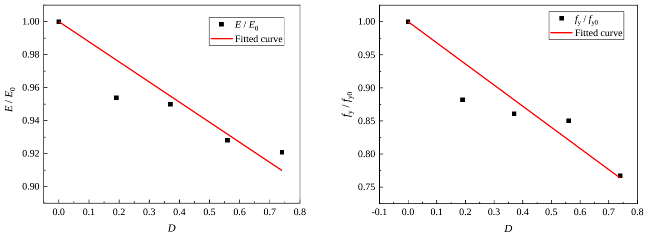

(a) Elastic modulus (b) Yield strength

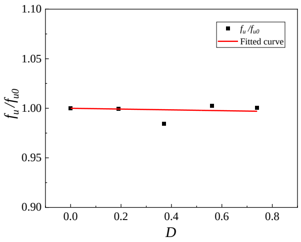

(c) Ultimate strength

Fig. 5 Relationship between mechanical properties and fatigue damage

Comparing the slopes of the regression curves, it shows that the decrease in elastic modulus and yield strength is serious, while the degradation in ultimate strength and fracture strain is little. This indicates that fatigue damage has a significant impact on the elastic mechanical properties of steel. A quantitative relationship between mechanical properties and the degree of damage was established, as expressed in Eq. (1)-(3).

$$E/E_0 = -0.12185D + 1 \qquad R^2 = 0.99981 \tag{1}$$

$$f_y / f_{y0} = -0.31935D + 1 \qquad R^2 = 0.99851 \tag{2}$$

$$f_u / f_{u0} = -0.00403D + 1 \qquad R^2 = 0.99994 \tag{3}$$

2.2. Tensile test on Q690D with pre-fatigue damage

Q690D coupons in the test were taken from 14 mm Q690D steel plates. The experiments were carried out regarding the Q355B test. The geometric dimensions of the Q690D specimens are illustrated in Fig. 6.

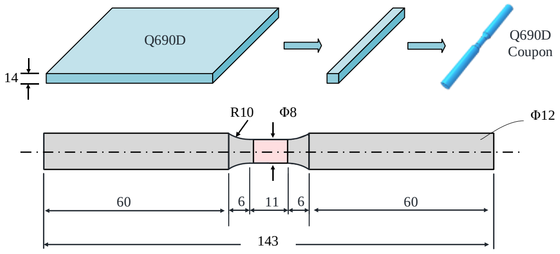

Fig. 6 Geometric dimensions of the Q690D specimens (unit:mm)

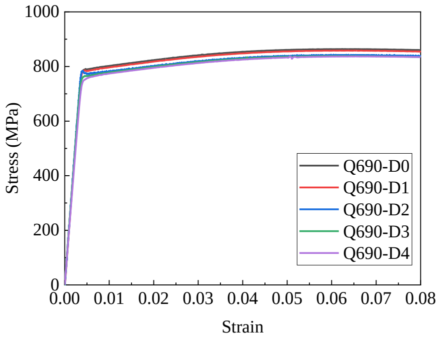

(a) Stress-Strain curve

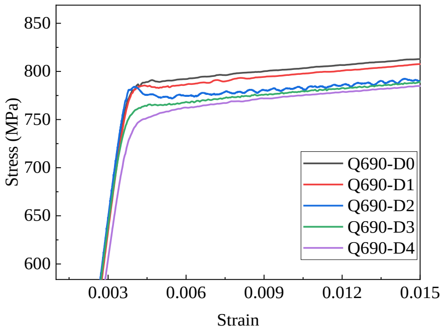

(b) Stress-Strain curve at the yield point

Fig. 7 Mechanical properties of Q690 steel after fatigue damage

The high cycle fatigue tests of Q690D were performed under a stress amplitude of 450MPa and a stress ratio of -1, with the QBG-300 high-frequency testing equipment as well. The fatigue life of the five specimens is 46.7×10^4, 56.8×10^4, 38.9×10^4, 39.5×10^4, and 53.5×10^4 respectively, and the high cycle fatigue life of Q690D at this stress amplitude was set as 50×10^4.

Same as the pre-fatigue loading procedure of Q355B, 20×10^4, 30×10^4, 40×10^4, and 45×10^4 cycles of pre-fatigue loading were conducted on the specimens respectively, to obtain Q690D specimens after fatigue damage. The monotonic tensile tests were conducted on the prepared coupons. During the experiments, the extensometer was taken off when the strain reached 8% before which necking had appeared and the loading force decrease had begun [15]. The engineering stress-strain curves and main mechanical properties can be found in Fig. 7 and Table 2, respectively.

Table 2
Mechanical properties of Q690 steel after fatigue damage

Coupons	*D*	*E* (MPa)	f_y (MPa)	f_u (MPa)	f_u / f_y
Q690-D0	0	217100	791	863	1.09
Q690-D1	0.4	216800	784	858	1.09
Q690-D2	0.6	215900	783	853	1.09
Q690-D3	0.8	208500	766	840	1.10
Q690-D4	0.9	202900	761	837	1.10

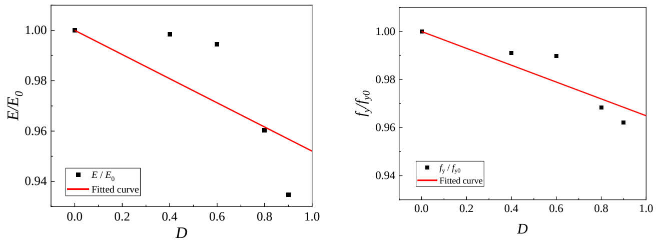

(a) Elastic modulus (b) yield strength

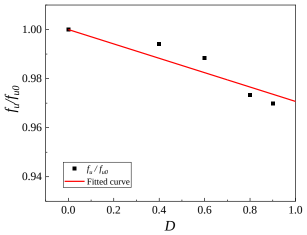

(c) ultimate strength

Fig. 8 Relationship between mechanical properties and fatigue damage

From the experimental result, the influence of fatigue damage on the mechanical properties of Q690D is similar to that of Q355B, and the elastic modulus, yield strength, and ultimate strength of Q690D decrease with the increase of fatigue degree. The variation of the mechanical parameters with the increase of damage variables was described with the normalized parameters, as shown in Fig. 8.

The quantitative relationships between mechanical properties and the pre-fatigue damage degree are established, as expressed in Eq. (4)-(6).

$$E / E_0 = -0.04796D + 1 \qquad R^2 = 0.99965 \tag{4}$$

$$f_y / f_{y0} = -0.03504D + 1 \qquad R^2 = 0.99995 \tag{5}$$

$$f_u / f_{u0} = -0.02929D + 1 \qquad R^2 = 0.99998 \tag{6}$$

3. Numerical simulation methods

3.1. Related theories

The current research on fatigue damage models of metals is mainly divided into the following two categories: The continuous damage mechanics model and the meso-damage mechanics model. Continuous damage mechanics is an image-only approach further developed based on the ductile fracture criterion. It considers the evolution of the microstructure during plastic deformation as an irreversible dissipative process based on the theory of continuous damage mechanics and continuous damage thermodynamics. Kachanov [16] first proposed the concept of continuity in 1958 when studying the problem of the creep of metals. On this basis, Rabotnov [17] proposed the concept of damage degree, as shown in Eq. (7). In the following decades, with the growing interest of scholars, damage mechanics has been continuously developed and has become an increasingly vital tool for the study of material damage.

$$D = 1 - \varphi = 1 - \frac{A}{A_0} \tag{7}$$

where *D* is the damage degree, *A* is the effective area, and A_0 is the apparent area of the material. Lemaitre and Chaboche further developed the damage mechanics theory and established the fatigue damage evolution equation based on irreversible thermodynamics and continuous medium mechanics. Li [18] established the fatigue damage evolution equation for the condition of pulsating loads in uniaxial fatigue problems:

$$\frac{\delta D}{\delta N} = \frac{\sigma_m^{(\beta+3)}}{B(\beta+3)(1-D)^{a_2}} \tag{8}$$

where σ_m is the maximum value of the stress cycle when the minimum stress equals 0, *B* is the material constant, and β and a_2 could be obtained from data fitting with fatigue tests.

According to meso-damage mechanics, the damage of fatigue is the result of the generation and development of micro-defects in materials. These micro-defects include dislocation, slip, micro-voids, and micro-cracks of grains, among which micro-voids and micro-cracks are the main forms of defects. Gurson [19] proposed a method for calculating approximate yield loci via an upper-bound approach for porous ductile materials. Tvergaard and Needleman [20] proposed the Gurson-Tvergaard-Needleman (GTN) model based on the Gurson damage model, considering the interactions between the pores, in which the damage is described as the volume fraction of spherical or ellipsoidal pores.

At the microscale, Angelika Brückner-Foit [21] used the Voronoi method to generate representative volume elements (RVEs) for polycrystalline materials and performed numerical simulations of crack initiation in martensitic steels by introducing the fatigue cracks into the finite element model. M. Mlikota [22] predicted the initiation of short fatigue cracks based on the Tanaka-Mura model and studied the effect of grain size on the fatigue initiation life.

3.2. Simulation method and process

For metallic materials, the whole fatigue damage process mainly consists of the initiation, extended stages of micro-cracks, and the extended stages of long cracks [23, 24]. With most of the fatigue life consumed in the micro-crack stage, the phenomenon on the microscopic scale is the formation and propagation of many micro-cracks in the grain, as shown in Fig. 9. The square hexagon in Fig. 9 represents the grains that make up the material, and the short red lines represent the micro-cracks induced by fatigue loading.

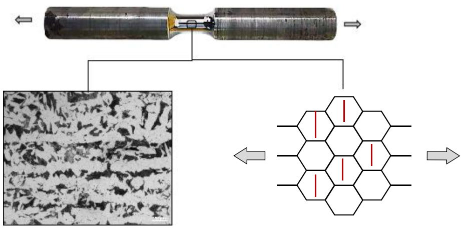

Fig. 9 Schematic diagram of micro-cracks

To define the micro-crack dominated fatigue damage variable, the total number of micro-cracks generated in the specimen under fatigue loading is noted as *n*, and the length of each micro-crack is noted as CRACK[i]. It is assumed that these micro-cracks are randomly distributed in the specimen. To further simplify the model, the direction of each micro-crack is set to be vertical to the force direction and the projection of each micro-crack in the vertical direction of the force has no overlapping part. With the above assumption, according to the continuous damage mechanics model, the damage degree *D* of the material specimen is calculated as

$$D=\sum_{i=0}^{n}\mathrm{CRACK[i]}/W \tag{9}$$

where *W* and *L* are the width and length of the specimen respectively. In this paper, *W* and *L* were taken as the diameter and length of the effective part of the specimen correspondingly. Then the *i*-th micro-crack would start at (X[i], Y[i]) and end at (X[i], Y[i]+CRACK[i]) as the direction and length of the micro-crack have been determined. Assuming that the micro-cracks are randomly distributed in the vertical direction of the force, the vertical distance (*d*) between the *i*+1th micro-crack and the *i*-th micro-crack is *d*=random.uniform(0,1)×(1-*D*)/*D*×Crack[i+1], as shown in Fig. 10.

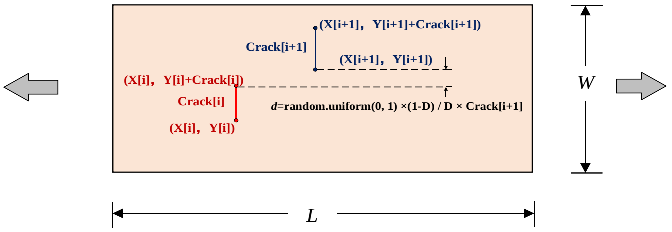

Fig. 10 Coordinates of microcracks

At present, there is no standard criterion for determining fatigue crack emergence, and some scholars [25, 26] take 3-5 times the grain size as the critical value for crack emergence. For structural steel engineering, it is more practical to develop different fatigue crack initiation thresholds depending on the accuracy of the observation, with the crack size at fatigue crack initiation usually being in the range of 0.1 mm to 0.5 mm, while some literature adopts a more precise range (0.25 mm to 0.3 mm). In this paper, it is assumed that the size of the micro-crack is in the range of 0.1mm to 0.3mm.

The simulation of the mechanical properties of steel with pre-fatigue damage could be divided into the following steps:

1. Determine the geometry dimensions W and L of the model, as well as the damage degree (*D*). Define three integers in Python to represent the above three parameters, and define three empty arrays X[], Y[], and CRACK[], which would be used to store the starting coordinates of each micro-crack in the model and the length of the micro-crack.

2. Define a micro-cracks generating loop with the "while" commend, in which a random line segment of length between 0.1 and 0.3 mm is continuously generated to represent the micro-cracks caused by fatigue damage, and the loop stops until the total length of the generated micro-cracks is greater than *D*×*W*, and finally outputs the length of each micro-crack, i.e. CRACK[i].

3. Randomly generate the ordinate of the first micro-crack. Then the ordinate of the starting point of the *i*+1th micro-crack can be calculated according to the formula in Fig. 11.

4. Random numbers with the same number of micro-cracks were generated in the range of 0.5 to *L*-0.5 as the abscissa of each micro-crack. To avoid the influence of the too-close distance between two adjacent micro-cracks on the convergence of the FE model, it is assumed that the horizontal distance between two adjacent micro-cracks is greater than 0.3 mm.

The extended finite element method (XFEM) was used to consider the micro-cracks caused by fatigue load. XFEM is suitable for arbitrary boundary conditions, geometric shapes, and nonlinear geometric problems. Based on XFEM, numerical simulations of steel material containing inner micro-cracks were carried out with the general finite element software ABAQUS.

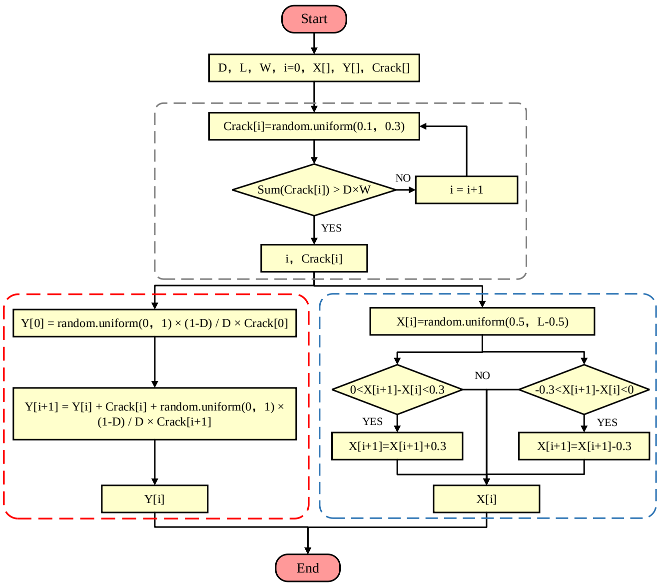

Fig. 11 Flow chart of the modeling

4. Validation of simulation method

To verify the accuracy and reliability of the numerical simulation method proposed in this paper, numerical simulations of pre-fatigued Q355B and Q690D under static tensile loading were carried out using the finite element software ABAQUS. In ABAQUS, the engineering stress-strain curve of the specimen without damage was converted into the true stress-strain curve as the constitutive relationship of the material in the finite element model, and the isotropic hardening was selected as the hardening type of the material. The two-dimensional finite element models corresponding to the geometry of the Q355B and Q690D specimens were established using the CPS4R element.

4.1. Verification and calculation of FE model of Q355B specimen

According to the simulation method of steel after fatigue damage proposed in this paper, the Python programming language was adopted to automatically generate Q355B FE models with different damage degrees corresponding to the pre-fatigue loading test, as shown in Fig. 12.

As mentioned above, the XFEM was used to simulate micro-cracks, as shown in Fig. 13(a). It is worth mentioning that to better reflect the change of yield platform, the lower yield point in the stress-strain curve of Q355b steel obtained from the test was selected as the yield stress when defining the material properties. The boundary conditions of the FE model are as follows: the left boundary was fixed, and the reference point was defined to couple the right side surface to apply displacement load to the specimen, as shown in Fig. 13(b).

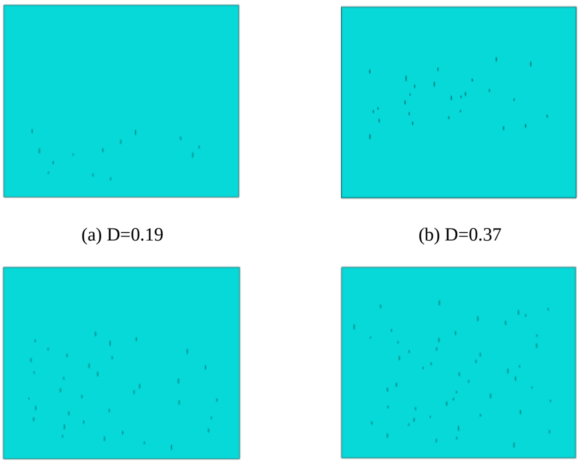

(a) D=0.19

(b) D=0.37

(c) D=0.56

(d) D=0.74

Fig. 12 Finite element model of Q355 after fatigue damage

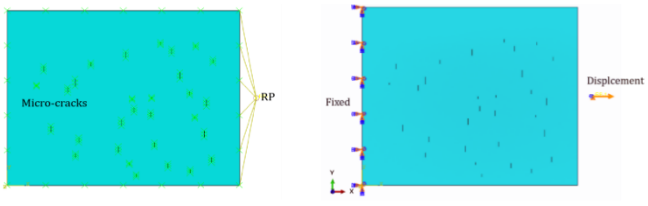

(a) Interaction

(b) Boundary condition

Fig. 13 Specific settings of the FE model

Fig. 14 shows the Mises stress of the Q355B specimen under different fatigue damage degrees. It can be seen that when there is no fatigue damage, the stress distribution of the model is relatively uniform, and necking occurs in the middle of the model. With the introduction of micro-cracks, the stress concentration at the crack tip is obvious, and the necking position of the FE model is different from that of the non-damage model.

The STATUSXFEM of the FE model when the step time is 0 is shown in Fig. 14(d). It can be seen that the value of STATUSXFEM at the micro-crack is 1.0 when the analysis step time is 0, that is, when the FE model starts to calculate, which indicates that the displacement on both sides of the micro-crack is discontinuous, and the crack is successfully considered.

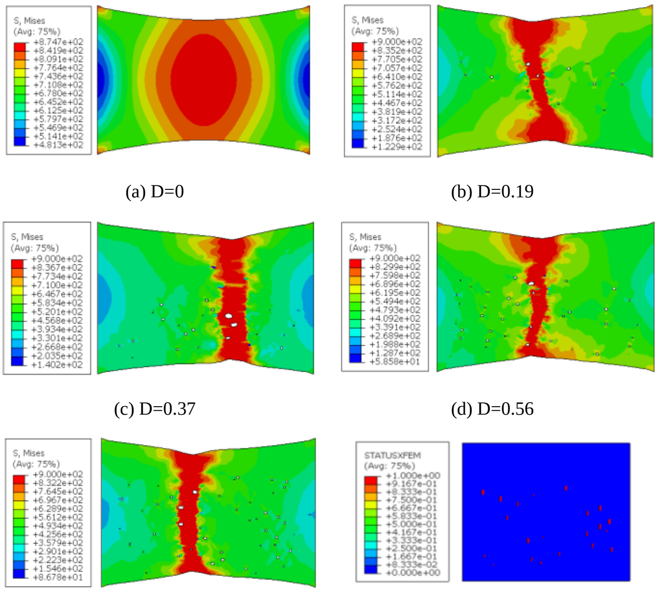

(a) D=0

(b) D=0.19

(c) D=0.37

(d) D=0.56

(d) D=0.74

(d) STATUSXFEM

Fig. 14 Nephogram of the finite element model of Q355

The engineering stress-strain curve of the Q355 specimen under different damage degrees obtained by simulation was shown in Fig. 15. It reflects that the yield platform of Q355 steel gradually disappears with the increase of fatigue degree. The yield strength of Q355B steel decreases with the increase of fatigue strength, and the variation trend of the FE results is consistent with the test results.

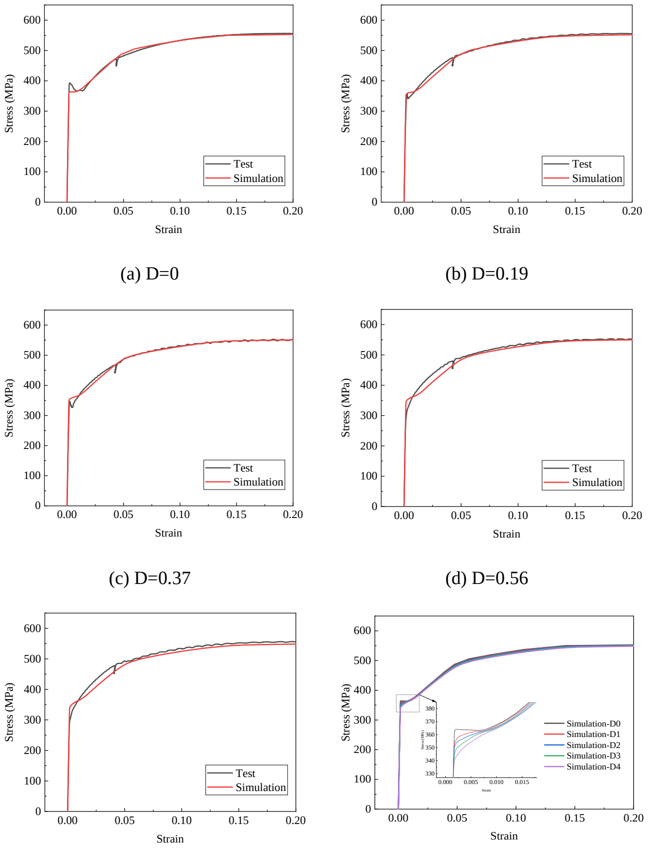

(a) D=0

(b) D=0.19

(c) D=0.37

(d) D=0.56

(e) D=0.74

(f) simulation results

Fig. 15 Comparison of calculation results of Q355B FE models

The yield and ultimate strengths obtained from the simulation were compared with the test values, as shown in Table 3. For the Q355B material after fatigue damage, the maximum difference between the yield strength obtained by the FE simulation and the experimental results is 7.57%, and the maximum difference between the ultimate strength obtained by the FE simulation and the experimental value is 1.80%, which shows the accuracy of the simulation method.

Table 3
Comparison between FE and test results of Q355B

D	f_y (MPa)			f_u / (MPa)		
	FE	Test	Deviation (%)	FE	Test	Deviation (%)
0.19	353	357	1.12	551	556	0.90
0.37	349	346	0.87	550	548	0.36
0.56	339	330	2.73	549	558	1.61
0.74	327	304	7.57	547	557	1.80

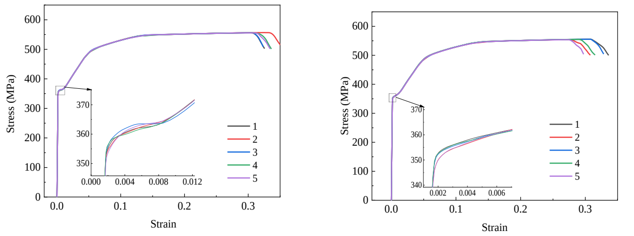

(a) D=0.19

(b) D=0.37

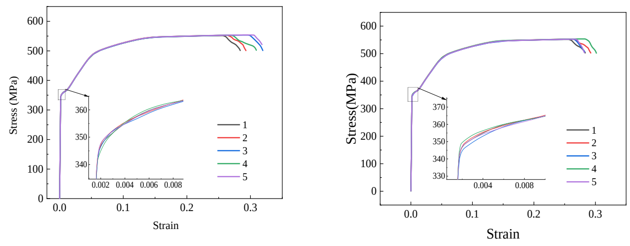

(c) D=0.56 (d) D=0.74

Fig. 16 Results of Q355B FE models

To avoid accidental errors and fully verify the feasibility of the simulation method proposed in this paper, five corresponding finite element models were generated for each damage degree and calculated, and the results obtained are shown in Fig. 16.

The stiffness, yield strength, and ultimate strength calculated by the finite element method have little change in the same damage degree, and the curves obtained by the finite element method almost coincide with the experimental results, which indicates that the simulation method proposed in this paper has good stability and accuracy for Q355B steel.

4.2. Verification and calculation of FE model of Q690D specimen

Based on the simulation method proposed in this paper, the finite element models of Q690 with different damage levels corresponding to the pre-fatigue loading tests were established in ABAQUS. The geometric dimensions of the generated finite element model refer to the dimensions of the effective section. The contact, mesh, and boundary conditions of the Q690 FE model are consistent with those of the Q355B FE model.

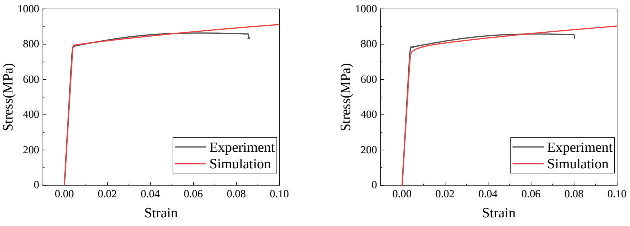

(a) D=0 (b) D=0.4

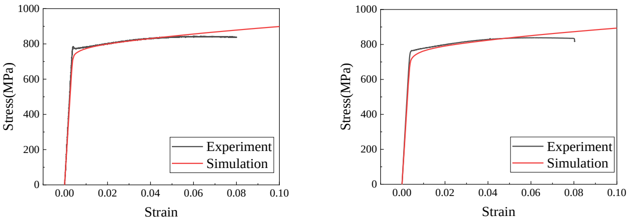

(c) D=0.6 (d) D=0.8

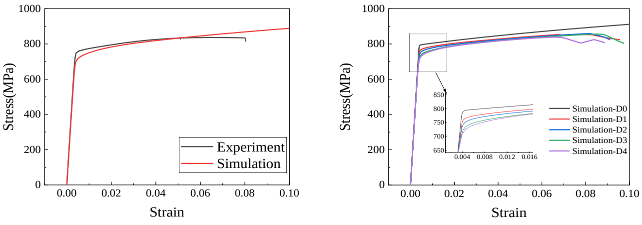

(e) D=0.9 (f) simulation results

Fig. 17 Comparison of calculation results of Q690D FE models

Fig. 17 shows the comparison between the engineering stress-strain curves of the Q690D specimen under different damage degrees obtained by finite element simulation and the test results. The yield and ultimate strengths obtained from the simulation were compared with the test values, as shown in Table 4.

Table 4
Comparison between FE and test results of Q690D

D	f_y (MPa) FE	Test	Deviation (%)	f_u / (MPa) FE	Test	Deviation (%)
0.4	757	784	3.44	877	858	2.21
0.6	744	783	4.98	876	853	2.70
0.8	725	766	5.35	872	840	3.81
0.9	711	761	6.57	863	837	3.11

According to the comparison results, for the Q690D material after fatigue damage, the maximum difference between the yield strength obtained by the FE simulation and the experimental value is 6.57%, and the maximum difference between the ultimate strength obtained by the FE simulation and the experimental value is 3.81%. It can be seen that the simulation values are in good agreement with the test values, indicating the feasibility of the simulation method proposed in this paper.

Similar to the numerical simulation of the Q355B specimen, five FE models corresponding to Q690 steel in each damage degree were established and calculated. The calculation results are shown in Fig. 18. The curves under the same damage state are almost coincident and consistent with the experimental values, which shows that the proposed method has good accuracy and stability for Q690D steel.

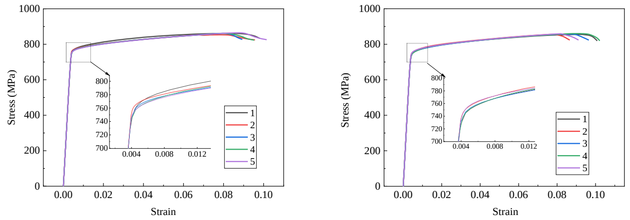

(a) D=0.4 (b) D=0.6

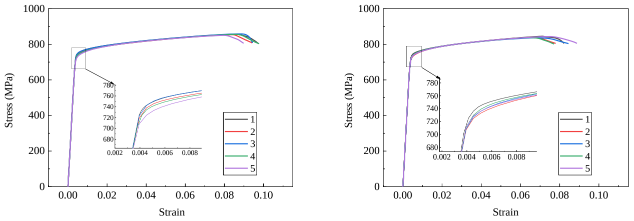

(c) D=0.8 (d) D=0.9

Fig. 18 Results of Q690D FE models

5. Conclusions

The residual mechanical properties of Q355B and Q690D structural steel after exposure to varying degrees of pre-fatigue damage were investigated in the present study. The main conclusions are as follows:

(1) Under monotonic loading, with the increase of pre-fatigue damage, the Young's modulus and yield strength of Q355B steel tended to decrease, and the yield plateau in the stress-strain curve gradually disappeared, while the ultimate strength remained effectively unchanged.

(2) The change of mechanical properties of Q690D after fatigue damage is similar to that of Q355B, but the change of ultimate strength of Q690D after the damage is more obvious than that of Q355B.

(3) The numerical simulation method of steel after fatigue damage proposed in this paper can accurately simulate the mechanical properties of Q355B and Q690D after fatigue damage.

Acknowledgement

The reported research work was sponsored by the National Key Research and Development Program of China (2018YFC1504304).

References

[1] Moćko W, Brodecki A, Radziejewska J. Effects of pre-fatigue on the strain localization during tensile tests of DP 500 steel at low and high strain rates[J]. The Journal of Strain Analysis for Engineering Design, 2015, 50(8): 571-583.

[2] Cockings H L, Cockings B J, Perkins K M. On the effect of pre-strain and pre-fatigue on the monotonic behaviour of ultra-high strength steels[J]. Heliyon, 2020, 6(7): 4440.

[3] Zhang C, Wang R, Song G. Effects of pre-fatigue damage on mechanical properties of Q690 high-strength steel[J]. Construction and Building Materials, 2020, 252: 118845.

[4] Wu Z. Investigation for the relation between the fatigue damage and the degeneration of mechanical properties in metal materials[J]. Journal of Mechanical Strength, 2001, 23(2): 216-218.

[5] Tang Z, Hu X, Jiang J, et al. Effects of pre-fatigue damages on ultimate strength of steel columns: From material to structure[J]. Journal of Constructional Steel Research, 2022, 195: 107358.

[6] Sun B, Guo Y. High-cycle fatigue damage measurement based on electrical resistance change considering variable electrical resistivity and uneven damage[J]. International Journal of Fatigue, 2004, 26(5): 457-462.

[7] Sánchez-Santana U, Rubio-González C, Mesmacque G, et al. Effect of fatigue damage on the dynamic tensile behavior of 6061-T6 aluminum alloy and AISI 4140T steel[J]. International Journal of Fatigue, 2009, 31(11-12): 1928-1937.

[8] Xin H, Veljkovic M. Fatigue crack initiation prediction using phantom nodes-based extended finite element method for S355 and S690 steel grades [J]. Engineering Fracture Mechanics, 2019, 214: 164-176.

[9] Xin H, Correia J A F O, Veljkovic M. Three-dimensional fatigue crack propagation simulation using extended finite element methods for steel grades S355 and S690 considering mean stress effects [J]. Engineering Structures, 2021, 227: 111414.

[10] Zhang W, Hu Y, Ma X, et al. Very-high-cycle fatigue behavior of AlSi10Mg manufactured by selected laser melting: Crystal plasticity modeling[J]. International Journal of Fatigue, 2021, 145: 106109.

[11] Tanaka K, Mura T. A dislocation model for fatigue crack initiation[J]. Journal of applied mechanics, 1981, 48, 97-103.

[12] Brückner-Foit A, Huang X. Numerical simulation of micro-crack initiation of martensitic steel under fatigue loading[J]. International journal of fatigue, 2006, 28(9): 963-971.

[13] Glodež S, Jezernik N, Kramberger J, et al. Numerical modelling of fatigue crack initiation of martensitic steel[J]. Advances in Engineering Software, 2010, 41(5): 823-829.

[14] Si Q, Ding Y, Zong L, et al. Effect of pre-fatigue damage on static and hysteretic behavior of Q355 steel[J]. International Journal of Fatigue, 2022, 160: 106874.

[15] Zong L, Liu H, Si Q, Chung K. Pre-fatigue damage on the mechanical properties of Q690D steel[J]. International Journal of Fatigue, 2022. (under review)

[16] Kachanov L M. Time of the rupture process under creep conditions[J]. Izv AN SSSR Otd Tekhn Nauk, 1958, 8:26-31.

[17] Rabotnov Y N. Paper 68: On the equation of state of creep[C]. Proceedings of the Institution of Mechanical Engineers, Conference Proceedings. Sage UK: London, England: SAGE Publications, 1963, 178(1): 2-117-2-122.

[18] Sun B, Li Z. A multi-scale damage model for fatigue accumulation due to short cracks nucleation and growth[J]. Engineering Fracture Mechanics, 2014, 127: 280-295.

[19] Gurson A L. Continuum theory of ductile rupture by void nucleation and growth: Part I—Yield criteria and flow rules for porous ductile media[J]. 1977.

[20] Tvergaard V, Needleman A. Analysis of the cup-cone fracture in a round tensile bar[J]. Acta metallurgica, 1984, 32(1): 157-169.

[21] Brückner-Foit A, Huang X. Numerical simulation of micro-crack initiation of martensitic steel under fatigue loading[J]. International journal of fatigue, 2006, 28(9): 963-971.

[22] Mlikota M, Dogahe K, Schmauder S, et al. Influence of the grain size on the fatigue initiation life curve[J]. International Journal of Fatigue, 2022, 158: 106562.

[23] Hussain K, De Los Rios E R, Navarro A. A two-stage micromechanics model for short fatigue cracks[J]. Engineering Fracture Mechanics, 1993, 44(3): 425-436.

[24] Hong Y, Qiao Y. An analysis on overall crack-number-density of short-fatigue-cracks[J]. Mechanics of materials, 1999, 31(8): 525-534.

[25] Ge L. Predicting Fatigue Life Based on the Behavior of Short Fatigue Crack[J]. Materials For Mechanical Engineering, 2001. 25(2), 18-20. (in chinese)

[26] Wu Z. Statistical Investigation for the Behavior of Short Fatigue Cracks in Medium Carbon Steel[J]. Journal of Mechanical Strength, 20(4), 295-299 ,1998. (in chinese)

Advanced Steel Construction – Vol. 19 No. 1 (2023) 77–85
DOI:10.18057/IJASC.2023.19.1.10
(**Special Issue:** *10th International Conference on Advances in Steel Structures, ICASS'2020, Chengdu, China*)

SEISMIC RESILIENCE ASSESSMENT OF A SINGLE-LAYER RETICULATED DOME DURING CONSTRUCTION

Tian-Long Zhang and Jun-Yan Zhao *

School of Civil Engineering and Architecture, Hainan University, Haikou, China
** (Corresponding author: E-mail: jzhaojunyan@hainanu.edu.cn)*

ABSTRACT

The seismic bearing capacity of an incomplete single-layer reticulated dome during construction is significantly lower than that of a complete dome. To assess the seismic resilience of incomplete single-layer reticulated domes and find the most unfavorable construction stage, a new curve of recovery functionality and a new methodology of seismic resilience during construction were established in this study. Under the combined action of the bending moment and axial force, the damage state criterion of circular steel pipes was improved through hysteresis simulation analysis. Based on the elastoplastic time-history analysis of different construction models, the damage state levels of all structural members were employed to estimate the functionality loss after an earthquake event. The repair path and the repair time of damaged steel pipes were defined, and the structural recovery functionality was computed to assess the seismic resilience. The proposed methodology in this paper was demonstrated using a 40-meter span of the Kiewitt-8 dome with six circular grids considering both the construction process and seismic hazards. The results indicate that seismic resilience is related to the incomplete structural form of the dome during construction. The repair time will be the longest and the seismic resilience will be the lowest if the incomplete dome suffers an earthquake during the construction period when installing the fourth circular grid from outside to inside.

ARTICLE HISTORY

Received:	20 July 2022
Revised:	22 August 2022
Accepted:	10 January 2023

KEYWORDS

Single-layer reticulated dome;
Seismic resilience;
Construction model;
Damage state criterion

1. Introduction

Due to their light weight, thin thickness, reliable force, and beautiful shape, single-layer reticulated domes are widely used in large span buildings such as airports, stadiums and exhibition halls. Although this type of structure has the mechanical properties of a bar system and a thin shell structure, the existing earthquake hazard shows that members of a dome may experience damage, buckling and fracture to reduce the bearing capacity, threatening lives and the security of property. The dynamic responses and damage modes of complete single-layer reticulated domes under earthquakes have been researched deeply, laying foundations for performance-based seismic design methods of this spatial structure. Fan F. *et al.* [1] defined two types of failure modes of single-layer reticulated domes under a strong earthquake, including dynamic instability and plastic collapse. Zhi X.D. *et al.* [2] proposed different seismic performance levels based on the quantitative damage degree and established a criterion for the dynamic strength failure of single-layer reticulated domes. Nie G.B. *et al.* [3] analyzed the vulnerability curves of single-layer reticulated domes with the IDA method and suggested different overall damage indications. However, the seismic analysis of incomplete domes under construction has rarely been studied.

When a reticulated dome is under construction, the incomplete structural form is constantly changing, and therefore, the internal forces and boundary constraint conditions of the incomplete structure are quite different from those of the complete structure. Many scholars have simulated and analyzed the mechanical performance of spatial reticulated domes during the whole construction process. Liu X.W. *et al.* [4] combined a birth-death finite element technology and a step-by-step model simulation method to conduct a mechanical analysis of steel structures in construction. Tian L.M. *et al.* [5] analyzed the internal force and deformation of a complicated stadium during the construction process by using the finite element method for a large-span structure. Li Y.Y. *et al.* [6] used the finite element software Midas/Gen to simulate construction schemes for a long-span steel roof and studied the effect of different temporary supports under construction. However, the bearing capacity of a structure under construction has not yet been formed, so in this process, the incomplete dome may easily collapse under a strong earthquake, which will seriously affect construction safety, quality and cost. Previous research on the structural construction process has not considered the effect of earthquakes, and few studies have been performed on the seismic response of spatial structures during the construction period.

Seismic resilience refers to the ability to maintain and restore the original function of a structure after earthquake excitation. In the earliest research, Bruneau *et al.* [7] pointed out that seismic resilience can be evaluated from four aspects: robustness, redundancy, rapidity and resourcefulness. In recent years, the study of seismic resilience has mainly been focused on medical systems, water supply systems, bridge engineering and so on. Vásquez *et al.* [8] studied the response and resilience of the healthcare network in Iquique after the Pisagua earthquake in 2014. Favier *et al.* [9] investigated the effect of the Illapel earthquake on local hospitals in 2015. Domaneschi *et al.* [10] studied the immediate seismic resilience of a controlled cable-stayed bridge. Biondini *et al.* [11] studied the life-cycle resilience of deteriorating bridge networks under earthquake scenarios. Dong Y. *et al.* [12] proposed a framework for the probabilistic assessment of an interdependent healthcare-bridge network system under seismic hazards. Pang Y.T. *et al.* [13] assessed the life-cycle seismic resilience of highway bridges with fiber reinforced concrete piers in a corrosive environment by using the improved Cloud Analysis. There are some international standards for seismic resilience assessment of buildings, namely, FEMA-P58 [14], REDi Rating System [15], and USRC Building Rating System [16]. The Chinese standard, GB/T 38591-2020 "Standard for seismic resilience assessment of buildings" [17], was released in 2020. Lu X. [18] proposed a new quantification method of seismic resilience by FEMA-P58 and applied it to evaluate the seismic resilience of typical reinforced concrete frame core pipe tall buildings. Fang D.P. *et al.* [19] assessed the seismic resilience, including the building repair costs, repair time and casualties, in a typical community based on the Chinese standard, GB/T 38591-2020. Clearly, the application of building resilience evaluation standards is gradually becoming mature, and various researchers have carried out partial studies on the seismic resilience evaluation of different structures. However, there has been little research on the seismic resilience assessment of single-layer reticulated domes, especially incomplete domes during construction.

Based on the existing standard for seismic resilience assessment of buildings in China, the process of seismic resilience assessment of a single-layer spherical reticulated dome during construction was developed in this study, and two damage state criterion curves of steel pipe members, with bending moments or axial forces as the main damage, were improved. By taking a 40-meter span of a single-layer spherical reticulated dome as a case study, the seismic resilience in the whole construction process is evaluated.

2. Seismic resilience assessment process during construction

Proposed by Bruneau et al. [7], the curve of building recovery functionality $Q(t)$ after an earthquake with time history is presented, as shown in Fig. 1(a). When a building system suffers earthquake action at time t_0, the building functionality is reduced from 100% to a certain percentage in this figure. Then, the system functionality is later recovered to 100% by a repair path with repair time T_{RE}. Bruneau pointed out that the value of seismic resilience is related to the repair time and the recovery functionality curve $Q(t)$. However, this curve is widely used in whole structural and nonstructural members during building operation without considering the change in functionality during construction. The structure of a single-layer reticulated dome during construction is incomplete, leading to the seismic bearing capacity of the incomplete structure being much lower than that of the complete dome. In addition, the seismic bearing capacity of incomplete structures varies greatly at different times during construction. In this paper, seismic resilience curves during construction are put forward in Fig. 1(b). The structural functionality *Q(t)* monotonically increases from the beginning to the end of the construction. When the incomplete dome suffers an earthquake at time t_0 during construction, the functionality will decrease to some degree as well, but it will vary compared to that of a complete dome. The seismically damaged members of incomplete domes must be repaired before construction proceeds. The original construction time T_C will be extended by the repair time T_{RE}.

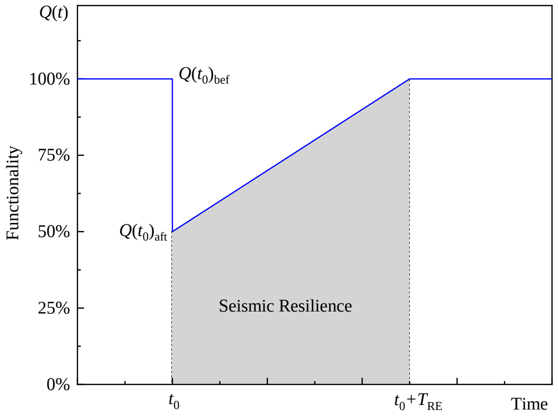

(a) Seismic resilience during operation

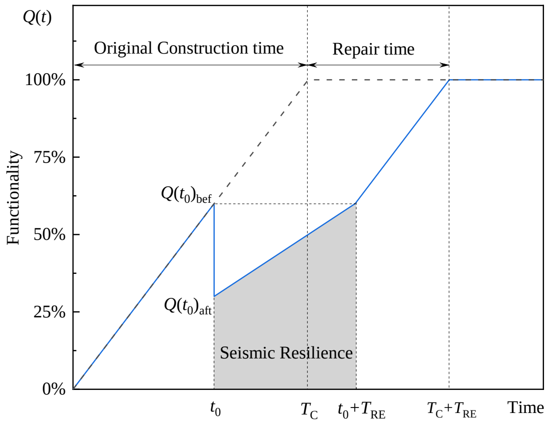

(b) Seismic resilience during construction

Fig. 1 Curve of recovery functionality and seismic resilience

The seismic resilience assessment of a single-layer reticulated dome during construction should be based on the construction scheme, elastoplastic time-history analysis and damage state criterions of structural and nonstructural members based on the Chinese standard, GB/T 38591-2020. The incomplete structure has not been equipped with nonstructural members, so the damage states of nonstructural members are ignored during construction. Circular steel pipes, welded hollow spherical joints and temporary supports are usually used in single-layer reticulated domes during construction, as shown in Fig. 2, which leads to structural members bearing both large axial forces and bending moments at the bar ends, so circular steel pipes in the dome under earthquakes may have two modes of failure: bending failure modes and axial failure modes. As a result, two damage state criteria of structural members were determined in this study. The whole assessment process of the seismic resilience of a single-layer reticulated dome during construction is shown in Fig. 3 and is described in the following steps.

Step 1: The rational construction scheme of a single-layer reticulated dome must be defined first, especially the construction sequences of different structural members. Then, finite element models in different construction periods should be established, including incomplete structural members and temporary construction support systems.

Step 2: Based on different earthquake hazards, elastoplastic time-history analysis should be carried out using the selected ground motions and the IDA method.

Step 3: Combined with hysteresis experiments or numerical simulations of circular steel pipes, two damage state criteria of structural members considering two failure modes should be determined, including the bending failure mode and axial failure mode.

Step 4: According to the damage criterion, the damage status of all structural members is estimated in different construction models under predetermined earthquake hazards.

Step 5: The repair cost and the repair time of different construction models should be calculated considering the reasonable repair process.

Step 6: The reduced structural functionality should be defined to assess the seismic resilience of a single-layer reticulated dome during construction.

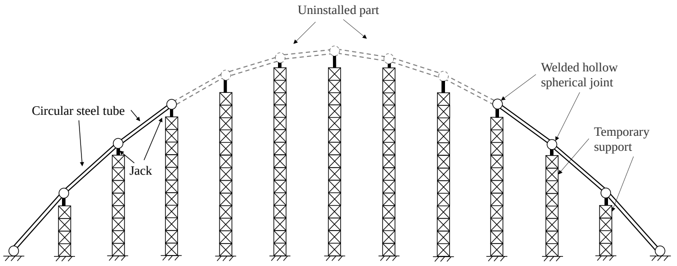

Fig. 2 The model of a single-layer reticulated dome during construction

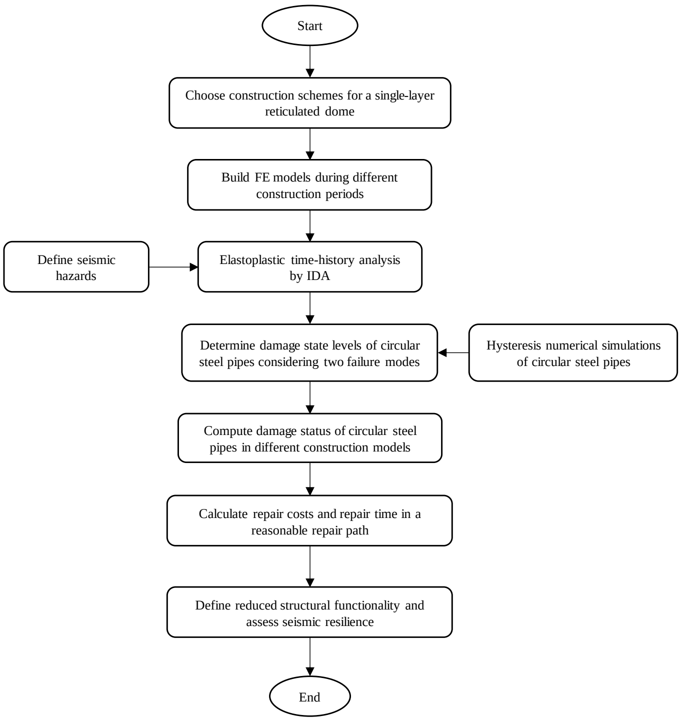

Fig. 3 The methodology for seismic resilience assessment during construction

3. Damage criterion of circular steel pipes

The Chinese standard, GB/T 38591-2020, suggests the damage state criterion in the moment-angle (M-θ) curve of steel frame members and force-displacement (N-Δ) curve of steel support members with an H-section and rectangular pipes, but the members of a single-layer reticulated dome adopt a circular steel pipe with a large axial force and bending moment at both ends; these characteristics are not specified in this standard. The bending failure of the member may occur when the bending moment is larger, but when the axial force becomes larger, the bar may yield by tension or buckle by compression. As a result, the mode of bending failure or axial failure must be distinguished by the damage criteria. To obtain the different damage criterion curves of circular steel pipes in a single-layer reticulated dome, hysteresis analysis must be carried out by component tests or numerical simulations. In this paper, two mechanical models are established to study the damage criterion of circular steel pipes with rigid connection joints under cyclic bending moments or cyclic axial forces by finite element analysis simulation, as shown in Fig. 4. Because the bending stress or axial stress in a circular steel pipe is dominant, two types of mechanical models are taken as the research object by the numerical simulation method. The hysteretic performances of different types of members are analyzed in different loading systems and member parameters, such as component length and sectional dimension.

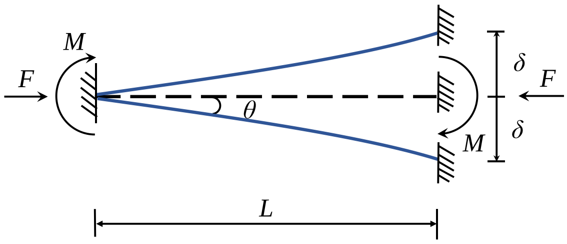

(a) Hysteresis simulation of the bending moment

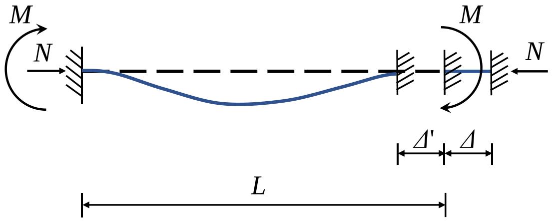

(b) Hysteresis simulation of the axial force

Fig. 4 Mechanical models of the circular steel pipe

Fig. 4(a) shows the mechanical model of a circular steel pipe with a cyclic bending moment. One end of the bar is consolidated, and the lateral loading system at the other end is controlled by the lateral displacement δ , while the axial compression force *N* in the bar remains constant. The lateral displacement adopted the cyclic loading method, and the loading system is shown in Fig. 5(a). A schematic diagram of the loading system is shown in Fig. 5(a), in which the X-axis *n* represents the number of loading cycles, and the Y-axis represents the ratio of the lateral displacement δ to the yield displacement δ_y. The yield lateral displacement δ_y of the circular steel pipe is calculated by Eq. 1:

$$\delta_y = \frac{2\left(f_y - F / A\right)L^2}{3ED} \tag{1}$$

where δ_y is the lateral yield displacement; f_y is the actual yield stress of steel; *L* is the length of the bar; *F* is the constant axial compression force; *E* is the elastic modulus of steel; and *D* is the outer diameter of the bar section.

Fig. 4(b) shows the mechanical model of the circular steel pipe with an axial force. One end of the bar is consolidated, and the loading system at the other end is controlled by axial displacement Δ when the bending moment *M* is constantly 0.2 times the bending yield bearing capacity. The axial displacement adopts the cyclic loading method, and the loading system is shown in Fig. 5(b), in which abscissa n represents the number of loading cycles and ordinate Δ represents the cyclic axial displacement. *L* represents the length of the bar, a positive value indicates tensile displacement, and a negative value indicates compressive displacement. The yield axial displacement Δ_y of the circular steel pipe is calculated by Eq. 2:

$$\Delta_y = \frac{\left(f_y - M / W\right)L}{E} \tag{2}$$

where Δ_y is the axial yield displacement; f_y is the actual yield stress of steel; *L* is the length of the bar; *M* is the constant bending moment; *E* is the elastic modulus of steel; and *W* is the section modulus of the bar.

The aforementioned hysteresis simulation of circular steel pipes should yield the skeleton curves of the *M-θ* and *N-Δ* models. These skeleton curves can be the damage state criterion of circular steel pipes in a single-layer reticulated dome, and according to the Chinese standard, GB/T 38591-2020, the damage state of steel structural members is divided into five levels, as shown in Fig. 6. The five levels include Level 0 (Intact), which means no damage occurs; Level 1 (Slight), which means that only minor damage affecting appearance occurs; Level 2 (Moderate), which means moderate damage that can be repaired simply occurs; Level 3 (Extensive), which means general damage that can be repaired to full structural function by conventional methods occurs; and Level 4 (Complete), which means serious damage that affects the bearing capacity or requires component replacement occurs.

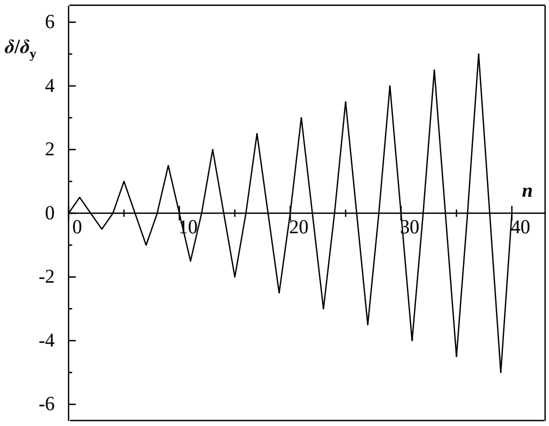

(a) Cyclic lateral displacement

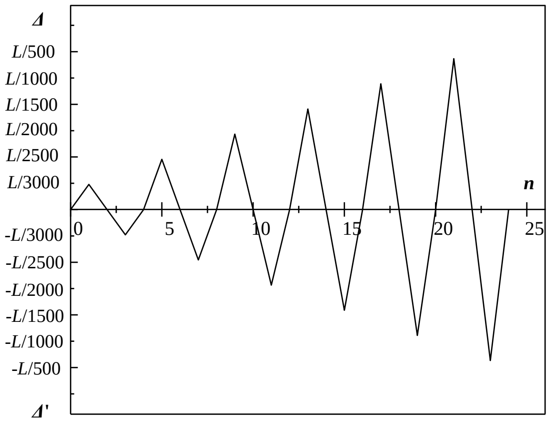

(b) Cyclic axial displacement

Fig. 5 Hysteresis load curves of the circular steel pipe

As shown in Fig. 6, the *M-θ* criterion of bending failure and *F-Δ* criterion of tensile failure or compressive failure are represented by 4 broken line models. θ_B , θ_{IO} , θ_{LS} , θ_C and θ_{CP} represent the angle of the component corresponding to nominal yield point B, performance point IO, performance point LS, peak point C and failure point CP, respectively. Δ_B, Δ_{IO}, Δ_{LS}, Δ_C and Δ_{CP} represent the tensile displacement of the component corresponding to nominal yield point B, performance point IO, performance point LS, peak point C and failure point CP, respectively. Δ'_B, Δ'_{IO}, Δ'_{LS}, Δ'_C and Δ'_{CP} represent the compressive displacement of the component corresponding to nominal yield point B, performance point IO, performance point LS, peak point C and failure point CP, respectively. The damage state level of each member should be determined by the most unfavorable index calculated in the *M-θ* and *F-Δ* damage state criteria.

4. Calculation of seismic resilience

4.1. Calculation of repair time

To assess the seismic resilience, the repair time must be calculated according to Fig. 1. The repair time of a single-layer reticulated dome are closely related to different grid positions and repair paths of damaged structural members. In this study, the repair path of the damaged dome is from low grids to high grids, namely, from outside grids to inside grids. The repair path of each grid is that the damaged radial members should be repaired at first, and then the damaged annular members and damaged diagonal members are repaired subsequently. According to the repair principle of a reticulated dome after a disaster proposed by Reference [20], the repair methods of structural members in different damage state levels are shown in Table 1.

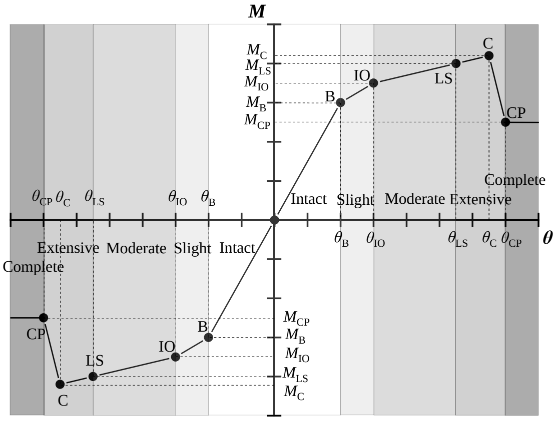

(a) *M-θ* curve for bending failure

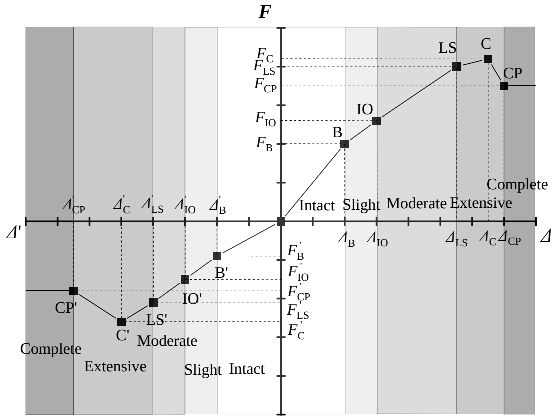

(b) *F-Δ* curve for axial failure

Fig. 6 Damage state criteria of the circular steel pipe

Table 1
Repair method of structural members at different damage state levels

Level 0 (Intact)	Level 1 (Slight)	Level 2 (Moderate)	Level 3 (Extensive)	Level 4 (Complete)
Reserve the intact bar	Straighten the bar with special machines	Replace the damaged bar with new one		

The total construction repair time of all damaged structural members should meet the requirements to recover structural function. To facilitate calculation, it is not necessary to include the time spent in seismic damage assessment, repair path planning, repair material procurement, construction equipment leasing and other preparatory work before repair. The repair time of different types of structural members under different damage states is calculated by Eq. 3, which is related to the repair time of a single worker to complete the work, the number effect of the damaged structural members and efficiency improvement of member repair.

$$Q_i = \sum_{j=1}^{n} (Q_{(i,j)} \times n_{(i,j)}) \times \zeta_{\mathrm{T}(i)} \tag{3}$$

where Q_i is the repair time of type *i* members (man-days); $Q_{(i,j)}$ is the repair time of type *i* members under damage state *j*, which was suggested by Reference [20] and Reference [21], as shown in Table 2; $n_{(i,j)}$ is the number of type *i* members under damage state *j* (man-days); and $\xi_{\mathrm{T}(i)}$ is the reduction coefficient of the repair time considering the damaged number of type *i* member, as shown in Table 3.

Table 2
Repair time of structural members in different damage state levels

i	Structural member type	Repair time in different damage state levels *j* (man-days)				
		Level 0 (Intact)	Level 1 (Slight)	Level 2 (Moderate)	Level 3 (Extensive)	Level 4 (Complete)
1	Radial bar	0	2	15	15	15
2	Diagonal bar	0	2	15	15	15
3	Annular bar	0	2	15	15	15

Table 3
Reduction coefficient of repair time considering the number of damaged members

i	Structural member type	Number of damaged members		
		≤10	11~49	≥50
1	Radial bar	1.0	linear interpolation	0.8
2	Diagonal bar	1.0		0.8
3	Annular bar	1.0		0.8

The total repair time of all damaged structural members is calculated by Eq. 4, which is related to the number of repaired workers and the sum of the repair time for different types of damaged structural members.

$$T_{\mathrm{RE}} = \frac{\sum_{i=1}^{3} Q_i}{N} \tag{4}$$

where T_{RE} is the total repair time of the single-layer reticulated dome (man-days), and *N* is the number of workers repairing damaged structural members.

4.2. Calculation of structural recovery functionality

The structural recovery functionality suggested in FEMA-P58 refers to the relationship between the time and the structural recovery functionality before or after an earthquake. Due to the concepts of redundancy and robustness, the structural recovery functionality of the single-layer reticulated dome is related to the number of damaged members and the damage state level of each damaged member. To establish the relationship between the damaged members and the structural recovery functionality, by combining the different repair methods and different damage state levels, it is assumed that the influence coefficient of the damaged member is linearly proportional to its repair time, and the influence coefficient of the member to be replaced is 1.0 in this paper. The overall structural damage index of the single-layer reticulated dome is specified as Eq. 5:

$$\overline{D} = \frac{\sum_{j=0}^{4} D_j \times n_j}{\sum_{j=0}^{4} n_j} \tag{5}$$

where $\overline{D}$ is the overall structural damage index of the dome; D_j is the damage index of each member in damaged state level *j*, with the values shown in Table 4; and n_j is the total number of members in damaged state level *j*.

Table 4
Damage index of each damaged structural members

i	Structural member type	Damage index in different damage state levels *j*				
		Level 0 (Intact)	Level 1 (Slight)	Level 2 (Moderate)	Level 3 (Extensive)	Level 4 (Complete)
1	Radial bar	0	0.1	1	1	1
2	Diagonal bar	0	0.1	1	1	1
3	Annular bar	0	0.1	1	1	1

The structural functionality of the incomplete single-layer reticulated dome during construction is related to the percentage of installed bars so that at time

t_0 before the earthquake, the structural functionality $Q(t_0)_{\text{bef}}$ is specified as Eq. 6:

$$Q(t_0)_{\text{bef}} = \frac{n_{\text{install}}}{n_{\text{total}}} \times 100\% \tag{6}$$

where n_{install} is the number of installed members at time t_0 during construction, and n_{total} is the total number of installed members of the complete single-layer reticulated dome. After the earthquake, the structural functionality of the damaged dome $Q(t_0)_{\text{aft}}$ is specified as Eq. 7:

$$Q(t_0)_{\text{aft}} = Q(t_0)_{\text{bef}}(1-\overline{D}) \tag{7}$$

Because the single-layer reticulated dome in this study only consists of structural members but no nonstructural components during construction, the linear recovery functionality suggested by Reference [18] is adopted as Eq. 8:

$$Q(t, T_{\text{RE}}) = a\left(\frac{t-t_0}{T_{\text{RE}}}\right) + b \tag{8}$$

where t_0 is the time when the earthquake occurs; T_{RE} is the repair time of all damaged structural members after the earthquake; and a and b are constant values of 1 and -1, respectively. Based on the recovery functionality during construction and the repair time T_{RE}, the seismic resilience of a single-layer reticulated dome during construction is expressed as Eq. 9, as recommended by Reference [23]:

$$R = \frac{\int_{t_0}^{t_0+T_{\text{RE}}} Q(t, T_{\text{RE}})dt}{T_{\text{RE}}} \tag{9}$$

Eq. 9 shows that the smaller the reduction area of structural functionality is, the larger seismic resilience R is, and the shorter the repair time is, the larger seismic resilience R is.

5. Case study

5.1. Finite element model

The presented methodology for the seismic resilience during construction was studied by a typical Kiewitt-8 dome, as shown in Fig. 7. The span of this dome is 40 m, and the rise-to-span ratio is 1/4. The boundary conditions include fixed hinge supports, and the material is Q235 steel, with a yield strength of 235 MPa, a density of 7850 kg/m^3 and an elastic modulus of 2.06×10^5 MPa. The number of gird circles is 6, and the roof dead load is 1 kN/m^2. Different pipe sections of the single-layer reticulated dome and temporary support system during construction are shown in Table 5. The type of temporary support system is a latticed column.

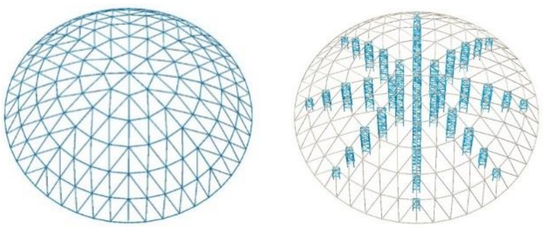

(a) Single-layer reticulated dome (b) Temporary support system

Fig. 7 Case model

The finite element model was established by ABAQUS software. The element type of the members is B31, and the beam sections are circular pipes. The connection of the structural member of the single-layer reticulated dome is rigid, and the joints of the temporary support members are hinge joints. The connector element was adopted to simulate the interaction between the temporary support and the dome structure. Temporary support only provides vertical compressive force and does not provide tension force when separating during earthquake actions. The constitutive model of the steel material and the mechanical model of the connector element are shown in Fig. 8.

Table 5
Pipe section of the single-layer reticulated dome and temporary support system

Kiewitt-8 dome	Pipe section	Temporary supports	Pipe section
Radial bar	Φ133×4	Vertical bar	Φ108×8
Annular bar	Φ133×4	horizontal bar	Φ90×6
Diagonal bar	Φ114×3	Diagonal bar	Φ90×6

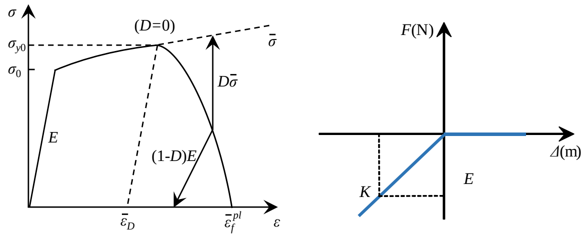

(a) Stress–strain curve of steel (b) Force displacement curve of connector elements

Fig. 8 Mechanical curves of the FE model

5.2. Damage criterion of dome members

Hysteresis simulations of different circular steel pipes in the dome were carried out under a cyclic bending moment or a cyclic axial force. As a result, two damage failure modes of the circular steel pipe by hysteresis simulation are shown in Fig. 9. Fig. 9 indicates that bending failure under cyclic bending moment leads to the overall instability of the member and that axial failure under cyclic axial force leads to the local buckling of the member.

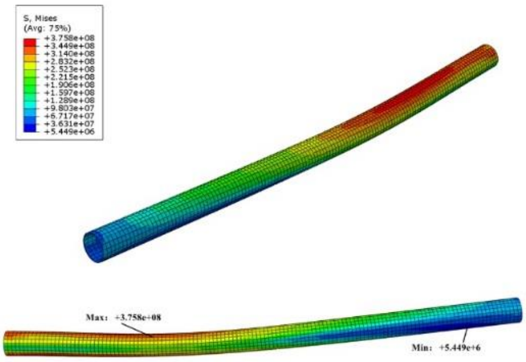

(a) Bending failure under cyclic bending moment

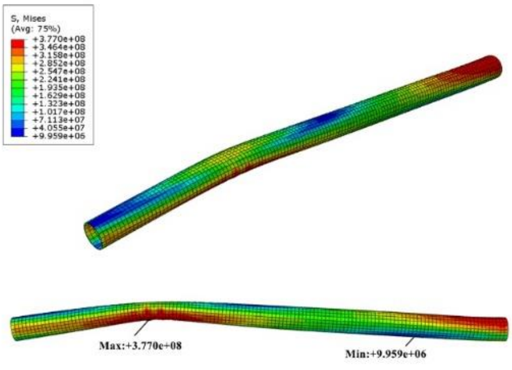

(b) Axial failure under cyclic axial force

Fig. 9 Two types of failure modes for dome pipes

Hysteresis curves of the radial bar, the diagonal bar and the annular bar in the dome under two loading systems are shown in Fig. 10. Fig. 10 (a) indicates that the diagonal bar with a larger slenderness ratio has a lower bending moment capacity and easily undergoes bending failure. Fig. 10 (b) indicates that the compressive bearing capacity of the dome member is much lower than its tensile bearing capacity. The skeleton curve was the outsourcing curve by connecting the maximum peak points of each cycle in the hysteresis curve. Fig. 11 shows skeleton curves of the radial bar, the diagonal bar and the annular bar in the dome under two loading systems.

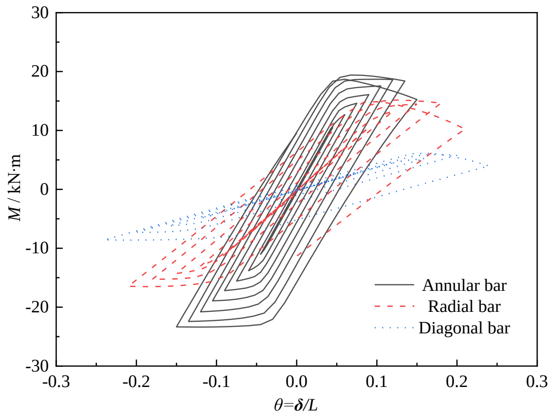

(a) *M-θ* curve under cyclic bending moment

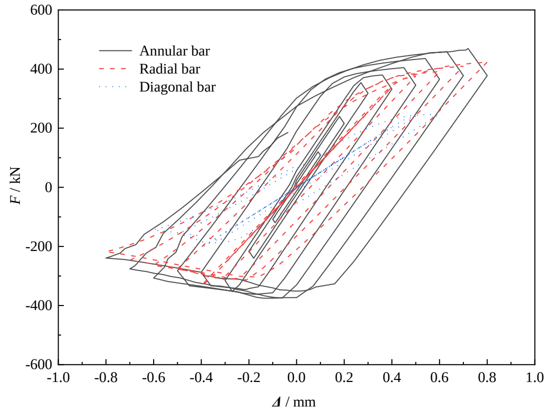

(b) *F-Δ* curve under cyclic axial force

Fig. 10 Hysteresis curves of the circular steel pipes

From the skeleton curves, the damage criterion of different types of dome members was obtained, as shown in Table 6, Table 7 and Table 8. Compared with the Chinese standard, GB/T 38591-2020 [17], the values of *θ* and *Δ* at each damaged state level are smaller. This is because steel structural members in a single-layer reticulated dome are both bearded with simultaneous bending moments and axial forces. The combined action of the bending moment and axial force facilitates damage to the structural members so that the index of the damage criterion is reduced, especially the index of axial displacement *Δ*. Taking the annual bar as an example, the *M-θ* damage criterion and *F-Δ* damage criterion are shown in Fig. 12.

Table 6
θ value of the damage state criterion of steel structural members

Representative specification	Structural member type	Member section	θ_{IO}/θ_y	$\theta_{LS}/\theta y$	θ_u/θ_y
Chinese Standard: GB/T 38591-2020	Steel beam	H-section	1.25	4	5
	Steel column	H-section	1.25	4	5
	Steel column	Rectangular tube	1.25	4	5
Recommended in this paper	Radial bar	Circular pipe	1.1	2.5	3
	Diagonal bar		1.1	2.5	3
	Annular bar		1.1	4	5

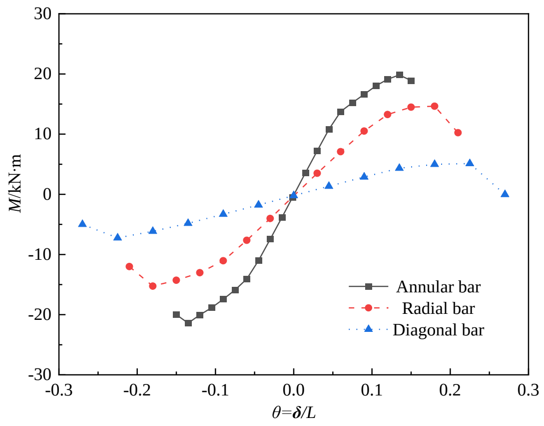

(a) *M-θ* curve under cyclic bending moment

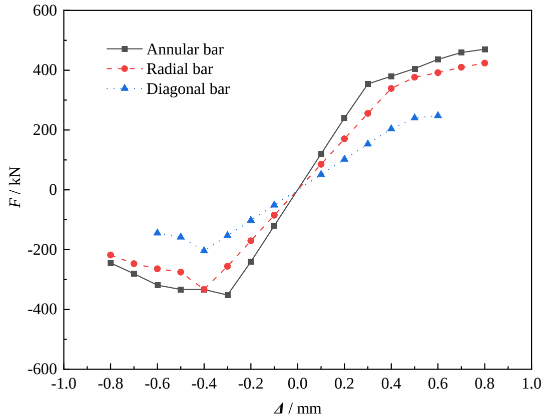

(b) *F-Δ* curve under cyclic axial force

Fig. 11 Skeleton curves of the circular steel pipes

Table 7
Δ' value of the damage state criterion of compressive structural members

Representative specification	Structural member type	Member section	Δ'_{IO}/Δ'_y	Δ'_{LS}/Δ'_y	Δ'_u/Δ'_y
Chinese Standard: GB/T 38591-2020	Steel Support	H-section	1.5	8	9
		Rectangular tube	1.5	7	8
Recommended in this paper	Radial bar	Circular pipe	1.1	1.3	1.5
	Diagonal bar		1.1	1.3	1.5
	Annular bar		1.1	1.5	2.0

Table 8
Δ value of the damage state criterion of tensile structural members

Representative specification	Structural member type	Member section	Δ_{IO}/Δ_y	Δ_{LS}/Δ_y	Δ_u/Δ_y
Chinese Standard: GB/T 38591-2020	Steel Support	H-section	1.5	8	10
		Rectangular tube	1.5	8	10
Recommended in this paper	Radial bar	Circular pipe	1.3	1.8	2.5
	Diagonal bar		1.3	1.8	2.5
	Annular bar		1.3	2.1	2.7

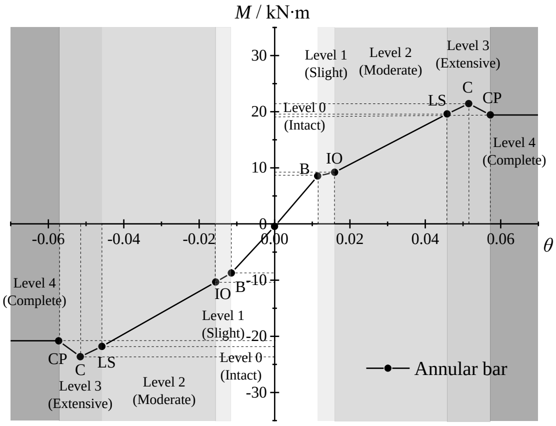

(a) *M-θ* damage state criterion

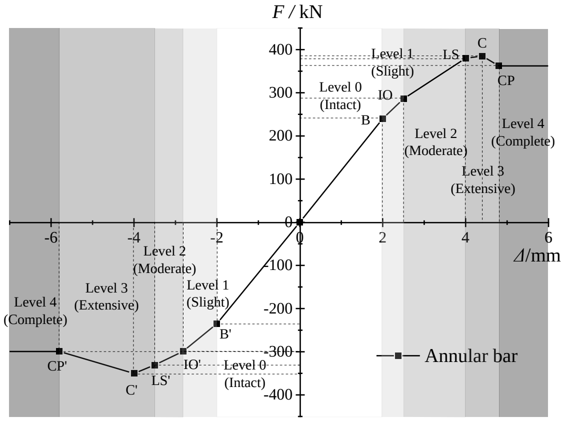

(b) *F-Δ* damage state criterion

Fig. 12 Damage state criterion of the annual bar

5.3. Seismic resilience assessment of the dome during construction

By dividing the single-layer reticulated dome into six circular grids from outside to inside, scattered assembly technology at high altitude was adopted during construction. As temporary supports, the latticed columns were arranged under each joint at both ends of all dome members. Because the dome structure is symmetrical, the symmetrical construction method was adopted to ensure construction safety. The specific construction steps and temporary support models are shown in Fig. 13. According to Chinese code GB 50011-2016: "Code for Seismic Design of Buildings" [24], seismic hazards are defined as frequent earthquakes, moderate earthquakes and rare earthquakes. Taking the peak ground acceleration (PGA) as the index of ground motion intensity. 3D earthquakes, including the El Centro Earthquake wave, Taft Earthquake wave, Loma Prieta Earthquake wave and Tianjin Earthquake wave, were adopted to conduct an elastoplastic time-history analysis. The PGA of the seismic waves was adjusted to 110 cm/s^2, 300 cm/s^2 and 510 cm/s^2. The PGA ratio in the X, Y and Z directions was 1:0.85:0.65.

The time-history analysis of incomplete dome models under different construction steps was carried out by using ABAQUS. The relative axial displacement and relative rotation angle were calculated by obtaining the coordinates of each member joint. Combined with the proposed *M-θ* damage criterion in Table 6 and the *F-Δ* damage criterion in Table 7, the damage state level and the final failure mode of each member were determined by the higher value of the damage state criteria. The average damage state levels and the average failure modes of all members in different construction models under different rare earthquakes were calculated, as shown in Fig. 14. Fig. 14(a) shows that the percentage of damaged members varies widely at different construction steps, as does the seismic bearing capacity of the incomplete dome during construction. The percentage of damaged members in the model under construction Step 14 is 40.51%, which is the maximum value during construction. That is, when the fourth circular grid is installed in Step 14, this construction model is the most unfavorable with the most damaged members. Fig. 14(b) indicates that there are two failure types of damaged members in the single-layer reticulated dome during construction, and the percentage of member failure modes changes widely at different construction steps. The results also show that the construction model under Step 14 is the most unfavorable model during construction. When the dome is completely built, there are no damaged members under rare earthquakes, so the seismic bearing capacity of the complete single-layer reticulated dome is larger than that of the incomplete dome.

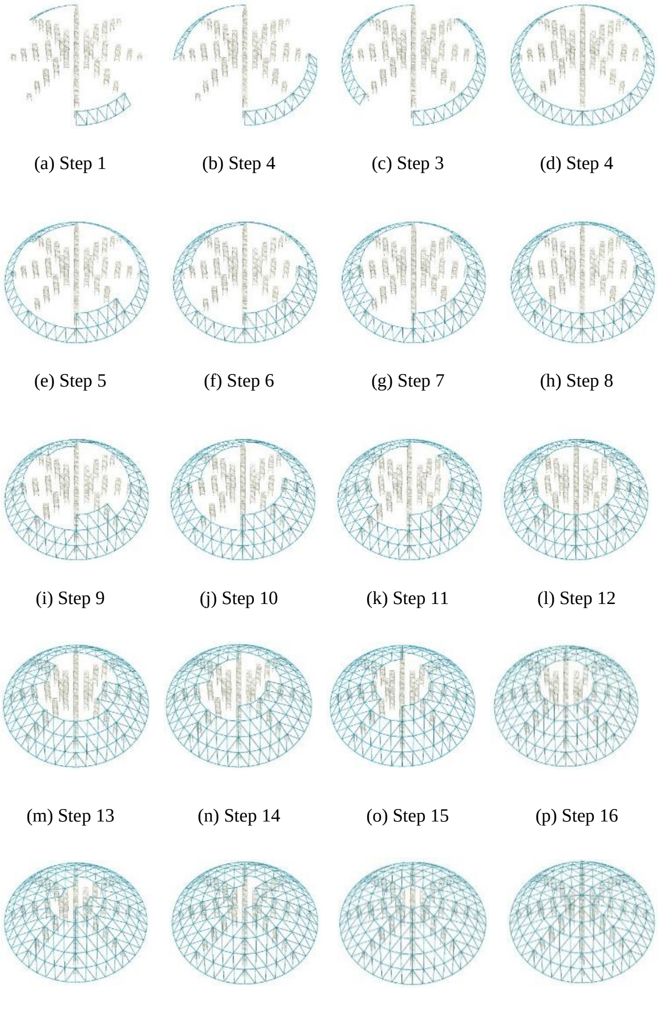
(a) Step 1 (b) Step 4 (c) Step 3 (d) Step 4

(e) Step 5 (f) Step 6 (g) Step 7 (h) Step 8

(i) Step 9 (j) Step 10 (k) Step 11 (l) Step 12

(m) Step 13 (n) Step 14 (o) Step 15 (p) Step 16

(q) Step 17 (r) Step 18 (s) Step 19 (t) Step 20

Fig. 13 Construction models of a single-layer reticulated dome

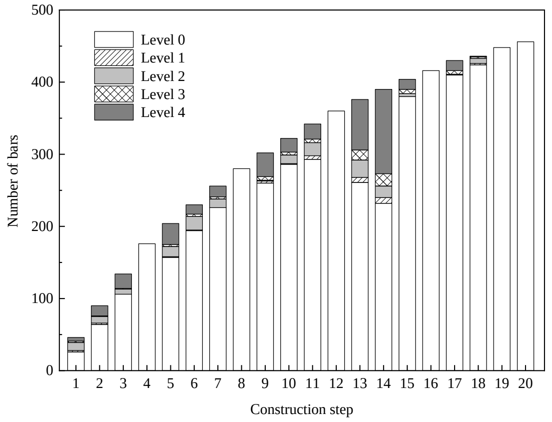

(a) Damage state levels

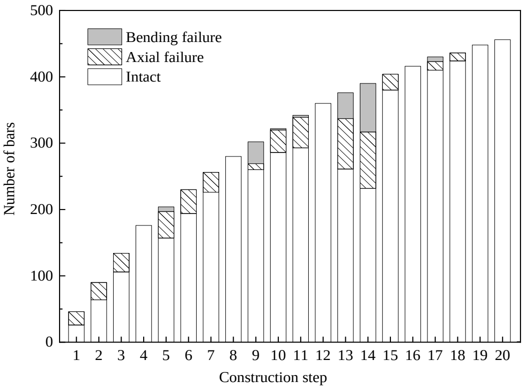

(b) Member failure modes

Fig. 14 Damaged member results under each construction step

Through Eq. 3~Eq. 4, the average repair time (T_{RE}) in different construction models under different rare earthquakes was calculated, as shown in Fig. 15(a). Fig. 15(a) shows that the repair time is when the fourth circular grid is installed at Step 14. The average repair time reaches 1814 man-days after a rare earthquake, and 90% of the damaged members need to be replaced. That is, if 26 workers are arranged to repair the damaged members, then the repair time is 70 days, and the total construction period is extended by 70 days. Through Eq. 5~Eq. 9, the average seismic resilience of different construction models under different rare earthquakes was calculated, as shown in Fig. 15(b). Fig. 15(b) suggests that the value of seismic resilience at construction Step 1 is 80.14% and the value of seismic resilience at construction Step 14 is 80.63%, which are the two lowest numbers. This result demonstrates that when the first and fourth circular grids are under construction, the structural functionality decreases the most significantly during these two periods. Special attention should be given to the seismic safety of these two construction periods.

Taking the construction model at step 14 as an example, the average value of seismic resilience (R) and recovery functionality curves under different earthquake hazards are shown in Fig. 16. This result illustrates that the average seismic resilience under frequent earthquakes, moderate earthquakes and rare earthquakes is 0.91, 0.85 and 0.81, respectively, and if 26 workers are arranged to repair the damaged members, the repair time under frequent earthquakes, moderate earthquakes and rare earthquakes is 33 days, 51 days and 70 days, respectively. With increasing earthquake intensity, the value of seismic resilience decreases, and the repair time increases. Special measures should be taken to control the seismic safety of the most unfavorable construction periods by seismic resilience assessment.

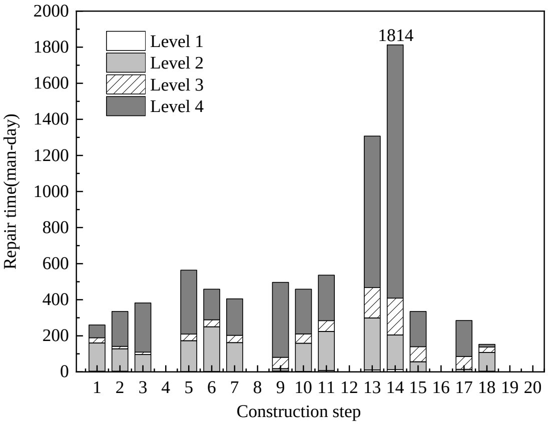

(a) Value of repair time

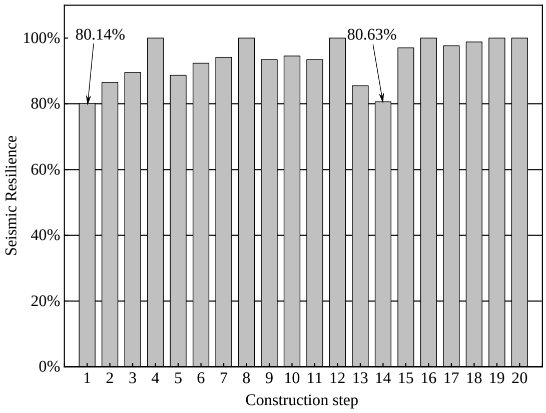

(b) Value of seismic resilience

Fig. 15 Seismic resilience assessment under construction

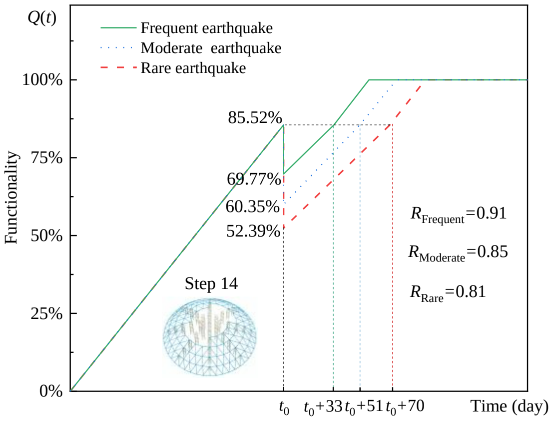

Fig. 16 Seismic resilience of different earthquake hazards at construction step 14

6. Summary and conclusions

By improving the curve of recovery functionality, the framework for seismic resilience assessment of a single-layer reticulated dome during construction was established in this study. The hysteresis analysis of the circular steel pipe under the combined action of bending moment and axial force was conducted by numerical simulation, and the damage state criterion of two failure modes was presented. Based on the advanced computational formulas of the repair time and recovery functionality considering different construction periods, the elastoplastic time-history analysis of an incomplete single-layer reticulated dome was carried out, and the seismic resilience during construction was assessed by using the Kiewitt-8 dome as an example. The main conclusions are as follows:

(1) There are two failure modes of the single-layer reticulated dome under seismic action: the bending failure mode caused by the bending moment and the axial failure mode caused by the axial force. Because members in single-layer reticulated domes often suffer from combined greater bending and greater axial force, the index of circular steel pipes at different damaged state levels obtained by the hysteretic curve and the skeleton curve is lower than the index in the existing Chinese standard. The damage state level of each member in the dome should be determined by the most unfavorable index calculated in the M-θ and F-Δ damage state criteria.

(2) The seismic bearing capacity of the complete single-layer reticulated dome is larger than that of the incomplete dome, and the seismic bearing capacity varies greatly under different construction periods. The number of damaged members and the percentage of member damage state levels are significantly influenced by the different construction stages. The construction models of the whole process must be established to find the most unfavorable construction state under seismic action.

(3) The repair time and the seismic resilience value of the incomplete dome also vary greatly under different construction periods. The repair time is related to the number of damaged members and the damage state levels of each damaged member. The repair time is longer if the number of damaged members is greater and the state level of the damaged member is higher. The seismic resilience of incomplete domes under earthquakes is smaller, and the

functionality of the dome under construction will decrease. Special measures should be taken to control the seismic safety of the most unfavorable construction periods by seismic resilience assessment.

Acknowledgements

The authors acknowledge the financial support of the Hainan Provincial Natural Science Foundation of China (Grant No. 520QN232).

References

[1] Fan F., Zhi X.D. and Shen S.Z., “Failure mechanism of large span reticulated shells subjected to severe earthquakes”, Journal of Building structures, 31(6), 153-159, 2010. (in Chinese)

[2] Zhi X.D., Fan F. and Shen S.Z., “Failure and damage of single-layer reticulated cylindrical shells under earthquakes”, China Civil Engineering Journal, 40(8), 29-34, 2007.(in Chinese)

[3] Nie G.B., Xie K., Zhi X.D. and Dai J.W., “Performance-based seismic design of reticulated shells”, China Civil Engineering Journal, 51(S1), 8-12+19, 2018. (in Chinese)

[4] Liu X.W. and Guo Y.L., “State Nonlinear Finite Element Method for Construction Mechanics Analysis of Steel Structures”, Engineering Mechanics, 25(10), 161-169, 2008. (in Chinese)

[5] Tian L.M., Hao J.P., Chen T., Zheng J. and Wang Y., “Simulation analysis on erection procedure of main stadium for the Universiade Sports Centre”, Journal of Building structures, 32(05), 70-77, 2011. (in Chinese)

[6] Li Y.Y., Wang W. and Cao P.Z., “Comparison on Construction Schemes of the steel Shell in the Variety Hall of Jiangsu Grand Theater”, Progress in Steel Building Structures, 20(01), 106-112, 2018. (in Chinese)

[7] Bruneau M, Chang S E, and Eguchi R T, “A framework to quantitatively assess and enhance the seismic resilience of communities”, Earthquake Spectra, 19(4), 733-752, 2003.

[8] Vásquez A, Rivera F and De la Llera J, “Healthcare network’s response and resilience in Iquique after the 2014 Pisagua earthquake”, 16th World Conference on Earthquake Engineering, Paper No. 3639, 2017.

[9] Favier P, Rivera F and Poulos A, “Impact on chilean hospitals following the 2015 Illapel earthquake”, 16th World Conference on Earthquake Engineering, Paper No. 4415, 2017.

[10] Domaneschi M, Martinelli L and Cimellaro G P, “Immediate seismic resilience of a controlled cable-stayed bridge”, 16th World Conference on Earthquake Engineering, Paper No. 482, 2017.

[11] Biondini F, Capacci L and Titi A., “Life-cycle resilience of deteriorating bridge networks under earthquake scenarios”, 16th World Conference on Earthquake Engineering, Paper No. 939, 2017.

[12] Dong Y and Frangopol D M., “Probabilistic assessment of an interdependent healthcare-bridge network system under seismic hazard”, Structure and Infrastructure Engineering, 13(1), 160-170, 2017.

[13] Pang Y, Wei K and Yuan W., “Life-cycle seismic resilience assessment of highway bridges with fiber-reinforced concrete piers in the corrosive environment”, Engineering Structures, 222:111120, 2020.

[14] Seismic performance assessment of buildings: Volume 1 - Methodology., Federal Emergency Management Agency, Washington D C, U.S., 2012.

[15] REDi rating system: resilience-based earthquake design initiative for the next generation of buildings., Arup Group, London, UK, 2013.

[16] Rating building performance in natural disasters., U.S. Resiliency Council, U.S., 2021.

[17] Code for seismic resilience assessment of buildings: GB/T 38591—2020., Standards Press of China, Beijing, China, 2020. (in Chinese)

[18] Lu X., “Seismic resilience evaluation of a reinforced concrete frame core tube structure”, Journal of Building structures, 42(05), 55-63, 2021. (in Chinese)

[19] Fang D.P., Li Q.W. and Li N., “An evaluation system for community seismic resilience and its application in a typical community”, Engineering Mechanics, 37(10), 28-44, 2020. (in Chinese)

[20] Fan S.G., Shu G.P., Lu Z.T. and Meng X.D., “Strengthening and Renovation Design of The Space Grid Structure After Fires”, Industrial Construction, 32(10), 69-71+68, 2002. (in Chinese)

[21] Ren J.Y., Pan P., Wang T., Zhou Y., Wang H.S., Shan M.Y., “Interpretation of GB / T 38591—2020 ‘Standard for seismic resilience assessment of buildings’”, Journal of Building Structures, 42(1), 48-56, 2021. (in Chinese)

[22] Xiao Y., Zhou Y., Wu H., Pan P. and Wang T., “Comparative study on GB / T 38591—2020 ‘Standard for seismic resilience assessment of buildings’ and relevant international standards”, Journal of Building Structures, 42(7), 194-202, 2021. (in Chinese)

[23] Cimellaro G P, Reinhorn A M and Bruneau M, “Framework for analytical quantification of disaster resilience”, Engineering Structures, 32(11), 3639-3649, 2010.

[24] Code for seismic design of buildings: GB 50011—2016., China Architecture & Building Press, Beijing, China, 2016. (in Chinese)

Advanced Steel Construction – Vol. 19 No. 1 (2023) 86–90
DOI:10.18057/IJASC.2023.19.1.11
(**Special Issue:** *10^{th} International Conference on Advances in Steel Structures, ICASS'2020, Chengdu, China*)

RESEARCH ON DYNAMIC LOAD CARRYING CAPACITY OF ASSEMBLED INTERNAL STIFFENING WIND TURBINE TOWER BASED ON MULTI-SCALE MODELING

Fa-Wu Wang [*], Kai-Mming Zhou and Shi-Tang Ke

College of Civil Aviation Engineering Nanjing University of Aeronautics &Astronautics, Nanjing, China

** (Corresponding author: E-mail: fwwang@nuaa.edu.cn)*

ABSTRACT

The development of wind power technology requires higher and larger wind turbines, which requires the bearing tower to increase its height and diameter. The assembled internal stiffened wind turbine tower divides the tower into multiple arc plates along the longitudinal direction, which can be easy transported to the site for assembly. That can solve the problem of height limit in highway transportation. At the same time, the internal stiffener provides better stability and can replace the bottom tower section of conventional wind turbine tower. In this study, the tower section of assembled internal stiffened wind turbine is modeled, and the longitudinal segmented tower section is assembled to the actual full-scale tower section model for nonlinear dynamic analysis. The influence of weld is considered by multi-scale modeling, combined with the plastic damage theory of steel materials. The whole collapse process of tower wall instability and deformation failure of wind turbine tower under the extreme wind condition is simulated, and the influence of various parameters of tower section on its bearing capacity is analysed. The damage position and damage development during tower collapse are predicted by using plastic damage theory, so as to provide reference for the design of assembled internally stiffened wind turbine tower.

ARTICLE HISTORY

Received: 20 July 2022
Revised: 22 August 2022
Accepted: 10 January 2023

KEYWORDS

Wind turbine tower;
Multi-scale modelling;
Prefabricated;
Internal stiffening;
Plastic damage

1. Introduction

As a clean and efficient energy, wind power generation has developed very rapidly in recent years, and wind power technology has also developed rapidly. As the main load-bearing component of wind turbine, tower plays an important role in ensuring the stable operation of wind turbine. Considering the height limit of highway transportation, the wind turbine tower with a bottom diameter of more than 4.5m has exceeded the height limit of highway transportation. For the future development of higher power wind turbines, the transportation of larger diameter towers will be a problem. The split assembly towers can well solve the problems of height and width limitation in transportation.

Wind turbine tower belongs to cylindrical shell structure in classification. In the research field of inner stiffened cylindrical shell, Wang M.G. [1] studied the stability of stiffened cylindrical shell by theoretical analysis and Yan H.X. [2] by finite element calculation. It is found that the bearing capacity of non-stiffened shell is the lowest under the action of horizontal wind pressure; The effect of longitudinal stiffening is greater than that of circumferential stiffening, and the effect of external stiffening is better than that of internal stiffening. The longitudinal stiffeners arranged along the height direction can improve the overall stiffness of the tower to a certain extent. Rotter J M. [3] studied in detail the nonlinear buckling forms of cylindrical shell structures with different lengths under overall bending. Comparing the critical moment calculated by ABAQUS analysis and the critical moment calculated by the traditional calculation formula, it is found that for cylindrical shells with short length, the critical moment at buckling is greater than the elastic critical moment; For medium length cylindrical shells the critical moment is close to the elastic critical moment; For long cylindrical shell structures the buckling critical moment is lower than the elastic critical moment. The influence of boundary conditions on the buckling capacity of long columns is lower than that of short columns.

In this paper, the collapse failure mechanism of wind turbine tower under extreme wind conditions is analysed by considering the assembled internal stiffener and combined with the material plastic damage theory. It is based on the plastic damage theory of stress triaxial [4]. This theory can simulate the fracture phenomenon of materials under different stress states and can predict the collapse failure of large wind turbine structures. Zhou T.H. [5] have used the plastic damage theory to analyze the structural damage of frame joints and steel frame structures under low cycle loading. The results show that the plastic damage theory can accurately predict the degradation of bearing capacity and stiffness of members and steel frame structures under loading, and accurately predict the damage location and damage development of structures. Duan H.X. [6] applied the plastic damage theory to the dynamic time history analysis of steel frame structure, and predicted the failure position and damage development of frame structure under seismic load. As a method to predict the actual damage of structures, the material plastic damage theory is widely used in the node analysis and collapse analysis of steel frame structures, but there are few applications in the wind turbine tower and the analysis of collapse failure mechanism of the tower. Therefore, the application of material plastic damage theory to the tower structure analysis has practical research significance and value.

At present, scholars have less research on split assembly internal stiffened towers, especially the dynamic bearing performance of such towers and the collapse failure mechanism under extreme conditions need to be furtherly studied. Based on the consideration of fabricated internal stiffening and material plastic damage, this paper studies the dynamic bearing performance of tower under different stiffening schemes, and uses the plastic damage theory to predict the location and development degree of structural damage.

2. Dynamic response analysis of assembled internal stiffener wind turbine

2.1. Simplified finite element model

Taking NREL 5wm wind turbine as the research object, the finite element model is created in ABAQUS. The main parameters of the wind turbine are showed in table 1.

Table 1
Main parameters of NREL 5MW wind turbine

Wind turbine parameters	Numerical value
Diameter of wind turbine/m	126
Hub height/m	90
Tower height/m	87.6
Wind turbine mass/kg	1.1×10^4
Engine room quality/kg	2.4×10^5
Tower mass/kg	3.47×10^5

The bottom diameter of the tower is 6m, the wall thickness is 0.027m, the top diameter of the tower is 3m, and the wall thickness is 0.019m. The shell wall is modeled by shell element SR4. The material is Q355 steel, the density is 7850kg/m^3, the yield strength is 325MPa, the Poisson's ratio is 0.3, and the elastic modulus is 2.1×10^{11}, the total height of the tower is 87.6m. Taking 8.76m as a tower section, a reference point RP is set on the top of the tower, and the reference point is connected with MPC on the top of the wind turbine tower, the bottom of the wind turbine tower is rigidly connected with the foundation. For the tower section with a diameter greater than 4.5m, the distribution scheme is adopted, as shown in Fig. 1 (the gray part of the tower section is arranged in pieces). The stiffener is TW75×150 section steel, flange thickness 20mm, Fig. 1 shows the cross section of the tower.

Fig. 1 Simplified finite element model

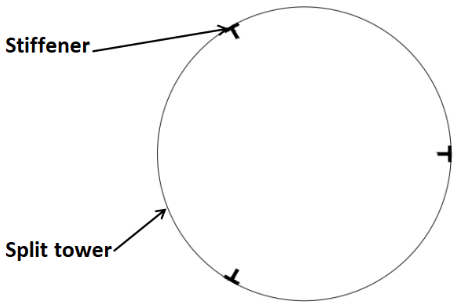

Fig. 2 Schematic diagram of tower section

2.2. *Wind load extraction*

In this paper, according to the design load condition of wind turbine, the simulation time T=60s and time step ΔT=0.1s are set by OpenFAST software parameters to calculate the turbulent wind speed under the average wind speed of 70m/s at the hub under the extreme wind condition once in 50 years. The turbulent wind field is generated by TurbSim software to obtain the time domain diagram of wind speed at the hub height, as shown in Fig. 3 extract the wind load time history on the top of the wind turbine tower under the current wind condition, where Fx, Fy and Fz are the axial forces in the X, Y and Z directions respectively, and Mx, My and Mz are the moments around the X, Y and Z axes respectively, which is shown in Fig. 4.

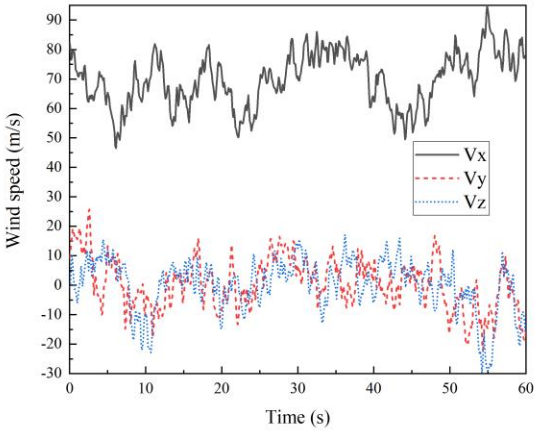

Fig. 3 Wind speed time history at hub

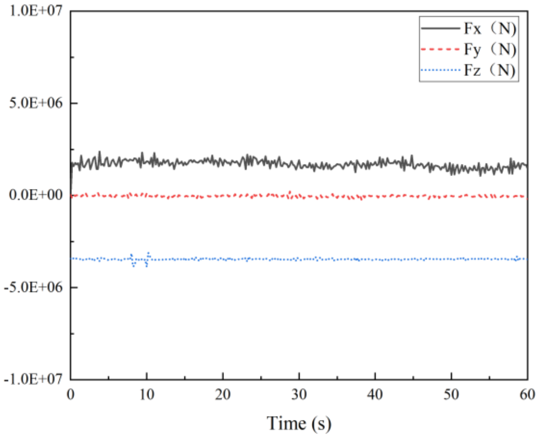

(a) axial forces

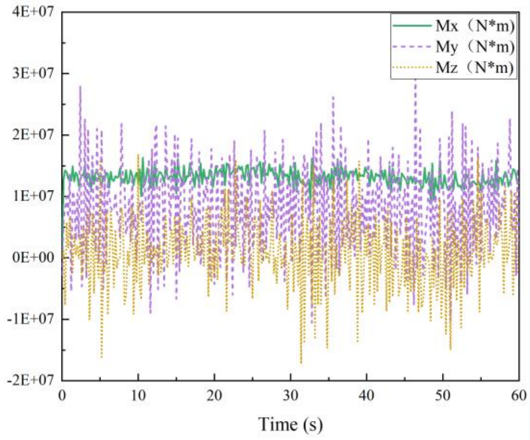

(b) moments

Fig. 4 Time history of tower top wind load

2.3. *Dynamic buckling failure of tower*

Fig. 5 shows the structural Mises stress of instability collapse failure of wind turbine tower under the flange thickness of 20mm and the stiffener is TW 75×150 section steel.

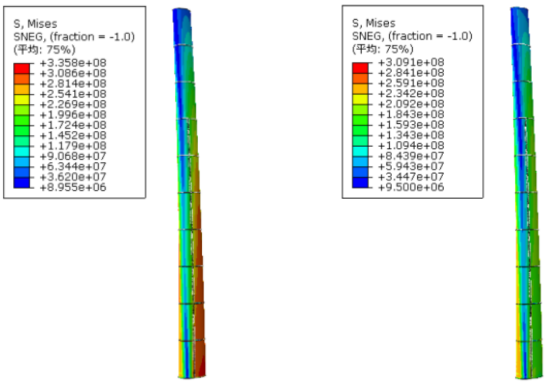

(a) 10s (b) 20s

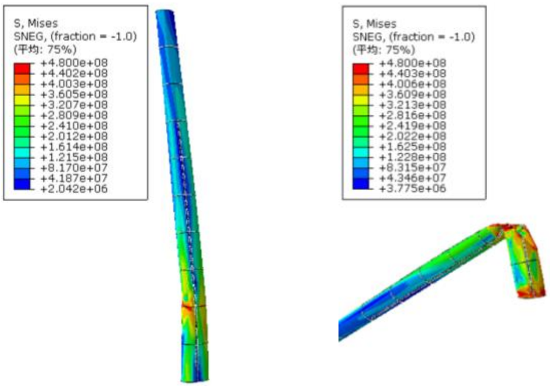

(c) 25s (d) 30s

Fig. 5 Stress of wind turbine tower structure at different times

It can be seen from Fig. 5 that the structure has dynamic instability and collapse failure after 20s. The failure position is at the connection of tower section 2 and tower section 3, with an elevation of 17.52m. The section thickness changes greatly here (the section thickness of tower section 2 is 0.027m, and the section thickness of tower section 3 is 0.026m). The stiffness is discontinuous, and dynamic buckling instability is easy to occur.

3. Weld simulation and material plastic damage theory

3.1. *Finite element simulation of weld*

On the premise of multi-scale modeling, the weld is introduced into the local structure. By comparing with the non-weld model, the influence of the weld on the dynamic collapse of the structure is studied. Here, the inherent strain method is used to simulate the weld. In this paper, the equivalent trapezoidal strain method proposed in reference [7] is used to overcome the problem that the calculation of constant strain method is difficult to converge due to the sudden change of strain field at the edge of the model, as shown in Fig. 6.

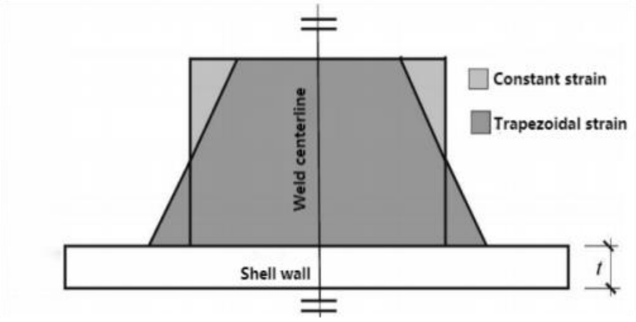

Fig. 6 Schematic diagram of inherent strain method

The 5m tower section at the bottom of a 5MW wind turbine is used for modeling. The tower barrel has a radius of 3m and a thickness of 40mm. The shell element SR4 is used for modeling the wall. The material is Q355 steel with a yield strength of 325MPa. Loading inherent strain value, the tower barrel produces the welding residual stress and deformation allowed by the specification. The comparison between the residual stress distribution along the vertical weld direction of the shell and the measured welding data in reference [8] is shown in Fig. 7. The peak value of residual stress through inherent strain simulation is 320MPa, and the peak value of measured data in reference [8] is 275MPa. The curve is in good agreement within 50mm from the weld line. Although the stress outside 50mm is slightly different, the stress values are small, all less than 50MPa, and the difference is within 25MPa. It can be considered that the inherent strain method can meet the simulation requirements of wind turbine tower weld.

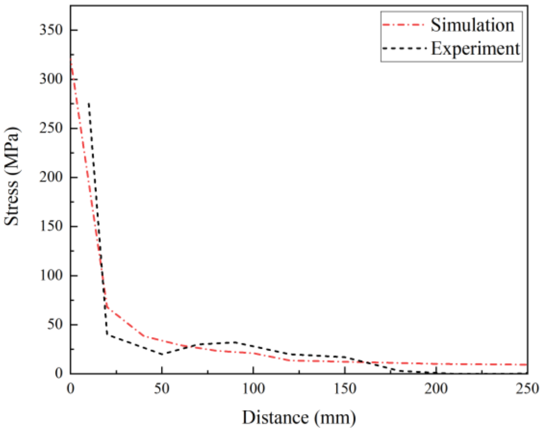

Fig. 7 Comparison of residual stress

3.2. Material micro plastic damage initiation criteria

The internal micro fracture of metal materials is the main reason for the decline of material bearing capacity and stiffness. Due to the expansion of internal micro trauma surface, the effective area of external load borne by metal materials continues to decrease, resulting in the loss of metal material bearing capacity and stiffness. Therefore, for metal materials, the moment of micro fracture in the material is the moment when the material enters the damage state.

Based on Xue and Wierzbicki [9-10] damage criterion as the damage initiation criterion of structural steel, this paper selects the simplified stress triaxial damage initiation criterion suitable for explaining the damage mechanism of structural steel proposed by Li W.C. [11] and Zhou T.H. [5] on the basis of Bao and Wierzbicki [4] equivalent plastic damage strain and stress triaxial path. Through the round bar tensile test of Q355 steel, the plastic damage evolution criterion of steel is determined, so as to provide a suitable material plastic damage theoretical model for the later analysis of the bearing capacity of wind turbine tower.

Xue and Wierzbicki metal material damage initiation criterion considers that the over accumulated equivalent plastic strain is the main reason for the degradation of stress and stiffness of metal materials. When the equivalent plastic strain of metal material reaches a certain critical value $\overline{\varepsilon}_0^{pl}$, micro fracture occurs in the material, and then enters the plastic damage state. Among them, the critical value of the equivalent plastic strain at the micro fracture time of the material $\overline{\varepsilon}_0^{pl}$ is defined as the equivalent plastic damage strain. How to determine the equivalent plastic damage strain of the material is the main purpose of Xue and Wierzbicki damage initiation criterion. The damage criterion holds that the equivalent plastic damage strain of metal materials $\overline{\varepsilon}_0^{pl}$ is a function of material stress triaxial and stress state parameters:

$$\overline{\varepsilon_0}^{pl} = F(\eta,\xi) \tag{1}$$

$$\eta = \sigma_m/\sigma \tag{2}$$

$$\sigma_m = \frac{1}{3}(\sigma_1 + \sigma_2 + \sigma_3) \tag{3}$$

$$\sigma = \sqrt{\frac{1}{2}[(\sigma_1-\sigma_2)^2 + (\sigma_2-\sigma_3)^2 + (\sigma_3-\sigma_1)^2]} \tag{4}$$

$$\xi = \frac{27}{2}\frac{J_3}{\sigma^3} \tag{5}$$

Where, σ_m and σ are hydrostatic stress and Mises equivalent stress of the material. σ_1、σ_2、σ_3 respectively is the principal stress in three directions of the material; J_3 is the third deviatoric stress which can be expressed as:

$$J_3 = \sigma_1\sigma_2\sigma_3 \tag{6}$$

In Bao and Wierzbicki damage criterion, the damage strain function needs to be calibrated by the fracture of various notch specimens. Yu [12] simplified the path of steel stress triaxial and equivalent plastic damage strain through analysis, removed the parameteron under the premise of ensuring accuracy, and greatly reduced the difficulty of determining the parameters, The simplified material equivalent plastic damage strain can be expressed as follows.

$$\overline{\varepsilon}_0^{pl} = \begin{cases} \infty \\ C_1/(1+3\eta) \\ C_1+(C_2-C_1)(\eta/\eta_0)^2 \\ C_2\eta_0/\eta \end{cases} \tag{7}$$

Where η_0 is the limit value of the fracture performance of the material in high stress triaxial and low stress triaxial, C_1 and C_2 is the material parameter. From the formula, it can be seen that the plastic damage strain of material can be expressed as a piece-wise function of stress triaxial. The conversion relationship between C_1 and C_2 is shown in formula (8). C_2 is the equivalent plastic strain of the material round bar specimen during uniaxial tensile fracture, the parameters can be determined by testing the reduced area A_R of the section at the fracture of the smooth round bar specimen. K, n is the material hardening parameter, which can be calculated from the material stress-strain curve.

$$C_1 = C_2(\sqrt{3}/2)^{1/n} \tag{8}$$

$$C_2 = -\ln(1-A_R) \tag{9}$$

$$\sigma = K(\varepsilon)^n \tag{10}$$

The simplified curve path of equivalent plastic damage strain and stress triaxial of steel is shown in Fig. 8.

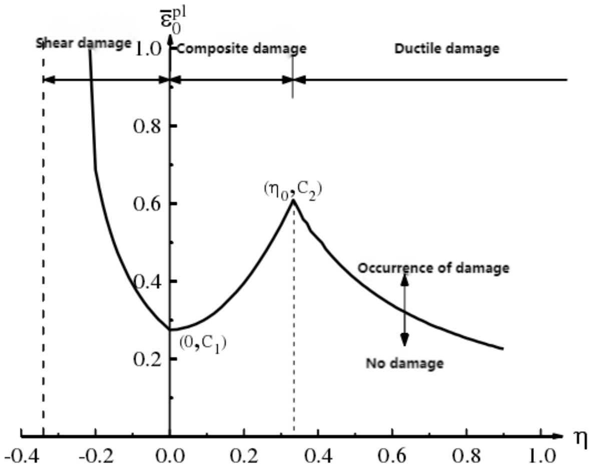

Fig. 8 Stress triaxial and equivalent plastic damage strain path

3.3. Micro plastic damage evolution of materials

The material plastic damage initiation criterion only gives the equivalent plastic strain position when the steel damage occurs, but does not give the stress decline path after the damage occurs. After the steel enters the damage stage, the bearing capacity and stiffness of the material decay, and the damage factor can represent the attenuation degree of the material stress and elastic modulus, Therefore, the relationship between material residual stress, residual elastic modulus and damage factor *D* can be expressed by the following formula:

$$\overline{\sigma} = (1 - D)\sigma \tag{11}$$

$$\overline{E} = (1 - D)E \tag{12}$$

It can be seen from formulas 11 and 12 that when the damage factor *D*=0, the material does not enter the damage state, and the stiffness and bearing capacity of the material do not degrade. When *D*>0, the material begins to enter the damage state, and the stiffness and bearing capacity of the material degrade. When *D*=1, the steel is destroyed. At this time, the residual modulus and residual stress of the material are reduced to 0. The damage factor function of steel is determined through the round bar tensile test of steel, and the material plastic displacement and failure plastic displacement $\overline{u}^{pl}$are introduced to determine the damage factor *D*. the difference between the total tensile displacement and elastic displacement of the member is defined as the plastic displacement$\overline{u}^{pl}$, the plastic displacement when the member is completely damaged is defined as the failure plastic displacement$\overline{u}_f$, and the damage factor *D* can be expressed as the function of $\overline{u}^{pl}/\overline{u}_f$:

$$D = F\left(\overline{u}^{pl}/\overline{u}_f\right) \tag{13}$$

Reference [13] once expressed the damage factor *D* as a linear function of $\overline{u}^{pl}/\overline{u}_f$. This method has obvious approximation. After the steel specimen reaches the peak stress, there will be obvious necking phenomenon, which is reflected in that the decline path after the steel tensile peak stress is not a straight line, but an approximate power exponential curve. Through the tensile test of Q355 steel round bar in document [13] and the fitting of the function of steel damage factor D by Zhou T.H. [4], the damage factor *D* can be expressed as the power function of the ratio of plastic displacement to ultimate failure displacement of Q355 steel:

$$D = 1.3\left(\frac{\overline{u}^{pl}}{\overline{u}_f}\right)^{7.6} \tag{14}$$

According to the above material plastic damage theory, the values of material parameters are as follows:

n=0.189, K=876MPa, C_1=0.293, C_2=0.63, η_0=1/3, $\overline{u}$=0.02m

4. Damage and collapse mechanism analysis of wind turbine based on multi-scale modeling

4.1. Development of wind turbine damage

Due to the introduction of fatigue damage theory in the model, the local damage location and development degree of the wind turbine under extreme wind conditions can be predicted. With the continuous accumulation of material equivalent plastic strain, some elements finally reach the equivalent plastic strain at the initial damage, and then enter the damage state. Then, the bearing capacity of the damaged elements begins to deteriorate, which is manifested by the increase of damage factor *D*, The DUCTCRT index in ABAQUS is the damage initiation index of the material, which is used to determine the damage state of the element. If the parameter is equal to 1, it indicates that the element enters the damage state; The SDEG index is the damage factor *D*, which is used to measure the degradation degree of the stiffness and strength of the material. This index is 1, indicating the complete loss of the stiffness and strength of the material, which can basically be regarded as the fracture of the material.

Fig. 9 and Fig. 10 shows the structural damage development distributions of the two models with increasing time in dynamic time history analysis are given. From Fig. 9 it can be seen that the damage of the weld model first appears in the weld area. With the passage of time, the damage area will expand circumferentially along the weld, and the damage at the weld is particularly obvious. The DUCTCRT index of the damage state will be further increased on the original basis. With the passage of time, the DUCTCRT index of the weld area will reach 1, and most of the structure will be damaged. The damage is concentrated in the weld area. From Fig. 10 it can be seen that due to the large change of section stiffness the dynamic buckling damage is easy to occur. With the passage of time, the structural damage area gradually expands, and the damage is mainly concentrated at the connection of tower section. The damage location of the structure is basically consistent with the buckling failure location.

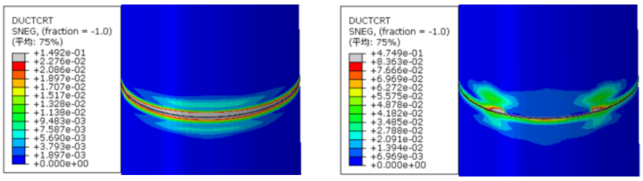

(a) Damage position of weld model at 10s (b) Damage position of weld model at 15s

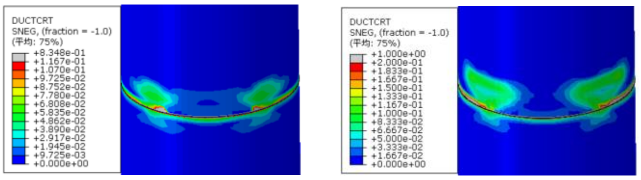

(c) Damage position of weld model at 20s (d) Damage position of weld model at 25s

Fig. 9 Development of damaged parts of weld model

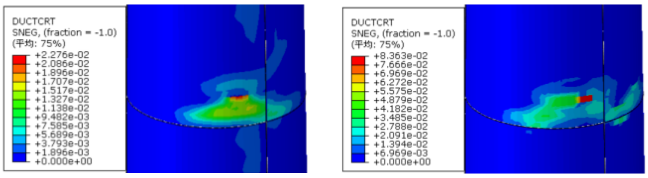

(a) Damage position of no weld model at 10s (b) Damage position of no weld model at 15s

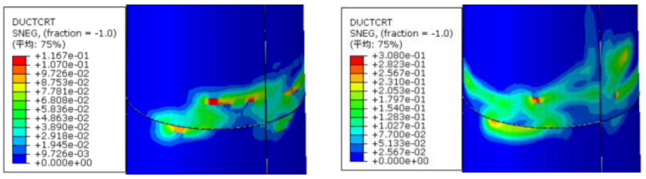

(c) Damage position of no weld model at 20s (d) Damage position of no weld model at 25s

Fig. 10 Development of damaged parts of no weld model

In terms of the damage development speed, the weld of the weld model enters the damage state fastest, mainly because a certain plastic strain has been accumulated at the weld, so it can enter the damage state faster.

In order to compare the influence of welds on the degree of structural damage, Fig. 11 shows the comparison of structural damage factor SDEG under different models. There are obvious differences in structural damage at the weld. According to the damage factor SDEG index, the stiffness and elastic modulus of the weld model are completely degraded along the weld at 25 seconds, which can be approximately considered that the structure is cracked, while the material is not completely degraded without the weld model at 25 seconds.

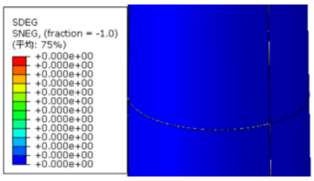

(a) Damage degree of model structure without weld at 25s

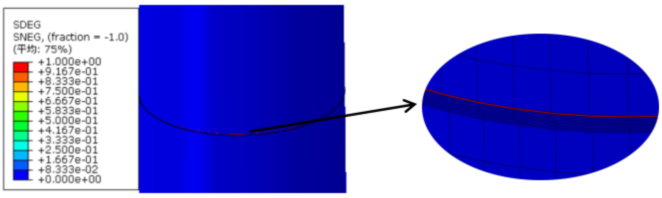

(b) Damage degree of weld model structure at 25s

Fig. 11 Comparison of damage degree

4.2. Stiffener damage development

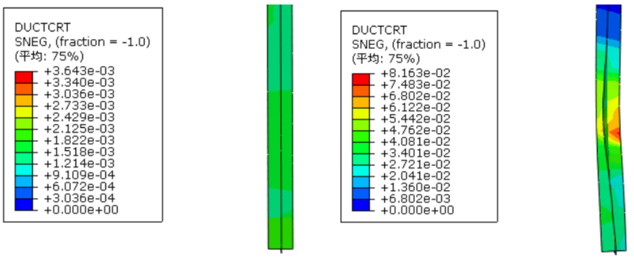

(a) Damage position of stiffener at 10s (b) Damage position of stiffener at 15s

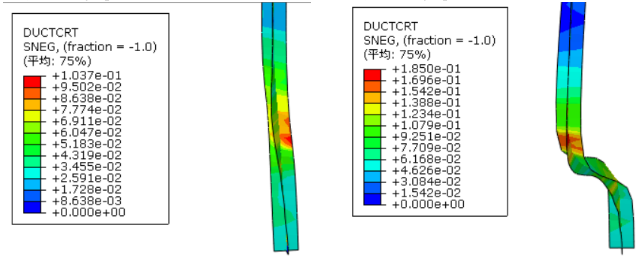

(c) Damage position of stiffener at 20s (d) Damage position of stiffener at 25s

Fig. 12 Stiffener damage development

Fig. 12 shows the development of stiffener damage with the increase of load time history in the weld model. It can be seen from the figure that the damage of stiffener is mainly concentrated in the connection position of tower, and there will be no damage in other positions. With the increase of wind load time history, the deformation and damage of stiffener also increase. At 25s, the DUCTCRT value of tower structure reaches 1, while the stiffener is only 0.185, indicating that the damage degree of tower is much greater than that of stiffener at the same time. Considering that the size of the stiffening rib under this stiffening scheme is small, the stiffening effect on the tower is not obvious.

5. Conclusions

With the aim to investigate the dynamic load carrying capacity and the collapse failure mechanism of wind turbine tower with assembled internal stiffening , this paper analyzed the influence of weld by multi-scale modeling, combined with the plastic damage theory of steel materials. The following points were concluded:

1) The damage position of weld model and non weld model is basically the same as that of structural dynamic buckling failure. The damage of weld model is mainly concentrated in the area near the weld, and the damage of non-weld model is mainly concentrated in the position where the variable section stiffness of tower is discontinuous.

2) With the increase of wind load time history, the area of structural damage area also increases gradually. The weld model develops along the weld circumferential direction, and the damage at the weld develops the fastest. The non-weld model shows irregular damage development at the discontinuity of structural stiffness, and the damage degree of the weld model is greater than that of the non weld model at the same time.

3) The stiffener at the connection of tower and tube will be damaged first, and the rest will not be damaged. With the increase of wind load time history, the deformation and damage of stiffener will also increase. At the same time, the damage degree of stiffener is much less than that of tower and tube.

Acknowledgments

This project is jointly supported by Projects of International (Regional) Cooperation and Exchanges NSFC (52211530086) and Jiangsu Provincial Science Fund for Distinguished Young Scholars (BK20211518), the opinions, findings, and conclusions or recommendations expressed in this paper are those of the authors and do not necessarily reflect the views of the sponsors.

References

[1] Wang M.G., Huang Y., “Study on wind stability of two-way multi ribbed shell structure”, Engineering mechanics, 2000 (04): 44-49.
[2] Yan H.X., “Combined with an example, the local stability of large diameter tower is studied”, Special structure, 2014,31 (04): 41-47.
[3] Rotter J.M., Sadowski A.J., Chen L., “Nonlinear stability of thin elastic cylinders of different length under global bending”, International Journal of Solids & Structures, 2014, 51(15-16): 2826-2839.
[4] Bao Y., Wierzbicki T., “On fracture locus in the equivalent strain and stress triaxiality space”, International Journal of Mechanical Sciences, 2004, 46(1): 81-98.
[5] Zhou T.H., Li W.C., Guan Y., Bai L., “Damage analysis of steel frame under cyclic loading based on stress triaxiality”, Engineering mechanics, 2014,31 (07): 146-155.
[6] Duan H.X., Li S.J., Liu Y.X., “Numerical simulation of damage process of steel structure under earthquake”, Engineering mechanics, 2011,28 (02): 198-204.
[7] Hübner A., Teng J.G., and Saal H., “Buckling behavior of large steel cylinders with patterned welds”, International Journal of Pressure Vessels and Piping, 2006, 83: 13-26.
[8] Yang N., Lin S., Su C., “Study on residual stress and damage distribution of thick plate welded joints”, Journal of Hunan University (Natural Science Edition), 2014,41 (11): 24-31.
[9] Wierzbicki T., Xue L., “On the effect of the third invariant of the stress deviator on ductile fracture”, Cambridge, MA, USA: MIT Impact and Crashworthiness Lab, 2005.
[10] Xue L., “Damage accumulation and fracture initiation in uncracked ductile solids under triaxial loading—Part I:Pressure sensitivity and Lode dependence”, Cambridge, MA, USA: MIT Impact and Crashworthiness Lab, 2005.
[11] Li W.C., Zhou T.H., Liao F.F., Lu Y., “Application of ductile damage criterion in dynamic time history analysis of steel frame structures”, Building structure, 2018, 48 (22): 21-27.
[12] Yu H.L., Jeong D.Y., “Application of a stress triaxiality dependent fracture criterion in the finite element analysis of unnotched Charpy specimens”, Theoretical and Applied Fracture Mechanics, 2010, 54(1): 54—62.
[13] Fang F.L., Wang W., Chen Y.Y., “Experimental Study to Calibrate Monotonic Micro mechanics-Based Fracture Models of Q345 Steel”, Advanced Materials Research, 2011, 1278(524):545-550.